

TOHOKU UNIVERSITY
Graduate School of Engineering

Effects of Magnetic-Field on Elemental Process for Microstructural
Development of Iron-Based Polycrystalline Materials
(鉄系多結晶材料の微細組織形成基礎過程に及ぼす磁場効果)

A dissertation submitted for the degree of Doctor of Philosophy (Engineering)

Department of Nanomechanics

by

Hiromichi FUJII

January 16, 2009

Effects of magnetic-field on elemental process for microstructural development of iron-based polycrystalline materials

Hiromichi FUJII

Abstract

Since the bulk properties such as mechanical and functional properties of polycrystalline materials are strongly affected by microstructure, the control and optimization of the microstructure are essential to obtain desirable properties and to develop high performance polycrystalline materials. The application of external fields such as stress, electric and magnetic fields have been noticed as a useful technique of controlling microstructure of structural and functional materials. However a magnetic field has never been applied to industrial technologies in the materials processing due to the difficulty of generating strong magnetic field enough to affect microstructural evolution of materials. For this reason, there were only a few reports of the observation of microstructural changes under a magnetic field during annealing, which were motivated not by industrial application, but by the academic interests. Then strategies for controlling microstructures and properties of materials by the application of a magnetic field have been suggested particularly since the helium-free superconducting magnet was developed in 1990's. Nowadays, the application of a strong magnetic field enough to affect the microstructural evolution of materials can be obtained without difficulty; the generators which can apply more than 10 T magnetic field are available. Although there have been reported many interesting metallurgical phenomena under a magnetic field, most of those mechanisms of magnetic field effects have not yet been revealed. The application based on the fundamental research infrastructure is essential to extensively apply magnetic processing to the technologies for materials development. Therefore, to conduct the systematic studies of EPM, the fundamental studies are required to clarify the elemental processes for microstructural development under a magnetic field.

The aim of current work is to obtain comprehensive knowledge of the mechanism of magnetic field effects on microstructural evolution in iron-based materials in order to conduct the structural and functional controls by the application of strong magnetic fields. The effects of strong magnetic fields on fundamental metallurgical phenomena (diffusion, grain nucleation and grain growth) were investigated to obtain comprehensive knowledge of the mechanism of the effects of magnetic field on microstructural evolution in iron-based materials. In addition, the fundamental physical properties of grain boundaries of iron closely concerning with the grain nucleation and growth were also investigated. The following results and conclusions were obtained in each chapter.

In Chapter 2, some experiments were conducted to investigate the effect of a magnetic field on the carbon diffusion and its solid solubility in pure iron. Measurements of carbon diffusion in iron under a magnetic field and the field gradient were conducted with the explosive welded diffusion couples of pure

iron (99.9 %) and eutectoid steel (Fe-0.87mass%C). The carbon diffusivities in pure iron were evaluated from the penetration profiles of carbon into iron measured by secondary ionization mass spectroscopy (SIMS) under non-magnetic and a magnetic field conditions using the solution of the Fick's 2nd law. The diffusivity of carbon in both α - and γ -iron decreased in a 6 T magnetic field by approximately 70 % and 40 %, respectively. The decrease in diffusivity is more significant in α -Fe than that in γ -Fe. The activation energy of carbon diffusion was less dependent on a magnetic field. The diffusion coefficients at 1150K was found to be lower than the values which was expected from the extrapolating the temperature dependence of diffusivity for without and with a 6 T magnetic field. This would indicate that the carbon penetration into α -Fe may have caused α -Fe to transform into γ -Fe, in which the carbon diffusivity is lower than that in α -Fe in the vicinity of the interface. The logarithm of carbon diffusion coefficient in α -Fe is a linear function of a magnetic field strength. This suggests that the activation entropy of diffusion decreases with increase in magnetic field. Consequently, the diffusivity of carbon in iron would decrease in a magnetic field. The decrease in activation entropy would be due to the magnetostriction of α -Fe. A "negative" magnetic field gradient can enhance the carbon diffusion in α -iron by approximately 115 %. The magnetic free energy gradient in α -Fe would give rise to increase in the flux of carbon atoms. The solid solubility limit of carbon increased by twice when a 6 T magnetic field was applied at the ferromagnetic temperature ranging from 950 K to 1000 K. The solid solubility limit of carbon will shift to higher concentration under a static magnetic field, as the free energy curve of ferrite phase will be lowered. In addition, the solid solubility limit of carbon increased with the increase in magnetic field strength and has a maximum value at 4 T magnetic field.

In Chapter 3, the physical and mathematical models were constructed to clarify the mechanism of the effect of a static magnetic field and a field gradient on the carbon diffusion in pure iron. These analyses were compared with experimental results obtained in Chapter 2 and the effects of a magnetic field and a magnetic field gradient on the carbon diffusivity in iron were discussed. At first, the effect of a static magnetic field on carbon diffusion was discussed from a viewpoint of site occupancy of carbon atoms in bcc iron using dual occupancy model. The carbon atoms occupy the octahedral and tetrahedral sites in bcc iron in this model. From the experimental results in Chapter 2, the fraction of the octahedral site occupancies was expected to increase under a magnetic field due to the change of entropy. The carbon diffusivity calculated on the basis of dual occupancy model was in good agreement with the experimental results under non-magnetic conditions. Whereas the carbon diffusivity calculated on the basis of assumption that all carbon atoms located at the octahedral sites was in good agreement with the experimental results under a 6 T magnetic field. The difference between the entropy of carbon atoms in tetrahedral and octahedral sites decreases by the application of a magnetic field due to the magnetostriction of ferromagnetic α -iron and its effect on site occupancy, so that the carbon diffusion would be retarded. The next, the effect of a magnetic field gradient on carbon diffusion was analyzed on the basis of the Fick's law with potential gradient. Numerically, it was proven that the increase in carbon diffusion by the application of a magnetic field gradient was caused by the increase in flux of carbon atoms induced by the magnetic potential gradient. The diffusion coefficient was found to increase monotonically with the increase in strength of magnetic field gradient. In addition, the diffusion coefficient could be described as the quadratic

function of a magnetic field gradient.

In Chapter 4, the effect of a magnetic field on the crystallization from amorphous $\text{Fe}_{78}\text{Si}_9\text{B}_{13}$ and $\text{Fe}_{73.5}\text{Si}_{13.5}\text{B}_9\text{Nb}_3\text{Cu}_1$ alloys has been studied with the aim of observing the nucleation and growth of α -Fe grains in the amorphous matrix under a magnetic field. The crystallization from an $\text{Fe}_{78}\text{Si}_9\text{B}_{13}$ amorphous alloy under a magnetic field of 6 T at 853 K causes a development of a {110} sharp texture when a magnetic field is applied in a direction parallel to the specimen surface. The <001> orientation, which corresponds to the easy magnetization direction in the {110} textured grain structure, lies randomly in the {110} ribbon surface. The {110} grains preferentially grow, and the fraction of crystallized volume is increased by the application of a magnetic field of 6 T in $\text{Fe}_{78}\text{Si}_9\text{B}_{13}$ alloy. A magnetic field of 6 T could decrease the crystallization rate at the temperature below the crystallization temperature and increase that at the temperature above the crystallization temperature. Furthermore, there would be threshold of magnetic field strength between 4 and 6 T where the magnetic field effects on the crystallization rate would appear. The crystallization of $\text{Fe}_{73.5}\text{Si}_{13.5}\text{B}_9\text{Nb}_3\text{Cu}_1$ amorphous alloy under a magnetic field also enhanced a {110} texture formation of α -Fe(Si) grains. The preferential nucleation of {110} oriented grains due to a magnetic field would be predominantly responsible for the texture formation rather than the preferential grain growth. The application of a magnetic field increased the nanocrystallization kinetics, particularly the nucleation rate of the ferromagnetic α -Fe(Si) grains from the paramagnetic $\text{Fe}_{73.5}\text{Si}_{13.5}\text{B}_9\text{Nb}_3\text{Cu}_1$ amorphous phase. The volume fraction of the nanocrystalline α -Fe(Si) phase was increased with the increase in magnetic-field strength. A primary role of the magnetic field may enhance the kinetics of nanocrystallization rather than modify the thermodynamics.

In Chapter 5, the grain boundary energy in iron with the purity of 99.9mass% under a magnetic field was investigated with particular emphasis on the effect of temperature and grain boundary character. From ICP qualitative analyses, the 99.9% iron was found to include Si, Mn, Co and Cu as impurities. The grain boundary energy was evaluated by the dihedral angle obtained from the cross-sectional profiles of grain boundary grooves measured by atomic force microscopy after determination of grain boundary character on the basis of the coincidence site lattice theory using FE-SEM/EBSD/OIM technique. Grain boundary energy in the iron increased with the increase in temperature under non magnetic conditions. On the other hand, the energy decreased with the increase in temperature under a 6 T magnetic field. This would be due to the retardation of grain boundary segregation of impurities by the application of a magnetic field. In addition, the energy discontinuously changed around the Curie temperature due to the difference between energetic contribution of the magnetic field to the Gibbs free energy in ferromagnetic state and that in paramagnetic state. The next, the effect of a magnetic field on the misorientation angle dependence of grain boundary energies was investigated. It was found that the energy cusps occurred at $\Sigma 3$, $\Sigma 7$ and $\Sigma 13$ CSL boundaries, irrespective of whether a magnetic field being applied. In addition, random grain boundary energy increased and its misorientation dependence was enhanced under a magnetic field in the 99.9%Fe. This is also due to retardation of solute and impurities segregation to grain boundaries by a magnetic field.

In Chapter 6, the electron energy loss spectroscopy was applied to measure the local magnetic moment near grain boundaries in pure iron and Fe-Sn alloy. The grain boundaries are characterized on the basis of the coincidence site lattice theory. To make standard curve for determination of the magnetic

moment from EELS data, the measurement of EELS spectra was conducted in pure iron and titanium, which are well-known magnetic moment. The white line ratios of them obtained in this study were in good agreement with the previous data. The relationship between white-line ratio of EELS spectrum and the local magnetic moment was revealed using linearization method. The local magnetic moment at random grain boundary increased by 5 - 9 % in comparison with the moment at neighboring grains, whereas the moment at $\Sigma 3$ grain boundary did not significantly change. The $\Sigma 3$ grain boundary is known to be geometrically coherent boundary, whereas the random boundary is incoherent boundary. Therefore the local magnetic moment would increase with the increase in the free volume between the atoms at the grain boundary due to its geometrical disordered structure. The corrected local magnetic moment at the random grain boundary, which can be obtained by the subtraction of the EELS spectrum occurred from grains, increased by approximately 20 % in comparison with the moment at grains. This is in good agreement with the previous calculation result. The local magnetic moments at grain boundaries do not change in the Fe-0.8at%Sn alloy. This would be due to the relaxation of geometrical disordered structure at grain boundaries by the grain boundary segregation of tin atoms.

In Chapter 7, this chapter gives concluding remarks of this study.

Contents

Chapter 1	Introduction	1
1.1	Backgrounds	1
1.2	Previous reports on magnetic field effect on metallurgical phenomena	3
1.2.1	Liquid/solid reaction	5
(a)	Solidification	5
(b)	Texture	5
1.2.2	Solid/solid reaction	6
(a)	Recrystallization, grain growth and texture	6
(b)	Phase transformation	8
(c)	Precipitation	10
(d)	Sintering	11
(e)	Nucleation and crystallization	12
(f)	Diffusion	12
1.3	Objectives of this study	14
References		17

Chapter 2	Diffusion in iron under a magnetic field and a magnetic field gradient	21
2.1	Introduction	21
2.2	Experimental	23
2.2.1	Material and preparation of diffusion couple	23
2.2.2	Diffusion annealing under a magnetic field and a magnetic field gradient	24
2.2.3	Measurement of diffusion coefficients	26
2.3	Results and discussion	28
2.3.1	Penetration profiles of carbon atoms to pure iron	28
2.3.2	Diffusivity of carbon in iron under a static magnetic field	30
(a)	Temperature dependence	30
(b)	Field strength dependence	36
2.3.3	Diffusivity of carbon in iron under a magnetic field gradient	39
2.3.4	Solid solubility of carbon in iron under a magnetic field	44
2.4	Summary	48
References		49

Chapter 3 Mathematical modeling of diffusion process in iron under a magnetic field	51
3.1 Introduction	51
3.2 Physical modeling of carbon diffusion in iron on the basis of dual occupancy model	52
3.2.1 Site occupancy of carbon atoms in bcc iron	52
3.2.2 Carbon diffusivity under a magnetic field	54
3.2.3 Mechanism of carbon diffusion in iron under a magnetic field	57
3.3 Numerical analysis of carbon diffusion in iron under a magnetic field gradient	58
3.3.1 Physical model and basic equations	58
3.3.2 Effect of magnetic potential gradient on carbon diffusion	62
3.4 Summary	68
References	69
Chapter 4 Nucleation and growth under a magnetic field	71
4.1 Introduction	71
4.2 Experimental	72
4.2.1 Materials and specimens	72
4.2.2 Annealing conditions for crystallization from amorphous alloys under a magnetic field	73
4.2.3 Microstructure analysis	73
(a) XRD analysis	73
(b) FE-SEM/EBSD/OIM observation	78
(c) TEM observation	78
4.3 Results and discussion	81
4.3.1 Crystallization of Fe ₇₈ Si ₉ B ₁₃ amorphous alloy under a magnetic field	81
(a) Crystallization under a magnetic field	81
(b) Control of grain orientation distribution on the application of a magnetic field	86
4.3.2 Nanocrystallization of Fe _{73.5} Si _{13.5} B ₉ Nb ₃ Cu alloy under a magnetic field	91
(a) Microstructural evolution during crystallization under a magnetic field	91
(b) Volume fraction of nanocrystallized grains	97
(c) Nucleation and growth kinetics under a magnetic field	99
4.3.3 Origin of the influence of a magnetic field on crystallization kinetics and texture formation	103

4.4 Summary	106
References	107
Chapter 5 Effect of a magnetic field on grain boundary energy	109
5.1 Introduction	109
5.2 Experimental	110
5.2.1 Material and specimen	110
5.2.2 Determination of grain boundary character	111
5.2.3 Measurements of grain boundary energy	114
5.3 Results and discussion	116
5.3.1 Measurement of the cross-sectional profiles of grain boundary grooves	116
5.3.2 Temperature dependence of grain boundary energy in iron	116
5.3.3 Effect of a magnetic field on temperature dependence of grain boundary energy in iron	120
5.3.4 Effect of a magnetic field on misorientation dependence of grain boundary energy	123
5.4 Summary	127
References	128
Chapter 6 Magnetism of grain boundary	129
6.1 Introduction	129
6.2 Experimental	130
6.2.1 Preparation of the specimens	130
6.2.2 Measurement of white lines using TEM-EELS method	131
6.2.3 Evaluation of magnetic moment	133
6.3 Results and discussion	135
6.3.1 Analysis of EELS spectra	135
6.3.2 Change of magnetic moment of atoms near the grain boundaries	139
6.4 Summary	145
References	146
Chapter 7 Conclusions	147
Acknowledgement	151

Chapter 1

Introduction

1.1 Backgrounds

Since the bulk properties such as mechanical and functional properties of polycrystalline materials are strongly affected by microstructure [1-3], the control and optimization of microstructure are important to obtain desirable properties and to develop high performance polycrystalline materials [4-6]. Thermomechanical treatments have been generally applied to control microstructure in metallic materials. In recent years, there are increasing demands for materials to be served in severe environmental conditions such as higher temperature and higher stress. Then it is essential to understand the relationship between the microstructure and mechanical or functional properties of materials in the development of high performance materials. Many reports concerning with the relationship between them have been reported so far. For example, it is well-known that the yield stress of materials increases with decrease in the grain size (the Hall-Petch relationship [1]). This is attributed to the increase in the density of grain boundaries with decrease in grain size, which act as barriers to dislocation migration. In addition, Goss found that the $\{110\}<001>$ textured microstructure drastically improved the soft magnetic properties in Fe-Si alloy in 1934 [4]. This microstructure has been extensively applied as grain-oriented silicon steel to transformers and magnetic core materials. The grain-oriented silicon steel has found to improve its magnetic softness by enhancement of the degree of $\{110\}$ texture formed under optimum thermomechanical conditions. In 1984, Watanabe proposed the concept of grain boundary design and control for strong and ductile polycrystals on the basis of structure dependent intergranular properties, aiming at the control of intergranular fracture [2]. The materials processing based on this concept developed to “grain boundary engineering”, which is known as the novel method of materials development by controlling the grain boundary microstructure, such as grain boundary character distribution (GBCD), grain boundary alignment and grain boundary connectivity. As described above, the precise control of microstructure has been strongly required to develop high performance materials which support rapidly evolving science and technology. However, since it has been required to

conduct the nano-scoptic microstructural control of materials in recent years, the microstructural control only by thermomechanical treatment is insufficient to fill the demands of current science and technology. Therefore the innovative method of materials processing should be developed.

The application of external field such as stress, electric and magnetic fields have been noticed as a useful technique for controlling microstructure of structural and functional materials. This is because the external fields can selectively change the Gibbs free energies of different phases in materials and also change the kinetics of some reactions. Note that it is a magnetic field that is a vector quantity unlike temperature. Therefore the application of a magnetic field can be a promising method for controlling microstructure and properties in crystalline materials using Lorentz force, magnetization force and spin chemistry. However a magnetic field had seldom been applied to industrial technologies in the materials processing due to the difficulty in generating strong magnetic field enough to affect microstructural evolution of materials. For this reason, there previously were only a few reports of the observation of microstructural changes under a magnetic field during annealing, which were motivated not by industrial application, but by the academic interests. Then strategies for controlling microstructures and properties of materials by the application of a magnetic field have been suggested particularly since the helium-free superconducting magnet was developed in 1990's. Nowadays, the application of a strong magnetic field enough to affect the microstructural evolution of materials can be obtained without difficulty; the generators which can apply more than 10 T magnetic field are available. Recently, many studies of the effect of applied magnetic fields on metallic materials have been carried out [7-9], and research on electromagnetic processing of materials (EPM) is continuing both in Japan, USA, France and so on. Especially in Japan, the effects of a magnetic field on many metallurgical phenomena, such as solidification and phase transformation, have been energetically investigated under academic-industrial collaboration in the society for the study of "Microstructural and functional controls of materials by the application of a strong magnetic field" organized by Iron and Steel Institute of Japan (ISIJ). The term of EPM firstly appeared in the sixth international iron and steel congress held in Nagoya, Japan in 1990, and was formally used for the first time at the first symposium of EPM held in Nagoya Japan, in 1994. The EPM has started in 1980's and grown in 1990's under the tight collaboration between France and Japan. At first it was growing in the utilization of the Lorentz force mainly relating with the development of steel making processes, especially in a continuous casting. Recently the activity of EPM has found another way in the utilization of magnetization force,

under the comfortable circumstance where a high magnetic field up to around 10 T has been easily obtained owing to the development of super-conducting technologies [7].

It can be expected that the industrial application of magnetic energy will bring out the full potential of each material and will develop novel properties of materials. Especially, iron based materials which various microstructural changes and magnetic transformation intricately intertwine are important materials of the studies of microstructural and functional controls by the application of a magnetic field. Although many interesting metallurgical phenomena under a magnetic field have been reported, most of those mechanisms of magnetic field effects have not yet been revealed. The application based on the fundamental research infrastructure is essential to extensively apply magnetic processing to the technologies for materials development. Therefore, to conduct the systematic studies of EPM, fundamental studies are required to clarify the elemental processes for microstructural development under a magnetic field. The great potential of EPM application awaits future application to the development of advanced materials. The progress of this study will contribute enormously to develop engineering beyond the mechanical and materials science.

1.2 Previous reports of magnetic field effect on metallurgical phenomena

Studies of the control of microstructure of materials by the application of a magnetic field stem from a report by Pender and Jones [10]. In 1913, they reported that annealing under an alternating magnetic field exerted a beneficial influence on the microstructure, resulting in 50% increase in the permeability of iron-3.46mass% silicon steel. Since then, particularly after development of a helium-free superconducting magnet in 1990's, it has been found that a magnetic field can affect many metallurgical phenomena such as diffusion [11-22], recrystallization [23-31], grain growth (grain-boundary migration) [10, 32-38], grain boundary segregation [39-41], crystallization of amorphous alloy [42-51] and phase transformation [52-78] as summarized in Table 1-1. Thus, magnetic field applied to processing of materials (presently a term "Electromagnetic Processing of Materials, EPM" is widely used) is expected as a promising route for achievement enhanced properties.

Table 1-1 Chronological table of the studies on electromagnetic processing of materials.

	Diffusion	Phase transformation	Grain growth	Recrystallization	Crystallization from amorphous precursor	Grain boundary engineering
1913			H. Pender [10]			
1948			R. Smoluchowski [23]			
1964 W. V. Youdellis	[11]					
1967		V. D. Sadovsky				
1973		C. T. Peters				
1980			P. Hausler [42]			
1981				H. O. Martikainen [24]		
1985 H. Nakaiima	[12]	T. Kakeshita T. Kakeshita G. Sauthoff [52-53] [54] [79]				
1986					Y. Wolffus [43]	
1987						
1990				T. Watanabe [78]	Y. Otani [44]	
1991						
1992						
1993 A. V. Pokoev	[13]	T. Kakeshita [55]				
1997 A. V. Pokoev	[14]		D. A. Moldov D. A. Moldov T. Matsuzaki [32] [33] [34]	N. Masahashi [25]		
1998 D. V. Mironov	[15]	T. Kakeshita K. Mauta M. Shimotomai J. K. Choi Y. Xu H. D. Joo H. Ohtsuka C. C. Koch H. Guo W. Liu M. Enomoto K. Mauta X. J. Hao P. D. Rango X. J. Hao H. D. Joo Y. Zhang M. Enomoto Y. Zhang R. A. Jaramillo Y. D. Zhang H. Ohtsuka T. Ono H. Ohtsuka H. Ohtsuka X. J. Liu			S. Tsurekawa [47]	
1999 D. V. Mironov	[15]					
2000						
2001 A. V. Mironov			J. Probašzka A. D. Sheikh-Ali C. Bacalchuk K. Harada A. D. Sheikh-Ali T. Matsuzaki [26] [27] [28]			
2002						
2003						
2004				X. Wang [45]	S. Tsurekawa [39]	
2005 E. Rabkin	[16]	Y. Zhang M. Enomoto Y. Zhang R. A. Jaramillo Y. D. Zhang H. Ohtsuka T. Ono H. Ohtsuka H. Ohtsuka X. J. Liu	[68] [69] [70] [71] [72] [73] [74] [75] [76] [77]		T. Watanabe [46]	S. Tsurekawa [40]
2006 H. Ohtsuka	[19]		D. A. Molodov S. Bhaumik Y. Wu [29] [30] [31]	H. Fujii H. Fujii S. Tsurekawa V. A. Yardley [47] [48]		
2007 Z. F. Li	[20]		D. A. Molodov [38]			
M. Verzhakovskaya	[21]					
M. Verzhakovskaya	[22]					
2008					H. Fujii [51]	R. Sumi [41]

1.2.1 Liquid/solid reaction

(a) Solidification

The possibility of the control of mass transportation and crystals rotation by the application of a magnetic field was examined under solidification processes [79-83]. Noudem *et al.* investigated that the optimum conditions required in the melt to maximize the effect of a magnetic field on grain orientations in bulk textured $\text{Bi}_{1.8}\text{Pb}_{0.4}\text{Sr}_2\text{Ca}_{2.2}\text{Cu}_3\text{O}_{10.3+x}$ (2223) ceramics prepared by solidification under a magnetic field [79]. They obtained highly textured ceramics exhibiting critical current densities of 1450 A/cm^2 as compared to 900 A/cm^2 without a magnetic field or 882 A/cm^2 by classical sintering. Legrand *et al.* showed that the oriented specimens of Sm-Co compounds used for permanent magnets could be obtained by the processing under a magnetic field [80]. They successfully obtained the textured structure in SmCo_5 and $\text{Sm}_2\text{Co}_{17}$ binary compounds by solidification under a magnetic field of several tesla. Morikawa *et al.* proposed the theoretical expressions which determine the alignment of a precipitating phase and the crystal orientation under a magnetic field [81]. They found that the application of a magnetic field made the primary dendrite arms of MnBi in a Bi-4mass%Mn alloy align along the magnetic field, and the Al-7mass%Si-5mass%Fe intermetallic compound precipitated in a planar shape from an Al-11mass%Si-2mass%Fe molten alloy aligns in perpendicular to the magnetic field.

(b) Texture

Wu *et al.* conducted the theoretical analysis of crystal alignment of non-magnetic materials under a magnetic field [84]. They considered that there is a size range of crystal particles in which the crystals could be aligned by a strong magnetic field under actions of Brownian motion of crystals and gravity force. Chen *et al.* investigated the grain orientation of calcium HAp ceramics prepared by a novel process combining magnetic alignment and polymerization techniques [85]. They found that the HAp particles in the low viscosity slurry were aligned by magnetic force and then in situ locked via polymerization of the slurry. Wu *et al.* observed the unidirectionally oriented hydroxyapatite (HAp)/collagen composite prepared by the application of a strong magnetic field [86]. Their experiments indicated that collagen fibrils were unidirectionally oriented with weakly crystallized HAp nanocrystals closely

attached along the surfaces of the collagen fibrils under a magnetic field.

1.2.2 Solid/solid reaction

(a) Recrystallization, grain growth and texture

A magnetic field is one of the thermodynamic parameters that change free energy of a system as well as the temperature and pressure (or stress). And it is a vector quantity unlike the temperature and pressure. Therefore the application of a magnetic field shows promising abilities of the control of microstructures and mechanical and functional properties in metallic materials processing. Texture or crystallographic preferred orientation is produced as a consequence of grain boundary migration during recover, recrystallization and grain growth that is affected by magnetocrystalline anisotropy in energy, grain boundary mobility and stored free energy. Accordingly, a special interest has been paid to the expected effect of a magnetic field on the recrystallization, especially on the control of grain orientations. The magnetic annealing has been expected to offer a useful means to obtain the predetermined texture during recrystallization being applicable to improve the materials properties. Here some examples of the magnetic field effects are picked up in some details in the following sections.

Smoluchouski and Turner investigated the effect of a magnetic field on recrystallization in Fe-Co alloy and confirmed the formation of [110](100) texture by the application of a magnetic field in 1949 [23]. Bhandary and Cullity studied the texture of swaged iron wire by annealing the specimens under a weak magnetic field less than one hundredth of Tesla. They expected that the difference in magnetostrictive strains between different crystal orientations is larger than that of not fully magnetized crystals. Indeed, they observed not only <110> fiber texture, but also a substantial amount of <111> and <112> components. Thereafter Martikainen and Lindroos found that the recrystallization in armco Fe was retarded under a 1.5 T magnetic field in 1981 (Fig. 1-1 [24]). Under the applied magnetic field of 1.5 T, they observed the preferential nucleation of grains whose <100> axes, the direction of easy magnetization of iron, were parallel to the field. They explained that the retardation effect of recrystallization was caused by the low mobility of grain boundaries between matrix and oriented-grains by a magnetic field. Selective oriented recrystallized grains at the {100} due to a magnetic field of 10 T were also found in Fe-3.25%Si alloy [25]. Also, Watanabe *et al.* reported that a magnetic field retarded recrystallization and affected grain boundary character

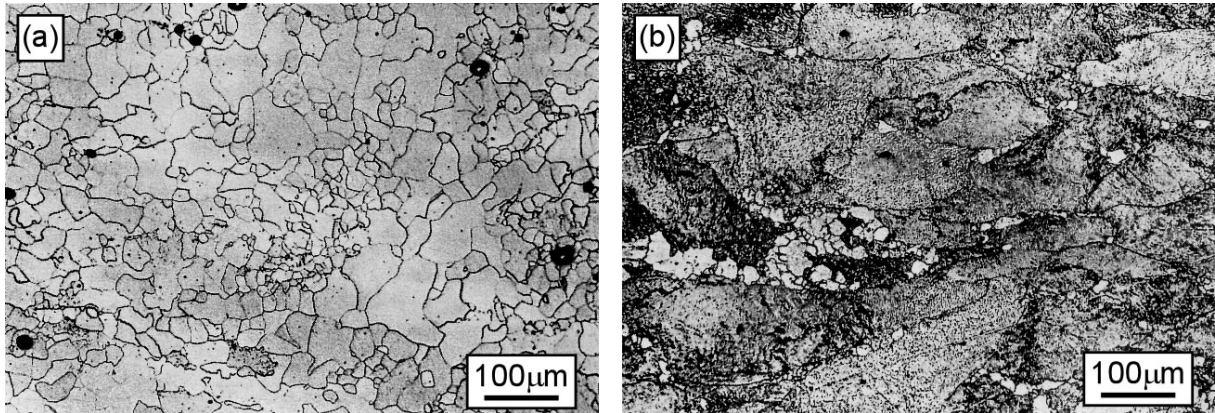


Figure 1-1 Recrystallized stage in Armco iron (a) after annealing 240s at 973K and (b) after annealing 1.8ks at 973K in a magnetic field [24].

distribution (GBCD), particularly the frequency of low angle boundaries in Fe-9at%Co alloy (Fig. 1-2 [87]). Recently Bacaltchuk *et al.* reported that {110}[001] Goss texture was increased by annealing under a magnetic field of 13 T even above Curie temperature [32]. Harada *et al.* investigated the effect of a magnetic field on grain growth in nanocrystalline nickel prepared by electrodeposition [88]. They found that a magnetic field could produce a very uniform grain boundary microstructure and could enhance grain growth at the early stage of annealing.

The effects of a magnetic field on the microstructural change have been confirmed even in non-magnetic materials. Bhaumik *et al.* observed the recrystallization behavior of cold rolled aluminum alloy 3103 under a magnetic field of 17 T [30]. They measured the crystallographic texture and grain microstructure during annealing. Consequently they revealed that a magnetic field could decrease the incubation time of recrystallization and significantly accelerate the recrystallization kinetics. Molodov *et al.* investigated the impact of a magnetic field of 17 T on texture and microstructure evolution in 75 % cold rolled commercially pure titanium [38]. They found that a magnetic field affects the grain growth kinetics by experiments and calculation and that the grains with energetically preferred orientations grow faster and their fraction becomes larger than the fraction of more slowly growing grains with disfavored orientations (Fig.1-3 [38]).

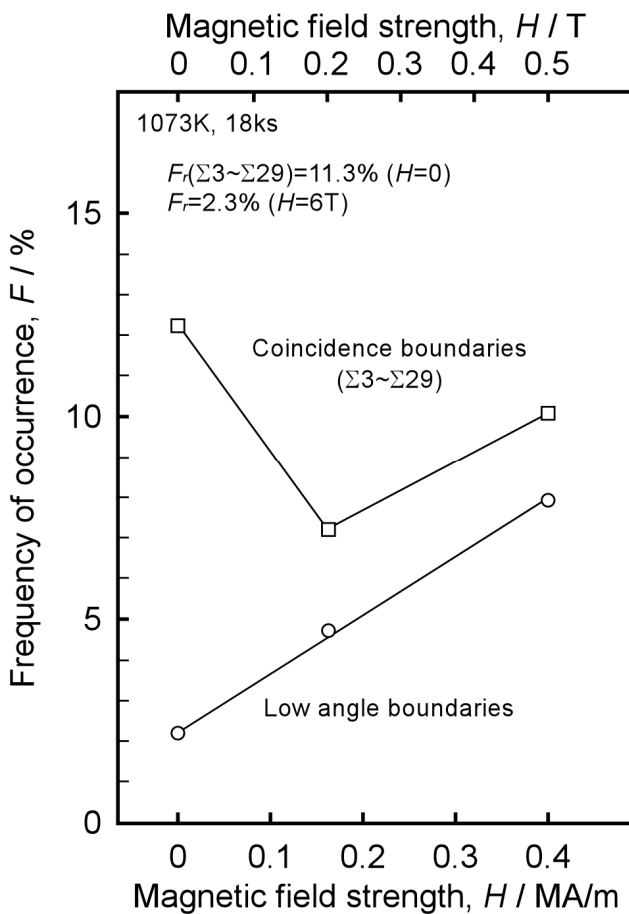


Figure 1-2 Magnetic field strength dependence of the frequency of low angle boundaries and of coincidence boundaries in magnetically annealed iron-9%cobalt polycrystals [79].

(b) Phase transformation

A magnetic field has been found to affect diffusional phase transformation in iron-based materials. Ohtsuka and coworkers [60, 61, 63] have conducted investigations of the effects of a strong magnetic field on the austenite-to-ferrite isothermal transformation in steels. They found that the transformation has been accelerated mainly because of the increase in the nucleation rate [61]. They also found that the transformed microstructure appears to align along the magnetic field direction [63]. Choi *et al.* first reported the effects of a strong magnetic field on the phase stability of plain carbon steels by their calculation [60], showing an increase in the eutectoid carbon content, critical temperatures ($A_{\text{e}1}$ and $A_{\text{e}3}$), and carbon

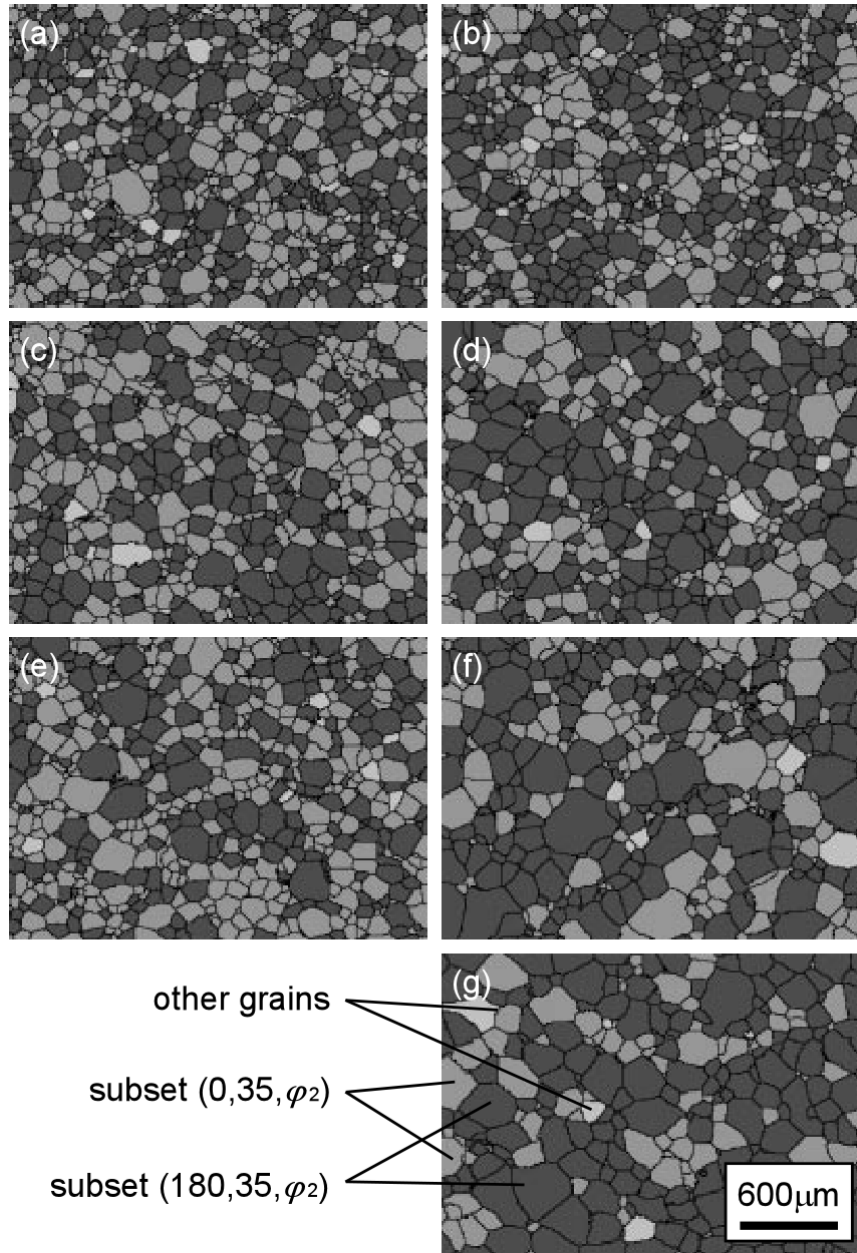


Figure 1-3 Grain microstructures of pure titanium obtained by orientation imaging with EBSD after annealing at 1023K for (a) 75 min, (c) 135 min and (e) 195 min at zero field and for 15 min at zero field and (b) 60 min, (d) 120 min, (f) 180 min and (g) 240 min in a magnetic field of 17 T [38].

solubility in ferrite phase (Fig.1-4 [60]), and the evolution of elongated ferrite phase in the direction parallel to the magnetic field direction. Maruta *et al.* revealed that the application of a magnetic field of 12 T during the α - γ phase transformation in Fe-0.1mass%C and Fe-0.6mass%C alloys yield two phase microstructures with the paramagnetic γ phase aligned as chains or columns along the direction of a magnetic field in the matrix of ferromagnetic α phase [66]. Zhang *et al.* investigated the thermodynamic and kinetic characteristics of γ - α phase transformation in medium carbon steel under a magnetic field of 6 - 14 T [69]. They found that the amount of newly formed ferrite increased and γ - α phase transformation was accelerated by the application of a magnetic field. Ono *et al.* estimated the magnetic susceptibilities of α and γ phases in Fe-C alloy from the magnetization forces measured under a magnetic field gradient and found that the nose shape in time-temperature-transformation (TTT) diagram was detected above the Curie temperature [75].

The effects of a magnetic field on martensitic transformation have been studied extensively [53-57]. Kakeshita *et al.* measured the spontaneous magnetization of parent and martensitic states as a function of temperature, which were obtained by magnetization measurements with low magnetic fields. They found that the martensitic transformation is induced at coercive force H_c and that the magnetoelastic martensitic transformation is realized in the ausaged Fe–Ni–Co–Ti alloy [53]. Furthermore they observed the entire view of a thermally-induced martensite phases in Fe-31.6at.%Ni alloy single crystals and investigated the effect of a magnetic field on the crystal orientation, formation temperature and its direction of magnetic field-induced martensites [55].

(c) Precipitation

In addition, various interesting effects of a magnetic field on any other metallurgical phenomena have been reported. Sauthoff and Pistch examined the effect of a magnetic field on precipitation of Fe_{16}N_2 particles in α -iron and demonstrated that those particles could be oriented by ageing under a magnetic field up to 2 T [89]. Fujii *et al.* investigated the effects of a magnetic field on the precipitation of ferromagnetic α -Fe particles in Cu-1.53mass%Fe alloy single crystals by the magnetic anisotropy measurement [90]. They found that the elongation of α -Fe particles to the [110] direction by annealing was accelerated under the magnetic field parallel to [110] direction. Similarly, Fujii *et al.* investigated the effects of magnetic field on precipitation of ferromagnetic cobalt particles also in Cu-2.7mass%Co single crystals [91]. They found that the cobalt particles which precipitate under a magnetic

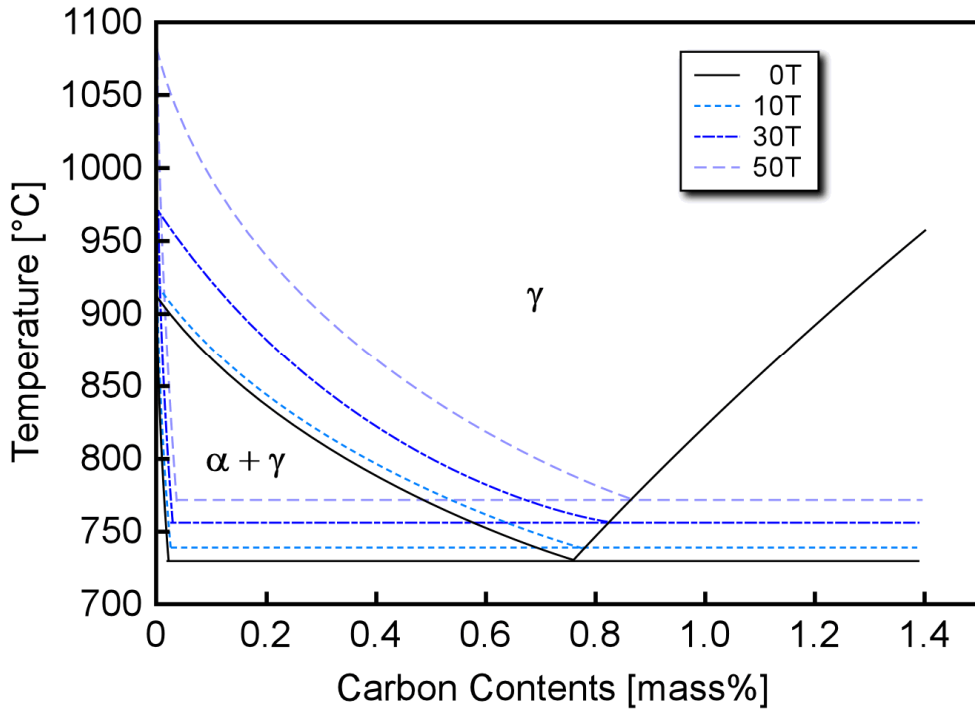


Figure 1-4 The Effect of a magnetic field on the calculated Fe-C binary phase diagram based on the molecular field theory [59].

field slightly elongate to the [001] direction parallel to the magnetic field.

(d) Sintering

Holloway *et al.* experimentally revealed that the effect of a magnetic field on the degree of grain alignment of $\text{HoBa}_2\text{Cu}_3\text{O}_{7-\delta}$ during sintering [92]. As a result, the orientation of grains was found to be controlled by the direction and magnitude of a magnetic field. Harada *et al.* revealed that the application of a magnetic field can shorten the sintering time necessary to reach a given level of densification, for example to 1/4 of the time required for 95% relative density under the nonmagnetic conditions [35, 93]. Suzuki *et al.* observed the texture development in alumina composites by slip casting under a magnetic field [94]. They found that the degree of orientation increased rapidly with increase in sintering temperature and depended on the grain size of alumina matrix under a magnetic field.

(e) Nucleation and crystallization

Many magnetic field effects on the crystallization from amorphous alloys have also been confirmed. Häußler and Baumann firstly reported that a magnetic field did not exert any influence on the crystallization temperature of amorphous Bi, Ga and Yb [42]. Wolfus *et al.* studied the effect of a magnetic field on the crystallization kinetics of Fe₈₃Si₅B₁₂ amorphous alloy [43]. They found that the growth rate of ferromagnetic α -Fe crystallites increased with increase in the magnetic field strength. The crystallization of a melt-spun Pr₂Co₁₄B amorphous ribbon under a magnetic field was performed by Otani *et al.* [44] for the purpose of achieving crystalline alignment. They found that the application of a magnetic field of 0.3 T slightly enhanced the development of the texture with easy magnetization *c*-planes oriented along the magnetic field direction during crystallization. Furthermore the magnetic field has found to significantly affect the nucleation process of crystals. Wang *et al.* [45] investigated the effect of a magnetic field on the nucleation of crystallites of diamagnetic Zr-based phases in Zr₆₂Al₁₈Ni₁₃Cu₁₇ amorphous alloy. They mentioned that difference between the permeability of the amorphous phase and that of crystalline phase suppressed the crystallization under a magnetic field.

(f) Diffusion

So far the effects of a static magnetic field on metallurgical phenomena have been discussed. Youdelis *et al.* investigated the effect of a magnetic field of 3 T on solid/solid diffusion in 1964 [11]. They revealed that a magnetic field retarded diffusion rate of copper in aluminum. On the other hand, Nakajima *et al.* did not find any effects of a magnetic field on the diffusion of nickel in titanium [12]. Pokoev and coworkers experimentally revealed that the effect of a magnetic field on the diffusivities of nickel in pure iron Fe-Si alloy and pure cobalt [13-15]. When the specimen is under a gradient magnetic field, both of a magnetic field and magnetic force are applied to the specimen simultaneously and some interesting phenomena can be observed. Nakamichi *et al.* investigated the effect of a magnetic field gradient on carbon diffusion in iron. They proposed that the magnetic free energy gradient in γ -iron matrix due to the magnetic field gradient would produce a flux of carbon atoms to achieve a homogeneous magnetic free energy in γ -iron matrix [17].

In recent years, there have been many papers on the approach to origin of magnetic field effects, which were discussed from the viewpoints of phase stability [54, 57, 60, 63], magnetism of crystals [58] or magnetostriction [44]. However, the origin of the magnetic field effects has not yet been necessarily understood and currently available basic knowledge of the application of strong magnetic fields is limited. Accordingly, it is particularly important to study fundamental metallurgical phenomena or properties under a magnetic field such as diffusion, nucleation, growth and grain boundary properties. In addition, we need more fundamental knowledge of the effect of magnetic fields on grain boundary/interphase boundary-related phenomena which always play important roles in the formation and evolution of microstructures in polycrystalline single- and multiphase materials.

1.3 Objective of this study

The aim of current work is to obtain comprehensive knowledge of the mechanism of magnetic field effects on microstructural evolution in iron-based materials in order to conduct the structural and functional control by the application of strong magnetic fields. It was focused especially on such fundamental metallurgical phenomena under a magnetic field as diffusion in solids, nucleation and growth of grains, grain boundary energy and magnetism of grain boundaries. We revealed these effects and mechanisms through experiments and theoretical analyses.

The approach and flow of this study are shown in Fig. 1-5.

In chapter 2, some experiments were conducted to investigate the effect of a magnetic field on the carbon diffusion and its solubility in pure iron. The carbon diffusivity in iron evaluated from the penetration profiles of carbon into iron measured by secondary ionization mass spectroscopy (SIMS). The diffusivities of carbon in both α - and γ -iron were decreased under a magnetic field. A decrease in the diffusivity was more significant in α -iron than that in γ -iron. The diffusivity in α -iron at 1000K exponentially decreased with the increase in a magnetic field strength. The solid solubility of carbon in α -iron increased by approximately twice under a 6 T magnetic field.

In chapter 3, physical and mathematical models were constructed to clarify the mechanism of the effect of a static magnetic field and a field gradient on the carbon diffusion in pure iron. These analyses were compared with experimental results obtained in chapter 2 and the effects of a magnetic field and a magnetic field gradient on the carbon diffusivity in iron were discussed.

In chapter 4, the effect of a magnetic field on crystallization from $\text{Fe}_{78}\text{Si}_9\text{B}_{13}$ and $\text{Fe}_{73.5}\text{Si}_{13.5}\text{B}_9\text{Nb}_3\text{Cu}_1$ amorphous precursors has been studied with the aim of observing the nucleation and growth of α -Fe grains in the amorphous matrix under a magnetic field. The nucleation rate of nanocrystalline α -Fe grains increased by the application of a 6 T magnetic field in $\text{Fe}_{73.5}\text{Si}_{13.5}\text{B}_9\text{Nb}_3\text{Cu}_1$ alloy. The significant effect of a magnetic field on the growth rate of nanocrystallites was not observed. In addition, the magnetic field increased the volume fraction of the crystalline ferromagnetic phase in a thermodynamic equilibrium state.

In chapter 5, the grain boundary energy in iron under a magnetic field was investigated with particular emphasis on the effect of temperature and grain boundary character. Without a magnetic field, the grain boundary energy increased with the increase in temperature. Under a

6 T magnetic field, on the other hand, it decreased with increasing temperature. A discontinuity of the energy was found at the Curie temperature. In addition, the misorientation dependence of grain boundary energy increased under a magnetic field.

In chapter 6, electron energy loss spectroscopy (EELS) was applied to measure the magnetic moment near grain boundaries in pure iron and Fe-Sn alloy. The grain boundaries are characterized on the basis of the coincidence site lattice theory. It was found that the magnetic moment near the random grain boundary increased in pure iron. Furthermore the magnetic moment near the grain boundary was approximately same as that in the grain when the impurities such as Sn segregated at the grain boundary.

In chapter 7, this chapter gives concluding remarks of this study.

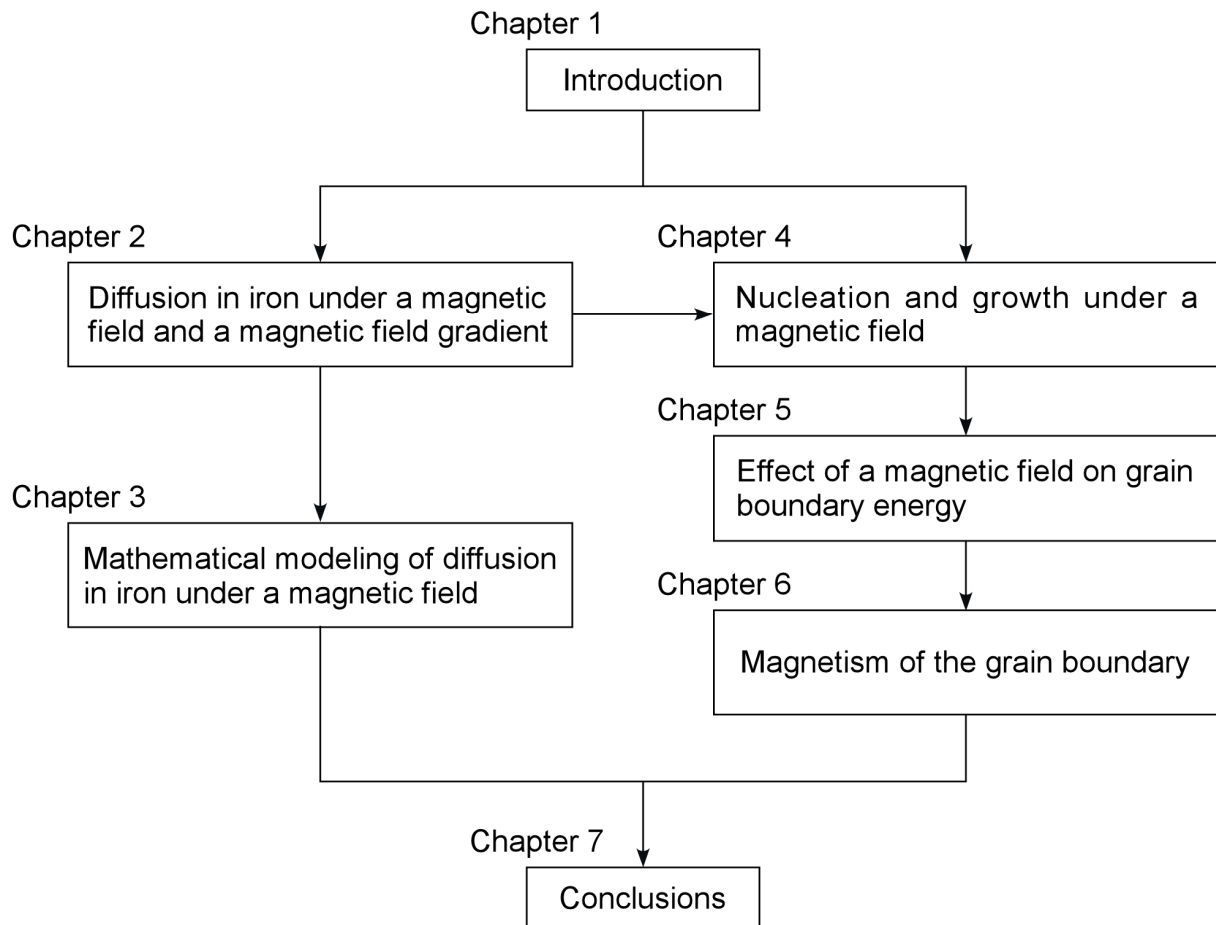


Figure 1-5 Approach and flow of this study.

References

- [1] E. O. Hall: *Proc. Phys. Soc., Ser. B*, **64**, (1951), 747.
- [2] T. Watanabe: *Res Mechanica*, **11** (1984), 47.
- [3] R. Brinnger, U. Herr and H. Gleiter: *Grain Boundary Structure and Related Phenomena Proceedings of JIMIS-4*, (1986), 43.
- [4] N. P. Goss: *Trans. Am. Soc. Met.*, **23** (1935), 511.
- [5] Y. Yoshizawa, S. Ogura and K. Yamauchi: *J. Appl. Phys.*, **64** (1988), 6044.
- [6] M. Michiuchi, H. Kokawa, Z. J. Wang, Y. S. Sato and K. Sakai: *Acta Mater.*, **54** (2006), 5179.
- [7] S. Asai: *Proc. 5th Inter. Symp. on Electromagnetic Processing of Materials*, (2006), 3.
- [8] T. Watanabe, S. Tsurekawa, X. Zhao, L. Zuo and C. Esling: *J. Mater. Sci.*, **41** (2006), 7747.
- [9] T. Watanabe, S. Tsurekawa, X. Zhao and L. Zuo: *Scripta Mater.*, **54** (2006), 969.
- [10] H. Pender and R. L. Jones: *Phys. Rev.*, **1** (1913), 259.
- [11] W. V. Youdelis, D. R. Colton, J. Cahoon: *Can. J. Phys.*, **42** (1964), 2217.
- [12] H. Nakajima, S. Maaekawa, Y. Aoki and M. Koiwa: *Trans. Jap. Inst. Metals*, **26** (1985), 1.
- [13] A. V. Pokoev, D. I. Stepanov, I. S. Trofimov and V. F. Mazanko: *Phys. Stat. Sol.*, **137** (1993), K1.
- [14] A. V. Pokoev and D. I. Stepanov: *Defect and Diff. Forum*, **143-147** (1997), 419.
- [15] D. V. Mironov, A. V. Pokoev and V. F. Mazanko: *Met. Phys. Adv. Tech.*, **18** (1999), 693.
- [16] E. Rabkin, A. Gabelev, T. Matsuzaki and T. Watanabe: *Defect and Diff. Forum*, **237-240** (2005), 560.
- [17] S. Nakamichi, S. Tsurekawa, Y. Morizono, T. Watanabe, M. Nishida and A. Chiba: *J. Mat. Sci.*, **40** (2005), 3191.
- [18] X. Liu, J. Cui, X. Wu, Y. Guo and J. Zhang: *Scripta Mater.*, **52** (2005), 79.
- [19] H. Ohtsuka and X. J. Hao: *Proc. of 5th Intern. Symp. on Electromagnetic processing of Materials (EPM2006)*, The Iron and Steel Institute of Japan (2006), 648.
- [20] Z. F. Li, J. Dong, X. Q. Zeng, C. Lu, W. J. Ding and Z. M. Ren: *J. Alloys Comp.*, **440** (2007), 132.
- [21] M. A. Verzhakovskaya, S. S. Petrov and A. V. Pokoev: *Tech. Phys. Lett.*, **33** (2007), 961.
- [22] M. A. Verzhakovskaya, S. S. Petrov and A. V. Pokoev: *Bulle. Rus. Acad. Sci. Phys.*, **71** (2007), 1674.
- [23] R. Smoluchowski and R. W. Turner: *J. Appl. Phys.*, **20** (1949), 745.
- [24] H. O. Martikainen and V. K. Lindroos: *Scnad. J. Metall.*, **10** (1981), 3.
- [25] N. Masahashi, M. Matsuo and K. Watanabe: *J. Mater. Res.*, **13** (1998), 457.
- [26] J. Prohaszka, B. Hidasi and J. Dobranszky: *J. Mater. Proc. Tech.*, **108** (2001), 205.
- [27] A. D. Sheikh-Ali, D. A. Molodov and H. Garmestani: *Scripta Mater.*, **46** (2002), 857.
- [28] C. M. B. Bacaltchuk, G. A. Castello-Branco, M. Ebrahimi, H. Garmestani and A. D. Rollett: *Scripta Mater.*, **48** (2003), 1343.
- [29] D. A. Molodov, S. Bhaumik, X. Molodova and G. Gottstein: *Scripta Mater.*, **54** (2006), 2161.

- [30] S. Bhaumik, X. Molodova, D. A. Molodov and G. Gottstein: *Scripta Mater.*, **55** (2006), 995.
- [31] Y. Wu, X. Zhao, C. S. He, Y. D. Zhang, L. Zuo and C. Esling: *Mater. Trans.*, **48** (2007), 2809.
- [32] D. A. Molodov, G. Gottstein, F. Heringhaus and L. S. Shvindlerman: *Scripta Mater.*, **37** (1997), 1207.
- [33] D. A. Molodov, G. Gottstein, F. Heringhaus and L. S. Shvindlerman: *Acta Mater.*, **46** (1998), 5627.
- [34] T. Matsuzaki, T. Sasaki, S. Tsurekawa and T. Watanabe: *The fourth Inter. Sonf. on Recrystallization and related Phenomena, JIM*. (1999), 529.
- [35] K. Harada, S. Tsurekawa, T. Watanabe and G. Palumbo: *Scripta Mater.*, **49** (2003), 367.
- [36] A. D. Sheikh-Ali, D. A. Molodov and H. Garmestani: *Scripta Mater.*, **48** (2003), 483.
- [37] T. Matsuzaki, T. Yamada, K. Jyuami, S. Tsurekawa, T. Watanabe and G. Palumbo: *Mater. Res. Soc. Symp. Proc.*, **788** (2004), 121.
- [38] D. A. Molodov, C. Bollmann, P. J. Konijnenberg, L. A. Barrales-Mora and V. Mohles: *Mater. Trans.*, **48** (2007), 2800.
- [39] S. Tsurekawa, K. Kawahara, K. Okamoto, T. Watanabe and R. Faulkner: *Mater. Sci. Eng.*, **A387-389** (2004), 442.
- [40] S. Tsurekawa, K. Okamoto, K. Kawahara and T. Watanabe: *J. Mater. Sci.*, **40** (2005), 895.
- [41] R. Sumi, N. Toda, H. Fujii and S. Tsurekawa: *Rev. Adv. Mater. Sci.*, (2009), accepted.
- [42] P. Häußler and F. Baumann: *Z. Phis. B*, **38** (1980), 43.
- [43] Y. Wolfus, Y. Yeshurun, I. Felner and J. Wolny: *Phil. Mag. B*, **56** (1987), 963.
- [44] Y. Otani, H. Sun, J. M. D. Coey, H. A. Davis, A. Manaf and R. A. Buckley: *J. Appl. Phys.*, **67** (1990), 4616.
- [45] X. Wang, M. Qi and S. Yi: *Scr. Mat.*, **51** (2004), 1047.
- [46] T. Watanabe, S. Tsurekawa, H. Fujii and T. Kannno: *Mater. Sci. Forum*, **495-497** (2005), 1151.
- [47] H. Fujii, S. Tsurekawa, T. Matsuzaki and T. Watanabe: *Phil. Mag. Lett.*, **86** (2006), 113.
- [48] H. Fujii, T. Matsuzaki and S. Tsurekawa: *Proc. 5th Inter. Symp.on Electromagnetic Processing of Materials*, (2006), 567.
- [49] S. Tsurekawa, H. Fujii, V. A. Yardley, T. Matsuzaki and T. Watanabe: *Mater. Sci. Forum*, **558-559** (2007), 1371.
- [50] V. A. Yardley, S. Tsurekawa, H. Fujii and T. Matsuzaki: *Mater. Trans.*, **48** (2007), 2826.
- [51] H. Fujii, V. A. Yardley, T. Matsuzaki and S. Tsurekawa: *J. Mater. Sci.*, **43** (2008), 3837.
- [52] V. D. Sadovsky, L. V. Smirov, Y. A. Fokina, P. A. Malinen and I. P. Soroskin: *Fiz. Met. Metalloved.*, **27** (1967), 918
- [53] T. Kakeshita, K. Shimizu, T. Maki, I. Tamura, S. Kijima, M. Date: *Scr. Metall.*, **19** (1985), 973.
- [54] T. Kakeshita, K. Shimizu and S. Fukuda, M. Date: *Acta Metall.*, **33** (1985), 1381.
- [55] T. Kakeshita, S. Furikado, K. Shimizu, K. Kijima and M. Date: *Mater. Trans., JIM*, **27** (1986) 477.
- [56] T. Kakeshita, K. Kuroiwa, K. Shimizu, T. Ikeda, A. Yamagishi and M. Date: *Mater. Trans., JIM*, **34** (1993), 423.
- [57] T. Kakeshita, T. Sabri and K. Shimizu: *Mater. Sci. Eng.*, **A273-275** (1999), 21.
- [58] K. Maruta and M. Shimotomai: *Mater. Trans., JIM*, **41** (2000), 902.

- [59] M. Shimotomai and K. Maruta: *Scripta Mater.*, **42** (2000), 499.
- [60] J. K. Choi, H. Ohtsuka, Y. Xu and W. Y. Choo: *Scripta Mater.*, **43** (2000), 221.
- [61] Y. Xu, H. Ohtsuka, H. Wada and J. K. Choi: *Trans. Mater. Res. Soc. Japan.*, **25** (2000), 505.
- [62] H. D. Joo, S. U. Kim, N. S. Shin and Y. M. Koo: *Mater. Lett.*, **43** (2000), 225.
- [63] H. Ohtsuka, Y. Xu and H. Wada: *Mater. Trans. JIM.*, **41** (2000), 907.
- [64] C. C. Koch: *Mater. Sci. Eng.*, **A287** (2000), 213.
- [65] M. Enomoto, H. Guo, Y. Tazuke, Y. R. Abe and M. Shimotomai: *Metall. Mater. Trans.*, **32A** (2001), 445.
- [66] K. Maruta and M. Shimotomai: *J. Crystal Growth*: **237-239** (2002), 1802.
- [67] X. J. Hao, H. Ohtsuka, P. D. Rango and H. Wada: *Mater. Trans.*, **44** (2003), 211.
- [68] X. J. Hao and H. Ohtsuka: *Mater. Trans.*, **45** (2004), 2622.
- [69] Y. Zhang, C. He, X. Zhao, L. Zuo and C. Esling: *J. Mag. Mag. Mater.*, **294** (2005), 267.
- [70] M. Enomoto: *Mater. Trans.*, **46** (2005), 1088.
- [71] Y. Zhang, G. Vincent, N. Dewobroto, L. Germain, X. Zhao, L. Zuo and C. Esling: *J. Mater. Sci.*, **40** (2005), 903.
- [72] R. A. Jaramillo, S. S. Babu, G. M. Ludtka, R. A. Kinser, J. B. Wilgen, G. Mackewicz-Ludtka, D. M. Nicholson, S. M. Kelly, M. Murugananth and H. K. D. H. Bhadeshia: *Scripta Mater.*, **52** (2005), 461.
- [73] Y. D. Zhang, C. Esling, J. S. Lecomte, C. S. He, X. Zhao and L. Zuo: *Acta Mater.*, **53** (2005), 5213.
- [74] H. Ohtsuka: *Mater. Sci. Eng.*, **A438-440** (2006), 136.
- [75] T. Ono, K. Sassa, K. Iwai, H. Ohtsuka and S. Asai: *ISIJ Int.*, **47** (2007), 608.
- [76] H. Ohtsuka: *Mater. Trans.*, **48** (2007), 2851.
- [77] H. Ohtsuka: *Sci. Tech. Adv. Mater.*, **9** (2008), 013004.
- [78] X. J. Liu, Y. M. Fang, C. P. Wang, Y. Q. Ma and D. L. Peng: *J. Alloys Comp.*, **459** (2008), 169.
- [79] J. G. Noudem, J. Beille, D. Bourgault, D. Chateigner and R. Tournier: *Physica C*, **264** (1996) 325.
- [80] B. A. Legrand, D. Chateigner, R. Perrier de la Bathie and R. Tournier: *J. Mag. Mag. Mater.*, **173** (1997) 20.
- [81] H. Morikawa, K. Sassa and S. Asai: *Mater. Trans., JIM*, **39** (1998) 814.
- [82] T. Taniguchi, K. Sassa and S. Asai: *Mater. Trans., JIM*, **41** (2000) 981.
- [83] H. Yasuda, K. Tokieda and I. Ohnaka: *Mater. Trans., JIM*, **41** (2000) 1005.
- [84] C. Y. Wu, S. Li, K. Sassa, Y. Chino, K. Hattori and S. Asai: *Mater. Trans., JIM*, **46** (2005), 1311.
- [85] W. W. Chen, Y. Kinemuchi, T. Tamura, K. Miwa and K. Watari: *Mater. Lett.*, **61** (2007), 6.
- [86] C. Y. Wu, K. Sassa, K. Iwai and S. Asai: *Mater. Lett.*, **61** (2007), 1567.
- [87] T. Watanabe, Y. Suzuki, S. Tanii and H. Oikawa: *Phil. Mag. Lett.*, **62** (1990), 9.
- [88] K. Harada, S. Tsurekawa, T. Watanabe and G. Palumbo: *Scripta Mater.*, **49** (2003), 367.
- [89] G. Sauthoff and W. Pitsch: *Phil. Mag. B*, **56** (1987), 471.
- [90] T. Fujii, K. Kusaka and M. Kato: *J. iron steel inst. Japan.*, **81** (1995), 696.
- [91] T. Fujii, T. Ono and M. Kato: *J. Japan Inst. Met.*, **61** (1997), 267.

Chapter 1

- [92] A. Holloway, R. W. McCallum and S. R. Arrasmith: *J. Mater. Res.*, **8** (1993), 727.
- [93] S. Tsurekawa, K. Harada, T. Sasaki, T. Matsuzaki and T. Watanabe: *Mater. Trans., JIM*, **41** (2000), 991.
- [94] T. S. Suzuki, T. Uchikoshi and Y. Sakka: *J. Cerami. Soc. Japan*, **114** (2006), 59.

Chapter 2

Diffusion in iron under a magnetic field and a magnetic field gradient

2.1 Introduction

As mentioned in chapter 1, it has been reported that a strong magnetic field can affect many metallurgical phenomena, such as recrystallization, grain growth, texture formation and phase transformation. Although most changes in microstructure occurring through those phenomena are governed by diffusion, the number of studies on the effect of a magnetic field on diffusion in solids is not large. Youdelis *et al.*, who used a 3 T magnetic field, first reported the effect of a magnetic field on solid/solid diffusion in 1964. They revealed that a magnetic field retarded diffusion of copper in aluminum [1]. On the other hand, Nakajima *et al.*, who used a 4 T magnetic field, did not find any magnetic field effects on the diffusion of nickel in titanium [2].

There have been some reports on solid/solid diffusion under a magnetic field using diffusion couple or tracer technique, since it has become easier to induce a strong magnetic field with the development of helium-free superconducting magnet in 1990's. Pokoев *et al.* revealed that the diffusivities of ^{63}Ni in pure iron and single crystal Fe-1.94at%Si increased under a magnetic field of 0.1 T [3, 4]. Moreover, they found that the diffusivity decreased with increase in the magnetic field strength up to the magnetization saturation field and that the diffusivity decreased under a magnetic field of 0.7 T. Mironov *et al.* experimentally investigated the effect of a magnetic field of 0.7 T on diffusion of nickel in pure cobalt, which has strong magnetocrystalline anisotropy due to hexagonal structure, and discussed the magnetic field effects from a viewpoint of bulk magnetostriction of cobalt [5]. Liu *et al.* investigated the effect of an alternative magnetic field of 0.5 T on the interdiffusion of Al/Zn and Al/Mg using diffusion couples respectively [6]. They estimated each diffusion coefficient from the growth rate of the intermediate phases whose growth rate is dominated by the parabolic rate law. As a result, it was found that the magnetic field increased the diffusivity and that the diffusivities increased through the pre-exponential frequency factor but not the

activation energy by the application of a magnetic field. Li *et al.* also reported same effects of a magnetic field in the Mg/Al diffusion couple [7]. As for the iron-based materials, the diffusion of carbon or solid solubility in iron under a strong magnetic field is incompletely understood although the carbon behavior plays important roles in most metallurgical phenomena related to microstructural evolution in iron and steels. This is because there have been only a few reports on carbon diffusion in iron under a strong magnetic field [8-10]. Nakamichi *et al.* reported that the diffusion of carbon in paramagnetic γ -iron, which occurs by interstitial mechanism, was retarded under a 6 T magnetic field [9]. Besides, they revealed that a static magnetic field and the field gradient could not affect the diffusion of titanium in γ -iron which occurs by vacancy mechanism. Then there may be difference between the effects of a magnetic field on the diffusion of atoms which occurs by interstitial and vacancy mechanisms. Ohtsuka *et al.* investigated the effect of a static magnetic field on formation of pearlite phase in the diffusion couple between Fe and Fe-0.8mass%C [10]. It was found that the formation rate of pearlite phase decreased due to the retardation of carbon diffusion by the application of a magnetic field.

In recent years, not only the effect of a static magnetic field but also an alternative magnetic field and pulsatile magnetic field on diffusion of atoms has been reported. Rabkin *et al.* observed grain boundary grooving process in pure iron and revealed that the surface self-diffusion of iron increased under an alternative magnetic field by the kinetic analyses of the development of grain boundary grooves [11]. Verzhakovskaya *et al.* investigated the effect of pulsed magnetic field on the diffusion of Al atoms in pure iron [12, 13]. They found that the pulsatile magnetic field increased the Al diffusion and discussed the magnetic field effect from the viewpoint of the interaction between magnetic domains and dislocations. It was concluded that the Al diffusion in pure iron under pulsatile magnetic field was determined by the frequency of pulsatile field, migration rate of magnetic domain and interaction energy between impurities and dislocations in the magnetic domains. Previous reports of the magnetic field effects on the diffusion of atoms were summarized in Table 2-1.

Although these phenomena were of particular important when the mechanism of magnetic field effects on the microstructural evolution in iron based materials were revealed, there have still remained a lot of questions related to the carbon behavior in iron under a magnetic field. For example, the effects of a magnetic field on carbon diffusion in α -iron have not been studied so far. In this chapter, the diffusivity and solid solubility limit of carbon in pure iron were experimentally investigated under a magnetic field and a magnetic field gradient.

Table 2-1 Summary of the magnetic field effects on the atomic diffusion in metals.

Author	Material	Diffusion medium	Magnetic field		Diffusivity
			type	strength	
Youdelis [1]	Al	Cu	static	3 T	retardation
Nakajima [2]	Ti	Ni	static	4 T	no effects
Pokoev [3]	Fe	Ni	static	0.05 – 0.5 T	acceleration
Pokoev [4]	Fe-1.94at%Si	Ni	static	0.05 – 0.7 T	acceleration
Mironov [5]	Co	Ni	static	0.1 – 0.7 T	acceleration
Liu [6]	Al-Zn	Al-Zn	alternative	0.5 T	acceleration
	Al-Mg	Al-Mg	alternative	0.5 T	acceleration
Li [7]	Mg-Al	Mg-Al	static	10 T	retardation
Nakamichi [9]	Fe-0.09mass%C	C	static	6 T	retardation
			gradient	2.08×10^2 T ² /m	acceleration
Ohtsuka [10]	Fe-0.8mass%C	C	static	10 T	retardation
Rabkin [11]	Fe	Fe	alternative	0.5 T	retardation
Verzhakovslaya [12]	Fe	Al	pulsed	0.05 – 0.5 T	acceleration
Verzhakovslaya [13]	Fe	Al	pulsed	0.05 – 0.7T	acceleration

2.2 Experimental

2.2.1 Material and preparation of diffusion couple

Measurements of carbon diffusion in iron under a magnetic field and a field gradient were conducted with a diffusion couple of pure iron (99.9 %) and eutectoid steel (Fe-0.87mass%C) [14]. The diffusion couples used in this study were prepared by an explosive welding method at the shock wave and condensed matter research center of Kumamoto University in order to prevent diffusion of carbon during joining. The plastic explosive (SEP) which consisted mainly of nitric ester was used as an explosive. Before joining, plates of pure iron and eutectoid steel, which were 100 mm × 50 mm × 5 mm and 100 mm × 50 mm × 2 mm in size respectively, were annealed at 973 K for 86.4 ks in a vacuum of 2 mPa. They were mechanically ground to remove the oxide scale. A preset angle stand-off configuration was used for the explosive welding method in this study as shown in Fig. 2-1. The specimens were cut from a joined iron/steel clad into the plate of 7 mm × 5 mm × 1 mm in dimensions. Thereafter, they were mechanically polished with waterproof papers of #320 –

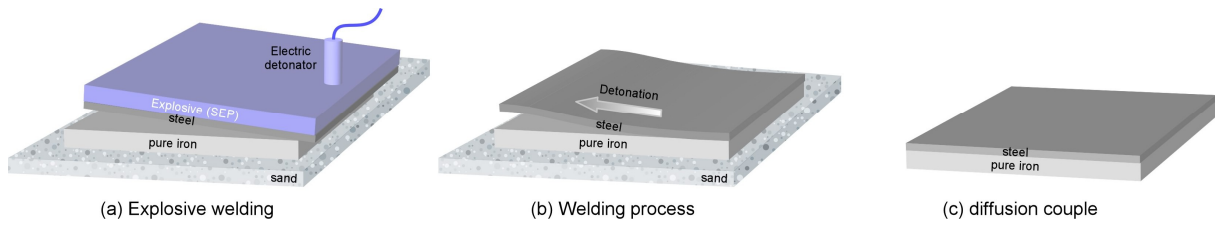


Figure 2-1 Schematic illustrations of explosive welding process of steel (Fe-0.88mass%C) and pure iron (99.9 %) used in this study.

#2000 and buff-polished with alumina particles of 3, 1 and 0.3 μm .

2.2.2 Diffusion annealing under a magnetic field and a magnetic field gradient

The superconducting magnet used in this study is HF6-100VHT-1 with the bore size of 100 mm in diameter from Sumitomo Heavy Machine Corporation, which is composed of 1 mm ϕ ultrafine multicore wire solenoidal coil of Nb-Ti alloy. Fig. 2-2 shows the whole view and the schematic illustration of superconducting magnetic field heat treatment system. The superconducting magnet is equipped with chiller which is driven by the compressor unit construction system. An electric furnace using Mo sheet heater was specially designed by Futek Furnace inc. so that it could work under a high magnetic field and achieve the maximum temperature of 1773 K. For annealing a carbon sample holder was used as shown in Fig. 2-3. A sample was sandwiched by tungsten sheets to prevent carbon contamination and they were inserted into the carbon holder. The annealing for diffusion was conducted at temperatures from 800 K (below Curie temperature (1043 K)) to 1200 K (above α - γ phase transformation temperature (1184 K)) in a vacuum of 1.0×10^{-3} Pa. The annealing times were determined so that carbon atoms would penetrate into pure iron by approximately 800 μm on the basis of previous data [15, 16]. The applied magnetic field strength was 0 - 6 T and applied magnetic field gradients was 45 T/m ($H(dH/dx) = 2.08 \times 10^2$ T $^2/\text{m}$). A magnetic field gradient was applied by placing the samples apart from a uniform magnetic field region. Fig. 2-4 shows the variation of magnetic field strength H and magnetic field gradient $-dH/dx$ along the position from the center of the magnet for different nominal magnetic field strength H_0 .

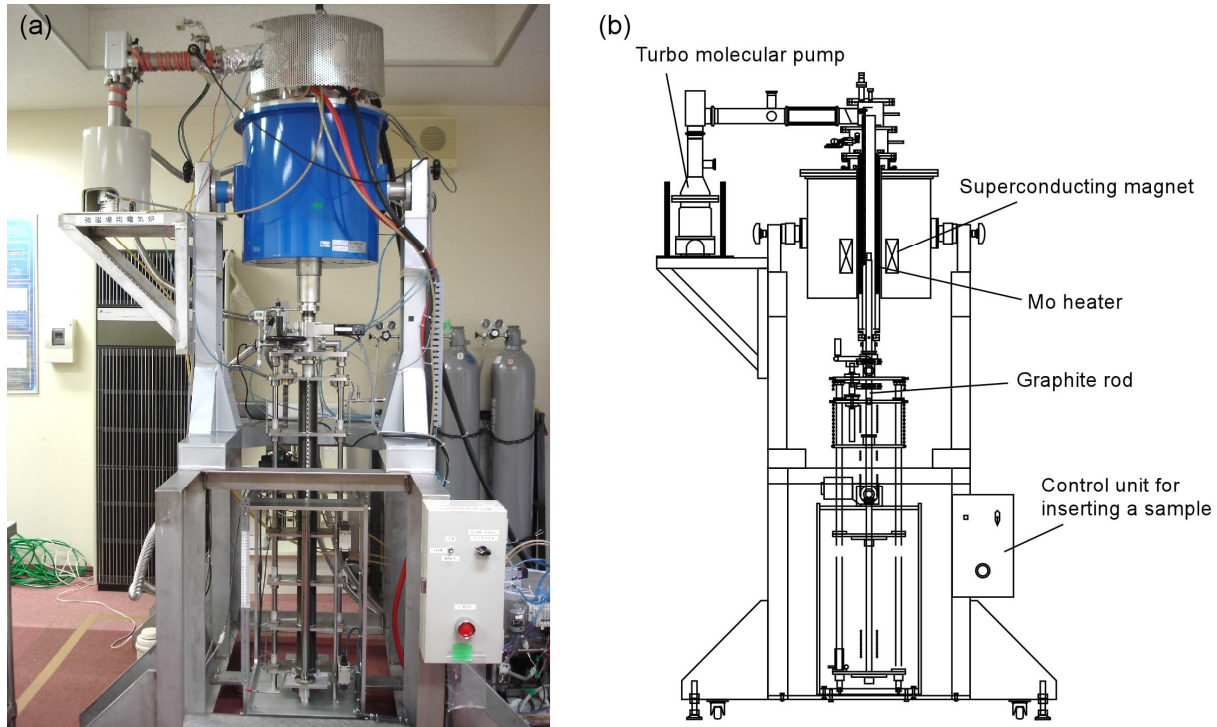


Figure 2-2 (a) The whole view and (b) the schematic illustration of superconducting magnetic field heat treatment system.

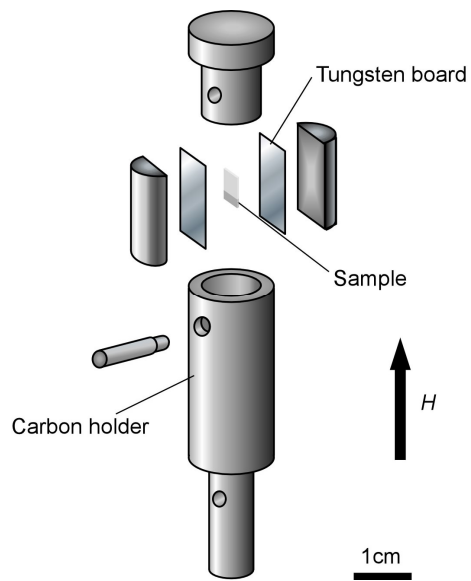


Figure 2-3 The schematic illustration of specially designed sample holder for annealing under a magnetic field.

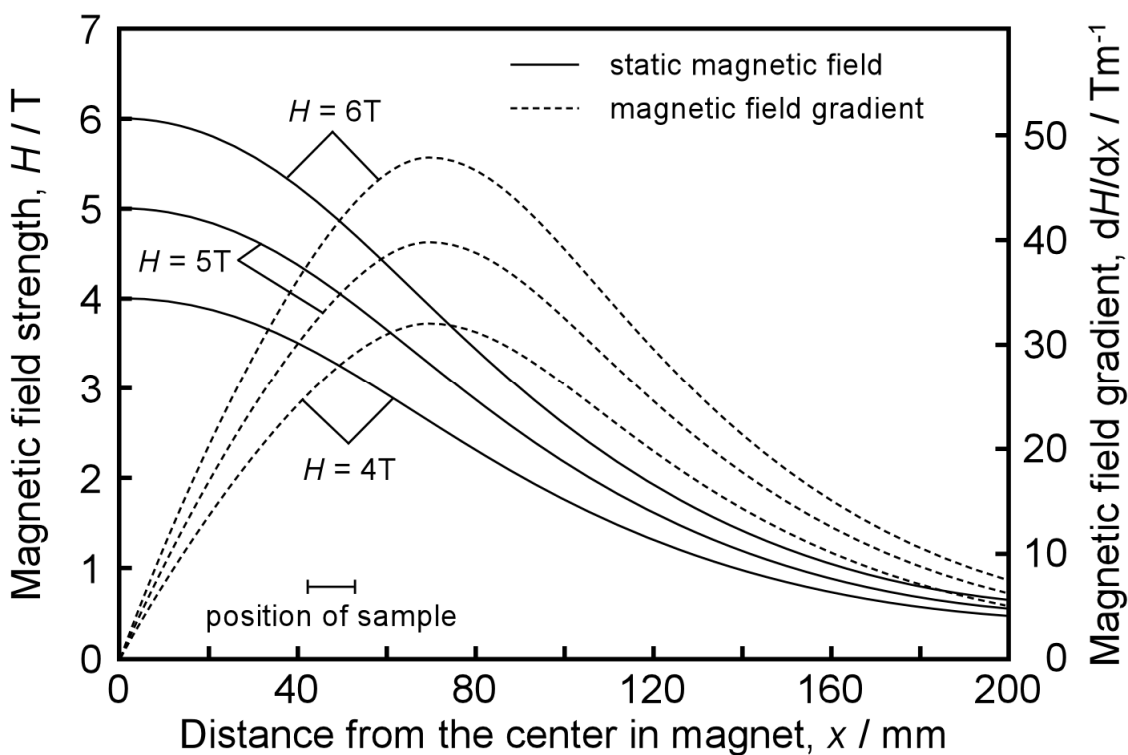


Figure 2-4 Variation of a magnetic field H and a magnetic field gradient dH/dx with the position x in the magnet for different nominal magnetic fields H_0 .

The direction of the applied magnetic field was perpendicular to the iron/steel interface, which was parallel to the diffusion direction. As the magnetic field was applied to the longitudinal direction of plate specimens, the demagnetization field which is induced within the specimens would be negligible small, indicating that the effective field strength exerting the specimen was equivalent to the applied field. Details of the annealing conditions for carbon diffusion in pure iron under a magnetic field are shown in Table 2-2.

2.2.3 Measurement of diffusion coefficients

The carbon penetration profiles from the iron/steel interface to iron were measured by secondary ionization mass spectroscopy (SIMS; ATOMIKA ION MICROPROBE 4100). Today, SIMS is widely used for analysis of trace elements in solid materials, especially

Table 2-2 Annealing conditions for Fe/steel specimens

Temperature, T / K	Annealing time, t / ks	Magnetic field	
		Strength, H / T	Gradient, dH/dx / T/m
850	133	0, 6	
900	30.5	0, 6	
950	15.4	0, 6	
1000	8.34	0, 2, 4, 6	45 (negative)
1100	2.89	0, 6	
1150	1.82	0, 6	
1200	41.2	0, 6	

semiconductors and thin films. The SIMS ion source is one of only a few sources to produce ions from solid samples without prior vaporization. The SIMS primary ion beam can be converged to the diameter of less than 100 μm . Controlling where the primary ion beam strikes the sample surface provides for microanalysis, which means the measurement of the lateral distribution of elements on a microscopic scale is possible. During SIMS analysis, the surface of a sample is gradually removed by ion sputtering, so that chemical distribution can be quantitatively measured as a function of depth, so called “a depth profile” is obtained. Continuous analysis while sputtering produces information as a function of depth, called a depth profile. The resulting ion fragmentation patterns contain information useful for identifying molecular species. The primary ion beam used in this study was O^{2+} ion at energy of 5.00 keV. Fig. 2-5 shows one example of ^{57}Fe and ^{12}C SIMS profiles obtained from the areas in eutectoid steel and pure iron. The carbon concentration from the detected counts of SIMS analysis was evaluated as a function of the distance from the interface. The distances were measured from the traces sputtered by ionic beam during SIMS analysis. Because the SIMS counts approached a constant value by sputtering for 300 s, it was defined the counts for carbon as the sum of the counts from 300 s to 600 s. The carbon concentration was quantitatively estimated from the carbon counts obtained at a position normalized by the counts from the steel with a ready-known carbon concentration. From these results, the diffusion coefficients of carbon in iron were determined according to Fick’s 2nd law given by,

$$\frac{\partial C}{\partial t} = D \frac{\partial^2 C}{\partial x^2}, \quad (2-1)$$

where C is the concentration of atoms, t is the diffusion time, D is the diffusion coefficient

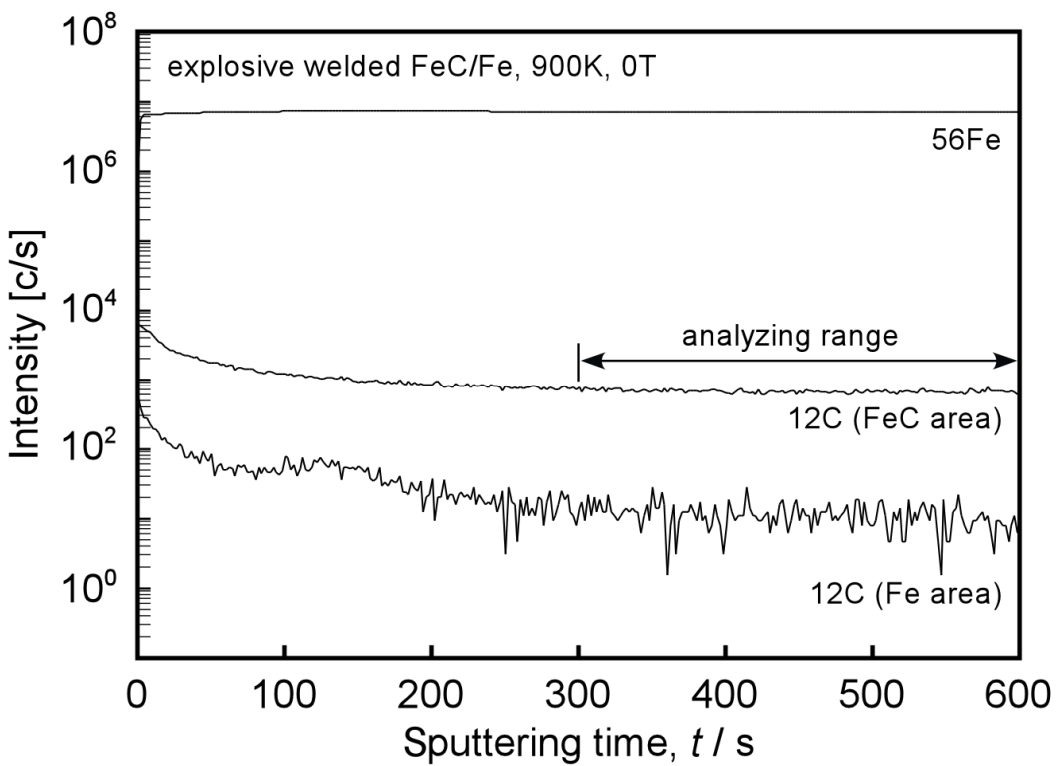


Figure 2-5 One example of SIMS profiles for ^{56}Fe and ^{12}C in steel and iron.

and x is the diffusion length. Finally the carbon concentration was assumed to reach the solid solubility limit at the interface between Fe and Fe-0.87mass% C in the diffusion couple. Thus, the solid solubility limit was determined by using the carbon concentration at the interface predicted by the carbon concentration distribution.

2.3 Results and discussion

2.3.1 Penetration profiles of carbon atoms to pure iron

The carbon penetration profiles were measured from the iron / steel interface to the pure iron in the diffusion couples annealed without and with a magnetic field. Fig. 2-6 represents optical microscope images showing traces sputtered by ion beam of SIMS for the specimens

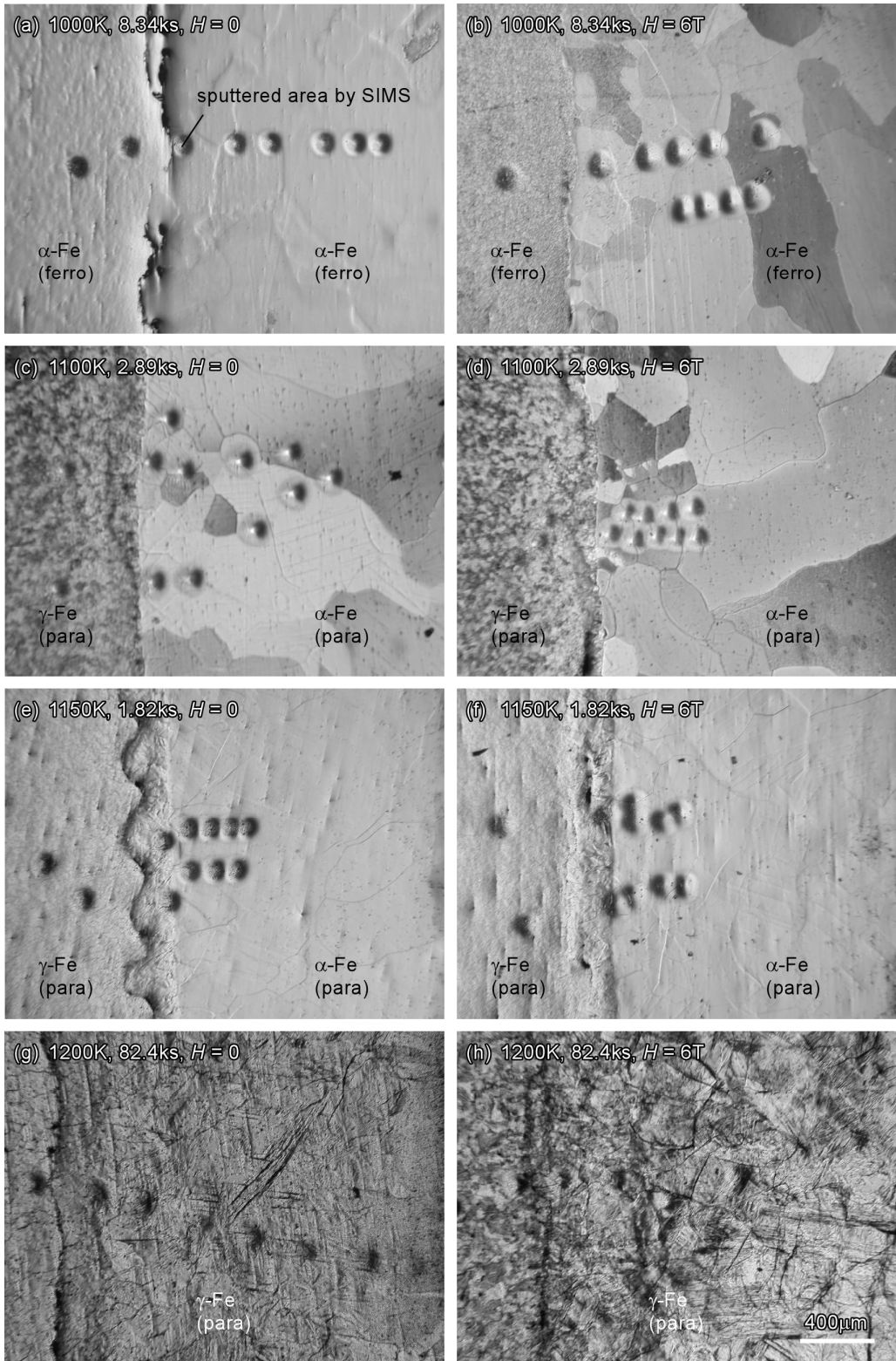


Figure 2-6 Optical microscope images after SIMS analysis in iron/steel diffusion couples annealed at (a), (b) 1000 K (ferromagnetic $\alpha\text{-Fe}$), (c), (d) 1100 K (paramagnetic $\alpha\text{-Fe}$), (e), (f) 1150 K (paramagnetic $\alpha\text{-Fe}$) and (g), (h) 1200 K (paramagnetic $\gamma\text{-Fe}$).

annealed at 1000 K (ferromagnetic α -Fe, (a), (b)), 1100 K (paramagnetic α -Fe, (c), (d)), 1150 K (paramagnetic α -Fe, (e), (f)) and 1200 K (paramagnetic γ -Fe, (g), (h)) under a 6 T magnetic field. No cementite (Fe_3C) precipitates occurred even at the iron / steel interface, grain boundaries and grain boundary triple junctions in iron after the specimens were annealed below 1100 K (Fig. 2-6 (a)-(d)). On the other hands, the fine cementite precipitates were observed in iron near the interface in the specimen annealed at 1150 K (Fig. 2-6 (e), (f)). This is because the α - γ phase transformation temperature microscopically decreased and started the phase transformation near the interface of the diffusion couple due to the penetration of carbon into pure iron from the interface. In other words, carbon atoms which solved in γ -iron at 1150 K precipitated as cementite phase at room temperature. The mixture of ferrite and cementite phases were observed everywhere in the specimens annealed at 1200 K (Fig. 2-6 (g), (h)).

Fig. 2-7 shows the changes of carbon concentration as a function of the distance from the interface between steel and iron in the diffusion couple annealed at (a) 1000 K (ferromagnetic α -Fe), (b) 1100 K (paramagnetic α -Fe) and (c) 1200 K (paramagnetic γ -Fe) without and with a 6 T static magnetic field. The carbon concentration C_C in iron exponentially decreased with increase in the distance from the interface irrespective of whether a magnetic field was applied for every specimens annealed at different temperatures. In addition, it is evident that the carbon concentrations near the interface are higher in the specimens annealed under a magnetic field than that under a non-magnetic field conditions. The carbon concentration of the specimens annealed under a magnetic field rapidly decreased with the increase in the penetration distance. As a result, the carbon concentration curves of the specimens annealed without and with a magnetic field at each temperature crossed each other as shown in Fig. 2-7. These results suggest that the solid solubility of carbon in iron increases and the diffusivity decreases by the application of a magnetic field.

2.3.2 Diffusivity of carbon in iron under a static magnetic field

(a) Temperature dependence

The carbon diffusivities under non-magnetic conditions and a magnetic field were quantitatively estimated from the carbon penetration profiles. For the case of the diffusion geometry used in this study, that is, for the case of a pair of semi-infinite system, a solution of diffusion equation given by concentration profile of carbon will be a function of the

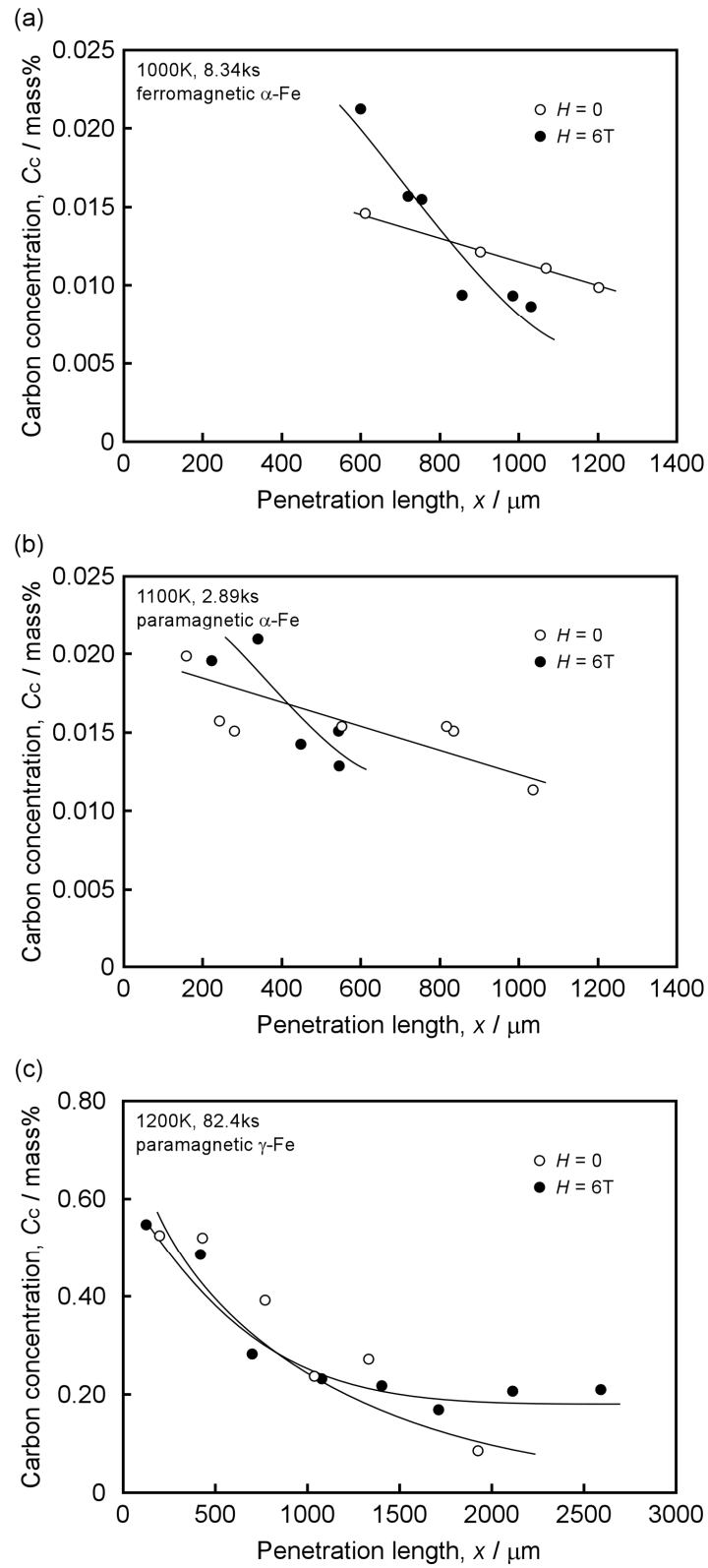


Figure 2-7 Carbon concentration distributions in pure iron as a function of diffusion length in explosive welded specimens annealed at (a) 1000K, (b) 1100K and (c) 1200K without and with a 6 T magnetic field.

error-function. Nevertheless, at the beginning of diffusion annealing, the profile cannot be different from the Gaussian distribution observed in thin-film geometry. Thus, the carbon penetration profile is assumed to obey the Gaussian function distribution. The solution of Fick's 2nd law is represented by the following eqn. (2-2) for the thin-film geometry.

$$C_C(x, t) = \frac{S_0}{\sqrt{\pi D t}} \exp\left(-\frac{x^2}{4 D t}\right), \quad (2-2)$$

where S_0 is the number of atoms at the interface of iron and steel per area, D is the carbon diffusion coefficient, t is the annealing time for diffusion and x is the penetration distance of carbon in iron. Diffusion coefficients of carbon can be evaluated according to the equation (2-2) when the relationship between the carbon concentration and diffusion distance is obtained. Following the eqn. (2-2), the natural logarithm of C_C was plotted as a function of the square of penetration depth as shown in Fig. 2-8. There was a good linear relationship between them irrespective of whether a magnetic field being applied or not, which indicated that the assumption made above is valid and then the eqn. (2-2) can be applied to measurements of carbon diffusion coefficient using the diffusion couple used in this study. Therefore the diffusion coefficients were estimated from the slope of the straight lines in Fig. 2-8. The results are presented in Table 2-3 with the rate of diffusivity change due to a 6 T magnetic field. The diffusion coefficients of carbon in iron were decreased by about 68 % at the ferromagnetic α -Fe temperature range, 69 % at the paramagnetic α -Fe and 38 % at the paramagnetic γ -Fe when a 6 T magnetic field was applied. As the reduction rates of diffusion coefficients at ferromagnetic α -Fe and paramagnetic one were almost the same within the experimental error, the magnetic field effect on carbon diffusion would not significantly change owing to the magnetic transformation. This is probably because the magnetic field induced magnetization occurs beyond the Curie temperature. Moreover, a magnetic field also retarded carbon diffusion in γ -Fe as well as in α -Fe. The reduction rate of carbon diffusivity in γ -Fe was about 38%, which is much less than that in α -Fe, as shown in Fig. 2-9.

Fig. 2-10 shows the Arrhenius plots of diffusion coefficients of carbon in α - and γ -iron without and with a 6 T magnetic field. For comparison, the reported data [14-16], which was obtained without a magnetic field, is shown in the figure by the broken lines and squares. The linear relationship was obtained between the logarithm of diffusion coefficients of carbon and the reciprocal absolute temperatures. The activation energies of the carbon diffusion were calculated by the slopes of the straight lines in Fig. 2-10. The activation energies of the carbon diffusion in α -Fe were evaluated to be approximately 115 ± 7 kJ/mol, irrespective of whether a magnetic field being applied or not. Moreover, those in γ -Fe without and with the 6 T

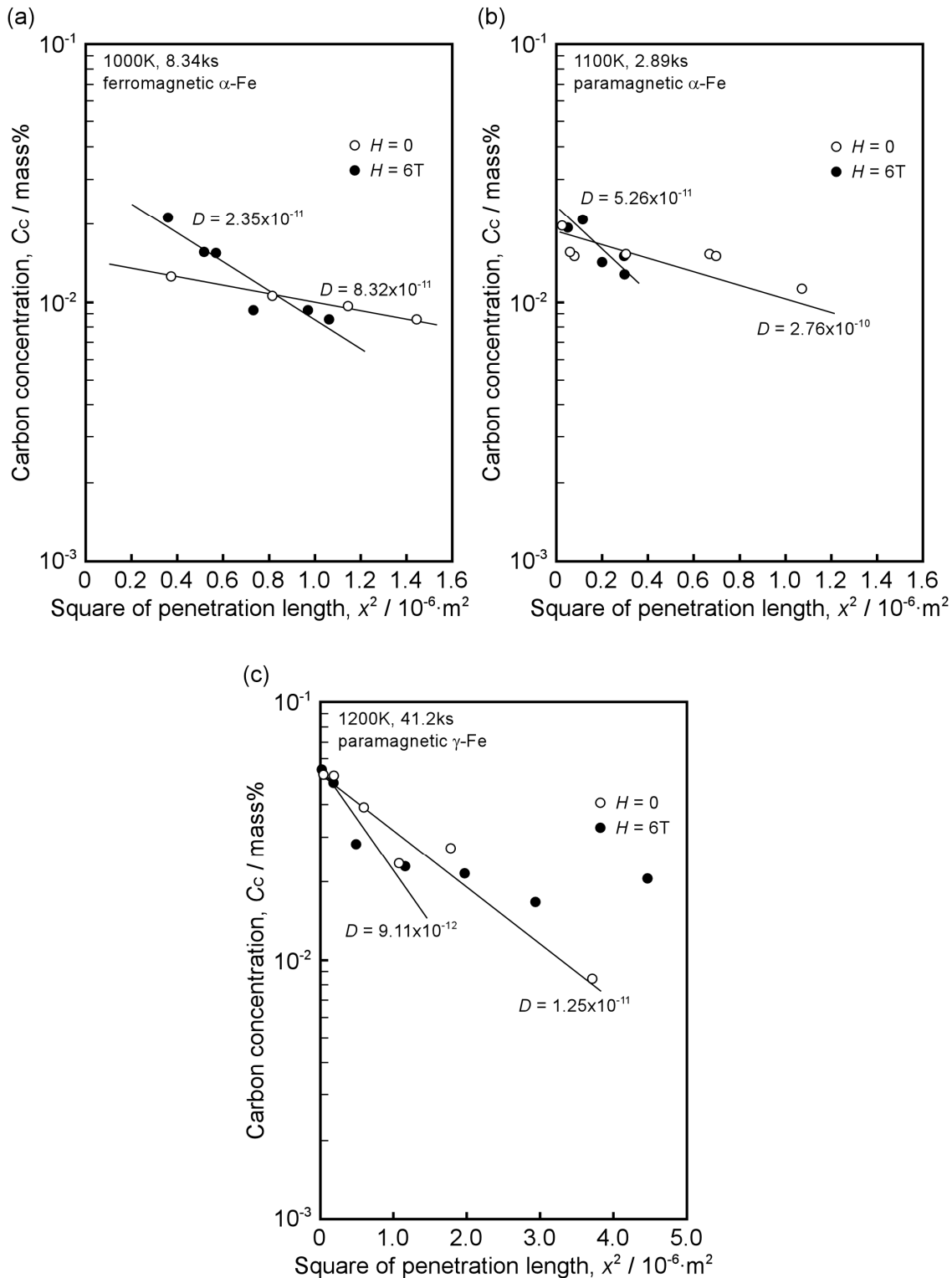


Figure 2-8 Carbon concentration distributions in pure iron as a function of square of diffusion length in explosive welded specimens annealed at (a) 1000K, (b) 1100K and (c) 1200K without and with a 6 T magnetic field.

Table 2-3 Carbon diffusion coefficient in pure iron

Temperature, T / K	Magnetic field		
	$H = 0$	$H = 6 \text{ T}$	$dH/dx = 45 \text{ T/m}$
850	6.27×10^{-12}	2.16×10^{-12}	-
900	1.15×10^{-11}	3.94×10^{-12}	-
950	3.00×10^{-11}	9.12×10^{-12}	6.41×10^{-11}
1000	7.39×10^{-11}	2.35×10^{-11}	1.58×10^{-10}
1100	1.19×10^{-10}	4.30×10^{-11}	-
1150	2.76×10^{-10}	6.93×10^{-11}	-
1200	(1.17×10^{-10})	(6.37×10^{-11})	-
1223*	1.25×10^{-11}	7.91×10^{-12}	3.7×10^{-11}
1273*	1.8×10^{-11}	1.1×10^{-11}	5.4×10^{-11}
1323*	3.8×10^{-11}	2.0×10^{-11}	1.1×10^{-10}

* Data from Nakamichi *et al.* [9]

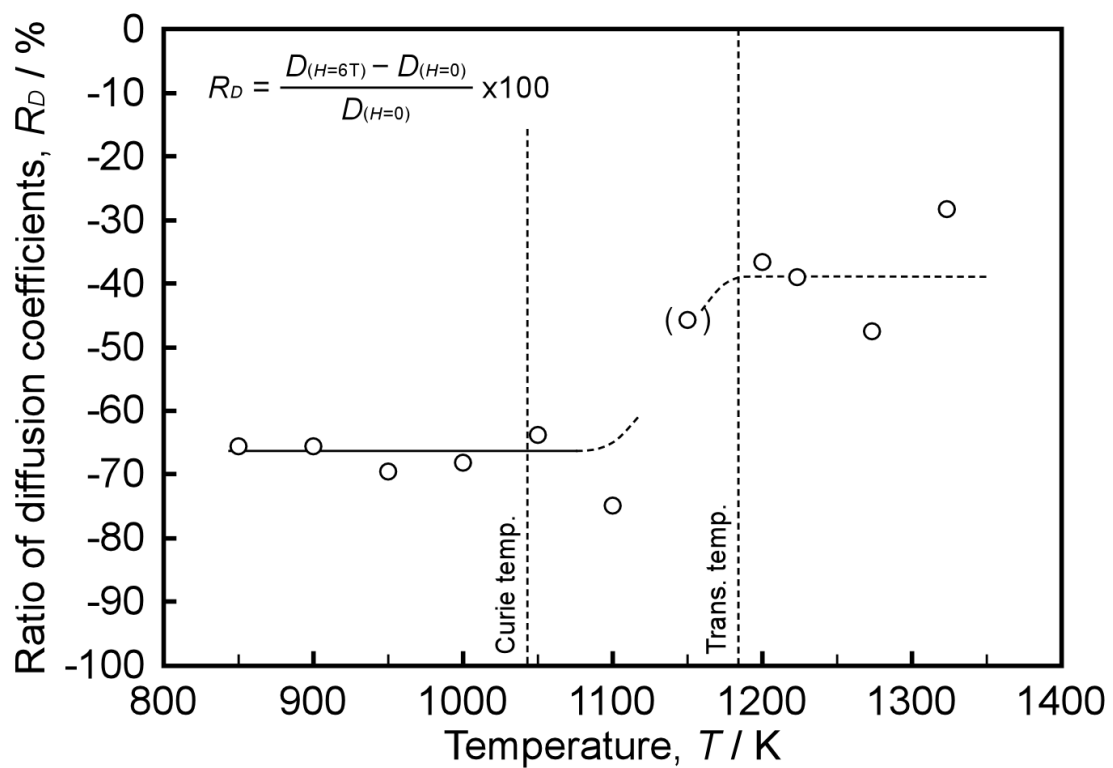


Figure 2-9 The retardation rate of diffusion coefficient by the application of a magnetic field as a function of annealing temperature.

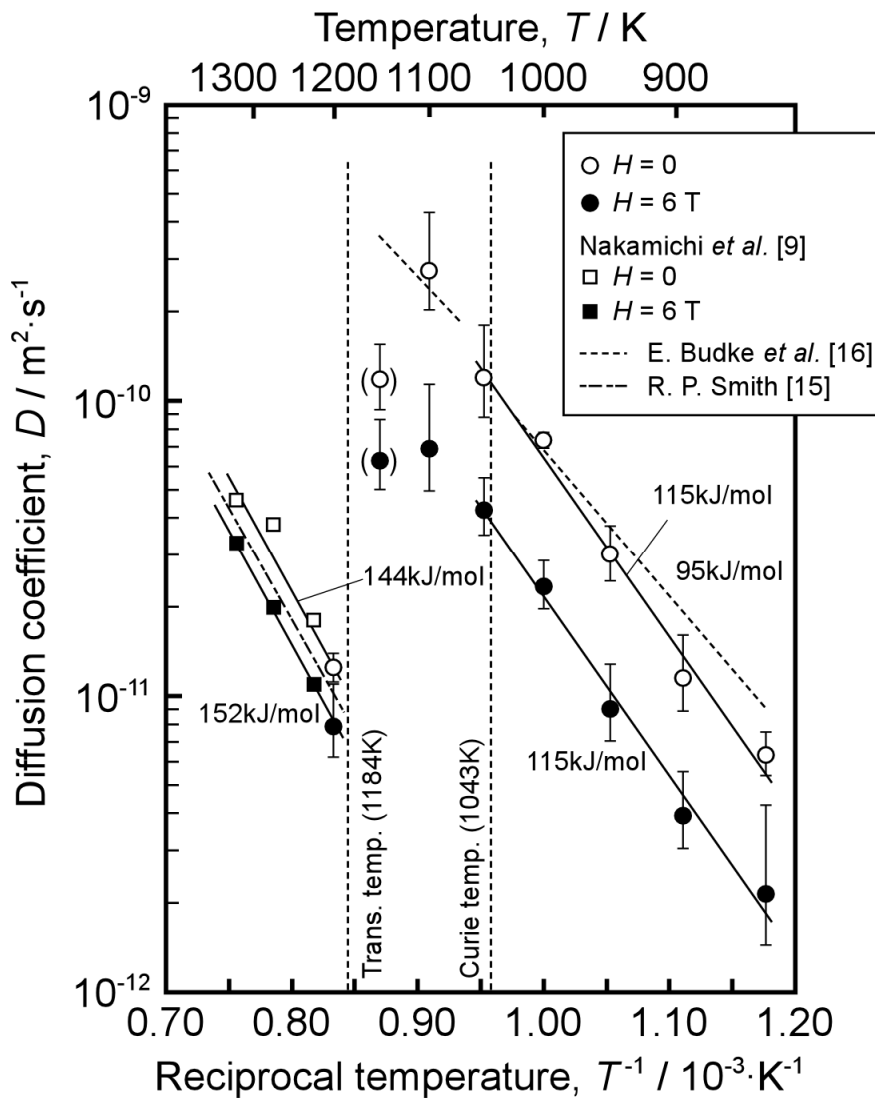


Figure 2-10 Arrhenius plots of the carbon diffusion coefficients in pure iron under static magnetic fields of 2 - 6 T.

magnetic field were evaluated to be 144 ± 25 kJ/mol and 152 ± 4 kJ/mol, respectively. Taking into consideration of the experimental error, it was concluded that the magnetic field cannot exert an observable influence on the activation energy of diffusion of carbon in both α - and γ -iron but on the pre-exponential factor. There are some reports that the static magnetic field predominantly affected the pre-exponential factor but not the activation energy in the thermally-activated process closely related to the diffusion by the application of a magnetic

field [17, 18].

The diffusion coefficients at 1150K showed lower than the values which was expected from the extrapolating the temperature dependence of diffusivity for without and with a 6 T magnetic field, because carbon penetration into α -Fe may have caused the transformation of α -Fe into γ -Fe, in which the carbon diffusivity is lower than that in α -Fe, in the vicinity of the interface. In particular, the decrease in diffusivity was significant without a magnetic field, implying that a magnetic field would increase the α - γ transformation temperature. It is well-known that the γ phase forms at the grain boundaries or triple junctions in the α - γ phase transformation because the carbon atoms segregate at the grain boundaries. Tsurekawa *et al.* has reported the grain boundary segregation of Sn atoms in iron was suppressed by the application of a magnetic field [19-21]. If it is assumed that a magnetic field can also decrease the grain boundary segregation of carbon atoms in iron, the α - γ phase transformation would be delayed during a magnetic field being applied. Moreover, there are some theoretical [22] and experimental [23, 24] reports showing that the α - γ transformation temperature increased under a magnetic field. As the result, the decrease in carbon diffusion coefficient with the magnetic field at 1150K obtained from the expected value was smaller than that without a magnetic field.

(b) Field strength dependence

The dependence of a magnetic field strength on carbon diffusivity in iron was investigated. Fig. 2-11 shows the logarithm of carbon diffusivity at 1000K as a function of a magnetic field strength. The logarithm of carbon diffusion coefficient in α -iron decreases linearly as a function of a magnetic field strength. The diffusivity of interstitial atoms such as carbon is well-known to be described by eqn. (2-3) [25] as follows,

$$D = \frac{1}{n} \nu d^2 \exp\left(\frac{S_D}{R}\right) \exp\left(-\frac{H_D}{RT}\right) \phi, \quad (2-3)$$

where ν is the frequency of atoms, d is the jump length of carbon, S_D is the activation entropy, R is the gas constant, H_D is the activation enthalpy, T is the absolute temperature and ϕ is the thermodynamic factor. From the experimental results shown in Fig.2-10, H_D in eqn. (2-3) is less dependent on an applied magnetic field. Although the jump length would slightly increase along the field direction due to the magnetostriction of iron in a magnetic field, the change in jump length can be negligible because the magnetostriction of iron is quite small [26]. In addition, the frequency of atoms ν and thermodynamic factor ϕ are assumed not to be

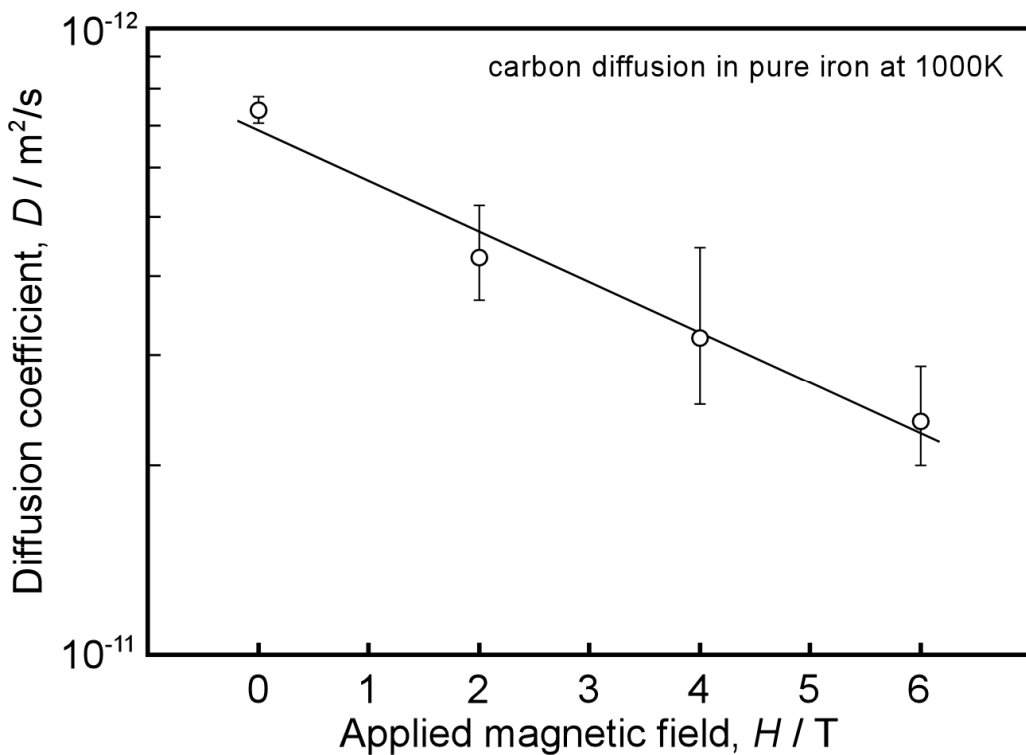


Figure 2-11 The dependence of magnetic field strength on the diffusion coefficient of carbon atoms in iron.

changed by a magnetic field. From the results of Fig. 2-11, the diffusivity exponentially decreased with increase in the field strength. Thus, the activation entropy will be a linear function of field strength. Therefore, it is concluded that a decrease in the activation entropy due to a magnetic field will be responsible for the decrease in the carbon diffusivity observed.

Here the activation entropy of carbon diffusion under a magnetic field was discussed from the viewpoint of carbon occupancy in iron. It is known that the carbon atoms in α -iron are located in the octahedral sites and tetrahedral sites of body centered cubic lattice as shown in Fig. 2-12. Fig. 2-13 [27] shows the fraction of octahedral site occupancies as a function of temperature, which was obtained by thermodynamic calculation. It is evident that the fraction of the tetrahedral site occupancies is quite small, which is at most 0.1% in α -Fe temperature range. There would be a large change of configurational entropy if a small number of carbon atoms are allowed to rearrange to the tetrahedral sites because there were large difference

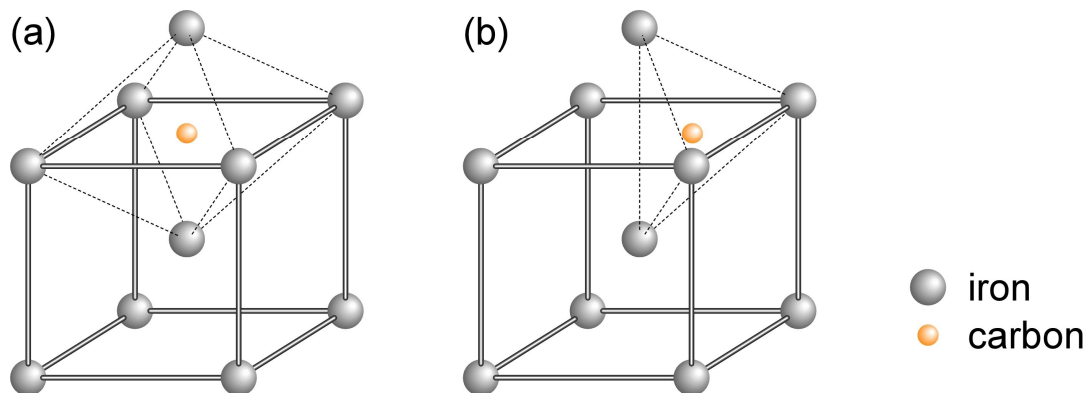


Figure 2-12 Schematic illustrations of carbon atoms in α -iron located in (a) octahedral site and (b) tetrahedral site.

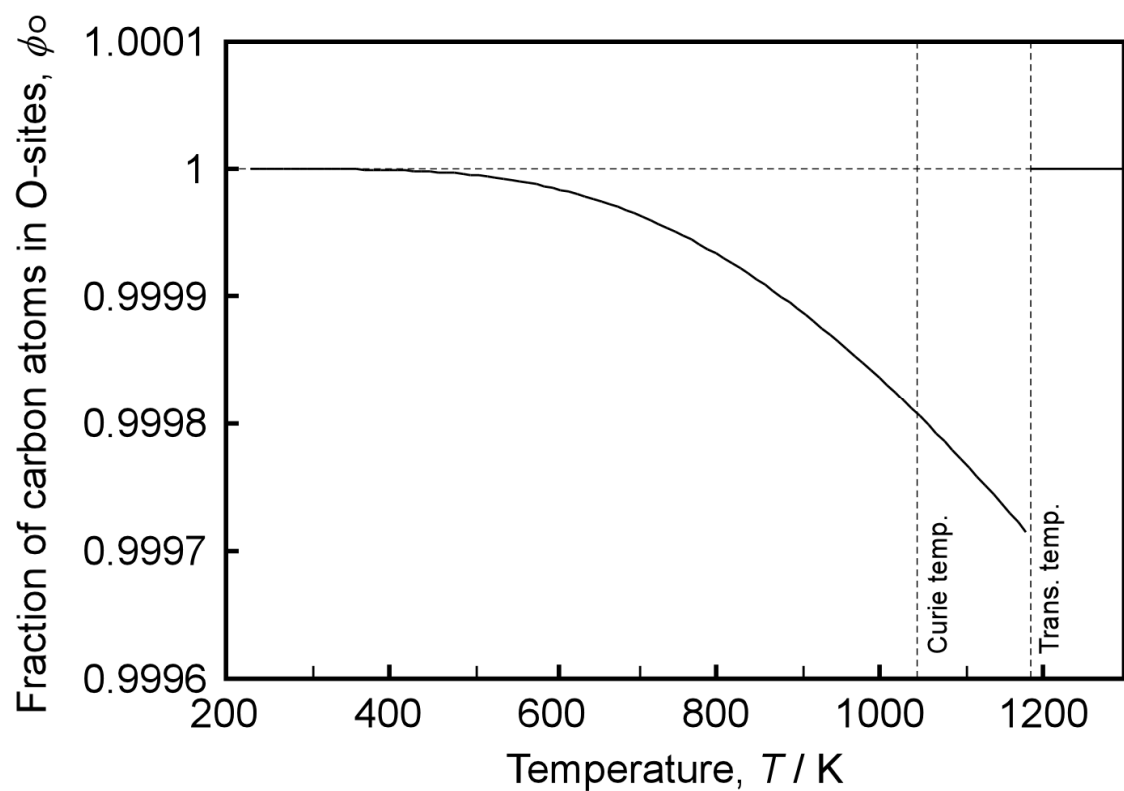


Figure 2-13 The fraction of carbon atoms located in octahedral sites in bcc iron as a function of temperature [27].

between the Helmholtz free energy of octahedra and tetrahedral [27]. Thus the fraction of octahedral site occupancies would significantly affect the activation entropy. If a magnetic field could change the fraction of octahedral site occupancies, the diffusivity of carbon would change in a magnetic field. Here a question arises: why the fraction of octahedral site occupancies can change in a magnetic field. The reason can be explained from the viewpoint of magnetostriction. The volume magnetostriction constant of the <100> type directions is known to be positive [26]. This means that the bcc iron lattice expands in the <100> directions. When the lattice expand to the <100> direction, the octahedral sites would be more favored because the nearest neighboring iron atoms in octahedra are located along the <100> directions in α -iron. Consequently the octahedral sites would be more favored for carbon atoms in α -Fe in a magnetic field. As the configuration of carbon atoms would significantly affect the diffusivity of carbon in α -Fe due to the large difference between the diffusivity of octahedra and tetrahedral [27], the application of a magnetic field could be expected to change the diffusivity of carbon. The configurational entropy of carbon atoms would decrease by the application of a magnetic field due to magnetostriction of ferromagnetic α -iron, so that the diffusivity of carbon would be retarded. The details of the discussion will be made in the next chapter on the basis of a dual occupancy model [27, 28]

Next, the carbon atoms in fcc γ -Fe are known to occupy only octahedral sites unlike α -Fe. Therefore the configurational entropy of carbon atoms in γ -Fe would not change even if a magnetic field is applied. The nearest neighboring iron atoms in octahedra are also located along the <100> directions in γ -Fe. However the volume magnetostriction constant of the <100> type directions in γ -Fe is known to be negative as opposed to α -iron. In other words, when a magnetic field is applied, the fcc iron lattice compresses in the <100> directions. This would make the retardation effect of carbon diffusivity in γ -Fe by a magnetic field as shown in Fig. 2-9.

2.3.3 Diffusivity of carbon in iron under a magnetic field gradient

Fig. 2-14 shows the changes of carbon concentration as a function of the distance from the interface between steel and iron in the diffusion couple annealed at (a) 950 K and (b) 1000 K without and with a magnetic field gradient of 45 T/m. For comparison, the profiles obtained from the specimens annealed under a static magnetic field of 6 T are also shown in Fig. 2-14. When a magnetic field gradient was applied to the specimen, the carbon concentration in pure iron increased in comparison with the specimen annealed without a magnetic field gradient.

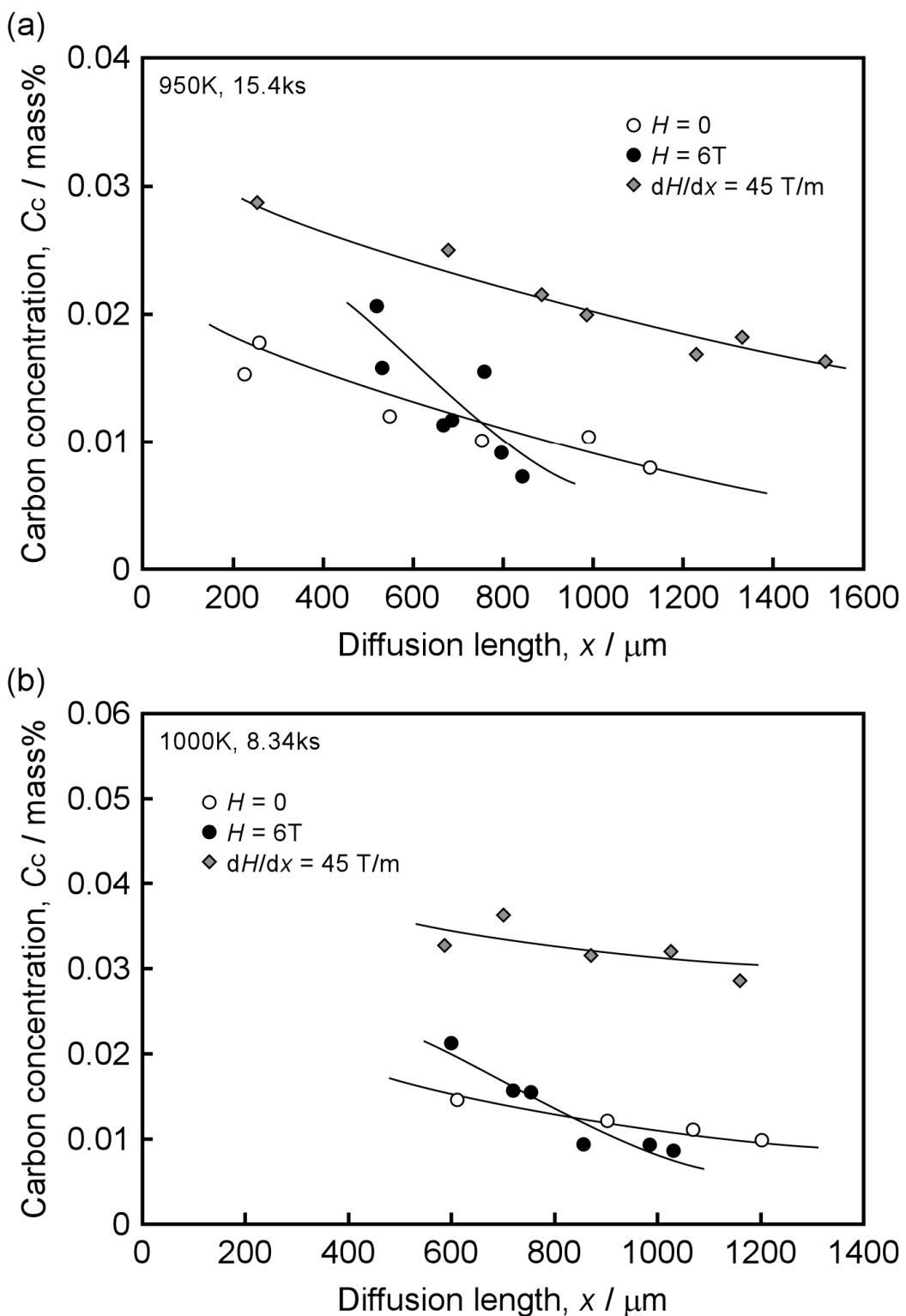


Figure 2-14 Carbon concentration distributions in pure iron as a function of diffusion length in explosive welded specimens annealed at (a) 950 K and (b) 1000 K without and with a magnetic field gradient of 45 T/m.

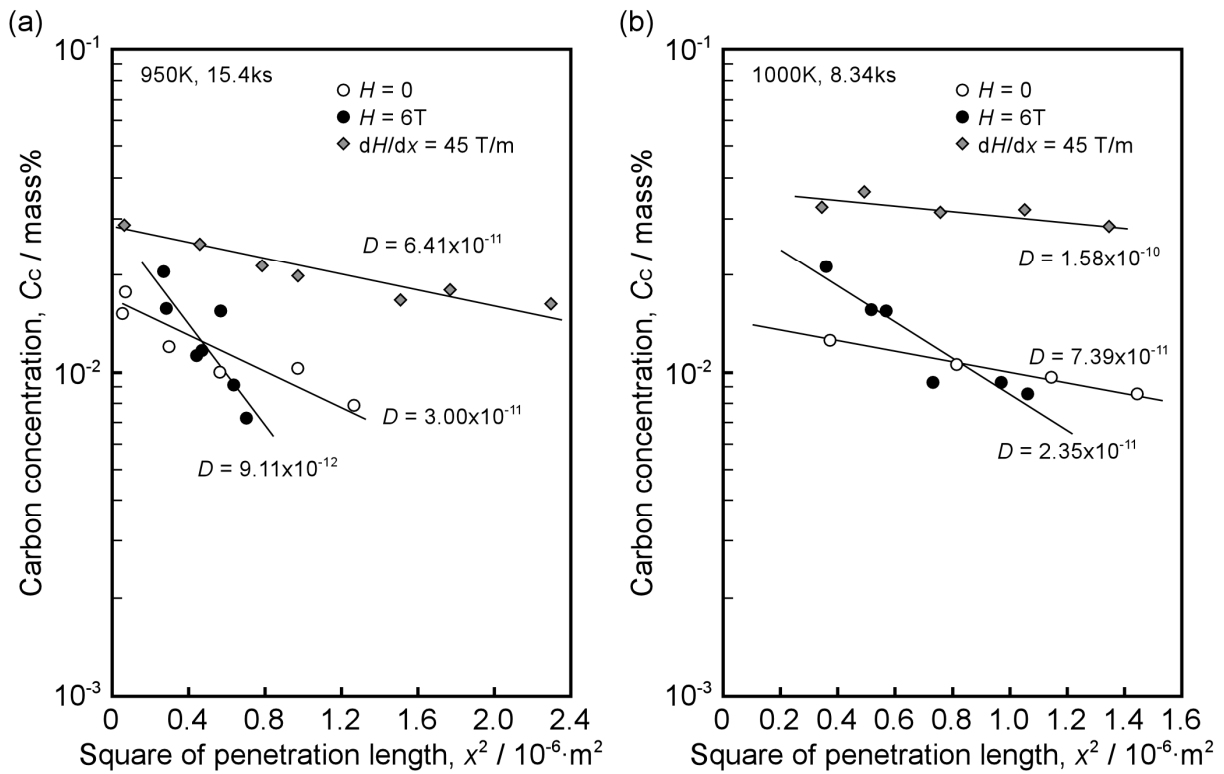


Figure 2-15 Carbon concentration distributions in pure iron as a function of square of diffusion length in explosive welded specimens annealed at (a) 950 K and (b) 1000 K without and with a magnetic field gradient of 45 T/m.

Besides, the gradient of carbon concentration in iron under a magnetic field gradient was smaller than that without a magnetic field. The relationship between the natural logarithm of C_c and the square of penetration depth is shown in Fig. 2-15. There is a good linear correlation between them, so that the carbon diffusion coefficients under a magnetic field gradient were evaluated from the slope of the straight line in Fig. 2-15. Fig. 2-16 shows the Arrhenius plots of the measured diffusion coefficients of carbon under a magnetic field gradient. For comparison, the diffusion coefficients without and with a static magnetic field are also shown. It was evident that the diffusion coefficient of carbon in iron was enhanced by the application of a magnetic field gradient.

Here, the sign of a magnetic field gradient is defined as schematically shown in Fig. 2-17. When a flux of carbon atoms produced by a concentration gradient occurs towards a

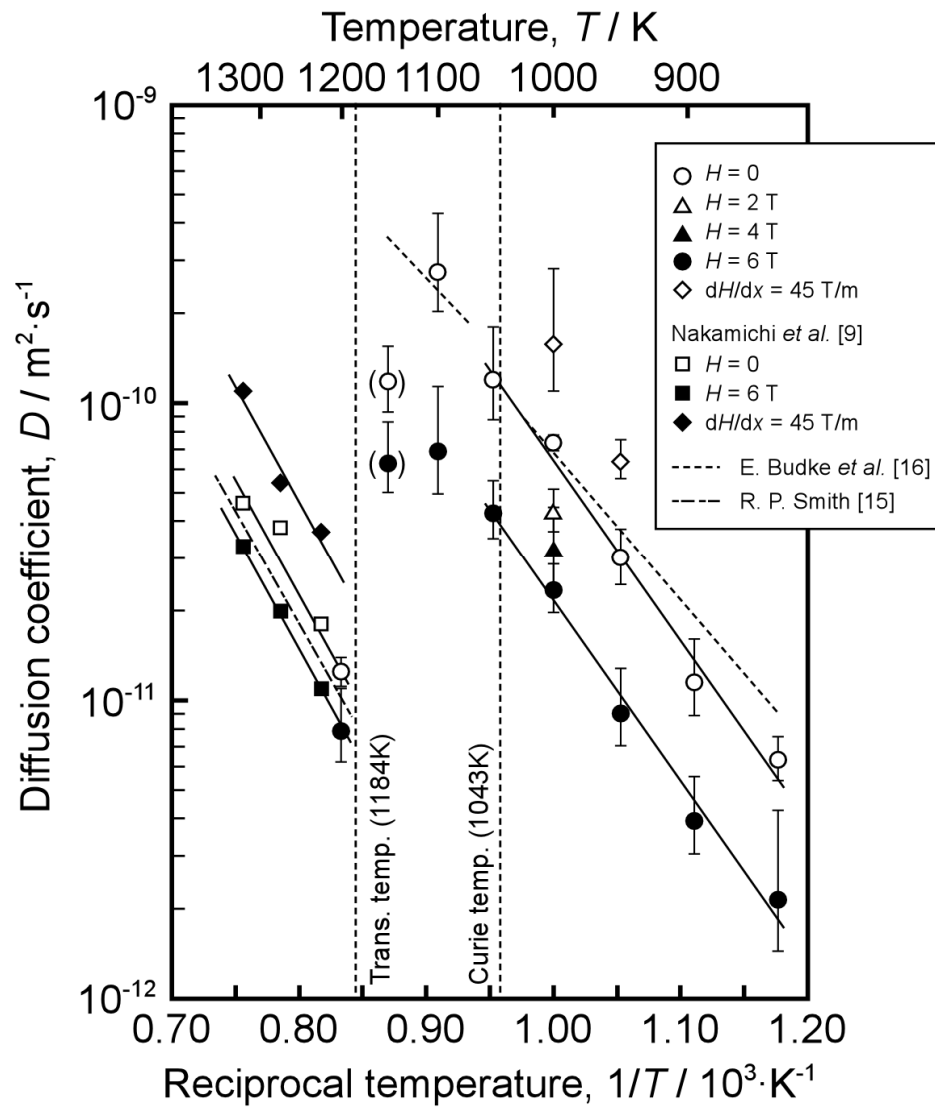


Figure 2-16 Arrhenius plots of carbon diffusion coefficients in pure iron under static magnetic fields of 2 – 6 T and a magnetic field gradient of 45 T/m.

higher magnetic field strength, the magnetic field gradient is defined as “negative”. Thus, the carbon diffusion in α -Fe is enhanced in a “negative” magnetic field gradient, which is consistent with the previous report by Nakamichi *et al.* [9]. The increase in diffusivity in a negative magnetic field gradient can be explained from the viewpoint of a potential gradient due to magnetic free energy. The “negative” magnetic field gradient involves a “positive” magnetic free energy gradient in α -Fe matrix because of a positive value of permeability for

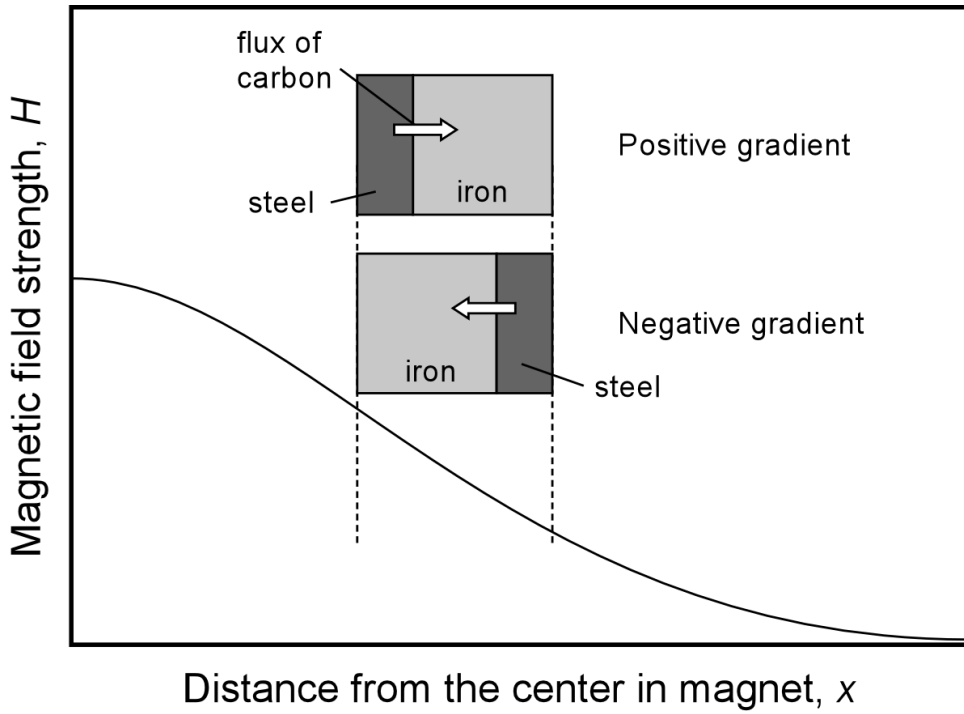


Figure 2-17 Definition of “negative” magnetic field gradient in this study.

α -Fe at annealing temperature: that is, the magnetic free energy of α -Fe increases with approaching to the iron/steel interface in the “negative” magnetic field gradient. This is because for the ferromagnetic state like α -Fe, the magnetic free energy is given for unit volume by,

$$\Delta G_M^f = -\mu_0 \left(H - \frac{NM_s}{2} \right) M_s \quad (2-4)$$

when $H \gg H_s$, where μ_0 is the magnetic permeability of vacuum, N is the demagnetizing factor, M_s is the saturation magnetization of iron and H_s is the magnetic field strength when the magnetization reaches to M_s . Here, as the demagnetizing factor N was extremely small in this experiment, second term of right-hand side in eqn. (2-4) can be negligible. It is reasonable to consider that the magnetic free energy gradient in α -Fe matrix would produce a flux of carbon atoms towards a lower magnetic free energy regime. Taking account of a potential gradient due to the magnetic free energy in α -Fe, the flux equation of carbon atoms is given by the following equation.

$$J = -D \left(\frac{dC}{dx} + \frac{CV}{kT} \frac{dU}{dx} \right), \quad (2-5)$$

where J is the flux of atoms, k is Boltzmann constant and dU is a potential gradient. If dU in eqn. (2-5) corresponds to ΔG_M^f , we have

$$J = -D \left(\frac{dC}{dx} - \mu_0 M_s \frac{CV}{kT} \frac{dH}{dx} \right). \quad (2-6)$$

Therefore, when a “negative” magnetic field gradient, $(dH/dx) < 0$, is applied, the total flux of carbon atoms would be increased. Conversely, the flux would be decreased in a positive magnetic field gradient, as Nakamichi *et al* observed [9]. This is a possible explanation for the enhancement of carbon diffusion in α -iron by the application of the “negative” magnetic field gradient. Using this equation, the numerical analysis of carbon diffusion in α -iron under a magnetic field gradient was performed and discussed the effect of a magnetic field gradient in next chapter.

2.3.4 Solid solubility of carbon in iron under a magnetic field

When it is assumed that the carbon concentration at the interface between Fe and Fe-0.87mass%C approaches the solid solution limit, it can be possible to estimate from the intercept obtained by extrapolating to the interface ($x=0$) of the lines in Figs. 2-8 and 2-15. The carbon solubility limits observed were plotted on the Fe-C binary phase diagram as shown in Fig. 2-18. The solid solubility of carbon without a magnetic field did not significantly change depending on the annealing temperature contrary to the expectations. However it is evident that the carbon solubility limit increased by twice under a 6 T magnetic field around 1000K. This is qualitatively in good agreement with previous calculation by Choi *et al.* [8], though several dozen tesla was necessary for observable effect of a magnetic field on the solubility limit of carbon in α -Fe from their calculation. A possible explanation to this magnetic field effect can be given from the viewpoint of magnetic free energy. In general, the magnetic free energy per unit volume for ferromagnetic materials is given by eqn. (2-4). On the other hand, that of paramagnetic materials is given by,

$$\Delta G_M^p = -\frac{1}{2} \mu_0 \chi (1 - \chi N) H^2, \quad (2-5)$$

where χ is the magnetic susceptibility. In our experiments, a magnetic field was applied parallel to the long axis of the specimens, so that the demagnetizing factor is assumed to be zero. Therefore the Gibbs free energy of ferromagnetic α phase would decrease when a strong

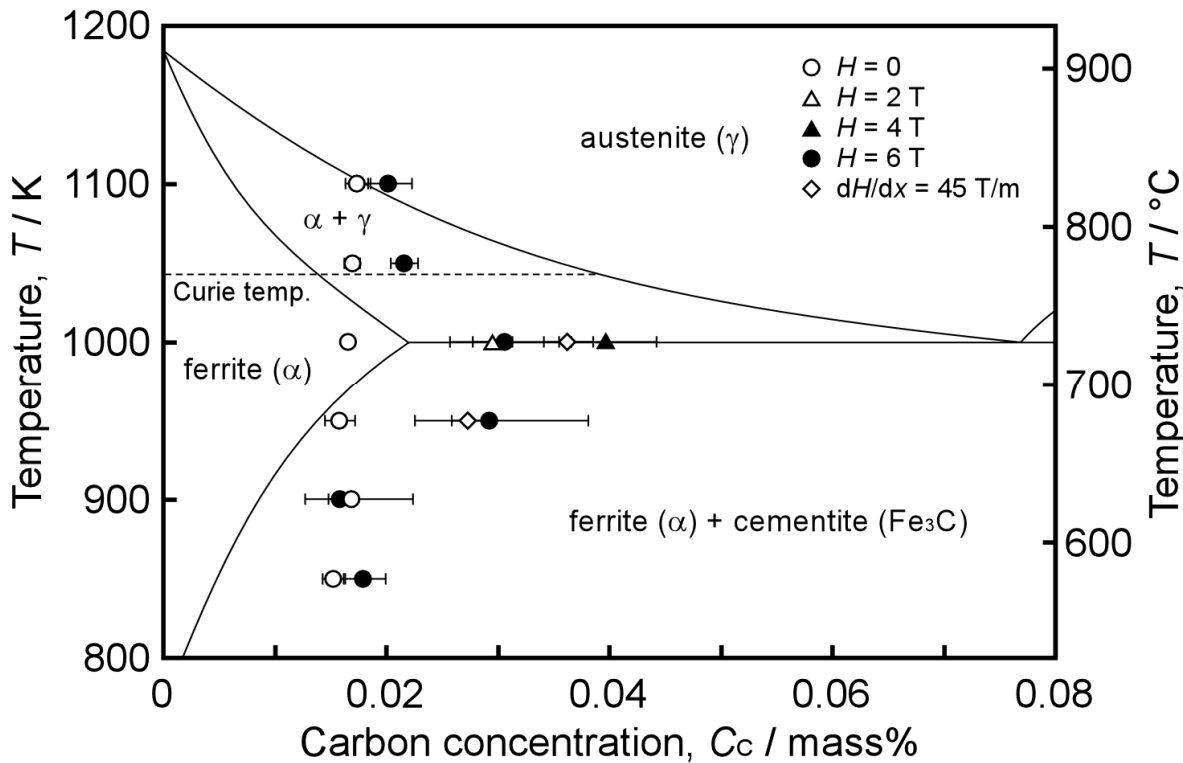


Figure 2-18 The temperature dependence of solid solubility limits of carbon in pure iron under static magnetic fields of 2 – 6 T and a magnetic field gradient of 45 T/m. The solid solubility limits were estimated from the intercept obtained by extrapolating to the interface ($x=0$) of the lines in Figs. 2-8 and 2-15.

magnetic field is applied. In contrast, that of paramagnetic γ phase would not significantly change even under a strong magnetic field because the magnetic susceptibility, χ , of paramagnetic γ iron is extremely small [29]. Fig. 2-19 shows the schematic illustration of the change of Gibbs free energy under a magnetic field and the effect of a magnetic field on the $\alpha+\gamma/\alpha$ equilibrium temperature (Ae_1) and the solid solubility limit of carbon in iron. When a strong magnetic field is applied, the solid solubility limit of carbon will shift to higher concentration, which is estimated from the common tangent to the free energy curves, as the free energy curve of ferrite phase is lowered.

Lastly, the dependence of solid solubility limit of carbon on magnetic field strength was investigated at 1000K because the most significant effect of a 6 T magnetic field was

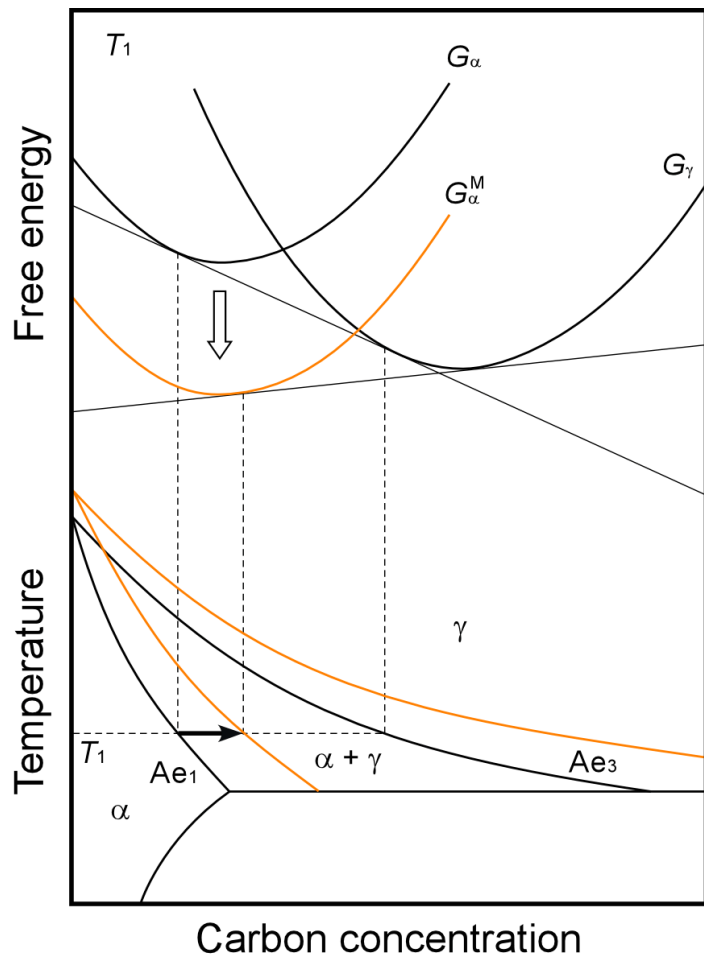


Figure 2-19 Schematic illustration of Gibbs free energy of ferrite and austenite phases under a magnetic field and binary phase diagram of Fe-C alloy which is obtained from the common tangent to the free energy curves. The orange lines indicate the free energy and transformation curves under a magnetic field.

confirmed at this temperature. Fig. 2-20 shows the solid solubility limit of carbon in iron as a function of magnetic field strength. The solid solubility limit under a magnetic field of 5 T was estimated from the intercept obtained by extrapolating to the interface ($x = 0$) of the lines in Fig. 2-15, which was measured in the specimen annealed under a magnetic field gradient of 45 T/m. In this experiment, the strength of an applied static magnetic field to the specimen was approximately 5 T when the specimen was set under a magnetic field gradient of 45 T/m as shown in Fig. 2-4. The solid solubility limit of carbon increased with the increase in

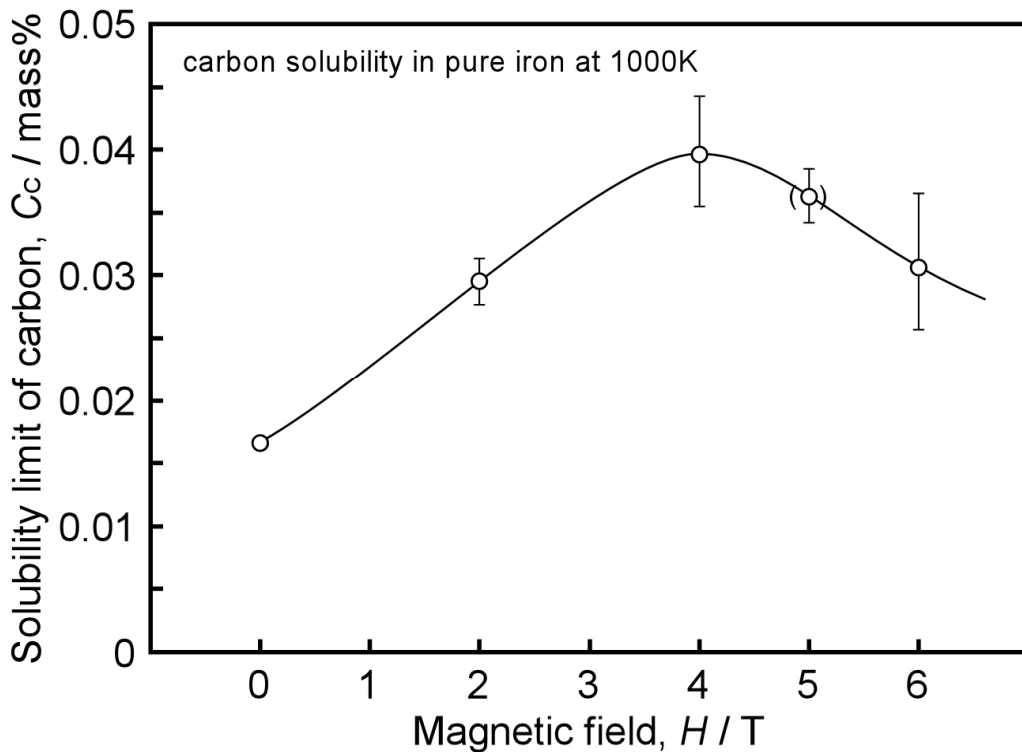


Figure 2-20 The change of solid solubility limit of carbon in pure iron at 1000 K as a function of magnetic field strength.

magnetic field strength and showed a maximum at 4 T magnetic field. This implies that the free energy of ferrite phase under a magnetic field can be determined not only magnetic free energy but also elastic potential energy due to magnetostriction and so on. That is, the solid solubility limit of carbon in iron under a magnetic field would be changed by the expansion and contraction of iron lattice induced by magnetostriction.

2.4 Summary

The effects of a static magnetic field and a magnetic field gradient on the diffusivity and solid solubility of carbon in pure iron were experimentally investigated using the diffusion couple between pure iron and eutectoid steel (Fe-0.87mass%C) by explosive welding technique. And the following conclusions were obtained.

- (1) The diffusivity of carbon in both α - and γ -iron decreased in a 6 T magnetic field by approximately 70 % and 40 %, respectively. The decrease in diffusivity is more significant in α -Fe than that in γ -Fe. The activation energy of carbon diffusion was less dependent on a magnetic field.
- (2) The logarithm of carbon diffusion coefficient in α -Fe is a linear function of a magnetic field strength. This suggests that the activation entropy of diffusion decreases with increasing magnetic field. Consequently, the diffusivity of carbon in iron would decrease in a magnetic field. The decrease in activation entropy would be due to the magnetostriction of α -Fe.
- (3) A “negative” magnetic field gradient can enhance the carbon diffusion in α -iron by approximately 115 %. The magnetic free energy gradient in α -Fe would give rise to increase in the flux of carbon atoms.
- (4) The solid solubility limit of carbon increased by twice when a 6 T magnetic field was applied at the ferromagnetic temperature ranging from 950K to 1000K. The solid solubility limit of carbon will shift to higher concentration under a static magnetic field, as the free energy curve of ferrite phase will be lowered. In addition, the solid solubility limit of carbon increased with the increase in magnetic field strength and has a maximum value at a magnetic field of 4 T.

References

- [1] W. V. Youdelis, D. R. Colton, J. Cahoon: *Can. J. Phys.*, **42** (1964), 2217.
- [2] H. Nakajima, S. Maaekawa, Y. Aoki and M. Koiwa: *Trans. Jap. Inst. Metals*, **26** (1985), 1.
- [3] A. V. Pokoev, D. I. Stepanov, I. S. Trofimov and V. F. Mazanko: *Phys. Stat. Sol.*, **137** (1993), K1.
- [4] A. V. Pokoev and D. I. Stepanov: *Defect and Diff. Forum*, **143-147** (1997), 419.
- [5] D. V. Mironov, A. V. Pokoev and V. F. Mazanko: *Met. Phys. Adv. Tech.*, **18** (1999), 693.
- [6] X. Liu, J. Cui, X. Wu, Y. Guo and J. Zhang: *Scripta Mater.*, **52** (2005), 79.
- [7] Z. F. Li, J. Dong, X. Q. Zeng, C. Lu, W. J. Ding and Z. M. Ren: *J. Alloys Comp.*, **440** (2007), 132.
- [8] J. K. Choi, H. Ohtsuka, Y. Xu, and W. Y. Choo: *Scripta Mater.*, **43** (2000), 221.
- [9] S. Nakamichi, S. Tsurekawa, Y. Morizono, T. Watanabe, M. Nishida and A. Chiba: *J. Mat. Sci.*, **40** (2005), 3191.
- [10] H. Ohtsuka and X. J. Hao: *Proc. of 5th Intern. Symp. on Electromagnetic processing of Materials (EPM2006)*, The Iron and Steel Institute of Japan (2006), 648.
- [11] E. Rabkin, A. Gabelev, T. Matsuzaki and T. Watanabe: *Defect and Diff. Forum*, **237-240** (2005), 560.
- [12] M. A. Verzhakovskaya, S. S. Petrov and A. V. Pokoev: *Tech. Phys. Lett.*, **33** (2007), 961.
- [13] M. A. Verzhakovskaya, S. S. Petrov and A. V. Pokoev: *Bulle. Rus. Acad. Sci. Phys.*, **71** (2007), 1674.
- [14] J. K. Stanley: *Metals Trans.*, **185** (1949), 752.
- [15] R. P. Smith: *Trans. Metall. Soc. AIME*, **224** (1962), 105.
- [16] E. Budke, C. Herzig and H. Wever: *Phys. Stat. Sol.*, **127** (1991), 87.
- [17] X. Liu, J. Cui, X. Wu, Y. Guo and J. Zhang: *Scripta Mater.*, **52** (2005), 79.
- [18] Z. F. Li, J. Dong, X. Q. Zeng, C. Lu, W. J. Ding and Z. M. Ren: *J. Alloy Comp.*, **440** (2007), 132.
- [19] S. Tsurekawa, K. Kawahara, K. Okamoto, T. Watanabe and R. Faulkner: *Mater. Sci. Eng.*, **A387-389** (2004), 442.
- [20] S. Tsurekawa, K. Okamoto, K. Kawahara and T. Watanabe: *J. Mater. Sci.*, **40** (2005), 895.
- [21] R. Sumi, N. Toda, H. Fujii and S. Tsurekawa: *Rev. Adv. Mater. Sci.*, (2009), accepted.
- [22] J. K. Choi, H. Ohtsuka, Y. Xu and W. Y. Choo: *Scripta Mater.*, **43** (2000), 221.
- [23] X. Jiang and H. Ohtsuka: *Mater. Trans., JIM*, **45** (2004), 2622.
- [24] Y. Zhang, C. He, X. Zhao, L. Zuo and C. Esling: *J. Mag. Mag. Mater.*, **294** (2005) 267.
- [25] T. Heumann: *Diffusion in Metallen*, Springer-Verlag (1992).
- [26] R. C. Hall: *J. Appl. Phys.*, **31** (1960), 1037.
- [27] R. B. McLellan, M. L. Rudee and T. Ishibachi: *Trans. Metall. Soc. AIME*, **233** (1965), 1938.
- [28] J. R. G. da Silva and R. B. McLellan: *Mater. Sci. Eng.*, **26** (1976), 83.
- [29] S. Chikazumi: *Physics of Magnetism*, Wiley, New York (1964).

Chapter 3

Mathematical modeling of diffusion process in iron under a magnetic field

3.1 Introduction

There exist many laws and theorems which dominate the physical phenomena, such as the Fick's law and the Hall-Petch relation. These make it possible to characterize the effect of microstructures on mechanical properties of materials. For example, the yield strength can be predicted from the grain size of the materials according to the Hall-Petch relationship and the grain size can be predicted from the annealing time. Therefore, the theoretical analyses on the basis of some laws and theorems are the effective means of the approaches to clarification of the issues which can not be investigated by any experiments in particular. On the other hand, it can be powerful tool to assess the validity of the mechanisms of physical phenomena based on the experiments.

In the previous chapter, it was found that the carbon diffusivity in iron decreased and increased by the application of a static magnetic field and a magnetic field gradient, respectively. From the qualitative discussion, a static magnetic field was considered to decrease the activation entropy of carbon diffusion due to the magnetostriction of bcc iron. Similarly, it was predicted that the increase in the carbon diffusivity by a magnetic field gradient was caused by the driving force due to the magnetic potential gradient. To clarify the mechanism of these effects of a static magnetic field and a magnetic field gradient on carbon diffusion, the construction of the physical model and the numerical analysis were performed.

The effect of a static magnetic field on carbon diffusion was discussed from a viewpoint of site occupancy of carbon atoms in bcc iron. The diffusivity of carbon atoms in bcc iron is known to significantly depend on the position of their occupied sites [1]. If the site occupancy of carbon atoms in bcc iron is affected by a static magnetic field, there is a possibility that the carbon diffusivity is also changed by a static magnetic field. Then the site occupancy model of carbon atoms under a static magnetic field was constructed to reveal a mechanism of magnetic field effect. On the basis of this model, the carbon diffusivity in iron under a static

magnetic field was quantitatively analyzed.

The effect of a magnetic field gradient on carbon diffusion was analyzed on the basis of the Fick's law with potential gradient. Although the diffusion of atoms in solid can be theoretically described according to the Fick's first and second laws, it is difficult to obtain the analytical solution of diffusion equation with potential gradient [2]. In addition, it is also difficult to obtain the numerical solution with certified accuracy and stability [3]. In these circumstances, the accuracy and stability approaches to the solution of diffusion equation with driving force due to the potential gradient have been performed [4, 5]. The issue of carbon diffusion in pure iron under a magnetic field gradient can be discussed as one dimensional phenomenon. However, as the diffusion term induced by the magnetic potential gradient is nonlinear, it must be careful to keep the convergence and stability of solution in the numerical analysis.

In this chapter, construction of a physical and numerical analysis were carried out concerning the carbon diffusion in pure iron under a magnetic field and a magnetic field gradient. Thereafter the mechanisms of magnetic field effects were discussed on the basis of results of theoretical analysis.

3.2 Physical modeling of carbon diffusion in iron on the basis of dual occupancy model

3.2.1 Site occupancy of carbon atoms in bcc iron

The carbon diffusivity decreased by the application of a static magnetic field as shown in chapter 2. As the configurational entropy of carbon atoms was expected to play an important role in its diffusivity from the experimental results in chapter 2, it was necessary to consider the physical model of carbon configuration in bcc iron under a static magnetic field. A model for dilute interstitial solid solutions is proposed in which the solute atoms can occupy both the octahedral and tetrahedral interstices in the bcc solvent lattice. The distribution function, according to which the solute atoms are apportioned between the two kinds of sites, is calculated. The partial thermodynamic functions of the solution are calculated from the distribution function. Then, the explanation can be given by the dual occupancy model suggested by McLellan *et al.* [6]. According to this model, the carbon atoms in ferrite occupy both octahedral (O) and tetrahedral (Te) holes, and those in austenite occupy

only octahedral holes.

First the fraction of octahedral site occupancies was discussed on the basis of thermodynamics. The solutions involved in this study were very dilute so the solute-solute interactions can be ignored and it can be assumed that all configurations have the same energy. Differentiating the Helmholtz free energy F with respect to the number of occupied tetrahedral sites N_v^{Te} yields,

$$\frac{dF}{dN_v^{Te}} = kT \ln \frac{N_v^{Te}}{N_v^O} \cdot \frac{N_v\beta_O - N_v^O}{N_v\beta_{Te} - N_v^{Te}} - T\Delta S + \Delta E, \quad (3-1)$$

where N_v^O is the number of occupied octahedral sites, N_v is the number of solvent atoms, ΔS is the difference between the changes in vibrational entropy occurring when a solute atom is inserted in an octahedral and tetrahedral sites and ΔE is the difference between the energies per atom of pure solvent octahedra and tetrahedra. In the equilibrium distribution $dF/dN_v^{Te} = 0$; if the eqn. (3-1) is assumed to equal to zero and the dilute-solution approximation that $N_v\beta_O \gg N_v^O$ and $N_v\beta_{Te} \gg N_v^{Te}$ is used, the equilibrium distribution can be described as,

$$\frac{N_{Te}}{N_O} = \frac{\beta_O}{\beta_{Te}} \exp\left(-\frac{\Delta E}{kT}\right) \exp\left(\frac{\Delta S}{k}\right). \quad (3-2)$$

For the bcc lattice $\beta_O = 3$ and $\beta_{Te} = 6$. Using this equation, the equation of the fraction of octahedral site occupancies for the whole solute carbon atoms can be derived as,

$$\begin{aligned} \phi_O &= \frac{N_O}{N_O + N_{Te}} \\ &= 1 - \left\{ 2 \exp\left(\frac{\Delta E}{kT}\right) \exp\left(-\frac{\Delta S}{k}\right) + 1 \right\}^{-1}. \end{aligned} \quad (3-3)$$

Here the fraction of octahedral site occupancies was calculated as a function of temperature using eqn. (3-3) and the values of physical constants reported by McLellan *et al.* as listed in Table 3-1. In addition, as the experimental results as shown in chapter 2 gave the prediction that the entropy term of carbon diffusivity would decrease by a static magnetic field, the entropy dependence of the fraction of octahedral site occupancies was also calculated. Fig. 3-1 shows the calculation results. The fraction of solute atoms located at Te sites is always small since the value of ϕ ranging from 1 at room temperature to 0.9997 at the α - γ phase transformation temperature. Thus at most approximately three atoms in 10000 are located at Te sites. The fraction of octahedral site occupancies was found to increase with the decrease in entropy. Therefore the octahedral site would become more favored when a static magnetic field was applied.

Table 3-1 Physical constants for equation 3-3.

Parameter	Value
$\Delta S/k$	-4.4
ΔE	30.1 kJ/mol

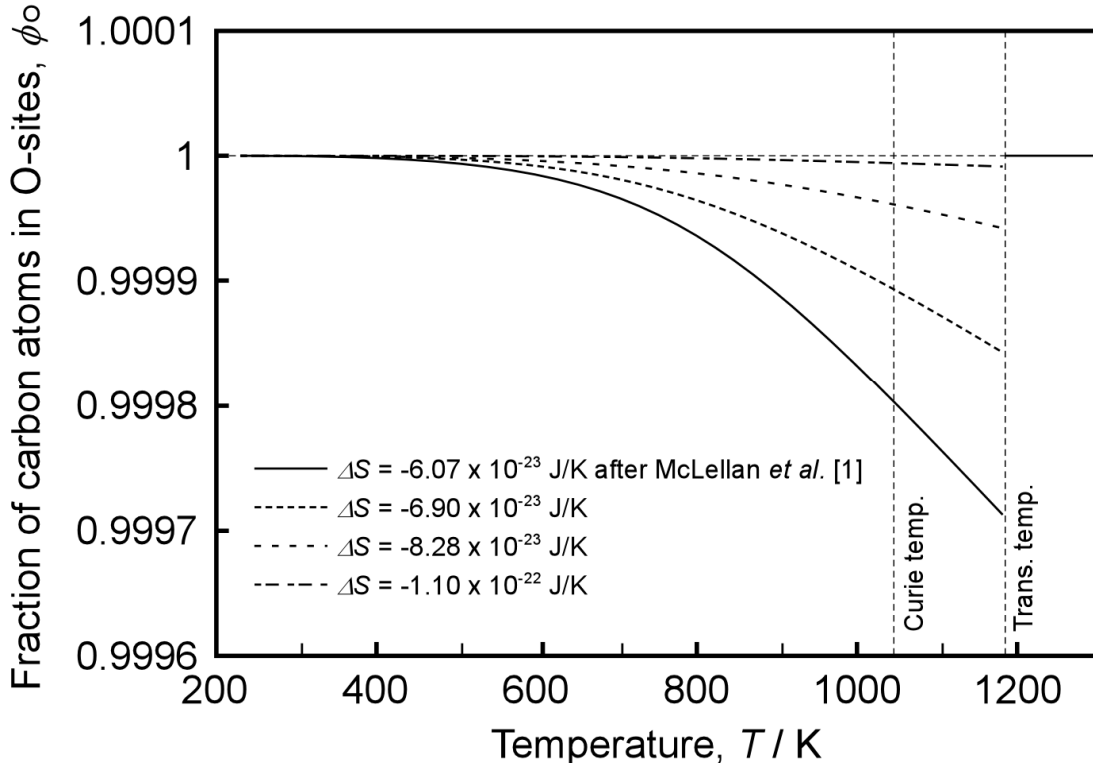


Figure 3-1 The entropy dependence of fraction of carbon atoms located in octahedral sites as a function of temperature.

3.2.2 Carbon diffusivity under a static magnetic field

In considering the diffusion of carbon in α -iron, the solute carbon atoms distributed among the O and Te sites at each stage during a diffusion process. Beshers has considered that the possible jumps that an interstitial atom can make in the bcc lattice [7]. The jumps are:

- (a) the path of an atom on an O to another O will be $O\text{-}Te\text{-}O$;
- (b) an atom on a T site has two alternative paths, $Te\text{-}O\text{-}Te$ and $Te\text{-}Te$.

There are three different diffusion paths of carbon in ferrite which are the *O-Te-O* route, *Te-O-Te* route and *Te-Te* route, because the direct jumps between neighboring octahedral sites must involve passage through a tetrahedral site. In a solution where both *O* and *Te* sites are occupied, the observed diffusivity will be a weighted linear sum of the diffusivities of the three diffusion paths. Then the total carbon diffusivity may be written by,

$$D = \phi_O D^{O-Te-O} + (1 - \phi_O) \{ \phi_{Te} D^{Te-Te} + (1 - \phi_{Te}) D^{Te-O-Te} \}, \quad (3-4)$$

where ϕ_{Te} is the fraction of atoms on *Te* sites that diffuse by the *Te-Te* mechanism. This equation can be simplified by noting that D^{O-Te-O} must equal $D^{Te-O-Te}$, as the paths are both sums of an *O-Te* and a *Te-O* jump; hence the rate-controlling mechanism must be same. The eqn. (3-4) can be described as eqn. (3-5).

$$D = \phi_O D^{O-Te-O} + (1 - \phi_O) \{ \phi_{Te} D^{Te-Te} + (1 - \phi_{Te}) D^{O-Te-O} \}. \quad (3-5)$$

The values of pre-exponential factors and activation energies at each diffusion path are shown in Table 3-2. Although the fraction of carbon atoms in the tetrahedral sites is quite small as calculated in the previous section, which is at most 0.03 % at α -Fe temperature range, the overall diffusion coefficient is significantly affected by the carbon atoms in tetrahedral sites because the diffusion coefficient of carbon with *Te-Te* route is approximately 1000 times larger than that with *O-Te-O* route. Then the overall carbon diffusion coefficient was calculated as a function of temperature with changes in the fraction of octahedral site occupancies ϕ_O . The calculation results were compared with the experimental results in the figure of Arrhenius plot as shown in Fig. 3-2. The solid line shows the calculation result of a carbon diffusion using dual occupancy model. This is in good agreement with the experimental results of carbon diffusion coefficients without a magnetic field. As mentioned in the previous section, the octahedral site occupancies would increase with decrease in the entropy due to the application of a static magnetic field. Accordingly the carbon diffusion coefficient was calculated on the assumption that all carbon atoms located at the *O* sites: $\phi_O = 1$ and $\phi_{Te} = 0$. The calculation result is shown by the dashed line in Fig. 3-2. This is in good agreement with the experimental results of carbon diffusion coefficients under a 6 T magnetic field. These results imply that the retardation effect on carbon diffusion under a static magnetic field is due to the decrease in entropy with configurational change of carbon atoms in α -iron.

Table 3-2 Physical constants for equation 3-5.

Parameter	Value
$D_{0, \text{O-Te-O}}$	$3.3 \times 10^{-7} \text{ m}^2/\text{s}$
$D_{0, \text{Te-Te}}$	$2.6 \times 10^{-4} \text{ m}^2/\text{s}$
$Q_{\text{O-Te-O}}$	80.8 kJ/mol
$Q_{\text{Te-Te}}$	61.5 kJ/mol
ϕ_{Te}	0.86

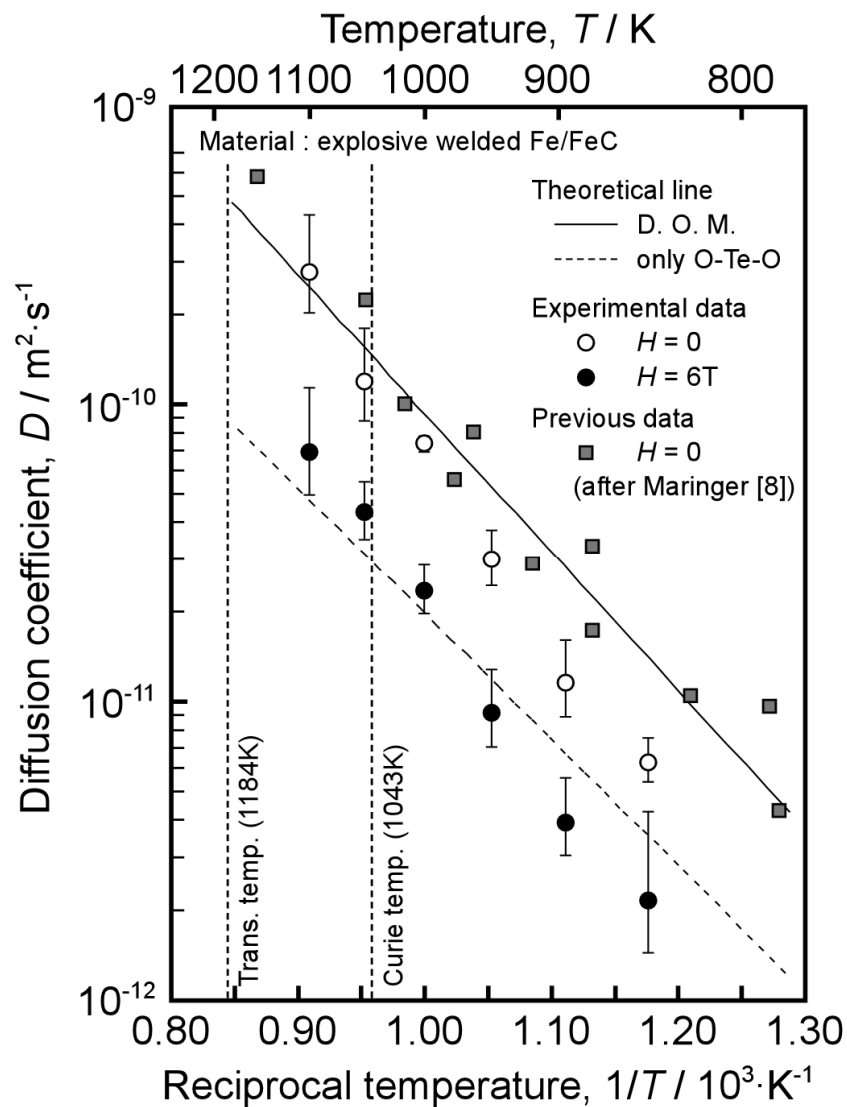


Figure 3-2 The comparison between the experimental results and calculation of diffusivity of carbon atoms in iron by dual occupancy model.

3.2.3 Mechanism of carbon diffusion in iron under a magnetic field

Here the mechanism of carbon diffusion in iron under a static magnetic field is discussed from the viewpoint of magnetostriction as noted in the chapter 2. McLellan *et al.* found that the energy per atom of pure solvent in *O* sites $E_u^O = -620.1$ kJ/mol and the vibrational entropy of carbon in *O* sites divided by the Boltzmann constant $\Delta S_u^O / k = 5.2$ [1]. Then the energy per atom of pure solvent in *Te* sites $E_u^{Te} = -590.0$ kJ/mol and the vibrational entropy of carbon in *Te* sites divided by the Boltzmann constant $\Delta S_u^{Te} / k = 0.8$ can be obtained from Table 3-1. Thus the carbon atom is less tightly bound to the *Te* sites than the *O* sites. This means that the *O* sites are more favored than the *Te* sites. As mentioned in the chapter 2, when a magnetic field is applied, the octahedral sites would be much more favored for carbon atoms than the tetrahedral sites due to the magnetostrictive expansion to the (100) direction. According to McLellan *et al.* [1], the small value of $\Delta S_u^{Te} / k$ may be due to a negligible contribution of the solvent matrix to the vibrational entropy. Therefore only the vibrational entropy of carbon in *O* sites will be affected by a static magnetic field. When a magnetic field is applied, the vibrational entropy of carbon in *O* sites is expected to increase due to the expanded *O* sites. The expanded *O* sites will make carbon atoms to vibrate more actively. Here the difference of entropy in eqn. (3-3) is given by,

$$\Delta S = \Delta S_u^{Te} - \Delta S_u^O. \quad (3-6)$$

When the vibrational entropy of carbon in *O* sites increases, the difference of entropy decreases as will be noted from eqn. (3-6). Thus, the difference of entropy decreases by the application of a static magnetic field. In other words, the fraction of octahedral site occupancies increases by the application of a static magnetic field as shown in Fig. 3-1. As a result, the carbon diffusion coefficient is considered to decrease under a magnetic field. Therefore it was concluded that the difference between the entropy of carbon atoms in *Te* and *O* sites decreases by the application of a magnetic field due to the magnetostriction of ferromagnetic α -iron and its effect on site occupancy, so that the carbon diffusion would be retarded.

3.3 Numerical analysis of carbon diffusion in iron under a magnetic field gradient

3.3.1 Physical model and basic equations

The schematic illustration of numerical analytic model in this study is shown in Fig. 3-3. The variable x is defined as a distance from the interface between iron and steel to iron side. In this case, the carbon concentration gradient is negative toward the positive direction of x . Conversely, the magnetic potential gradient is positive toward the positive direction of x . The relationship between the carbon concentration $C(x, t)$ and x was analyzed under these conditions.

As mentioned in chapter 2, the magnetic potential gradient due to a field gradient is assumed to work as a driving force for carbon diffusion. When a concentration gradient and a potential gradient are coexistent, the flux of atoms per unit time and area is given by eqn. (3-7) according to Fick's first law.

$$J = -D \left(\frac{dC}{dx} + \alpha \frac{C}{kT} \frac{dU}{dx} \right), \quad (3-7)$$

where J is the flux of atoms, C is carbon concentration, U is magnetic energy, k is the Boltzman constant, T is the absolute temperature and α is the weight coefficient. The time evolution of carbon concentration is represented as eqn. (3-8) according to Fick's second law. The basic equation of carbon diffusion under a magnetic field gradient is derived as eqn. (3-9) by the substitution of eqn. (3-7) into eqn. (3-8).

$$\frac{\partial C}{\partial t} = -\frac{\partial J}{\partial x}, \quad (3-8)$$

$$\frac{\partial C}{\partial t} = D \frac{\partial^2 C}{\partial x^2} + D \frac{\alpha}{kT} \left[\frac{\partial C}{\partial x} \frac{\partial U}{\partial x} + C \frac{\partial^2 U}{\partial x^2} \right]. \quad (3-9)$$

The numerical analysis in this study was conducted using eqn. (3-9) as basic equation. As the iron is in ferromagnetic state at the temperature focused in this analysis, the magnetic energy is given by,

$$U = -\mu_0 \left(H - \frac{NM_s}{2} \right) M_s, \quad (3-10)$$

where μ_0 is the magnetic permeability of vacuum, N is the demagnetizing factor and M_s is the saturation magnetization of iron. Here, as the demagnetizing factor N was extremely small in

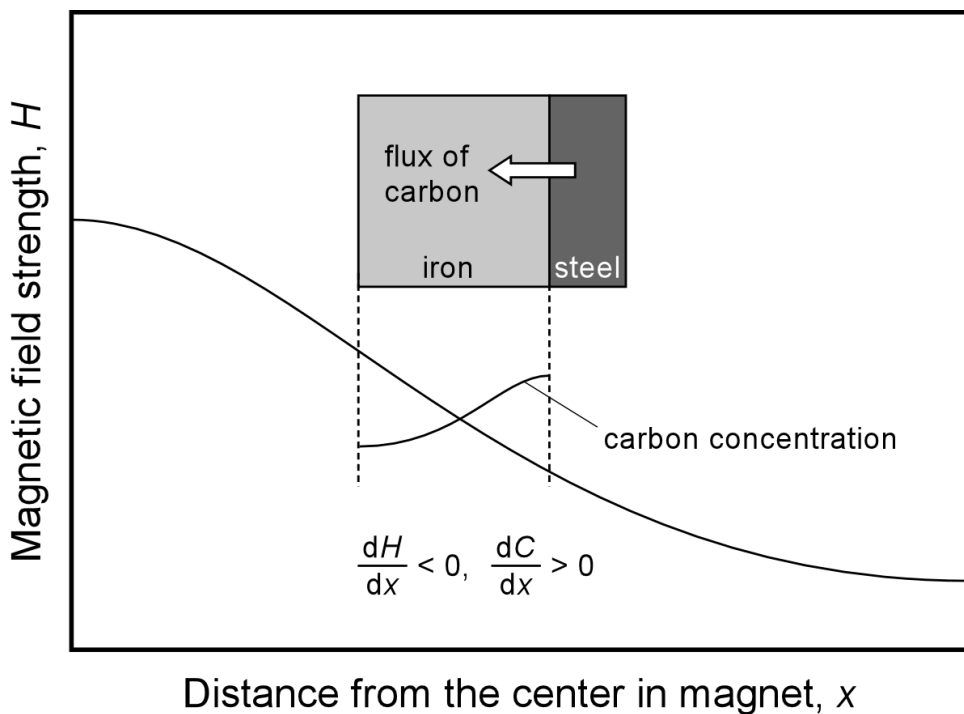


Figure 3-3 The schematic illustration of numerical analysis model of carbon diffusion under a magnetic field gradient.

this experiment, second term of right-hand side in eqn. (3-10) can be negligible. As the specimen is much smaller than the distribution of an applied magnetic field, the distribution is approximated by one-dimensional function as eqn. (3-11),

$$H = -ax + b, \quad (3-11)$$

where a is the gradient constant of a magnetic field and b is the intercept.

The nondimensionalization of variables was conducted to simplify the analysis and to make the general properties more visible by removing the units from the equation. The following nondimensionalized variables are used in this calculation:

$$x^+ = \frac{x}{l_0}, \quad C^+ = \frac{C}{C_0}, \quad t^+ = \frac{tD}{l_0^2}. \quad (3-12)$$

where l_0 is the distance of analytic range and C_0 is the initial carbon concentration at the interface between iron and steel. Substituting these variables into basic equation of carbon diffusion, the following nondimensionalized equation is obtained:

$$\frac{\partial C^+}{\partial t^+} = \frac{\partial^2 C^+}{\partial x^{+2}} + \frac{\alpha}{kT} \left(\frac{\partial C^+}{\partial x^+} \frac{\partial U}{\partial x^+} + C^+ \frac{\partial^2 U}{\partial x^{+2}} \right). \quad (3-13)$$

As the second-order derivative of U is found to be zero from the eqn. (3-11), the following eqn. (3-14) can be derive from eqn. (3-13). Note that the constants are replaced with η using eqn. (3-15).

$$\frac{\partial C^+}{\partial t^+} = \frac{\partial^2 C^+}{\partial x^{+2}} - \alpha\eta \frac{\partial C^+}{\partial x^+}, \quad (3-14)$$

$$\eta = \frac{1}{kT} \mu_0 al_0 M_s. \quad (3-15)$$

where η equals to 4.60×10^{24} for $T = 1000$ K. In this study, the carbon diffusion under a magnetic field gradient was analyzed by finite difference technique based on the Crank-Nicolson method using finite difference variables in eqn. (3-16).

$$x^+ = i\Delta x^+, \quad t^+ = n\Delta t^+, \quad (3-16)$$

where i is the step number of x direction, n is the step number of time, Δx^+ is the step size of x direction and Δt^+ is the step size of time. Here the eqn. (3-17) is derived from eqn. (3-14) discretized according to Crank-Nicolson implicit method as follows,

$$\begin{aligned} \frac{C_{i,n+1}^+ - C_{i,n}^+}{\Delta t^+} &= \frac{1}{2} \left\{ \frac{C_{i+1,n+1}^+ - 2C_{i,n+1}^+ + C_{i-1,n+1}^+}{(\Delta x^+)^2} + \frac{C_{i+1,n}^+ - 2C_{i,n}^+ + C_{i-1,n}^+}{(\Delta x^+)^2} \right\} \\ &\quad - \frac{1}{2}\eta \left\{ \frac{C_{i+1,n+1}^+ - C_{i-1,n+1}^+}{2\Delta x} + \frac{C_{i+1,n}^+ - C_{i-1,n}^+}{2\Delta x} \right\}. \end{aligned} \quad (3-17)$$

When the discretized eqn. (3-17) is expanded and reconstructed, it is represented as simultaneous equations of eqns. (3-18) and (3-19).

$$\begin{aligned} &- A(x)C_{i+1,n+1}^+ + (C(x) + 1)C_{i,n+1}^+ - B(x)C_{i-1,n+1}^+ \\ &= A(x)C_{i+1,n}^+ + (C(x) + 1)C_{i,n}^+ + B(x)C_{i-1,n}^+, \end{aligned} \quad (3-18)$$

$$A(x) = \lambda + \frac{\lambda}{2}\eta\Delta x^+, \quad B(x) = \lambda - \frac{\lambda}{2}\eta\Delta x^+, \quad C(x) = 2\lambda, \quad (3-19)$$

where

$$\lambda = \frac{\Delta t^+}{2(\Delta x^+)^2}. \quad (3-20)$$

Here the boundary conditions for both edges ($x = 0$ and $x = l_0$) in the analytic area were determined as eqn. (3-21). At this time, a condition at the interface between iron and steel ($x = 0$) was determined so that the initial carbon concentration was held in equilibrium. In addition, a condition at the other side of interface was determined so that the concentration approached

infinitely zero.

$$\left. \frac{\partial C^+}{\partial x^+} \right|_{x^+=0} = C - C_0, \quad \left. \frac{\partial C^+}{\partial x^+} \right|_{x^+=l_0} = 0. \quad (3-21)$$

In this theoretical analysis, the successive over relaxation (SOR) method was used to solve the discretized equation. This is one of the iteration methods to solve the simultaneous equations. The $(m+1)$ th solution can be estimated from the linear combination of the (m) th solution and the term by the Gauss-Seidel method multiplied by β in the SOR method. Using the relaxation coefficient β , the convergence of solution in the SOR method is improved more than that in the Gauss-Seidel method. The eqns. (3-18) and (3-19) can be generally written in the form of

$$\begin{bmatrix} & K_{ij} & \end{bmatrix} \begin{Bmatrix} x_i \end{Bmatrix} = \begin{Bmatrix} f_i \end{Bmatrix}, \quad (3-22)$$

where K_{ij} and f_i are the known term, x_i is the unknown term. When the SOR method applies to this equation, following equation can be obtained:

$$x_i^{(m+1)} = x_i^{(m)} + \beta \left\{ -x_i^{(m)} + K_{ij}^{-1} \left(f_i - \sum_{n=1}^{i-1} K_{ij} x_i^{(m+1)} - \sum_{j=i+1}^n K_{ij} x_j^{(m)} \right) \right\}. \quad (3-23)$$

On the basis of similar method, the eqn. (3-24) can be derived by the application of eqn. (3-23) of SOR method to eqn. (3-18) which is a finite difference equation in this analysis.

$$C_{i,n}^{(m+1)} = C_{i,n}^{(m)} + \beta \left\{ -C_{i,n}^{(m)} + \frac{1}{C(i)-1} (u(i) - B(i)C_{i-1,n}^{(m+1)} - A(i)C_{i+1,n}^{(m)}) \right\}, \quad (3-24)$$

where the superscript m is the step number in convergent calculation. In this equation, when the deviation as shown by eqn. (3-25) reaches enough small value, the time step number n goes to next.

$$\left| \frac{C_{i,n}^{(m+1)} - C_{i,n}^{(m)}}{C_{i,n}^{(m)}} \right| < \gamma, \quad (3-25)$$

where γ is the relative error. The conditions to describe time character of stable atomic concentration without the oscillation and divergence of the solution of eqn. (3-24) is known in the previous study [4]. Based on these conditions, the following conditions are required in order to perform accurate numerical analysis of this problem.

$$\frac{\Delta t^+}{(\Delta x^+)^2} \leq 0.3, \quad \beta = 0.8, \quad \gamma = 10^{-5}. \quad (3-26)$$

Table 3-3 Physical constants for numerical analysis.

Parameter	Value
$\mu_0 M_s$	2.15 kg/s ² A
k	1.38×10 ⁻²³ J/K
l_0	8.0×10 ⁻⁴ m
T	1000 K
a	3.69×10 ⁷ A/m ²

3.3.2 Effect of magnetic potential gradient on carbon diffusion

The numerical analysis of carbon diffusion under a magnetic field gradient was conducted using SOR method as shown in the previous section. The physical constants used in this analysis are shown in Table 3-3. The temperature was determined 1000 K to discuss the carbon diffusion at the temperature in ferromagnetic α -iron. The gradient constant of a magnetic field was determined from the distribution of a magnetic field in the superconducting magnetic field heat treatment system as shown in Fig. 2-4 in chapter 2.

At first, the carbon concentration distributions without and with a magnetic field gradient were calculated as time advances. To clearly observe the effect of a magnetic field gradient, the analysis was conducted under the condition significantly dominated by the magnetic field gradient term (the second term) in right hand side of eqn. 3-14. In other words, the analysis was conducted with the large value of weight coefficient α . When a “negative” magnetic field gradient was applied to the specimen, the carbon diffusion was enhanced and the concentration of carbon penetrated into iron increased as shown in Fig. 3-4. This is in good agreement with the experimental results as shown in Fig. 2-14. The carbon concentration obviously increased by the magnetic potential gradient of the second term in eqn. (3-9). It was proven that the increase in carbon diffusion by the application of a magnetic field gradient was due to the increase in flux of carbon atoms induced by the magnetic potential gradient.

When there exist no potential gradients, the flow rate of atoms is proportional to the concentration gradient of atoms according to the Fick’s first law as shown in eqn. (3-7). Therefore the apparent diffusion coefficient under a magnetic field gradient can be evaluated from this relationship using following equation.

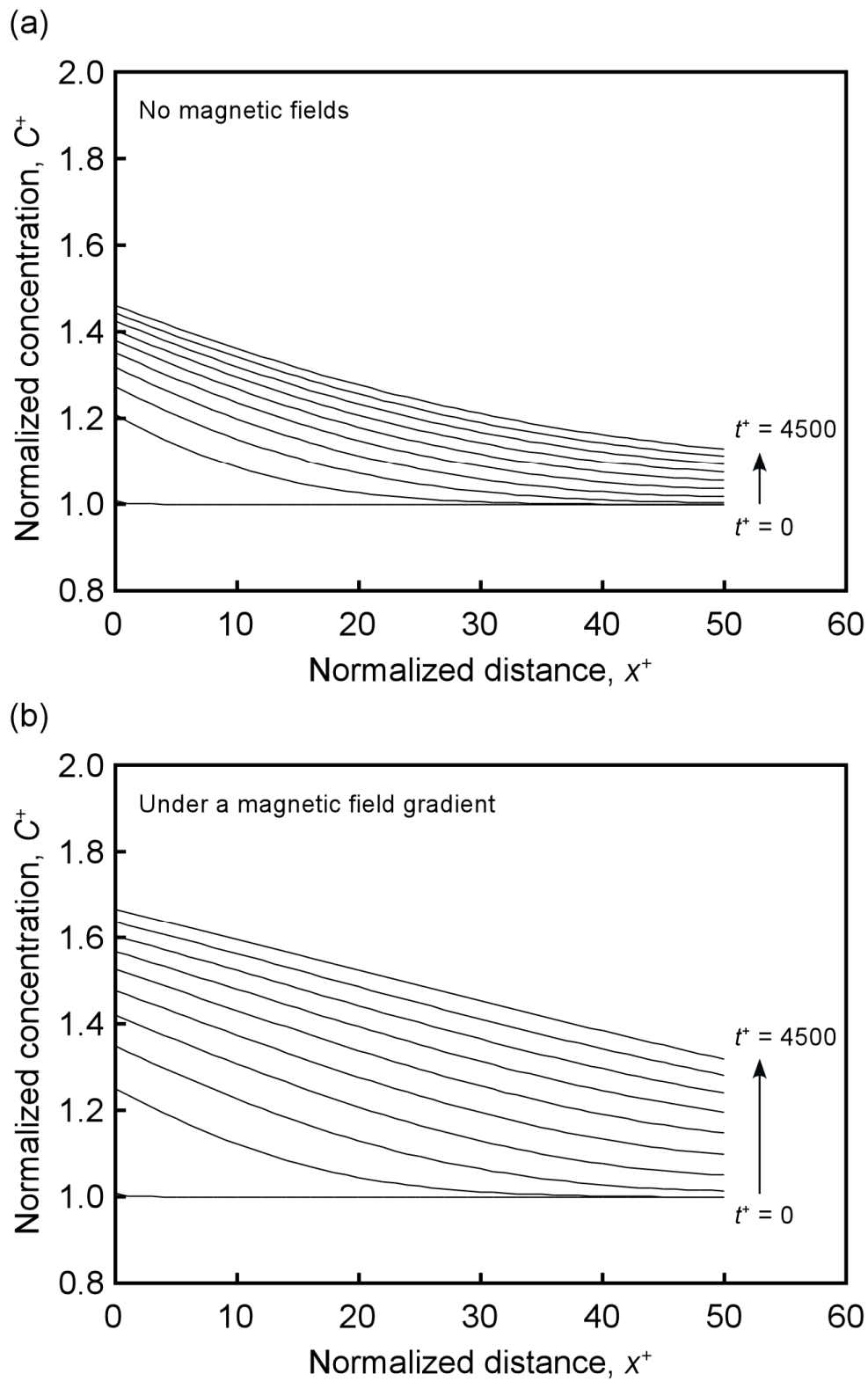


Figure 3-4 The normalized carbon concentration distribution under (a) non-magnetic conditions and (b) a magnetic field gradient.

$$D^*(x) = -\frac{J}{\frac{\partial C^+}{\partial x^+}}. \quad (3-27)$$

Then the flow rate of carbon atoms and the carbon concentration gradient were investigated as a function of nondimensional distance by calculation. Fig. 3-5 shows (a), (b) the flow rate of carbon atoms and (c), (d) the carbon concentration gradient as a function of nondimensional distance. The apparent diffusion coefficients of carbon atoms at each nondimensional distance x^+ were calculated using the values of the flow rate of carbon atoms and the carbon concentration gradient as shown in Fig. 3-5. The flow rates of carbon monotonically increased with the increase in diffusion time and monotonically decreased with the decrease in diffusion distance irrespective of whether a magnetic field gradient being applied or not. However, the flow rate under a magnetic field gradient was found to be higher than that under non-magnetic conditions. The carbon concentration gradients monotonically increased with the increase in diffusion distance at the early stage of diffusion. Thereafter the carbon diffusion was equalizing the distribution of the concentration gradient as the diffusion time advanced. Using these results, the apparent diffusion coefficients of carbon were calculated as a function of diffusion distance. As the apparent diffusion coefficients near the outer boundary were not stable, the evaluation of apparent diffusion coefficients was conducted in the region after removal of outer boundary at the nondimensional time of 4500. This was the time when the analytic values of apparent diffusion coefficients were in stable states.

To accurately analyze the apparent carbon diffusion coefficient, the values of the first diffusion term and magnetic potential gradient term in eqn. 3-14 were investigated by numerical analysis. Fig. 3-6 shows those values as a function of nondimensional distance. The second term in eqn. 3-14 took an extremely large value as compared with the first diffusion term. Therefore the weight coefficient α was determined as 3.8×10^{-29} to make the magnetic field gradient term (the second term) in eqn. 3-14 comparable with the first diffusion term, which is physically reasonable from the viewpoint of dimensional analysis as shown in Fig. 3-6. The apparent carbon diffusion coefficients were quantitatively estimated from eqn. 3-27 under consideration of the results of dimensional analysis. Fig. 3-7 shows the magnetic field gradient dependence of carbon diffusion coefficients as a function of nondimensional distance. The diffusion coefficient was found to increase monotonically with the increase in strength of magnetic field gradient. In addition, it was revealed that there was linear relationship between the flow rate of carbon and the carbon concentration gradient even in addition with the magnetic potential gradient when the diffusion time adequately advanced. Fig. 3-8 shows the carbon diffusion coefficient as a function of the strength of a magnetic field strength. It was

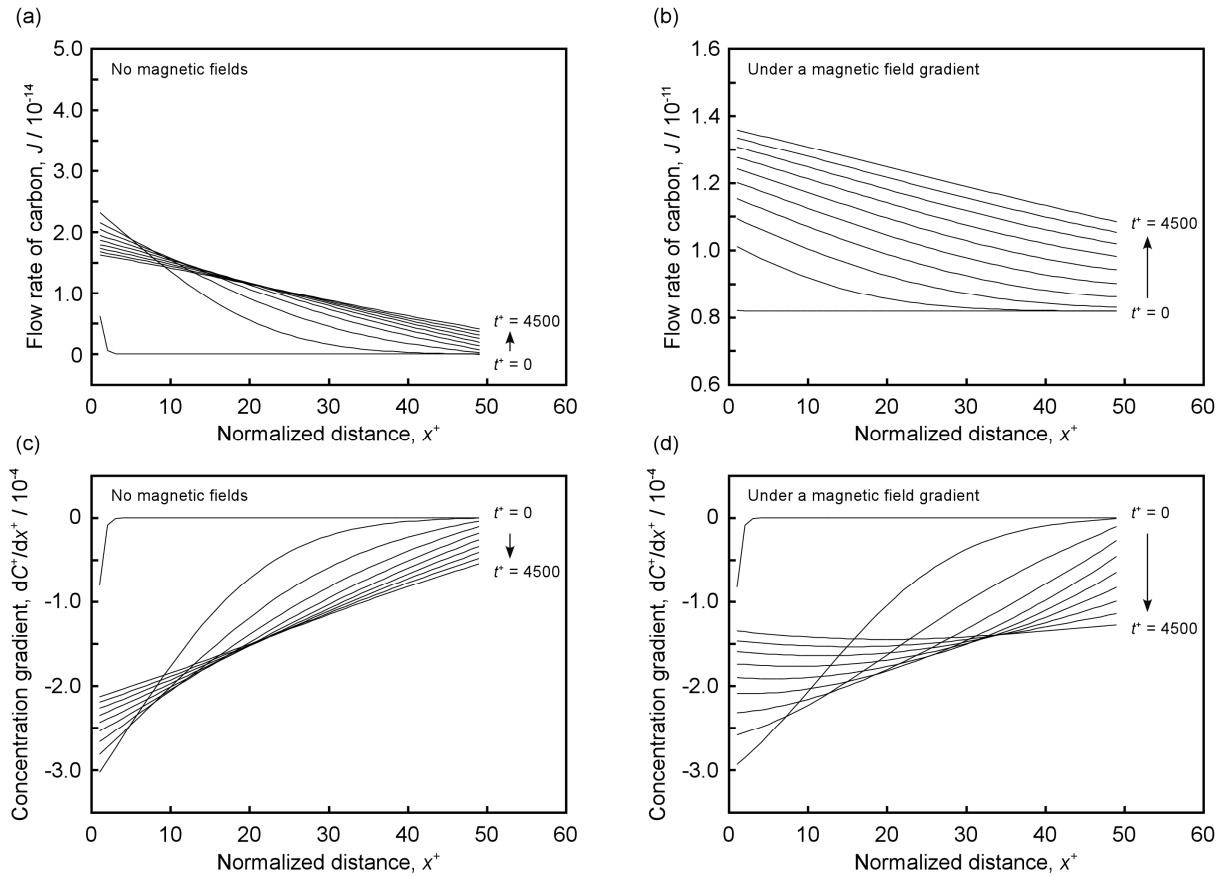


Figure 3-5 (a), (b) The flow rate of carbon atoms and (c), (d) the carbon concentration gradient as a function of nondimensional distance under non-magnetic conditions and a magnetic field gradient.

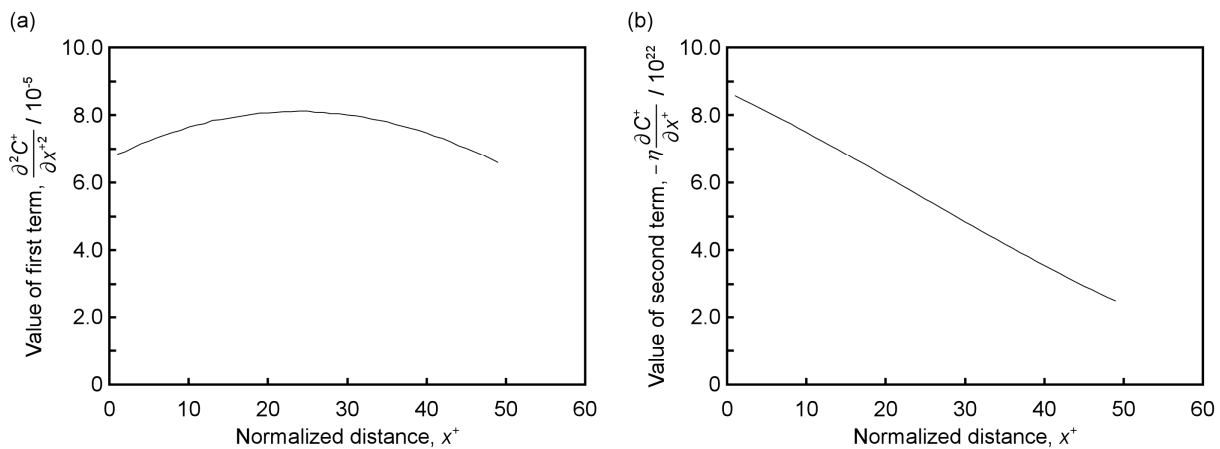


Figure 3-6 The order estimation of first diffusional term and magnetic potential gradient term in eqn. 3-14 as a function of normalized distance.

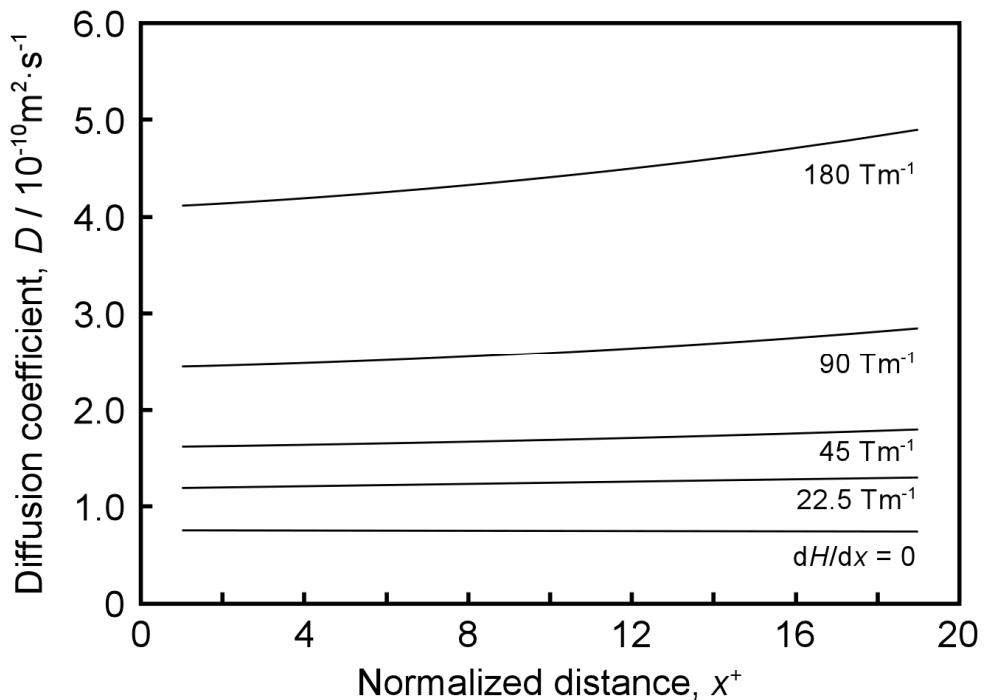


Figure 3-7 The magnetic field gradient dependence of carbon diffusion coefficient as a function of nondimensional distance.

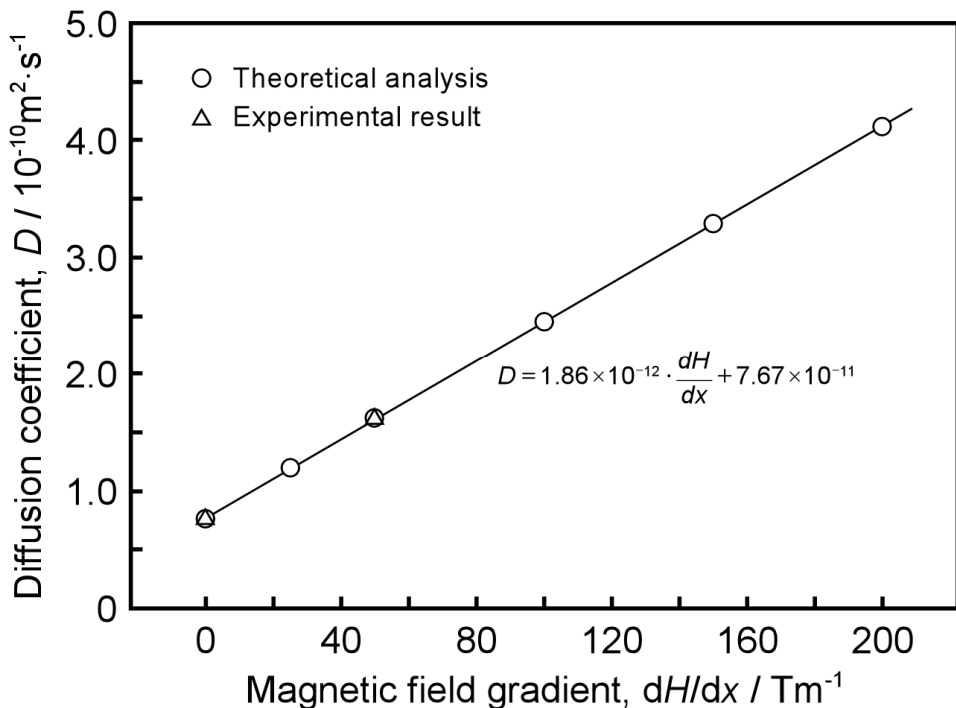


Figure 3-8 The change in diffusion coefficient of carbon as a function of an applied magnetic field gradient.

found that the acceleration effect of a magnetic field gradient on carbon diffusion increased with the increase in strength of a magnetic field gradient. In addition, the diffusion coefficient could be described as following linear function of a magnetic field gradient.

$$D(\dot{H}) = 1.86 \times 10^{-12} \cdot \dot{H} + 7.67 \times 10^{-11}, \quad (3-28)$$

where

$$\dot{H} = \frac{dH}{dx}. \quad (3-29)$$

On the basis of these concepts, the equation of carbon diffusivity was found to be described by the extended Fick's second law using diffusion coefficient in eqn. 3-28 even under a magnetic field gradient, which is given by,

$$\frac{\partial C}{\partial t} = D(\dot{H}) \nabla^2 C. \quad (3-30)$$

From these theoretical analyses, it was proven from the viewpoint of diffusion theory in solid that the enhancement of carbon diffusivity was caused by the potential gradient due to a magnetic field gradient. And it was found that the effect of a magnetic field gradient on carbon diffusion monotonically increased with the increase in strength of a magnetic field gradient.

3.4 Summary

In this chapter, the physical and numerical models were constructed concerning the carbon diffusion in pure iron under a static magnetic field and a magnetic field gradient. Thereafter the mechanisms of magnetic field effects were discussed on the basis of the results of theoretical analysis. And the following conclusions were obtained.

- (1) The difference between the entropy of carbon atoms in T_e and O sites decreases by the application of a magnetic field due to the magnetostriction of ferromagnetic α -iron and its effect on site occupancy, so that the carbon diffusion would be retarded.
- (2) Numerically, it was proven that the increase in carbon diffusion by the application of a magnetic field gradient was due to the increase in flux of carbon atoms induced by the magnetic potential gradient.
- (3) The diffusion coefficient was found to increase monotonically with the increase in strength of magnetic field gradient. In addition, the diffusion coefficient could be described as the linear function of a magnetic field gradient.

References

- [1] R. B. McLellan: *Trans. Met. Soc. AIME*, **233** (1965), 1664.
- [2] H. P. Leeuwen: *Corrosion*, **31** (1975), 42.
- [3] Y. Ueda and K. Fukuda: *Matrix structure and analysis*, *Proc. 7th Japan. Struct. Associat.*, (1973), 671.
- [4] A. T. Yokobori, Jr., T. Nemoto, K. Satoh and T. Yamada: *Eng. Fract. Mech.*, **55** (1996), 47.
- [5] A. T. Yokobori, Jr., Y. Chinda, T. Nemoto, K. Satoh and T. Yamada: *Corrosion Sci.*, **44** (2002), 407.
- [6] R. B. MacLellan, M. L. Rudee and T. Ishibachi: *Trans. Metall. Soc. AIME*, **233** (1965), 1938.
- [7] D. N. Beshers: *J. Appl. Phys.*, **36** (1964), 290.

Chapter 4

Nucleation and growth under a magnetic field

4.1 Introduction

The carbon diffusivity in iron can be controlled by the application of a magnetic field and a magnetic field gradient as described in chapter 2 and 3. The resultant microstructure is significantly subject to the nucleation and growth processes of grains in the microstructural evolution such as crystallization and phase transformation. As the nucleation and growth of grains occur by the diffusion of atoms, the application of a magnetic field during materials processing could control the microstructure and improve the mechanical and functional properties of materials. Therefore it is quite important to investigate the effect of a magnetic field on the grain nucleation and growth of phenomena for the development of EPM studies.

In the microstructural evolution of materials, the nucleation and growth of grains generally progress during solid-solid reactions. It is inevitable that the resultant microstructure after annealing is more or less affected by the initial state of a material [1, 2]. This is because viable nucleation sites are distributed heterogeneously in a polycrystalline structure, and the nucleation, growth and orientations of recrystallized grains are strongly affected by prior grain orientation before annealing [3]. However microstructural change during transformation from an amorphous to a crystalline state will be less restrictive than that from a polycrystalline to polycrystalline transformation because of the fairly homogeneous structure of amorphous phase. Therefore, the observation of crystallization process from amorphous alloy under a magnetic field would make it possible to conduct more precise investigation of the magnetic field effects on nucleation and growth without any effects of a former microstructure of matrix. In addition, the grain orientation dependence of nucleation and growth under a magnetic field can be expected to be revealed. From the reasons mentioned above, the Fe-Si-B amorphous alloys were chosen as starting materials for the observation of nucleation and growth processes under a magnetic field. One is $\text{Fe}_{78}\text{Si}_9\text{B}_{13}$ alloy [4-8], which is the fundamental composition in Fe-Si-B amorphous alloys, and the other is $\text{Fe}_{73.5}\text{Si}_{13.5}\text{B}_9\text{Nb}_3\text{Cu}_1$ amorphous alloy, which is the same composition as the commercially available nanocrystalline material “FINEMET” [9-17].

As for the crystallization from an amorphous alloy under a magnetic field, Häußler and Baumann [18] reported that the application of a magnetic field did not exert any influence on the crystallization temperature of amorphous Bi, Ga and Yb, even when a field of 18.5 T was applied in the direction parallel to the film surface. Wolfus *et al.* [19] studied the effect of a magnetic field (ranging from 3 mT to 1 T) on the crystallization kinetics of Fe₈₃Si₅B₁₂ amorphous alloy. They found that the growth rate of ferromagnetic crystallites increased with the increase in magnetic field strength. Magnetic crystallization of a melt-spun Pr₂Co₁₄B amorphous ribbon was performed by Otani *et al.* [20] for the purpose of achieving crystalline alignment. They found that magnetic crystallization in a field of 0.3 T slightly enhanced the development of the texture with easy magnetization *c*-planes oriented along the magnetic field direction. Recently, Wang *et al.* [21] investigated the effect of a magnetic field on the nucleation of crystallites of diamagnetic tI-Zr₂Cu, fcc-Zr₂Ni and hp-Zr₆Al₂Ni phases in Zr₆₂Al₁₈Ni₁₃Cu₁₇ amorphous alloy. They mentioned that difference between the permeability of the amorphous phase and that of crystalline phase suppressed the crystallization in a magnetic field. Thus many magnetic field effects on the crystallization from amorphous alloys have been confirmed. Then the magnetic field effects on nucleation, growth and orientation of iron grains can be investigated more closely during crystallization from iron-based amorphous alloys than that during recrystallization or phase transformation.

In this chapter, the effects of a magnetic field on the nature of nucleation-growth, their kinetics and texture formation were investigated through the observation of crystallization of Fe₇₈Si₉B₁₃ and Fe_{73.5}Si_{13.5}B₉Nb₃Cu₁ amorphous alloys.

4.2 Experimental

4.2.1 Material and specimens

Iron based amorphous alloys were chosen to observe the nucleation and growth phenomena of iron crystallites under a magnetic field. Recently Fe-Si-B alloys are known as fundamental materials in iron based soft magnetic amorphous alloys. The materials used in this study were an Fe₇₈Si₉B₁₃ alloy and an Fe_{73.5}Si_{13.5}B₉Nb₃Cu₁ alloy. The Fe₇₈Si₉B₁₃ alloy was prepared by vacuum melting of electrolytic iron (99.9 %), silicon (99.999 %) and boron (99.9 %). The Fe₇₈Si₉B₁₃ alloy ingot was re-melted and then rapidly solidified into amorphous ribbons of 0.75 mm in width and 18 μm in thickness by single-roller melt spinning at a roller

speed of 31.4 m/s in vacuum. An Fe_{73.5}Si_{13.5}B₉Nb₃Cu₁ melt-spun amorphous ribbon with 15 mm in width and 18 μm in thickness was supplied by Hitachi Metals Ltd.

4.2.2 Annealing conditions for crystallization from amorphous alloys under a magnetic field

A differential scanning calorimeter (DSC, Netzsch DSC-404C) was used to measure the Curie temperatures of the amorphous and crystalline phases and the crystallization temperature. The DSC measurements were carried out at a heating rate of 0.33 K/s (20 K/min) in an Ar gas flow of 50 ml/s, which revealed the Curie temperatures of the amorphous phase (T_{C}^{Am}) and the crystalline phase (T_{C}^{X}), and the crystallization temperature (T_x). For calibration of temperature, pure nickel, iron and cobalt ($T_{\text{C}}(\text{Ni}) = 630 \text{ K}$, $T_{\text{C}}(\text{Fe}) = 1043 \text{ K}$ and $T_{\text{C}}(\text{Co}) = 1288 \text{ K}$, respectively) were used as references. Fig. 4-1 shows the DSC heating curves of Fe₇₈Si₉B₁₃ and Fe_{73.5}Si_{13.5}B₉Nb₃Cu₁ amorphous alloys. The Curie temperature and crystallization temperature were determined from the endothermic and exothermic peaks of the curves, respectively. The measured specific temperatures are shown in Table 4-1. Thereafter, the amorphous ribbons were annealed at temperatures determined on the basis of the specific temperatures in a vacuum of $1.0 \times 10^{-3} \text{ Pa}$ and in a magnetic field up to 6 T using a specially designed superconducting magnetic field heating system as illustrated in chapter 2. The heating up to the annealing temperature was made at a rate of approximately 0.3 K/s (18 K/min). A magnetic field was applied in the direction either parallel or perpendicular to the ribbon surface. Details of the annealing conditions are shown in Table 4-2.

4.2.3 Microstructure analysis

(a) XRD analysis

An X-ray diffractometer (XRD, RIGAKU JDX-3530) was used to observe the progress in crystallization and to determine the nature of the crystallized phases. A Cu target (wave length $\lambda = 0.154 \text{ nm}$) was used, and the tube current and voltage were 40 mA and 40 kV, respectively. The measurements were conducted under the conditions as follows: the divergence and scattered slits angle were both 1° , light-receiving slit width was 0.2 mm, step angle was 0.2° , counting time was 2 s and the diffraction angle was within 30° to 130° . From the diffraction profiles obtained, crystalline phase and its volume fraction to amorphous phase were determined and also the degree of texture of crystallites was evaluated. The details of

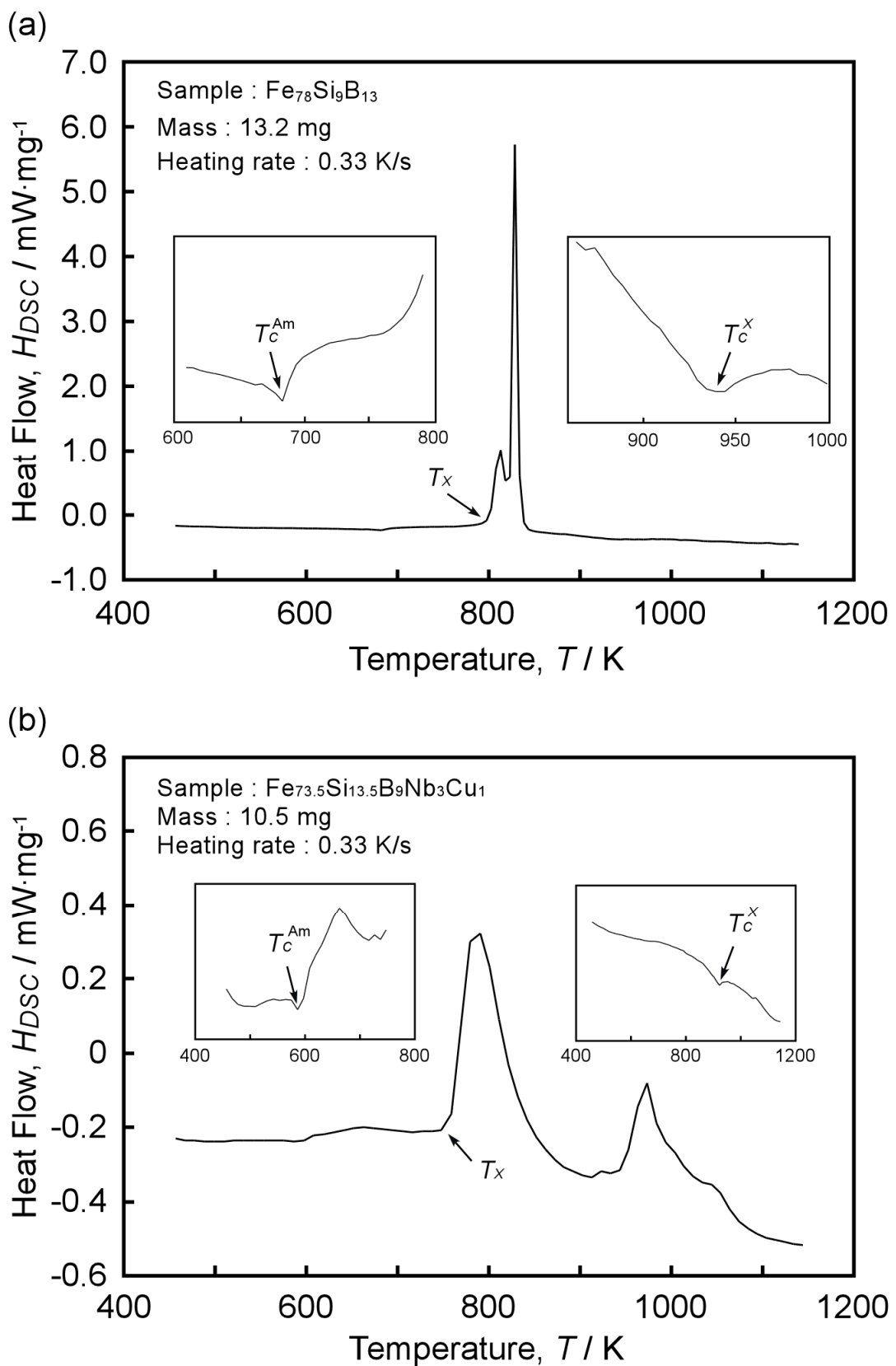


Figure 4-1 Differential scanning calorimetric analysis for rapidly solidified (a) $\text{Fe}_{78}\text{Si}_9\text{B}_{13}$ and (b) $\text{Fe}_{73.5}\text{Si}_{13.5}\text{B}_9\text{Nb}_3\text{Cu}_1$ amorphous alloy.

Table 4-1 The measured specific temperatures.

Material	Curie temperature of amorphous phase, T_c^{AM} / K	Crystallization temperature, T_x / K	Curie temperature of crystalline phase, T_c^X / K
Fe ₇₈ Si ₉ B ₁₃	680	800	940
Fe _{73.5} Si _{13.5} B ₉ Nb ₃ Cu ₁	586	750	920

Table 4-2 Annealing conditions for magnetic crystallization.

Material	Temperature, T / K	Time, t / ks	Magnetic field	
			Strength, H / T	Direction
Fe ₇₈ Si ₉ B ₁₃	653	1.8	0, 2, 4, 6	
	753	1.8	0, 2, 3, 4, 6	$H \parallel$ surface
	803	1.8	0, 2, 3, 4, 6	$H \perp$ surface
	853	1.8	0, 2, 4, 6	
Fe _{73.5} Si _{13.5} B ₉ Nb ₃ Cu ₁	673	2.6		
	723	0.8, 1.4, 2.6, 4.4		
	773	1.4	0, 2, 4, 6	$H \parallel$ surface
	793	1.4		$H \perp$ surface
	823	0.8, 1.4, 2.6, 4.4		

them are mentioned below.

Moreover, (110) pole figure was measured using X'pert Pro developed by Philips to investigate the orientation distribution of nuclei. A Cu-K α tube was used, and the tube current and voltage were 40 mA and 45 kV, respectively.

- Determination of crystalline phase

The crystalline phases formed in the amorphous matrix were determined from the diffraction angles at Bragg peaks. In X-ray diffraction technique, the sharp diffraction peaks are observed by Bragg scattering at specific diffraction angles that depend on each plane orientation of the crystals when there exist some crystalline phases. Then the crystalline structure of the materials can be determined by means of measuring these diffraction angles. In addition, as amorphous phase does not have periodic structure of atoms, Bragg peaks are not observed. Instead, broad peaks, that is called halo pattern, are observed.

- Estimation of the volume fraction of crystalline phase

The volume fraction of the α -Fe(Si) crystalline phase at the late stage of crystallization was estimated by a curve fitting procedure using a diffraction peak in XRD profiles. The XRD peak was fitted as shown in Fig. 4-2 according to the pseudo-Voigt function given by the following equation [22],

$$V(x) = (1 - \eta)L(x) + \eta G(x), \quad (4-1)$$

where $L(x)$ and $G(x)$ are the Lorentzian and Gaussian functions respectively, and η represents the Gaussian contribution to the peak. Here it was assumed that the XRD profiles from amorphous and crystalline phases could be expressed by Lorentzian and Gaussian functions as shown in eqns. (4-2) and (4-3), respectively.

$$L(x) = \frac{2A}{w\pi} \frac{1}{x^2 + 1}, \quad (4-2)$$

$$G(x) = \frac{A}{w} \sqrt{\frac{2}{\pi}} \exp\left(-\frac{1}{2}x^2\right). \quad (4-3)$$

And the parameter x is given by,

$$x = \frac{2\theta - 2\theta_0}{w}, \quad (4-4)$$

where 2θ is the diffraction angle, $2\theta_0$ is the angle at Bragg peak and w is the half-width of diffraction peak. The value of η for the best fitting curve was determined by the correlation coefficient.

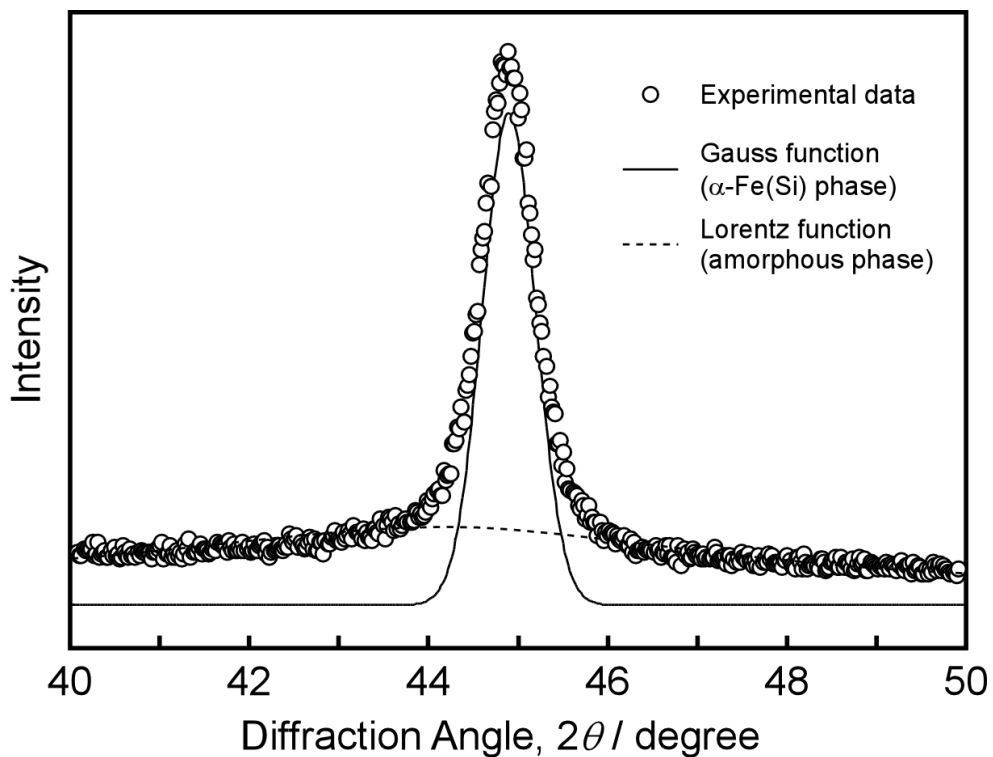


Figure 4-2 Experimental data (dots) and fitting pseudo-Voigt functions (lines) of the amorphous and nanocrystalline phases.

- Evaluation of degree of texture

The texture of grains after crystallization was evaluated using the orientation index $R(hkl)$ given by the following equation [23]:

$$R(hkl) = \frac{\frac{I(hkl)}{\sum I(h'k'l')}}{\frac{I_0(hkl)}{\sum I_0(h'k'l')}}, \quad (4-5)$$

where $I(hkl)$ is the XRD intensity obtained from experimental data and $I_0(hkl)$ is the intensity from a standard powder diffraction measurement. When the value of $R(hkl)$ is 1, the specimen has random texture, and when the value is more than 1, the specimen has (hkl) texture.

- Measurement of pole figure

The X-ray Shultz method was conducted to evaluate the orientation distribution along

not only the normal direction but also the rolling and transverse directions. Fig. 4-3 shows the schematic illustration of measurement method in X-ray Shultz method. In this method, the axis along normal direction of specimen surface is rotated about the axis of diffractometer to conform to the objective Bragg angle. Thereafter, the diffraction intensity is measured with the rotation of specimen holder about the axis along the specimen surface direction and the normal direction of surface. The pole figure is obtained from the distribution of diffraction intensity in each diffraction angle.

(b) FE-SEM/EBSD/OIM observation

In order to statistically evaluate the microstructure such as grain orientation distribution, it is necessary to analyze a large number of grains. Although the analysis of grain orientations using a Kikuchi diffraction method by transmission electron microscopy (TEM) has a higher precision, it is not easy to analyze many grains because of limitation of the area observed in a thin specimen. On the other hand, recently developed automated electron backscattered diffraction (EBSD) technique on a scanning electron microscope(SEM) makes it possible to measure the orientations of grains enough for statistical analysis in a bulk specimen. Especially by combination with a field emission (FE) type SEM, a special resolution of less than 50 nm can be achieved.. When the electron beam enters a crystalline solid, the electrons are inelastically scattered in all directions. Some electrons arriving at the Bragg angle at every set of lattice planes can undergo elastic scattering to give a strong backscattered beam. The backscattered beam produces Kikuchi-bands on a phosphor screen placed near a sample in an SEM chamber. In this study, the orientation imaging microscopy (OIM) from TSL Inc. was used for fully-automated EBSD analysis to observe the crystallized microstructure such as the grain orientation distribution. The EBSD/OIM observations were conducted on a HITACHI S-4200 FEG-SEM with 30 kV accelerating voltage and 15 mm working distance. The electron beam was scanned with a 50 nm step size. Clustered areas composed of more than four steps of the same orientation were defined as a single grain.

(c) TEM observation

The transmission electron microscopy (TEM) observation was conducted to analyze the microstructure in $\text{Fe}_{73.5}\text{Si}_{13.5}\text{B}_9\text{Nb}_3\text{Cu}_1$ specimens annealed without and with a 6 T magnetic field. Thin foils for TEM observations were prepared by the atom milling technique. An

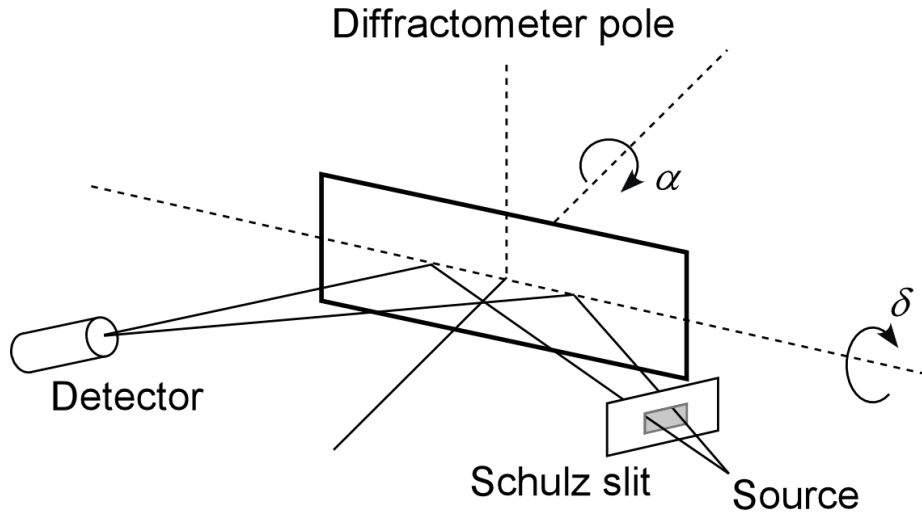


Figure 4-3 Schematic illustration of Schulz reflection method.

Fe_{73.5}Si_{13.5}B₉Nb₃Cu₁ sample of 1.5 mm × 1.5 mm × 0.02 mm in dimensions was put on the Mo single hole mesh with a glue Epoxi G2 and thinned by the Ar ion-irradiation at 5 kV , 2 mA and the beam angle of 15°. The specimen holder was cooled by liquid nitrogen to reduce the irradiation damage of the specimen.

Conventional TEM observations were performed on a HITACHI HF-2000 FEG-TEM operated at an accelerating voltage of 200 kV. From the TEM micrographs, we statistically analyzed the number density of nuclei per unit volume, the grain size distribution and the volume fraction of crystallized phase. To determine the volume of the observed area, the thickness of the area in TEM samples was measured using a contamination-spot separation method [24]. When the narrow electron beam irradiates to the specimen surface, the hydro-carbon contamination is formed at the superior and inferior surfaces as shown in Fig. 4-4 (a). Then the divided contamination spots can be observed (Fig. 4-4 (b)) when the specimen is inclined by enough large angle γ . The thickness t_0 can be estimated by measuring the distance between these spots (Fig. 4-4 (c)). The thickness t_0 is given by,

$$t_0 = \frac{r}{M \sin \gamma}, \quad (4-6)$$

where r is the distance between spots and M is the magnification for observation.

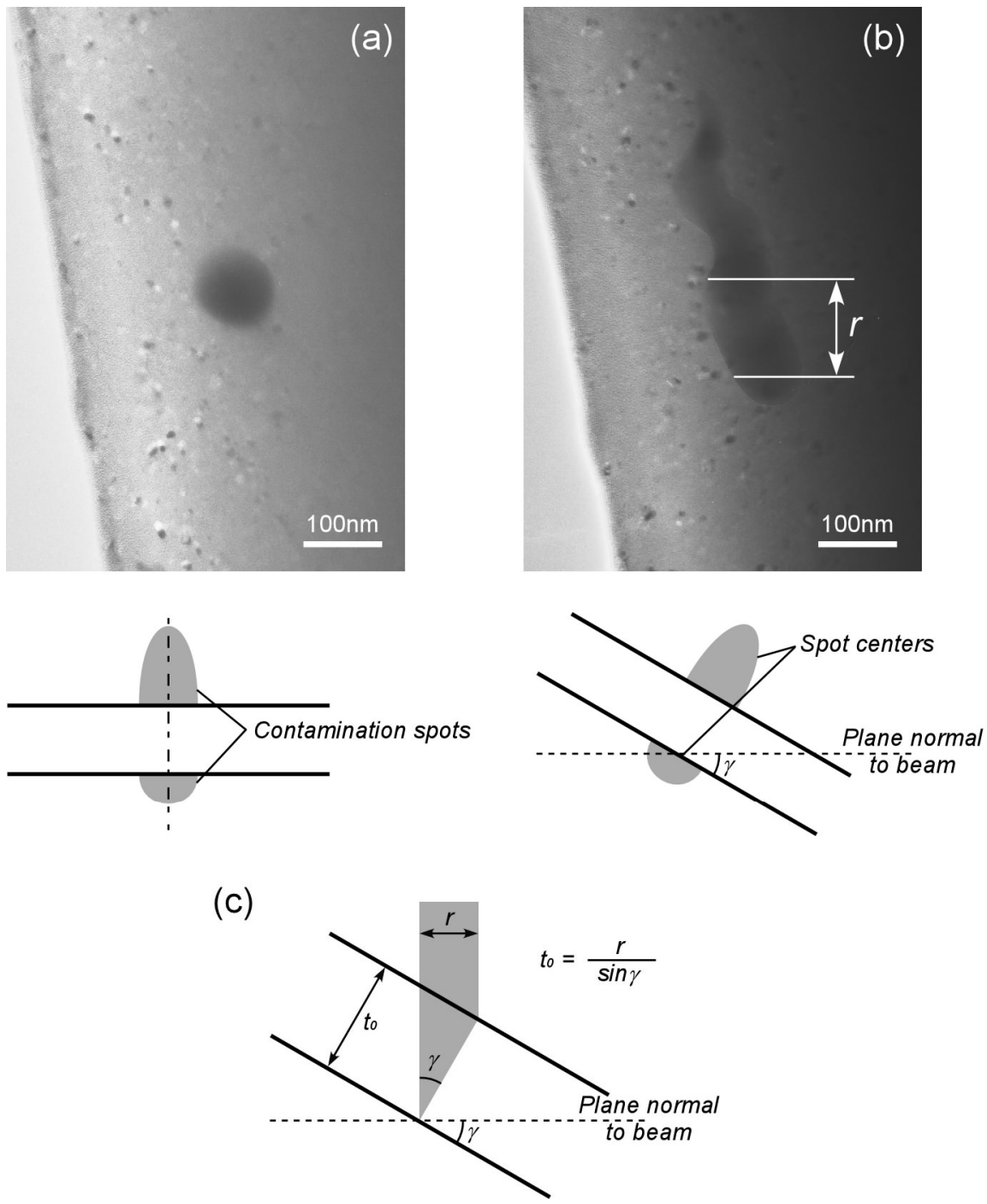


Figure 4-4 The contamination-spot separation method for thickness determination; (a) the contamination is deposited on both surfaces of the specimen and the separation is only visible in (b) when the specimen is tilted sufficiently. (c) Geometry required to determine thickness t_0 from the projected separating r of the contamination spots [20].

4.3 Results and discussion

4.3.1 Crystallization of $Fe_{78}Si_9B_{13}$ amorphous alloy under a magnetic field

(a) Crystallization under a magnetic field

XRD analyses were conducted with the specimens crystallized from the amorphous $Fe_{78}Si_9B_{13}$ alloy with and without a magnetic field. A significant effect of the magnetic field on the nature of crystallization was observed at 853 K (between $T_C^{Am} = 680$ K and $T_C^X = 940$ K), while there were no pronounced differences in XRD profiles for the specimens annealed at other temperatures, irrespective of whether a magnetic field was applied or not. Fig. 4-5 shows XRD profiles for the specimens crystallized at 853K in different magnetic field strengths. For comparison, an XRD profile for the amorphous alloy is shown in Fig. 4-5. Application of a magnetic field of 6 T in a direction parallel to the ribbon surface was found to intensify significantly the {110} peak associated with the α -Fe(Si) phase. This finding suggests that {110} texture is formed by application of a 6 T magnetic field. In addition, other phases apart from α -Fe(Si) were not observed after crystallization under any conditions used in the present experiments.

The volume fraction of the α -Fe(Si) crystalline phase at the late stage of crystallization was estimated by a curve fitting procedure using a diffraction peak in XRD profiles. Fig. 4-6 shows the magnetic field strength dependence of the volume fraction of crystalline phase. The fraction of crystallization phase of the specimen crystallized without a magnetic field was approximately 40 % as shown in Fig. 4-6 (a). When magnetic fields of 2 and 4 T were applied parallel to the specimen surface, the significant changes of the fractions were not observed. However, when a 6 T magnetic field was applied parallel to the specimen surface, it was evident that the fraction decreased down to approximately 20 % at 753 K and increased up to approximately 70 % at 853 K. On the other hand, when a magnetic field was applied perpendicular to the specimen surface, the effects of a magnetic field was not observed as shown in Fig. 4-6 (b).

Fig. 4-7 shows the temperature dependence of the volume fraction of crystalline phase under the magnetic fields up to 6 T. When a 6 T magnetic field was applied parallel to the specimen surface, it was evident that the fraction increased with the increase in temperature. On the other hand, when the magnetic fields of 2 and 4 T were applied, the fraction did not

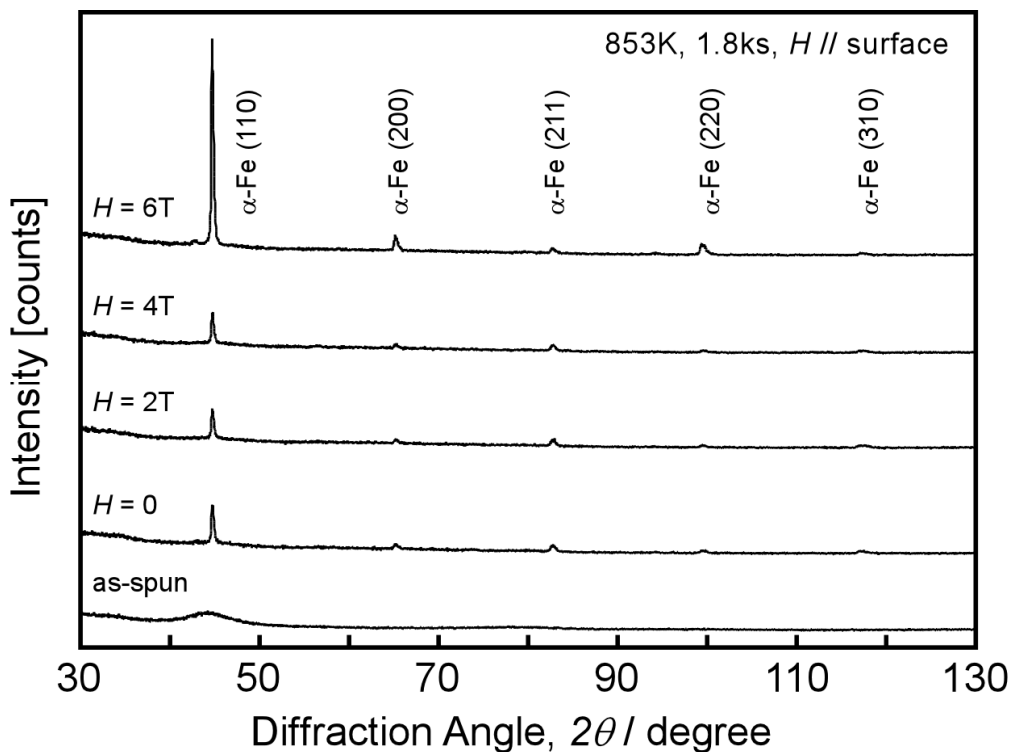


Figure 4-5 X-ray diffraction patterns of $\text{Fe}_{78}\text{Si}_9\text{B}_{13}$ ribbons crystallized at 853 K for 1.8 ks in magnetic fields of different strengths and of an as-spun amorphous ribbon.

depend on the temperature as well as that under non-magnetic conditions. Here the crystallization temperature of $\text{Fe}_{78}\text{Si}_9\text{B}_{13}$ amorphous alloy was determined to be 800 K by DSC analysis as shown in Fig. 4-1 (a). Then a 6 T magnetic field could decrease the crystallization rate at the temperature below the crystallization temperature and increase that at the temperature above the crystallization temperature. Furthermore, there would be threshold of magnetic field strength between 4 and 6 T where the magnetic field effects on the crystallization rate would appear. In the nucleation of grains during crystallization of $\text{Fe}_{78}\text{Si}_9\text{B}_{13}$ amorphous alloy, the grains homogeneously nucleate in the amorphous matrix. As there exist no active sites for nucleation such as additive elements in $\text{Fe}_{78}\text{Si}_9\text{B}_{13}$ amorphous phase, the nuclei of grains would generate from the cluster occurred by the microscopic fluctuation of composition in the amorphous phase. The annealing for crystallization was conducted above the Curie temperature of amorphous phase, so that the amorphous phase was paramagnetic state and the magnetic spins were significantly disordered during crystallization

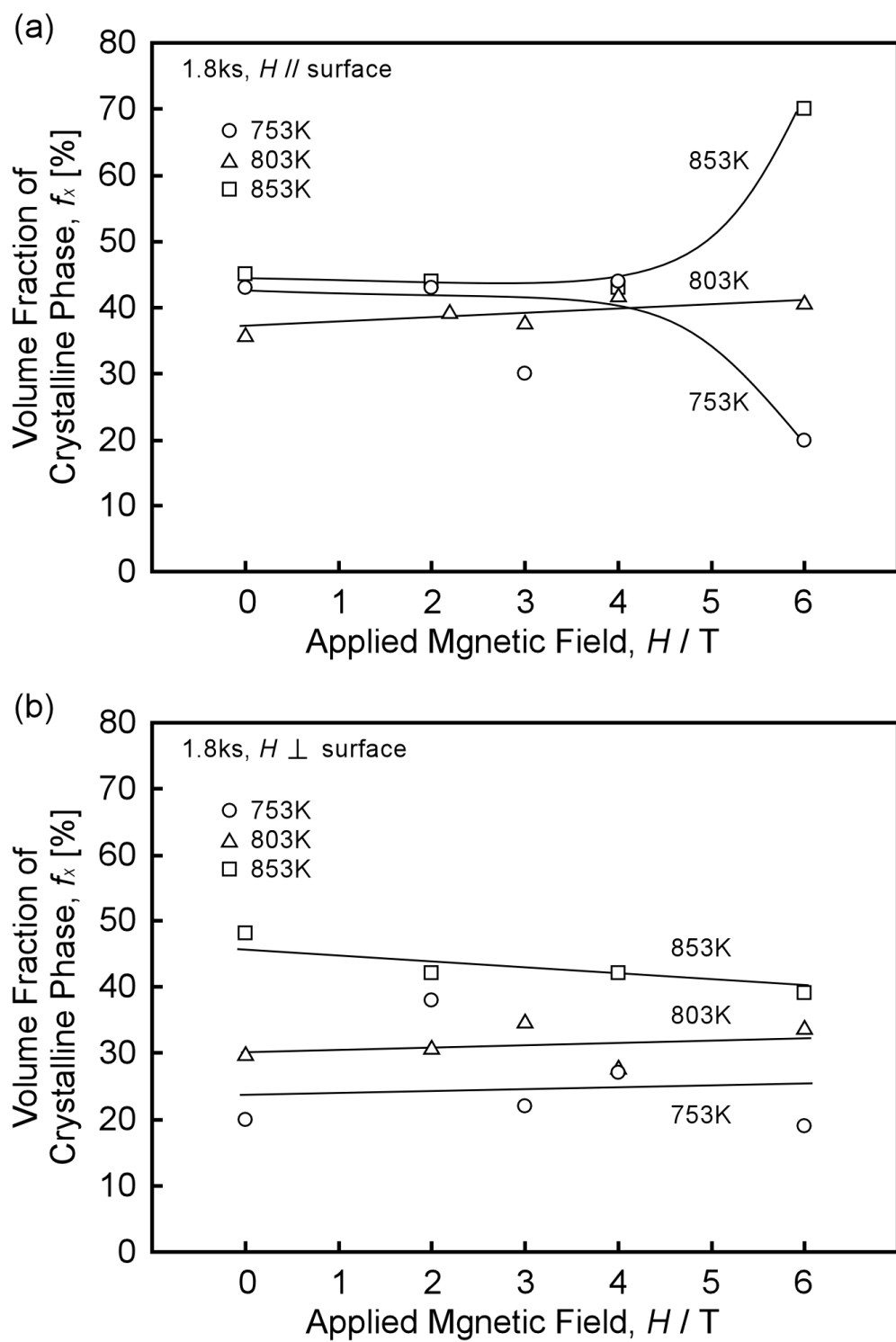


Figure 4-6 Change of volume fraction of crystalline phase as a function of magnetic field strength in crystallization of $\text{Fe}_{78}\text{Si}_9\text{B}_{13}$ amorphous alloys without and with a magnetic field (a) parallel and (b) perpendicular to the ribbon surface.

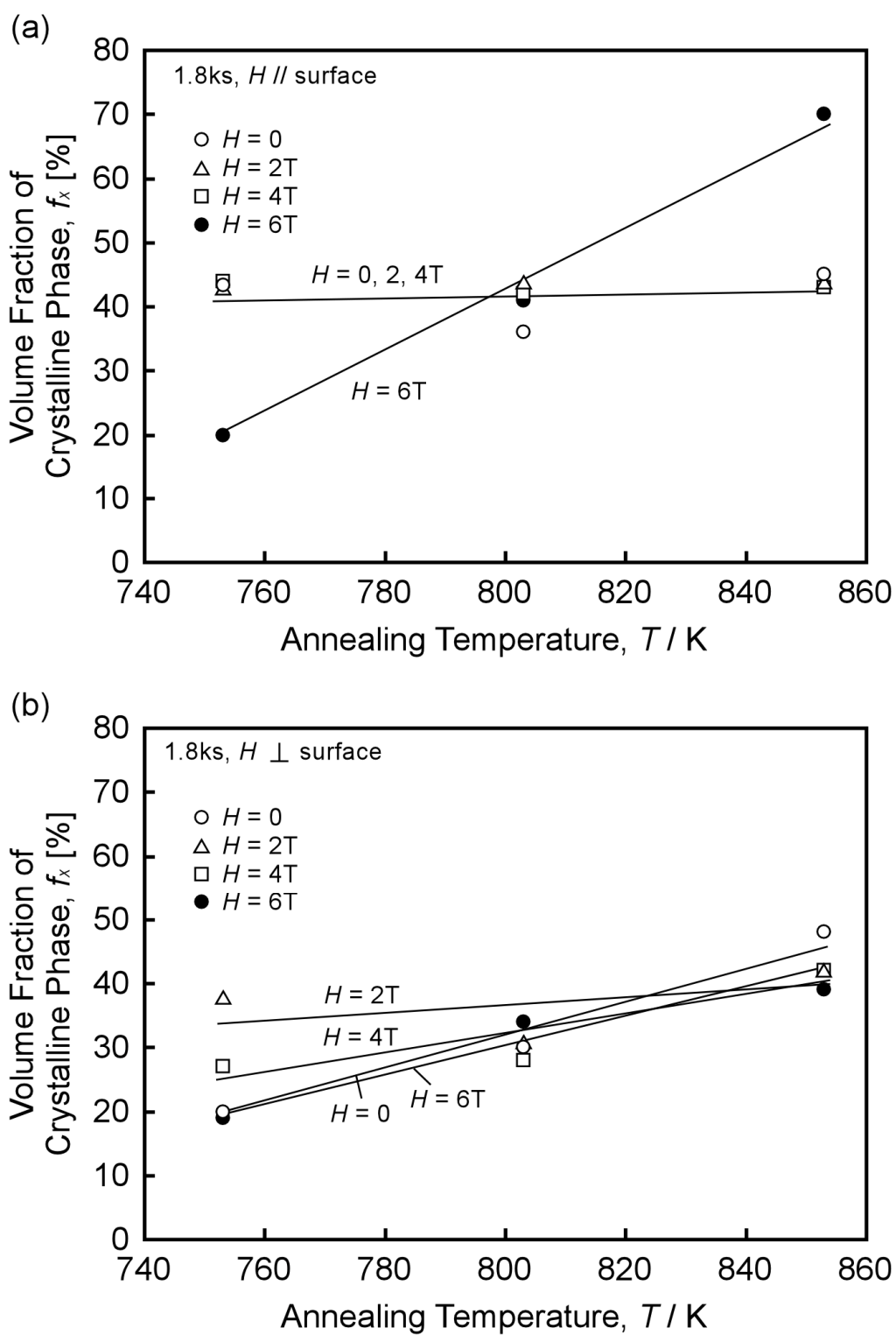


Figure 4-7 Change of volume fraction of crystalline phase as a function of annealing temperature in crystallization of $\text{Fe}_{78}\text{Si}_9\text{B}_{13}$ amorphous alloys without and with a magnetic field (a) parallel and (b) perpendicular to the ribbon surface.

without a magnetic field. On the other hand, the disorders of magnetic spin would be reduced during crystallization under a magnetic field because the magnetic spins could slightly align along the applied magnetic field even in the paramagnetic state [25]. As a result, the fluctuation of composition would decrease with the reduction of disorder of magnetic spins. Moreover, the diffusivity of interstitial atoms such as boron in iron below Curie temperature would decrease under a magnetic field as shown in chapter 2. This would be also decrease the nucleation rate during crystallization. Thereby a magnetic field would retard the crystallization rate at 753 K (between the Curie temperature of amorphous phase and the crystallization temperature). In contrast, the nucleation would significantly occur at the temperature above crystallization temperature because the diffusion of atoms was thermally activated. When a magnetic field was applied during crystallization at temperature between the crystallization temperature and the Curie temperature of crystalline phase, nucleation of crystallites could be enhanced by the extra driving force due to the magnetic energy difference between paramagnetic amorphous phase and ferromagnetic crystalline phase. This accelerative effect on nucleation would be much larger than the suppression effect below Curie temperature. This magnetic field effect of enhancement of crystallization rate will be discussed in more detail in the next section. Moreover, when a magnetic field was applied perpendicular to the specimen surface, the significant effects of a magnetic field were not observed as shown in Fig. 4-7 (b). The observed directional effect of a magnetic field on the crystallization rate may be attributed to the difference of the effective magnetic field strength due to demagnetization [26]. A demagnetization field becomes much larger when a magnetic field is applied perpendicular to the ribbon surface than that when it is applied parallel to the ribbon surface. Thus, a remarkable decrease in the effective magnetic field acting on the specimen occurs when a magnetic field is applied perpendicular to the ribbon surface. As mentioned above, as the magnetic field effect was found to appear above a magnetic field strength of 4 – 6 T as shown in Fig. 4-7 (a), a magnetic field of 6 T perpendicular to the specimen surface would not affect the crystallization rate.

The orientation index was calculated to evaluate grain orientation distribution (texture) from the intensity of Bragg peaks of XRD profiles shown in Fig. 4-5. Fig. 4-8 shows the orientation index $R(hkl)$ as a function of the magnetic field strength applied during crystallization at 853 K. It is found that the $R(110)$ is higher than unity, indicating that the surface orientation of crystallized grains is more localized around a {110} than other orientations. Although $R(110)$ is less dependent on the magnetic field strength up to 4 T, a significant increase of $R(110)$ occurs by application of a 6 T magnetic field, that is, formation

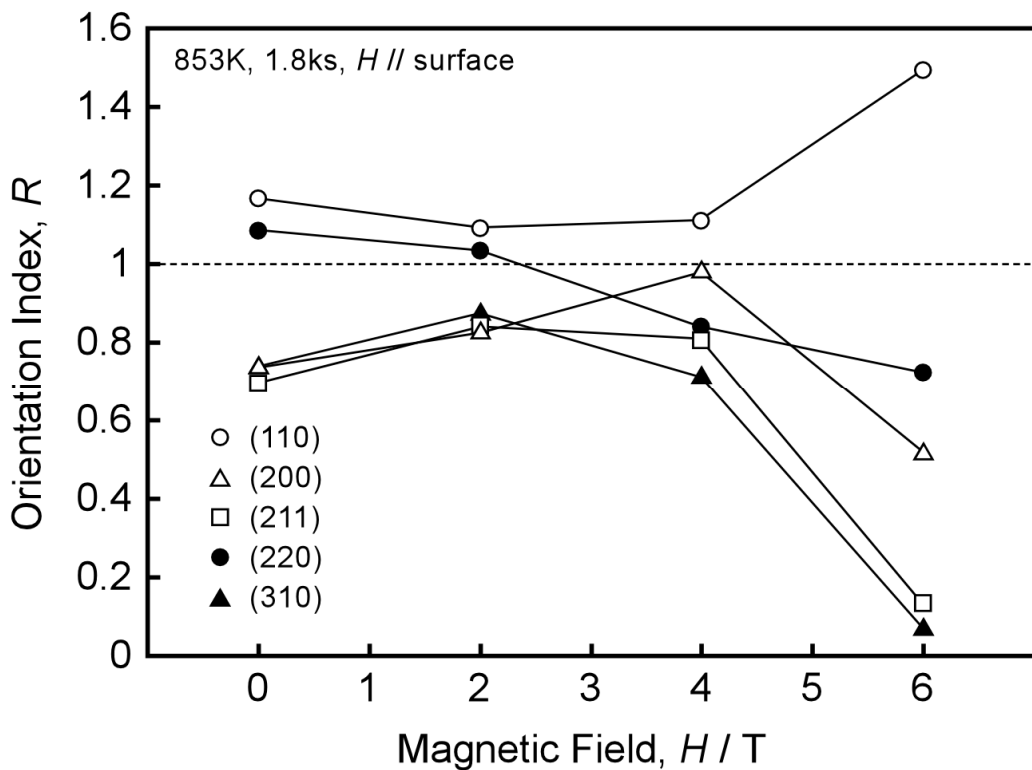


Figure 4-8 Orientation indices R as a function of magnetic field strength for different crystallographic planes in $\text{Fe}_{78}\text{Si}_9\text{B}_{13}$ ribbons crystallized at 853 K for 1.8 ks in a magnetic field.

of $\{110\}$ texture was enhanced during crystallization from the amorphous alloy in the 6 T magnetic field. The origin of the magnetic field effect on texture formation will be discussed in the next section.

(b) Control of grain orientation distribution on the application of a magnetic field

Fig. 4-9 represents OIM micrographs showing the grain orientation distribution of the $\text{Fe}_{78}\text{Si}_9\text{B}_{13}$ crystallized at 853 K for 1.8 ks (a) without a magnetic field (b) with a 6 T magnetic field parallel and (c) perpendicular to the ribbon surface. A sharp $\{110\}$ texture was found to be developed when a 6 T magnetic field was applied parallel to the ribbon surface, while the orientation of crystallized grains was not observably localized both when a magnetic field was

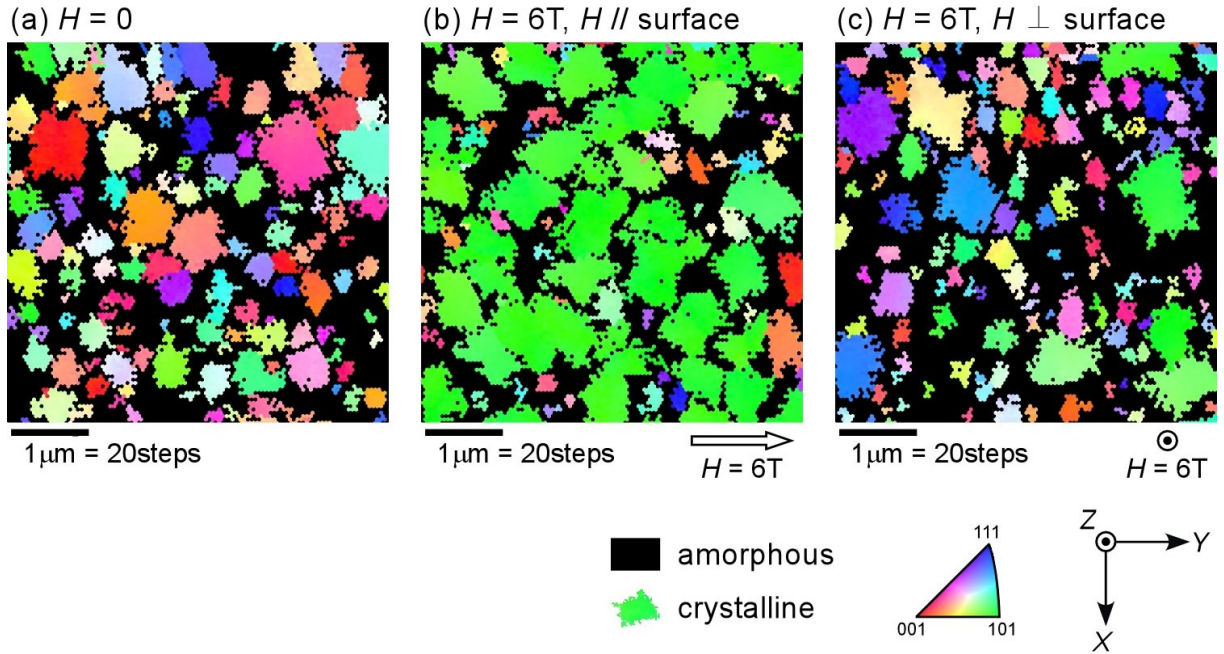


Figure 4-9 Orientation imaging microscope images for $\text{Fe}_{78}\text{Si}_9\text{B}_{13}$ ribbons crystallized at 853 K for 1.8 ks (a) without magnetic field, (b) with a 6 T magnetic field applied parallel to and (c) perpendicular to the ribbon surface. These images are colored according to the orientation of the sample normal (Z direction) in the cubic standard triangle.

applied perpendicular to the ribbon surface and when a magnetic field was not applied during crystallization. The observed directional effect of a magnetic field on the grain orientation distribution or texture evolution may be due to demagnetization [26] as well as the crystallization rate. As shown in Fig. 4-7, a magnetic field weaker than 6 T did not significantly affect the crystallization rate even when the field was applied parallel to the specimen surface. Therefore, a decrease in the effective magnetic field due to a strong demagnetization field in the direction perpendicular to the ribbon surface may cause the observed directional effect of a magnetic field on texture evolution.

Fig. 4-10 shows the inverse pole figures obtained from the same specimens as shown in Fig. 4-9. Of particular interest is Fig. 4-10 (b) of the specimen crystallized with a 6 T magnetic field applied parallel to the ribbon surface. It is found that the grain orientation perpendicular to the ribbon surface (Z-axis) is sharply localized in a $<101>$ direction. One

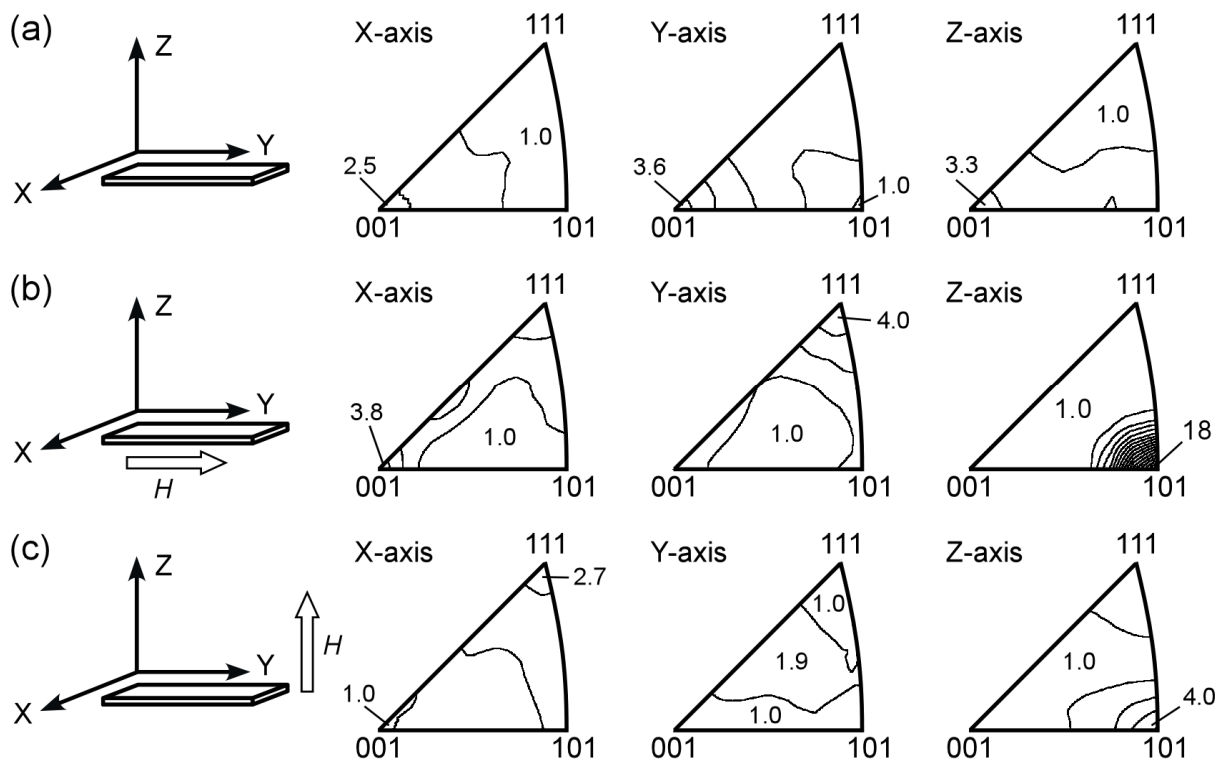


Figure 4-10 Inverse pole figures for $\text{Fe}_{78}\text{Si}_9\text{B}_{13}$ ribbons crystallized at 853 K for 1.8 ks (a) without magnetic field, (b) with a 6T magnetic field applied parallel and (c) perpendicular to the ribbon surface.

may expect that the grain orientation parallel to the magnetic field direction (Y-axis) also localizes in the $<001>$ direction, because the easy magnetization direction of iron is $<001>$. However, grain orientations parallel to the y-axis distribute between $<001>$, $<111>$ and $<101>$ directions. This finding accordingly indicates that one of the $<001>$ orientations of the crystallized grains randomly lies along the ribbon surface. Here, a question arises: how the sharp $\{110\}$ texture was formed in the 6 T magnetic field. Is it the result from preferential nucleation or preferential growth?

Fig. 4-11 shows the grain size distributions of the specimens crystallized at 853 K (a) without and (b) with a 6 T magnetic field parallel to the ribbon surface. The grain size distribution in the ordinarily crystallized specimen is a log-normal distribution as often observed in the case of normal grain growth. On the other hand, there are two peaks in the

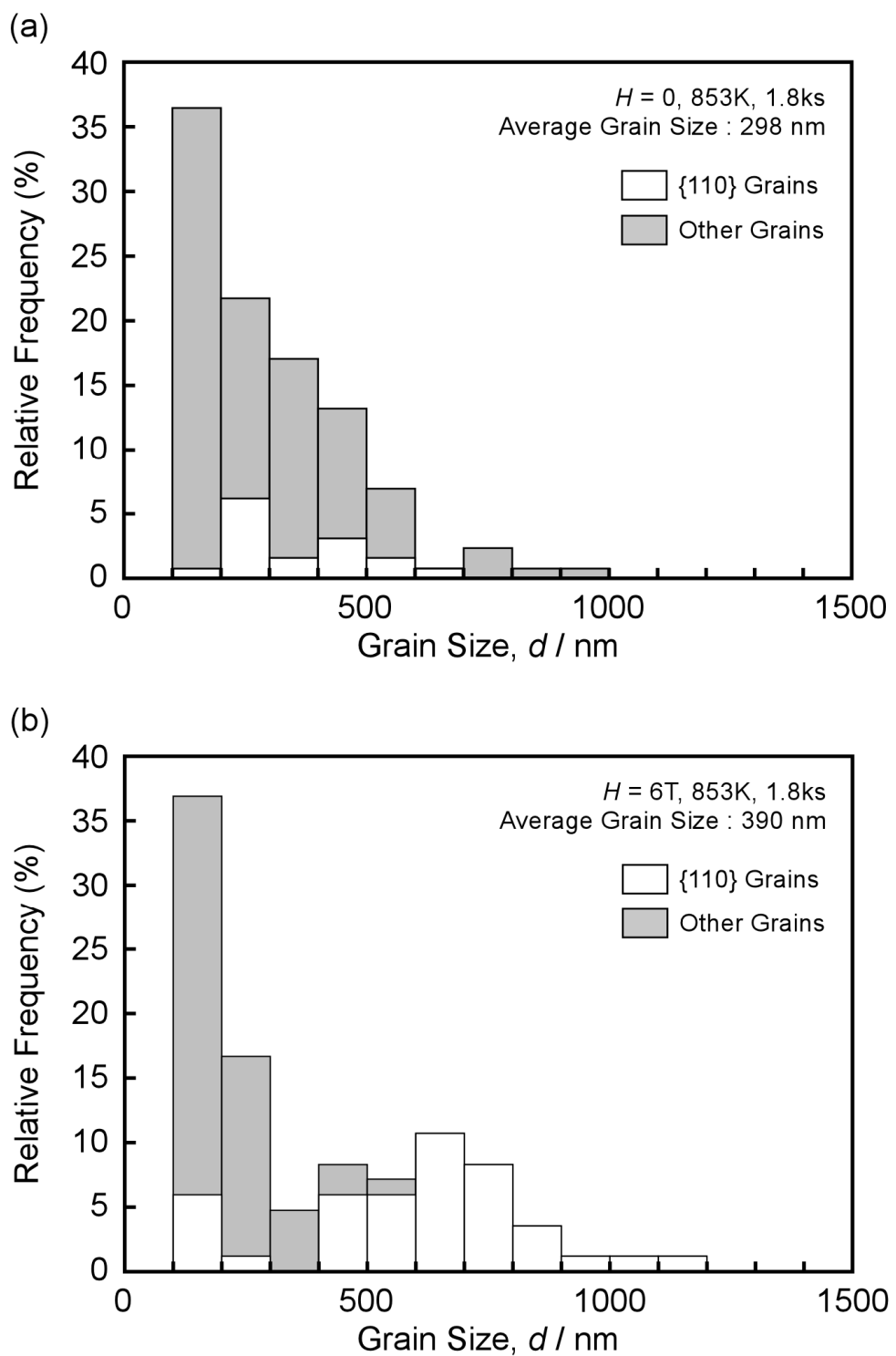


Figure 4-11 The grain size distributions of Fe₇₈Si₉B₁₃ ribbons differently crystallized at 853 K for 1.8 ks (a) without and (b) with a 6 T magnetic field applied parallel to the ribbon surface.

grain size distribution of the specimen crystallized in a 6 T magnetic field. It is interesting to observe that the peak in grain size distribution at larger grain sizes is almost composed of {110} grains. These findings suggest that the randomly oriented nuclei form from the amorphous alloy and then these {110} nuclei preferentially grow in the 6 T magnetic field. In general, the magnetocrystalline anisotropy energy E_a , which is an extra work required to turn the atomic spins from a nearby easy axis into the field direction, is given by the following equation for cubic crystals:

$$E_a = K_1(\alpha_1^2\alpha_2^2 + \alpha_2^2\alpha_3^2 + \alpha_3^2\alpha_1^2) + K_2(\alpha_1^2\alpha_2^2\alpha_3^2), \quad (4-7)$$

where K_1 and K_2 are the magnetocrystalline anisotropy constants, and α_1 , α_2 , α_3 are the directional cosines of the angle between the direction of magnetization and the three cubic axes. When a <001> axis of the grains orients parallel to the ribbon surface, one of three α_i parameters becomes zero according to eqn. (4-5). Thus, if {110} nuclei whose [001] orientation axis is parallel to the ribbon surface preferentially grow from randomly oriented nuclei, the magnetocrystalline anisotropy energy will be more significantly decreased than that when the nuclei with different orientations grow homogeneously. As the result, a sharp {110} texture is likely to be formed when the Fe₇₈Si₉B₁₃ amorphous alloy is crystallized in a magnetic field applied parallel to the ribbon surface. In order to confirm this suggestion, the early stage of magnetic crystallization should be more carefully observed.

From OIM micrographs shown by Fig. 4-9 (a) and (b), the area fraction of crystalline phase was evaluated to be 49% and 62% for the specimen crystallized at 853K without and a 6 T magnetic field, respectively. These values are in good agreement with the values estimated from XRD analysis. Therefore it is evident that the kinetics of crystallization from an amorphous precursor can be enhanced by application of 6 T magnetic field, as reported by Wolfus *et al.* [19]. This is probably because the ferromagnetic crystalline α -Fe(Si) phase is formed under a high magnetic field of 6 T in the paramagnetic amorphous phase at 853 K. The difference between the magnetic free energies of these two phases will act as an extra driving force and then accelerate crystallization in the magnetic field. An alternative explanation based on the classical nucleation-growth theory is possible. According to this theory, the activation energy of nucleation, ΔG^* , is an inverse square function of a volume free-energy change per unit volume, ΔG_v , associated with crystallization:

$$\Delta G^* = \frac{16\pi\gamma^3}{3\Delta G_v^2}, \quad (4-8)$$

where γ is the surface energy. In the case of our experiment, ΔG_v should be increased by

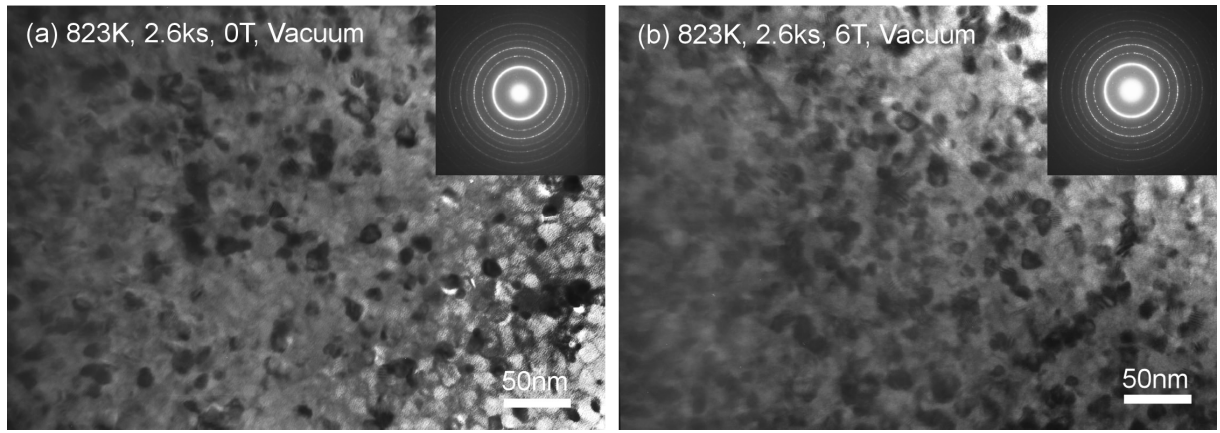


Figure 4-12 Bright-field TEM micrographs and diffraction patterns for the $\text{Fe}_{73.5}\text{Si}_{13.5}\text{B}_9\text{Nb}_3\text{Cu}_1$ ribbons nanocrystallized from its amorphous precursor by annealing at 823 K for 2.6 ks (a) without and (b) with a 6T magnetic field.

application of a magnetic field because the ferromagnetic α -Fe(Si) phase nucleates in the paramagnetic amorphous phase, which leads to a decrease in ΔG^* . Thus, the nucleation of the ferromagnetic α -Fe(Si) phase will be made easier by application of a magnetic field. Detailed analysis of this theory will be described in the next section.

4.3.2 Nanocrystallization of $\text{Fe}_{73.5}\text{Si}_{13.5}\text{B}_9\text{Nb}_3\text{Cu}_1$ alloy under a magnetic field

(a) Microstructure evolution during crystallization under a magnetic field

Fig. 4-12 shows TEM micrographs of $\text{Fe}_{73.5}\text{Si}_{13.5}\text{B}_9\text{Nb}_3\text{Cu}_1$ specimens crystallized at 823 K for 2.6 ks (a) without and (b) with a 6 T magnetic field applied parallel to the ribbon surface. Selected area electron diffraction (SAD) patterns obtained from the same area as the TEM micrographs are also shown in Fig. 4-12. Both specimens are composed of a residual amorphous phase and a nanocrystalline phase. There appears to be no significant difference between the microstructure of the two specimens. The average grain size of the crystalline phase, which is determined to be α -Fe(Si) as shown in Fig. 4-13, is approximately 15-20 nm irrespective of whether a magnetic field being applied.

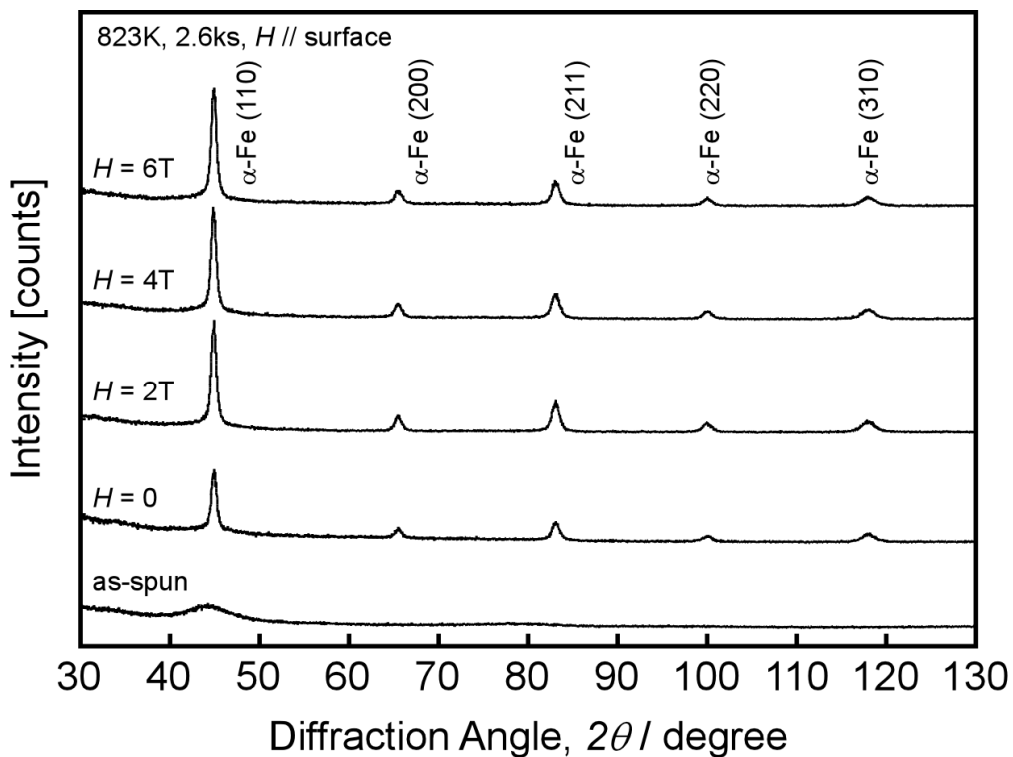


Figure 4-13 X-ray diffraction profiles for the Fe_{73.5}Si_{13.5}B₉Nb₃Cu₁ ribbons crystallized at 823 K for 2.6 ks with different magnetic-field strength. The magnetic field was applied parallel to the ribbon surface.

X-ray diffraction profiles for the specimens crystallized by annealing at 823K for 2.6ks with different field strengths are shown in Fig. 4-13. For comparison, the profile for the as-spun specimen is shown in the figure as well. Only some peaks associated with α-Fe(Si) phase are observed. No other phases except α-Fe(Si) were recognized from the XRD profiles. Of particular importance is the finding that the intensity of the {110} peak increases with the increase in magnetic-field strength. The degree of texture was evaluated by means of the orientation index defined in eqn. (4-5) from the XRD profiles, and the variation of this value with field strength is shown in Fig. 4-14. The orientation index of the {110} reflection is a monotonically increasing function of magnetic-field strength, indicating an increase of sharpness of the {110} texture as a result of the crystallization under a magnetic field. Here a question arises as to whether the {110} texture is induced by

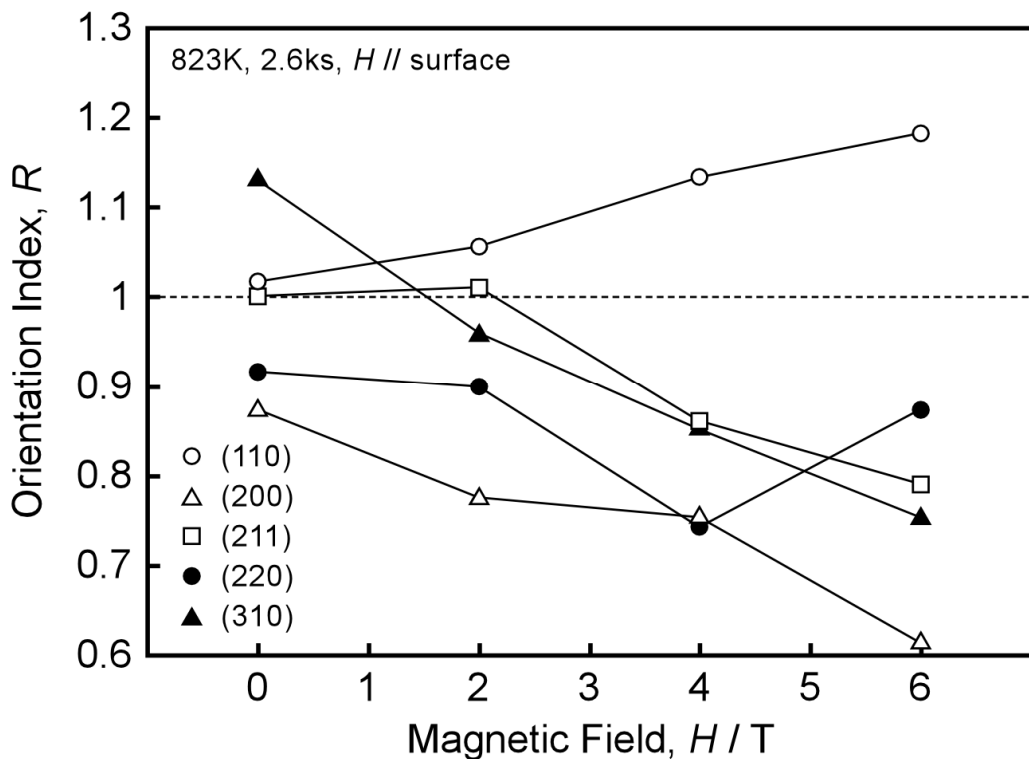


Figure 4-14 Orientation index for (hkl) reflections for $\text{Fe}_{73.5}\text{Si}_{13.5}\text{B}_9\text{Nb}_3\text{Cu}_1$ ribbons crystallized at 823 K for 2.6 ks as a function of a magnetic-field strength.

preferential nucleation or by preferential growth. In order to examine the further effect of a magnetic field on the orientation of nuclei, X-ray diffraction based on the Shultz method was applied to the specimen at an early stage of crystallization from amorphous phase, where the individual nucleated grains has not yet met each other. Fig. 4-15 shows (110) pole figures from specimens annealed at 723 K for 2.6 ks without and with a 6 T magnetic field. The $\{110\}$ poles of the assembly of crystallites are found to be somewhat localized at the center of the pole figure in the specimen crystallized with a 6 T magnetic field compared with those in the specimen annealed without a magnetic field; the intensity of $\{110\}$ poles at the center is higher by about 25 % in the magnetically annealed case. One may expect that one of the $\langle 100 \rangle$ directions which are the easy magnetization directions in bcc-iron might be aligned along the magnetic field direction in $\alpha\text{-Fe}(\text{Si})$ crystals. However, there is no significant evidence of localization of $\{110\}$ poles anywhere except at the center of the pole figure even

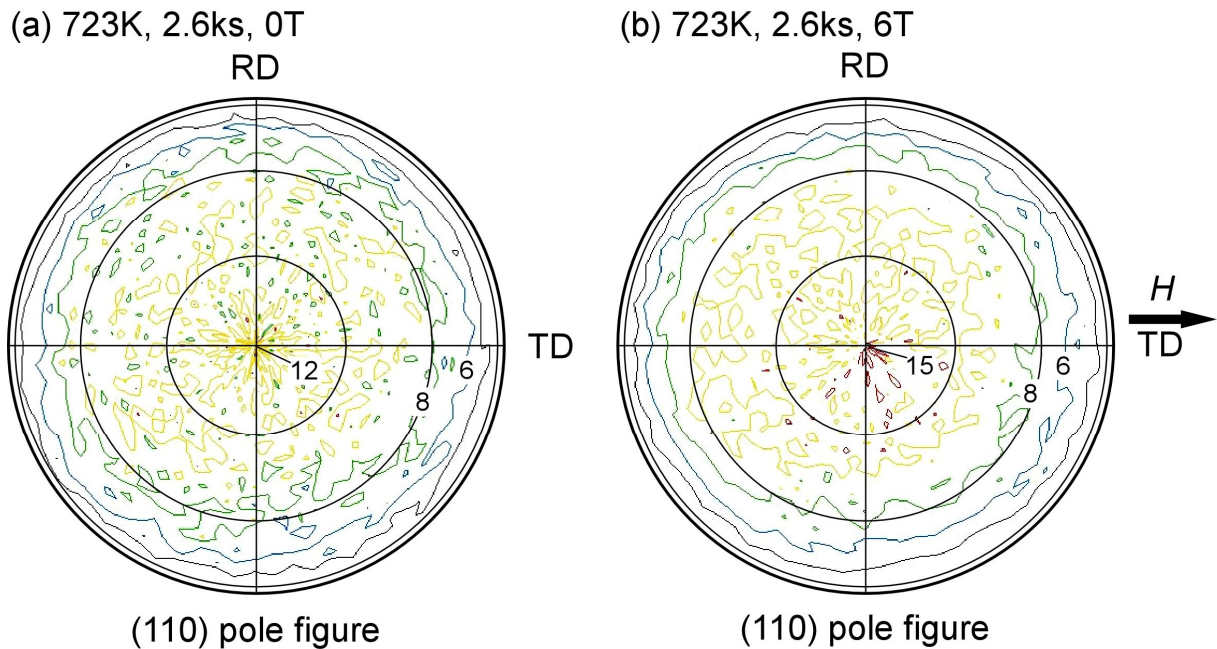


Figure 4-15 (110) pole figures of for the $\text{Fe}_{73.5}\text{Si}_{13.5}\text{B}_9\text{Nb}_3\text{Cu}_1$ ribbons at a nearly stage of crystallization by annealing at 723 K for 2.6 ks (a) without and (b) with a 6T magnetic field parallel to the ribbon surface.

in the specimen crystallized with a 6 T magnetic field. From these results, it can be concluded that the {110}-oriented nuclei are formed preferentially under a magnetic field, and one of the <001> orientations in these nuclei is oriented in a random direction in the plane of the ribbon surface. This result is in good agreement with the crystallization from an $\text{Fe}_{78}\text{Si}_9\text{B}_{13}$ amorphous alloy under a magnetic field as shown in inverse pole figures of Fig. 4-10.

Regarding grain growth under a magnetic field, grain size distributions were examined in the specimens crystallized under various annealing conditions. Fig. 4-16 shows changes in the grain size distribution with annealing time for specimens crystallized at 723 K without and with a 6 T magnetic field. These appear to be normal distributions irrespective of whether or not a magnetic field is applied; this indicates that normal grain growth of α -Fe(Si) crystals occurs. Looking through Figs. 4-16 (a)-(f), the average grain size and the standard deviation both change slightly with annealing time, and there is no observable difference between the nature of grain growth without and with a 6 T magnetic field. A similar result is obtained at

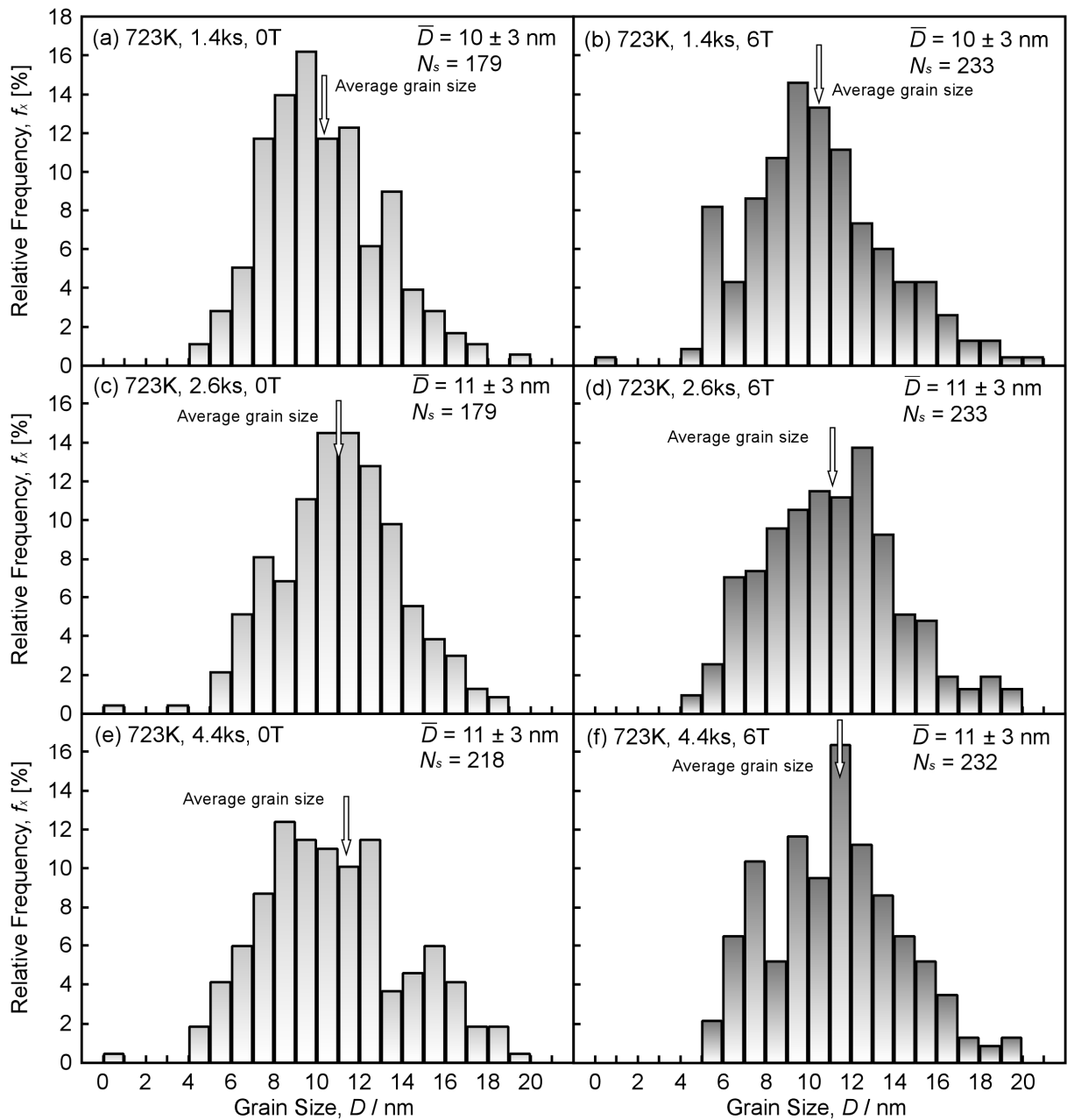


Figure 4-16 Changes in the grain size distribution in the nc- $\text{Fe}_{73.5}\text{Si}_{13.5}\text{B}_9\text{Nb}_3\text{Cu}_1$ alloy with annealing time at 723 K without (a, c, e) and with a 6T magnetic field (b, d, f).

different temperatures as shown in Fig. 4-17. Unlike the crystallization of the $\text{Fe}_{78}\text{Si}_9\text{B}_{13}$ alloy under a magnetic field, in which energetically preferred $\{110\}$ grains grew faster and a bimodal grain size distribution developed under a magnetic field, the grain growth in the

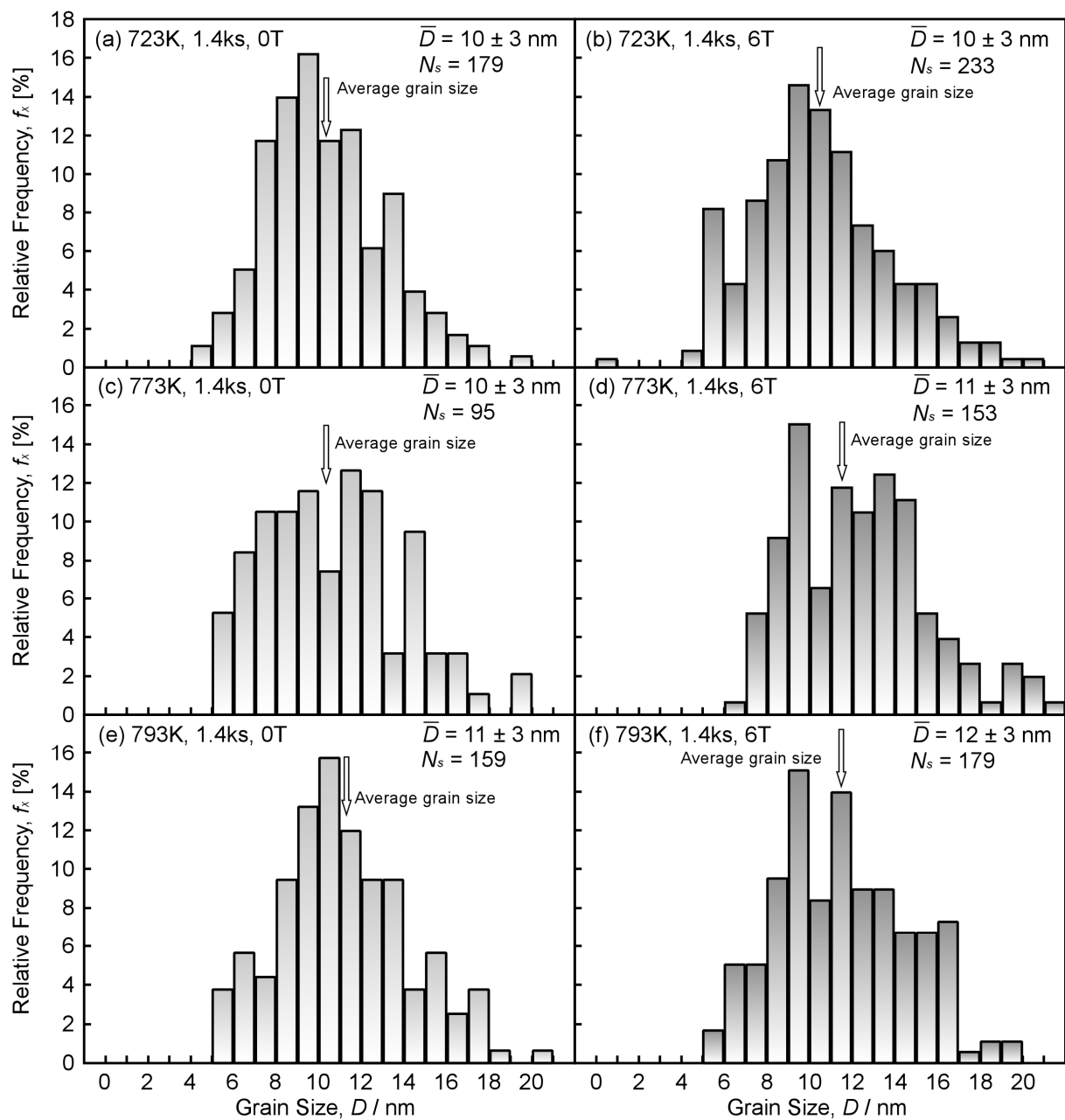


Figure 4-17 Changes in the grain size distribution in the nc- $\text{Fe}_{73.5}\text{Si}_{13.5}\text{B}_9\text{Nb}_3\text{Cu}_1$ alloy with annealing temperature for annealing time of 1.4 ks without (a, c, e) and with a 6T magnetic field (b, d, f).

$\text{Fe}_{73.5}\text{Si}_{13.5}\text{B}_9\text{Nb}_3\text{Cu}_1$ alloy is not affected by a magnetic field. This less effect of a magnetic field on grain growth is probably attributable to a pinning effect of solute atoms on interphase

migration. In the $\text{Fe}_{73.5}\text{Si}_{13.5}\text{B}_9\text{Nb}_3\text{Cu}_1$ alloy, Cu clusters formed in the amorphous phase prevent the migration of the interface between the crystallite and the amorphous phase, and the diffusivity of Nb atoms that are rejected from α -Fe(Si) crystallites to the amorphous phase is very low [27]. An increase in driving force for grain growth due to a magnetic field may be insufficient to overcome this pinning forces acting against interface migration. Judging from Figs. 4-15 – 4-17, it can be concluded that preferential nucleation of {110} oriented grains, rather than preferential growth, is the predominant reason for the development of {110} texture in the nanocrystalline $\text{Fe}_{73.5}\text{Si}_{13.5}\text{B}_9\text{Nb}_3\text{Cu}_1$ alloy annealed under a magnetic field.

Another question arises: why the {110} oriented grains are preferentially nucleated under a magnetic field. As mentioned in the previous section on the crystallization of the $\text{Fe}_{78}\text{Si}_9\text{B}_{13}$ alloy under a magnetic field, the reason for the {110} texture formation was discussed from the point of view of magnetocrystalline anisotropy energy because of suggestion of preferential growth of {110} oriented α -Fe(Si) grains. However, no significant effect of a magnetic field was observed on the grain growth in the nanocrystalline $\text{Fe}_{73.5}\text{Si}_{13.5}\text{B}_9\text{Nb}_3\text{Cu}_1$ alloy, so that a similar explanation to the case of $\text{Fe}_{78}\text{Si}_9\text{B}_{13}$ alloy seems to be insufficient to explain the preferential nucleation of {110} oriented grains observed. In the crystallization of $\text{Fe}_{73.5}\text{Si}_{13.5}\text{B}_9\text{Nb}_3\text{Cu}_1$ amorphous alloy, the mechanisms of nucleation and growth of α -Fe(Si) grains differ from those in $\text{Fe}_{78}\text{Si}_9\text{B}_{13}$ alloy due to the additional elements of niobium and copper. As the α -Fe(Si) grains nucleate inhomogeneously and those growth rate is significantly decreased by the pinning effect of additional elements, the effect of a magnetic field on nucleation and growth in $\text{Fe}_{73.5}\text{Si}_{13.5}\text{B}_9\text{Nb}_3\text{Cu}_1$ amorphous alloy would differ from that in $\text{Fe}_{78}\text{Si}_9\text{B}_{13}$ amorphous alloy. Then, several possible reasons of this should be further considered: *e.g.* the effect of a magnetic field on surface energy. When the surface energy of {110} oriented grains decreased under a magnetic field, the preferential nucleation of {110} grains would occur as mentioned above.

(b) Volume fraction of nanocrystallized grains

In the previous section on the crystallization of the $\text{Fe}_{78}\text{Si}_9\text{B}_{13}$ alloy under a magnetic field, it was found that the volume fraction of the crystalline α -Fe(Si) phase increased by application of a 6 T magnetic field. Accordingly, the volume fraction of the nanocrystalline α -Fe(Si) phase was evaluated in the $\text{Fe}_{73.5}\text{Si}_{13.5}\text{B}_9\text{Nb}_3\text{Cu}_1$ alloy using an XRD profile fitting procedure [22, 28]. The XRD {110} peak was fitted according to the pseudo-Voigt function given by the eqn. (4-1). Fig. 4-18 exhibits the volume fraction of α -Fe(Si) phase crystallized

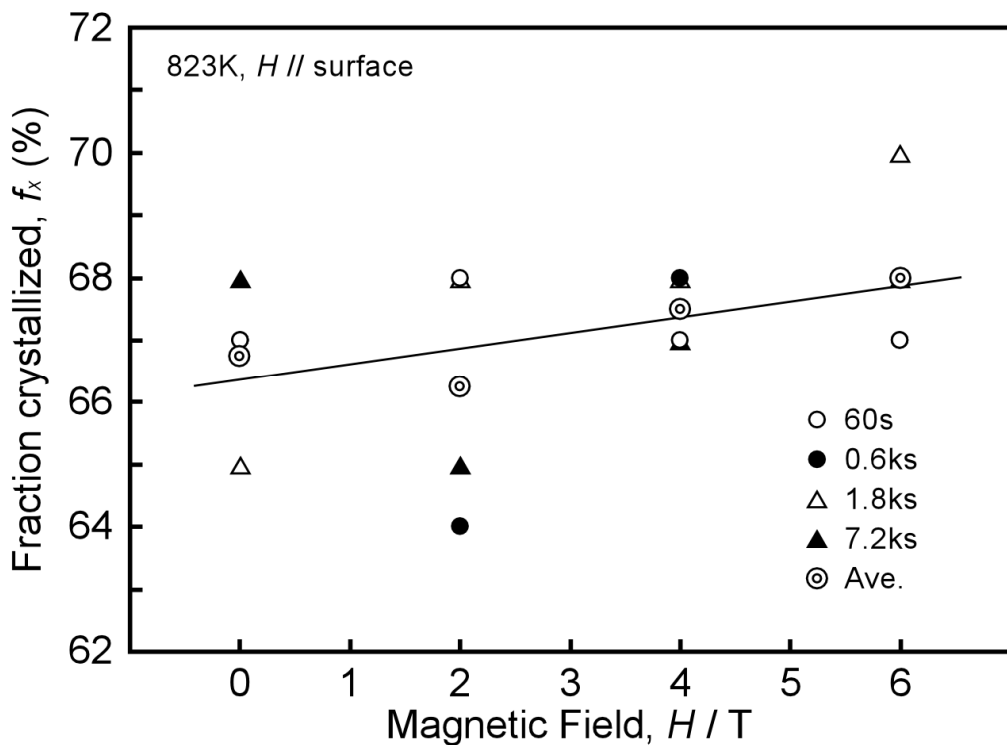


Figure 4-18 The volume fraction of α -Fe(Si) phase crystallized from the $\text{Fe}_{73.5}\text{Si}_{13.5}\text{B}_9\text{Nb}_3\text{Cu}_1$ amorphous precursor by annealing at 823 K for 60 s - 1.8 ks as a function of a magnetic field strength.

from the $\text{Fe}_{73.5}\text{Si}_{13.5}\text{B}_9\text{Nb}_3\text{Cu}_1$ amorphous alloy by annealing at 823 K for 60 s – 7.2 ks as a function of magnetic field strength. Considering the data for each value of magnetic field strength, there is no systematic variation of volume fraction with the increase in annealing time. Taking account of the experimental error, it is considered that the fraction crystallized may have almost approached to saturation even after annealing for only 60 s at 823 K. However, by observing the average values, the volume fraction of α -Fe(Si) phase somewhat increases with the increase in magnetic field strength, from 67 % at zero field to 68 % at 6 T magnetic field. These estimated values of volume fraction crystallized are in good agreement with those previously reported for nanocrystalline $\text{Fe}_{73.5}\text{Si}_{13.5}\text{B}_9\text{Nb}_3\text{Cu}_1$ alloy produced by fully annealing at similar temperatures [12, 22, 26, 29]. Regarding the increase in the volume fraction of α -Fe(Si) phase by the crystallization under a magnetic field, the

possibility of change in the equilibrium phase stability due to the energetic contribution of the magnetic field was discussed. Although the contribution of the magnetic free energy to the total Gibbs free energy was calculated on the basis of CALPHAD methodology [30], it was found that the energetic contribution from an applied magnetic field of 6 T was insufficient to predict the changes in α -Fe phase fraction in nanocrystalline $\text{Fe}_{73.5}\text{Si}_{13.5}\text{B}_9\text{Nb}_3\text{Cu}_1$ or the larger phase fraction differences observed in $\text{Fe}_{78}\text{Si}_9\text{B}_{13}$. To obtain the changes in the α -Fe fraction observed experimentally, a magnetic energy contribution of the order of $-2 \text{ kJ}\cdot\text{mol}^{-1}$ will be needed. This energy corresponds to an applied magnetic field of 180 T. A possible explanation for the observed differences in phase fraction is that the magnetic energy contribution, by increasing the nucleation rate, results in nuclei of crystalline phase in an amorphous matrix that still contains some quenched-in excess energy from the melt-spinning process. Slower nucleation kinetics, by contrast, would allow the matrix time to relax and to lower its energy. The position of local equilibrium between the amorphous and crystalline phases, and therefore the fraction of crystalline phase, would thus be different in the two cases.

(c) Nucleation and growth kinetics under a magnetic field

In order to study the effect of a magnetic field on the kinetics of nucleation and growth in the $\text{Fe}_{73.5}\text{Si}_{13.5}\text{B}_9\text{Nb}_3\text{Cu}_1$ amorphous alloy, TEM was used to observe the progress in crystallization, particularly at the early stages. Fig. 4-19 shows TEM micrographs of specimens crystallized at 723K for 1.4ks (a) without and (b) with a 6T magnetic field. The SAD patterns from each specimen are also exhibited in the figures. From these micrographs, the number of crystallites appears to be higher in the specimen annealed with a 6T magnetic field than without a magnetic field. In addition, the SAD pattern from the specimen annealed without a magnetic field displays a broader ring shape, whereas the ring pattern from the specimen annealed with a 6T magnetic field is clearer and sharper. Consequently, it is considered that a magnetic field can enhance the nucleation rate of ferromagnetic α -Fe(Si) grains from the paramagnetic amorphous phase.

The number density of nuclei per unit volume as a function of annealing time was quantitatively evaluated as shown in Fig. 4-20 (a). The density appears to be an exponential function of annealing time irrespective of whether or not a magnetic field being applied. However, these values were increased by 2 - 3 times by the application of a 6 T magnetic field. Anderson and Mehl have found that the nucleation rate \dot{N}_n as a function of annealing time

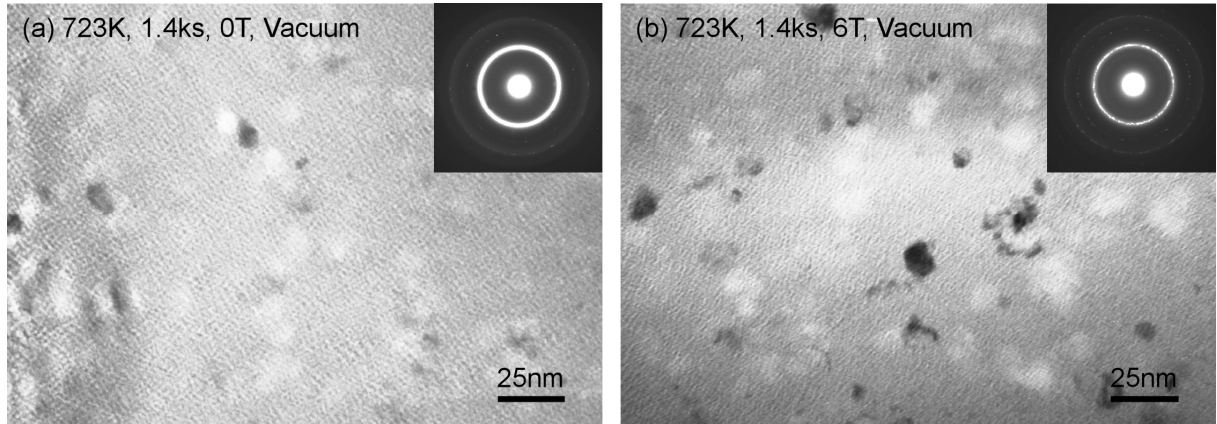


Figure 4-19 Bright-field TEM micrographs and diffraction patterns for the $\text{Fe}_{73.5}\text{Si}_{13.5}\text{B}_9\text{Nb}_3\text{Cu}_1$ ribbons at an early stage of crystallization by annealing at 723 K for 1.4 ks (a) without and (b) with a 6T magnetic field.

in the recrystallization of aluminum was given by the following exponential function, at least up to 30 % recrystallization [31].

$$\dot{N}_n = a \exp(bt), \quad (4-9)$$

where a and b are constants. Fig. 4-20 (b) shows the semi-logarithm plots of the number density of nuclei against annealing time. There is a good linear correlation between the natural logarithms of N_n and annealing time for specimens crystallized both without and with a magnetic field. Therefore, eqn. (4-9) can be applied to the crystallization of nanocrystalline $\text{Fe}_{73.5}\text{Si}_{13.5}\text{B}_9\text{Nb}_3\text{Cu}_1$ alloy under a magnetic field. The values of a and b in eqn. (4-9) were estimated to be $a = 1.2 \times 10^{21} \text{ m}^{-3}\text{s}^{-1}$, $b = 0.23$ for crystallization with a 6 T magnetic field and $a = 5.2 \times 10^{20} \text{ m}^{-3}\text{s}^{-1}$, $b = 0.20$ without a magnetic field.

Changes in the volume fraction of the α -Fe(Si) crystalline phase f_x during crystallization of the $\text{Fe}_{73.5}\text{Si}_{13.5}\text{B}_9\text{Nb}_3\text{Cu}_1$ amorphous alloy by annealing at 723K without and with a 6T magnetic field are shown in Fig. 4-21 (a) and (b). To determine the volume of each grain, grains were assumed to have a spherical shape. The volume fraction is found to be increased by 2-3 times by application of a magnetic field, as shown in Fig. 4-21 (a). The dependence of the crystallized fraction on annealing time was examined on the basis of the Johnson-Mehl-Avrami-Kolmogorov (JMAK) equation which is given by,

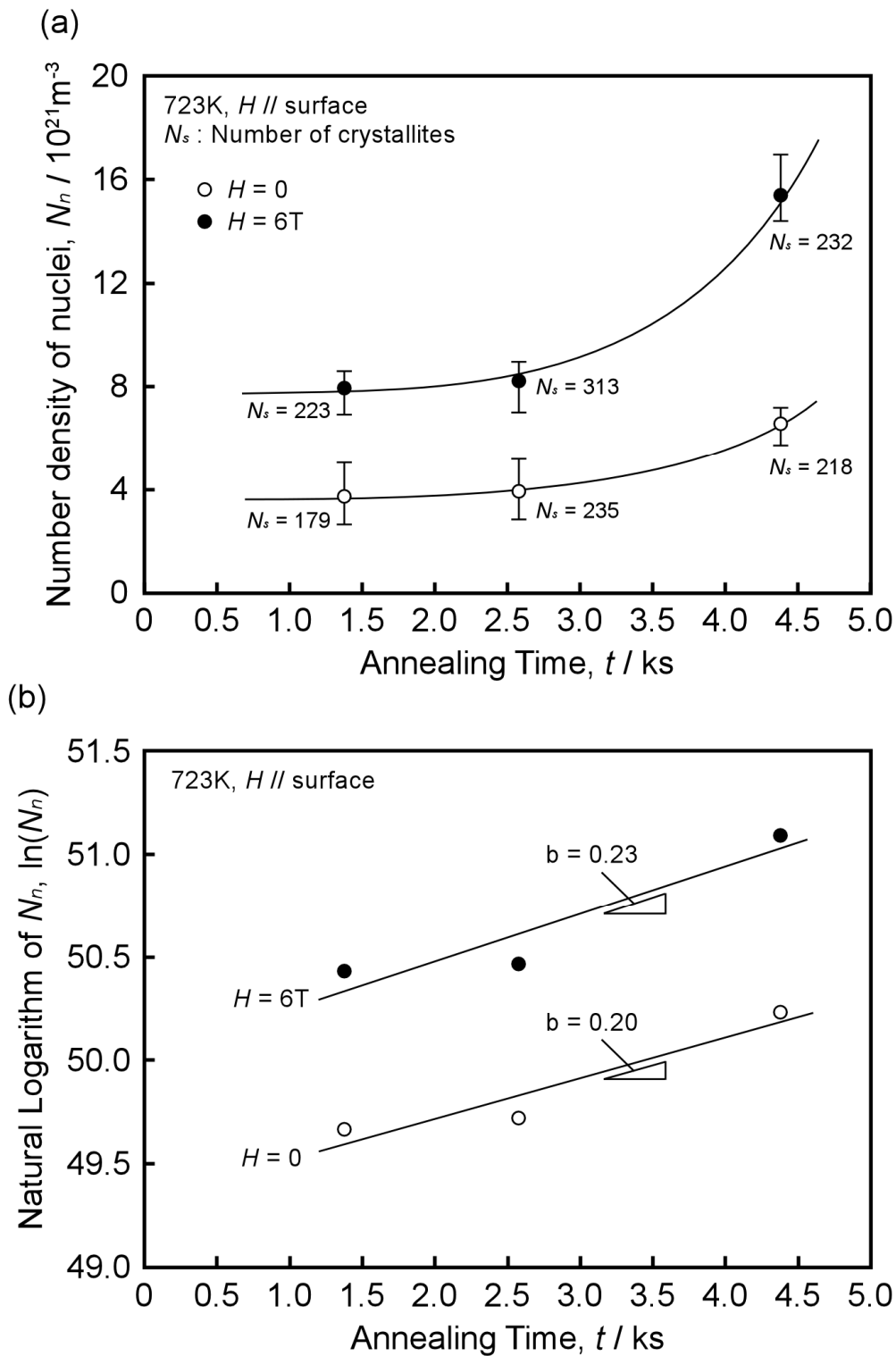


Figure 4-20 Changes in the number density of nuclei per unit volume in the Fe_{73.5}Si_{13.5}B₉Nb₃Cu₁ amorphous precursor with annealing time at 723K without and with a 6T magnetic field: (a) a normal plot and (b) a semi-logarithm plot of the density against annealing time.

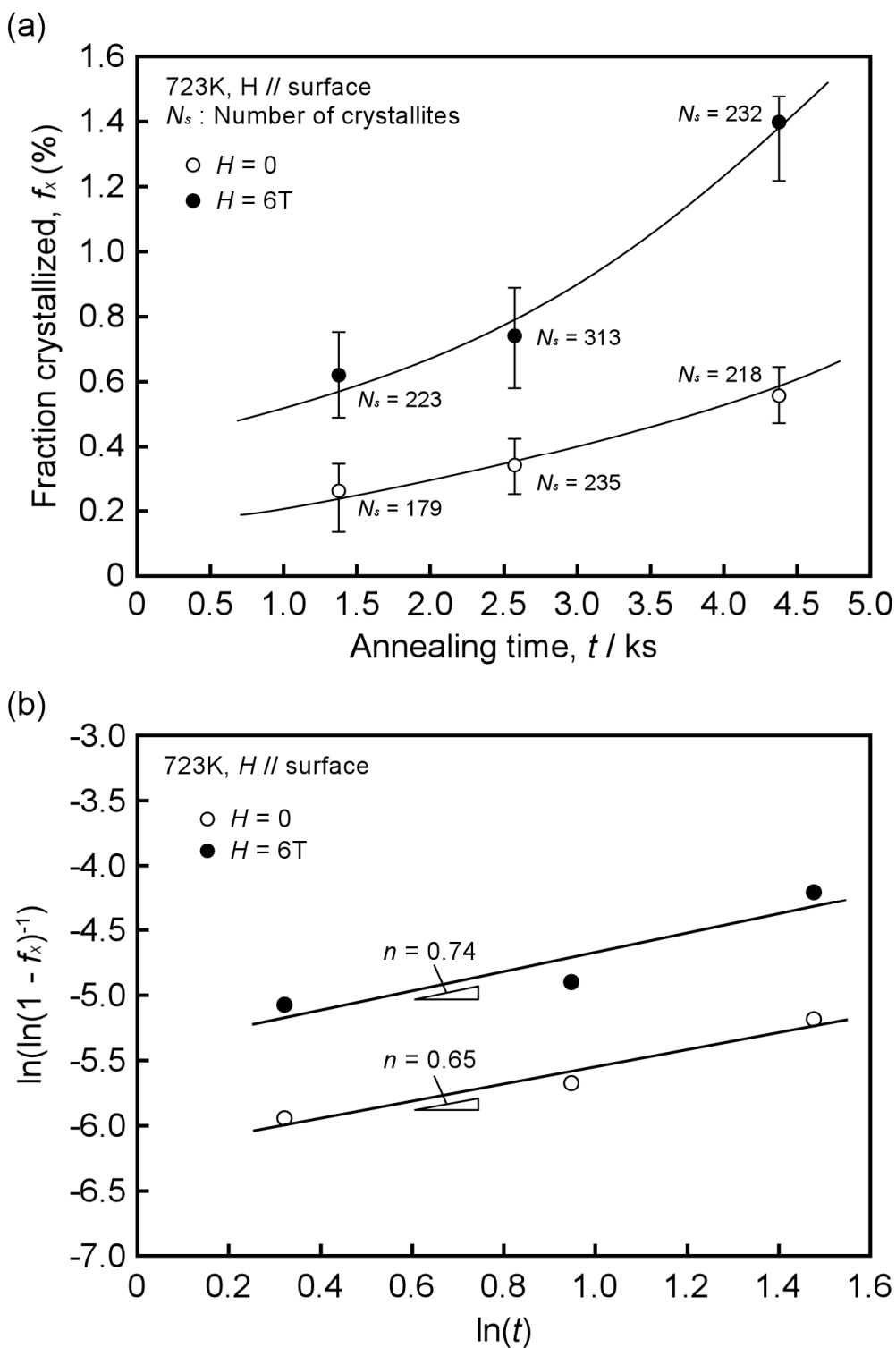


Figure 4-21 Changes in the volume fraction of α -Fe(Si) phase crystallized from $\text{Fe}_{73.5}\text{Si}_{13.5}\text{B}_9\text{Nb}_3\text{Cu}_1$ amorphous precursor with annealing time at 723K without and with a 6T magnetic field: (a) a normal plot and (b) a JMAK plot of the fraction crystallized against annealing time.

$$f_x = 1 - \exp(-Kt^n), \quad (4-10)$$

$$K = f N_n \dot{G}^3, \quad (4-11)$$

where f is a shape factor ($4\pi/3$ for spheres), and \dot{G} the growth rate. From the JMAK plot of the crystallization kinetics of the $\text{Fe}_{73.5}\text{Si}_{13.5}\text{B}_9\text{Nb}_3\text{Cu}_1$ alloy shown in Fig. 4-21 (b), the Avrami indices of the specimens crystallized without and with a 6 T magnetic field were estimated to be 0.65 and 0.74, respectively. The value of K , which is a function of both the nucleation rate and the growth rate of the grains, was higher by 2.2 times with the 6T magnetic field (4.47×10^{-3}) than those without the magnetic field (2.02×10^{-3}). As mentioned above, the nucleation rate increased by 2-3 times by the application of a magnetic field, however the growth rate was not significantly affected by a magnetic field. Therefore, it is considered that the increase in the volume fraction of crystallized phase due to a magnetic field is predominantly caused by the increase in nucleation rate rather than by any change in the growth rate.

4.3.3 Origin of the influence of a magnetic filed on crystallization kinetics and texture formation

According to the classical nucleation-growth theory, the activation energy barrier against nucleation, ΔG^* , is determined from the volume free energy change per unit volume, ΔG_v , associated with the phase transformation, and the surface energy, γ , of the nucleus as mentioned previous section. The same explanation can apply to the crystallization of $\text{Fe}_{73.5}\text{Si}_{13.5}\text{B}_9\text{Nb}_3\text{Cu}_1$ under a magnetic field. In addition, a magnetic contribution to the volume free energy should be considered in a magnetic field because the ferromagnetic α -Fe(Si) phase is formed from the paramagnetic amorphous phase. Therefore, the activation energy of nucleation, ΔG^* , and the critical radius of nucleation r^* , in a magnetic field are given by the following equations:

$$\Delta G^* = \frac{16\pi\gamma^3}{3(\Delta G_v + \Delta G_M)^2}, \quad (4-12)$$

$$r^* = -\frac{2\gamma}{\Delta G_v + \Delta G_M}, \quad (4-13)$$

where ΔG_M is the change in magnetic free energy associated with crystallization. Ignoring any influences of the magnetic field on the interface energy, and assuming that the magnetic free energy of the paramagnetic amorphous phase is negligible, the values of ΔG^* and r^*

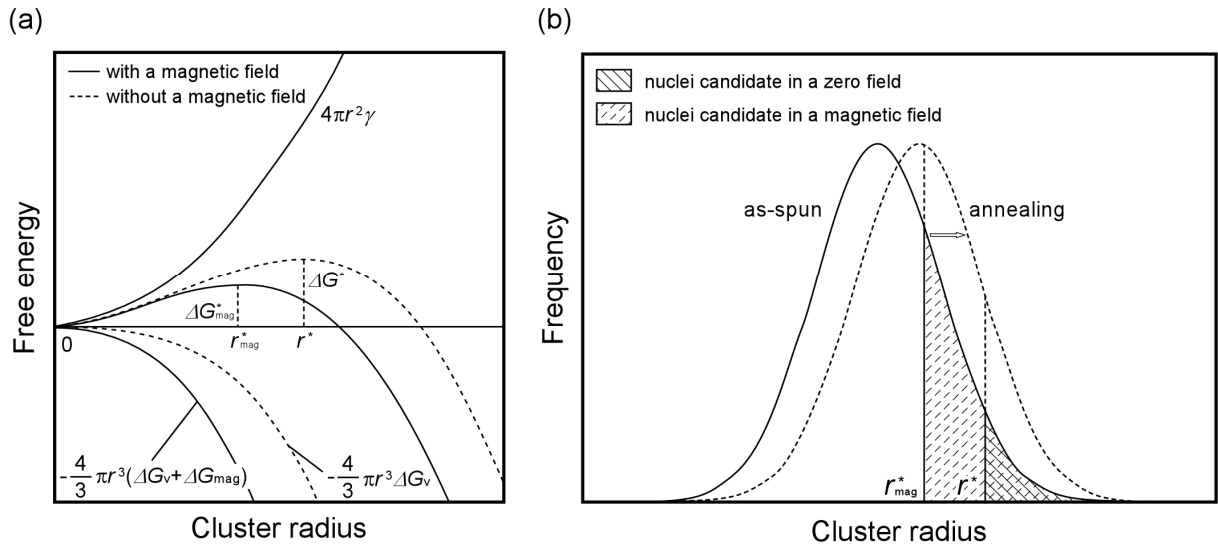


Figure 4-22 Schematic explanation for (a) the influence of a magnetic field on the activation energy for nucleation and the critical nucleation size, and for (b) a possible reason for the increase in nucleation rate under a magnetic field.

will decrease in a magnetic field as shown in Fig. 4-22 (a) because both ΔG_v and ΔG_M are negative. Thus, the nucleation of the ferromagnetic α -Fe(Si) phase will be made easier by application of a magnetic field.

Here, Fig. 4-20 should be noted again. When the exponential curves showing the relation between the number density of nuclei N_n and the annealing time t are interpolated to $t = 0$, the curves intersect the vertical axis at a finite value irrespective of whether a magnetic field being applied; that is the number density of nuclei does not become zero at $t = 0$. This is probably because some short-range ordered clusters (embryos), which could subsequently become the cores of nucleating crystals, may have existed in the amorphous alloy, unlike in the case of nucleation of crystals from a liquid phase. If it is assumed that the size distribution of the clusters is Gaussian, the number of clusters (embryos) that are super-critical and can grow into stable grains would increase with the decrease in the critical radius due to a magnetic field, as illustrated in Fig. 4-22 (b). Furthermore, if the size distribution of clusters could shift to a regime of larger cluster size by annealing, the increase in the nucleation rate would be higher in a magnetic field than in zero-field.

An attempt is made to test this proposition using some data from literatures and from equilibrium calculations in the framework of the CALPHAD methodology. In general, the magnetic free energy per unit volume for ferromagnetic materials is given by,

$$\Delta G_M^f = -\mu_0 \left(H - \frac{NM_s}{2} \right) M_s , \quad (4-14)$$

when $H \gg H_c$, where μ_0 is permeability in vacuum, N is the demagnetizing factor, M_s is the saturation magnetization and H_c is the critical magnetic field strength to achieve the saturation magnetization. In our experiments, a magnetic field was applied parallel to the ribbon surface, so that the demagnetizing factor is assumed to be zero. The saturation magnetization of crystalline phase was estimated to be $\mu_0 M_s = 1.82 \text{ kg/s}^2 \text{A}$ for the composition of $\text{Fe}_{73.5}\text{Si}_{13.5}$ by assuming that it decreases Si content. Actually, the data for the magnetic moment of Fe-Si alloys as a function of Si content can be found [32]. From eqn. (4-14), we can obtain a value of the magnetic free energy, $\Delta G_M^f = 8.69 \times 10^6 \text{ J/m}^3$ in a 6T magnetic field. Regarding the value of ΔG_v , which was calculated by CALPHAD methodology using for a nucleus of equilibrium composition ($\text{Fe}_{77}\text{Si}_{18}\text{Nb}_4\text{Cu}_1$), forming at 823 K in a matrix of composition $\text{Fe}_{73.5}\text{Si}_{13.5}\text{B}_9\text{Nb}_3\text{Cu}_1$. ΔG_v was obtained to be approximately $8.0 \times 10^8 \text{ J/m}^3$. Furthermore, $\gamma = 1.850 \text{ kJ/m}^2$ is used as the value of surface energy, which was reported for a Fe-3wt%Si alloy [33, 34]. Consequently, the critical radius of nucleus in zero-field and that in a 6T magnetic field are estimated to be 4.63 nm and 4.57 nm, respectively. Although the difference between them is found to be insufficient to predict the large changes in nucleation rate observed experimentally, it was found that the magnetic free energy would work as a driving force for nucleation of crystallization under a magnetic field.

4.4 Summary

The $\text{Fe}_{78}\text{Si}_9\text{B}_{13}$ and $\text{Fe}_{73.5}\text{Si}_{13.5}\text{B}_9\text{Nb}_3\text{Cu}_1$ amorphous alloys were crystallized by annealing at temperatures between the Curie temperature of the amorphous phase and that of crystalline α -Fe(Si) phase in a magnetic field up to 6 T. The texture formation and kinetics of crystallization under a magnetic field were discussed with a focus on the nucleation and growth of grains. The following conclusions were obtained.

- (1) The crystallization from an $\text{Fe}_{78}\text{Si}_9\text{B}_{13}$ amorphous alloy under a magnetic field at 853 K caused development of a $\{110\}$ sharp texture when a 6 T magnetic field was applied in a direction parallel to the specimen surface. The $\langle 001 \rangle$ orientation, which corresponds to the easy magnetization direction in the $\{110\}$ textured grain structure, lied randomly in the $\{110\}$ ribbon surface.
- (2) The $\{110\}$ grains preferentially grew, and the fraction of crystallized volume was increased by the application of a magnetic field of 6 T in $\text{Fe}_{78}\text{Si}_9\text{B}_{13}$ alloy.
- (3) The crystallization of $\text{Fe}_{73.5}\text{Si}_{13.5}\text{B}_9\text{Nb}_3\text{Cu}_1$ amorphous alloy under a magnetic field also enhanced a $\{110\}$ texture formation of α -Fe(Si) grains. The preferential nucleation of $\{110\}$ oriented grains due to a magnetic field may be predominantly responsible for the texture formation rather than the preferential grain growth.
- (4) The application of a magnetic field increased the nanocrystallization kinetics, particularly the nucleation rate of the ferromagnetic α -Fe(Si) grains from the paramagnetic $\text{Fe}_{73.5}\text{Si}_{13.5}\text{B}_9\text{Nb}_3\text{Cu}_1$ amorphous phase.
- (5) The volume fraction of the nanocrystalline α -Fe(Si) phase was increased with the increase in magnetic-field strength. A primary role of the magnetic field may be to enhance the kinetics of nanocrystallization rather than to modify the thermodynamics.

References

- [1] M. Michiuchi, H. Kokawa, Z. J. Wang, Y. S. Sato and K. Sakai: *Acta Mater.*, **54** (2006), 5179.
- [2] S. Tsurekawa, S. Nakamichi and T. Watanabe: *Acta Mater.*, **54** (2006), 3617.
- [3] S. Kobayashi, A. Kobylansky, T. Nagano, S. Tsurekawa and T. Watanabe: in *The 4th Intern. Conf. on Recrystallization and Related Phenomena*, (The Japan Institute of Metals, 1999), 167.
- [4] M. Letcher, G. A. Jones, D. G. Lord, M. Wun-Fogle and H. T. Savage: *J. Appl. Phys.*, **69** (1991), 5331.
- [5] Z. H. Lai, Y. S. Chao, H. Conrad and K. Chu: *J. Mater. Res.*, **10** (1995), 900.
- [6] G. Q. Teng, Y. S. Chao, Z. H. Lai and L. Dong: *Phys. Stat. Sol.*, **156** (1996), 265.
- [7] Z. H. Lai, H. Conrad, G. Q. Teng and Y. S. Chao: *Mater. Sci. Eng.*, **A287** (2000), 238.
- [8] G. A. Stergioudis, G. Vourlias, H. Morawiec, D. Stroz and E. K. Polychroniadis: *Mater. Res. Bull.*, **39** (2004), 231.
- [9] Y. Yoshizawa, S. Ogura and K. Yamauchi: *J. Appl. Phys.*, **64** (1988), 6044.
- [10] Y. Yoshizawa and K. Yamauchi: *J. Japan Inst. Metals*, **53** (1989), 241.
- [11] M. E. McHenry, M. A. Willard and D. E. Laughlin: *Prog. Mater. Sci.*, **44** (1999), 291.
- [12] G. Herzer: *IEEE Trans. Magn.*, **25** (1989), 3327.
- [13] G. Herzer: *IEEE Trans. Magn.*, **26** (1990), 1397.
- [14] G. Herzer: *Physica Scripta*, **T49** (1993), 307.
- [15] K. Hono, D. H. Ping, M. Ohnuma and H. Onodera: *Acta Mater.*, **47** (1999), 997.
- [16] S. U. Kim, K. H. Kim and Y. M. Koo: *J. Alloys Comp.*, **368** (2004), 357.
- [17] G. Herzer: *J. Magn. Magn. Mater.*, **294** (2005), 99.
- [18] P. Häußler and F. Baumann: *Z. Physik B*, **38** (1980), 43.
- [19] Y. Wolfus, Y. Yeshurun, I. Felner and J. Wolny: *Phil. Mag. B*, **56** (1987), 963.
- [20] Y. Otani, H. Sun, J. M. D. Coey, H. A. Davis, A. Manaf and R. A. Buckley: *J. Appl. Phys.*, **67** (1990), 4616.
- [21] X. Wang, M. Qi and S. Yi: *Scripta Mater.*, **51** (2004), 1047.
- [22] M. Baricco, C. Antonione, P. Allia, P. Tiberto and F. Viani: *Mater. Sci. Eng.*, **A179-180** (1994), 572.
- [23] K. S. Willson and J. A. Rogers: *Tech. Proc. Amer. Electroplat. Soc.*, **51** (1964), 92.
- [24] D. B. Williams and C. B. Carter: *Transmission Electron Microscopy – Spectrometry IV*, Plenum Press, New York (1996).
- [25] J. K. Choi, H. Ohtsuka, Y. Xu and W. Y. Choo: *Scripta Mater.*, **43** (2000), 221.
- [26] S. Chikazumi: *Physics of Magnetism*, Wiley, New York (1964).
- [27] F. van Bouwelen, J. Sietsma, C. D. de Haan and A. van den Beukel: *Appl. Phys. Lett.*, **61** (1992), 2536.
- [28] P. Allia, M. Baricco, P. Tiberto and F. Viani: *J. Appl. Phys.*, **74** (1993), 3137.

Chapter 4

- [29] Y. Takahara: *J. Japan Inst. Metals*, **63** (1999), 367.
- [30] V. A. Yardley, S. Tsurekawa, H. Fujii and T. Matsuzaki: *Mater. Trans.*, **48** (2007), 2826.
- [31] W. A. Anderson and R. F. Mehl: *Trans. AIME*, **161** (1945), 140.
- [32] H. Okumura, D. E. Laughlin and M. E. McHenry: *J. Magn. Magn. Mater.*, **267** (2003), 347.
- [33] E. D. Hondros: *Techniques of Metals Research*, R. Bunshah (ed.), Vol.IV(A), John Wiley & Sons, New York (1970).
- [34] E. D. Hondros and L. E. H. Stuart: *Phil. Mag.*, **17** (1968), 711.

Chapter 5

Effect of a magnetic field on grain boundary energy

5.1 Introduction

Grain boundaries play important roles as preferential sites in most metallurgical phenomena and generally exist in any kind of material. Their energy governs intergranular fracture in intrinsically brittle materials like molybdenum [1], and also acts as a driving force for grain growth [2], for example. Therefore the bulk properties of materials also significantly depend on their grain boundary characters and distributions [3]. From the experimental and theoretical studies so far, grain boundary energy has been found to depend considerably on the misorientation between two adjoining grains and on inclination of the grain boundary plane [4-13]. In addition, grain boundary energy varies significantly with solute or impurity segregation to grain boundaries [14, 15]. Hondros derived theoretically a relation between grain boundary energy and the amount of solute or impurity segregation by applying the Gibbs adsorption theorem, and experimentally evidenced that grain boundary energy decreases with increasing in grain boundary segregation [16].

Recently, processing by the application of strong magnetic fields has been suggested as a promising strategy for precisely controlling microstructures of materials, because a magnetic field can affect many metallurgical phenomena as described in the previous chapters. There have been some reports focused on the effect of a magnetic field on grain boundary energy [17-19]. Watanabe *et al.* reported that a magnetic field affected grain boundary character distribution (GBCD), particularly the frequency of low angle boundaries in Fe-9at%Co alloy [17]. They found that the frequency of low-angle boundaries increases with increase in the magnetic field strength. Zhang *et al.* investigated the change in the fraction of special boundaries, which are known to have much lower energy than that of general boundaries, in ferrite under a magnetic field [18]. They found that the magnetic field increased the fraction of special boundaries. Tsurekawa *et al.* have found that grain boundary energy in an Fe-0.8at%Sn alloy increases [19], and that tin segregation to grain boundaries suppresses by application of a magnetic field. They considered that this increase in grain boundary energy may be due to a decrease in grain boundary segregation of tin. However, the

origin of the increase in grain boundary energy in the Fe-Sn alloy by magnetic annealing is still unclear, that is, whether it is an extrinsic effect resulting from a decrease in tin segregation to grain boundaries, or an intrinsic effect of the magnetic field on grain boundary energy. Furthermore, the effect of a magnetic field on the misorientation dependence of grain boundary energy has not yet been understood. In addition, because the magnetic transformation at the Curie temperature exerts an influence on some properties of materials such as diffusion [20], it is expected that the magnetic field effect on grain boundary energy changes with magnetic transformation. To the author's knowledge, temperature dependence of grain boundary energy in α -iron has not been reported so far. These are motivations of this study concerning the effect of a magnetic field on grain boundary energy in pure iron.

In this chapter, the grain boundary energy, which closely relates to the nucleation and growth of grains, was investigated under a strong magnetic field. The effect of a magnetic field on the grain boundary energy was studied as functions of temperature and misorientation.

5.2 Experimental

5.2.1 Material and specimen

The material used in this study was commercially available pure iron (99.9 %). From ICP qualitative analyses, the 99.9 % iron was found to include C (5 ppm), S (<3 ppm), N (28 ppm), O (456 ppm), P (<3 ppm), Si (39 ppm), Mn (63 ppm) and Cu (11 ppm) as impurities. The chemical composition of the specimen is shown in Table 5-1. An ingot of the pure iron was cross-rolled into a sheet of 0.7 mm in thickness (rolling rate = 86.5 %). Specimens with 13 mm \times 7 mm \times 0.7 mm in dimensions were cut using a diamond cutter, and then mechanically polished, buff-finishing to a mirror surface with 0.3 μm Al_2O_3 suspension. Thereafter the specimens were recrystallized at 1163 K for 86.4 ks under a vacuum of 0.7 mPa, and polished again in the same way as mentioned above to remove any grooves on the surfaces. The average grain size of the recrystallized specimen reached approximately 580 μm . A thermal grooving method was applied to determine the grain boundary energies relative to surface energies, so the specimens were annealed at temperatures between 973 K in the ferromagnetic state and 1123 K in the paramagnetic state without and with a 6 T magnetic field under a vacuum of 0.52 - 1.0 mPa using the superconducting magnetic field heat

Table 5-1 Chemical composition of 99.9% Fe specimen in this study.

Component	C	S	N	O	P	Si	Mn	Cu
ppm	5	<3	28	456	<3	39	63	11

Table 5-2 Annealing conditions for thermal grooving of grain boundaries.

Temperature, T / K	Time, t / ks	Magnetic field, H / T	Number of GB	Number of GB profile
973	10.8	0	19	228
	32.4	6	50	1076
	97.2			
998	32.4	0	15	180
		6	14	168
1023	10.8	0	48	576
	32.4	6	34	408
	97.2			
1073	32.4	0	35	420
		6	39	468
1123	10.8	0	16	192
		6	16	192

treatment system, as shown in Table 5-2.

5.2.2 Determination of grain boundary character

Individual grain boundaries have inherent mechanical and functional properties according to their character and structure [1, 3]. Therefore, it is essential to determine the character of individual grain boundaries before grain boundary properties are examined. The character of the grain boundaries was determined using an automated FE-SEM/EBSD/OIM technique as illustrated in the chapter 4. The OIM observations were conducted at 20kV accelerating voltage, 10 μ A emission current, 15mm working distance and 10 - 15 μ m beam step size. The Euler angle according to Bunge's definition was used for the OIM analysis in this study. Fig. 5-1 shows the schematic illustration of Bunge's Euler angles. A certain grain orientation can be described by the three rotational manipulations. At first, the crystallographic coordinate system is rotated about the Z-axis by ϕ_l . The obtained new coordinate system is defined as (X', Y', Z') system. The next, this coordinate system is

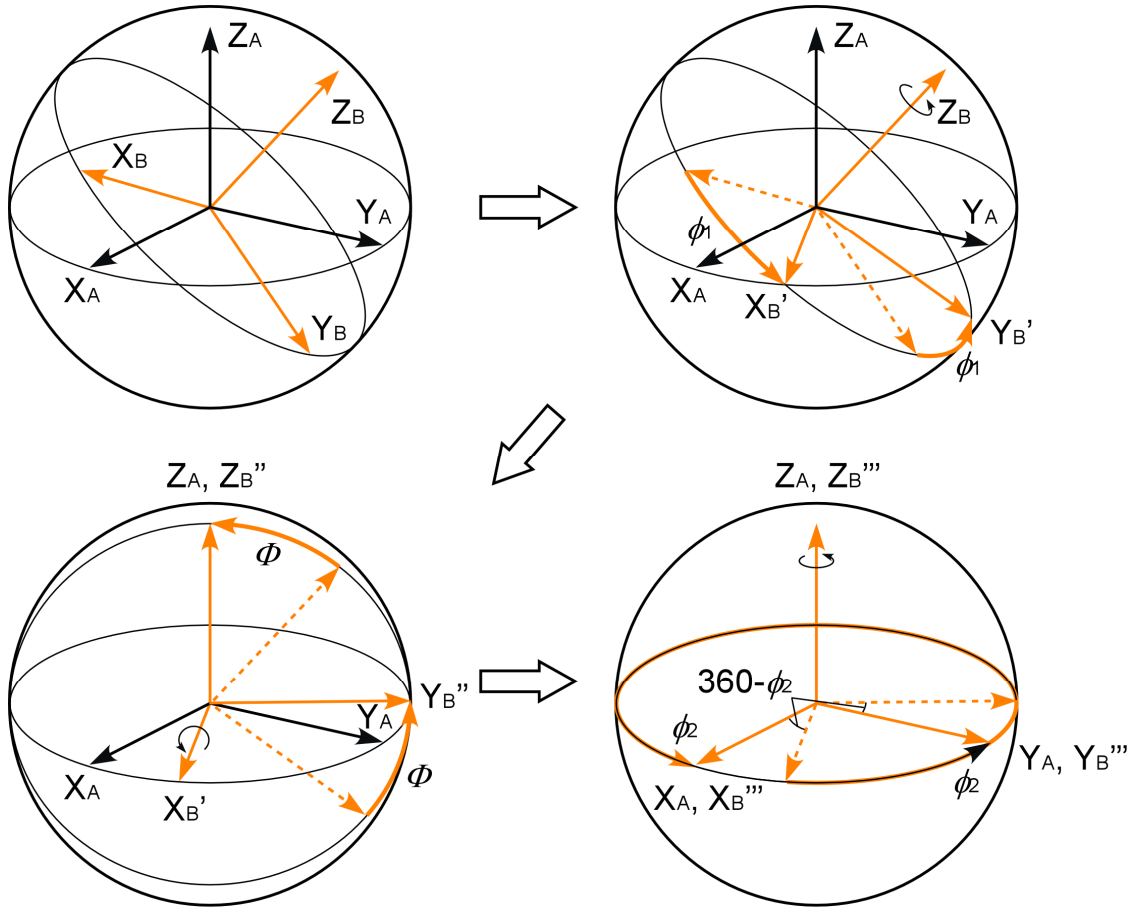


Figure 5-1 Schematic illustration of the definition of Bunge's Euler angles.

rotated about X' -axis by Φ to make the Z' -axis correspond to Z -axis of standard coordinate system. Lastly, the crystallographic coordinate system is rotated about Z' -axis by ϕ_2 . The grain orientations can be described by these rotation angles (ϕ_1 , Φ , ϕ_2) (Euler angle) in the three rotational manipulations.

In general, the grain boundaries are classified according to their crystallographic relative orientations relationship, that is called “misorientation”, between two adjoining grains. The misorientation angle between two adjoining grains across a grain boundary is calculated from the rotational matrices obtained from Euler angle of each grain. The grain boundaries with misorientation angle less than 15° is defined as low-angle boundaries. On the other hand, the grain boundaries with misorientation angle more than 15° is defined as high angle boundaries. The high angle boundaries are further classified into the random boundaries and

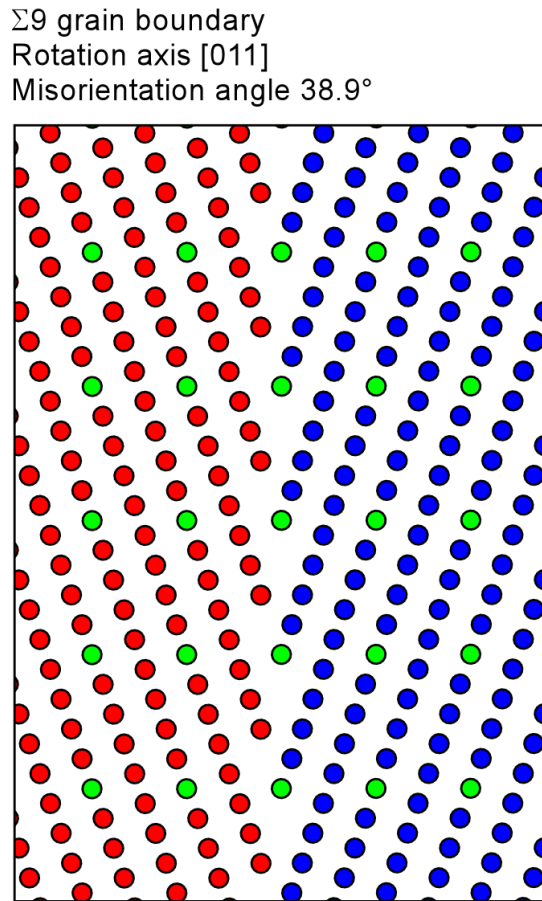


Figure 5-2 Schematic illustration of $<110>\Sigma 9$ symmetric tilt coincidenc-site-lattice (CSL) boundaries.

the coincidence site lattice (CSL) boundaries. The random boundaries have no periodic structure between two adjoining grains, so that they are high energy boundaries. However, when a high angle boundary has a certain geometrical relation (misorientation angle and common rotation axis), a periodical structure appears on the grain boundary.. These boundaries are called CSL boundaries. In the CSL theory, the degree of coincidence between two lattice is described by “ Σ value”, which is defined by the volume ratio of unit cells of a coincidence site lattice to a crystal lattice. For example, Fig. 5-2 shows the schematic illustration of $\Sigma 9$ boundary with the misorientation angle of 38.9° about a common rotation axis of $<110>$. The nine atoms are included in a unit cell of CSL, so that this orientation

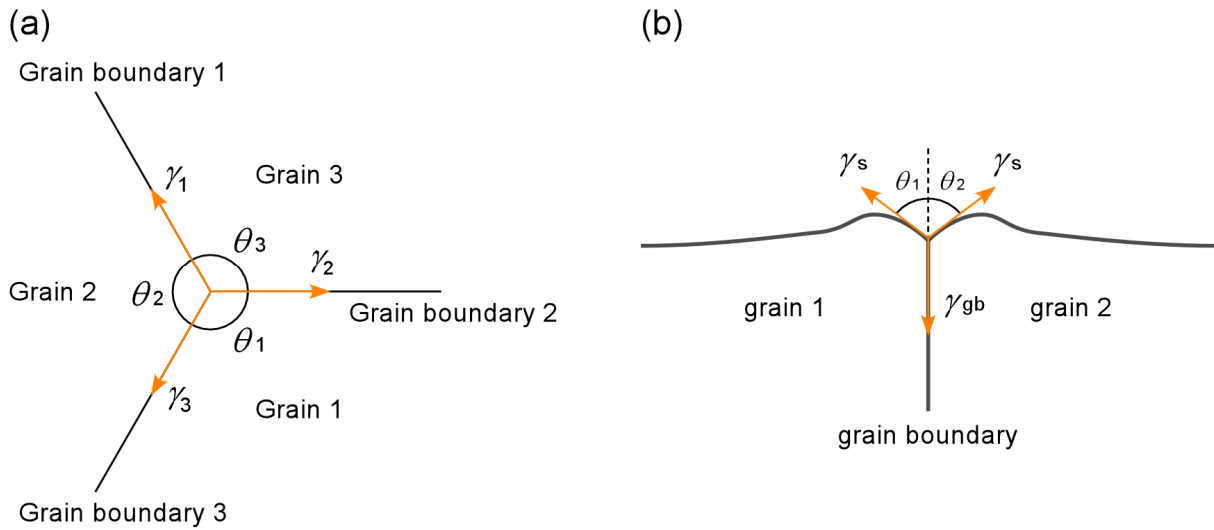


Figure 5-3 Schematic illustration for (a) equilibrium between tensions at grain boundary triple junction and (b) equilibrium between tensions at grain boundary grooving.

relation is defined as Σ relation. Such low Σ boundaries often possess special mechanical and functional properties. As the Σ value increases, special properties of CSL boundaries will disappear, though the value of Σ can be taken mathematically as large as infinite number. Although there is no strict definition, it was suggested that the maximum value where the grain boundaries can possess special properties should be approximately $\Sigma=29$ on the basis of experimental observations of grain boundary corrosion and the intergranular fracture [21].

5.2.3 Measurement of grain boundary energy

The interface energy including grain boundary energy is generally considered as a surface tension. Fig. 5-3 (a) shows the equilibrium of three forces at the grain boundary triple junction. This can be applied to the relationship between the grain boundary and surface energies. When a specimen with a mirror surface is annealed at specific temperature, the grain boundary is grooved on the specimen surface according to a force balance as shown in Fig. 5-3 (b). Accordingly, grain boundary energy can be estimated by measuring the geometrical profile of the grain boundary groove. Atomic force microscopy (AFM) was applied to

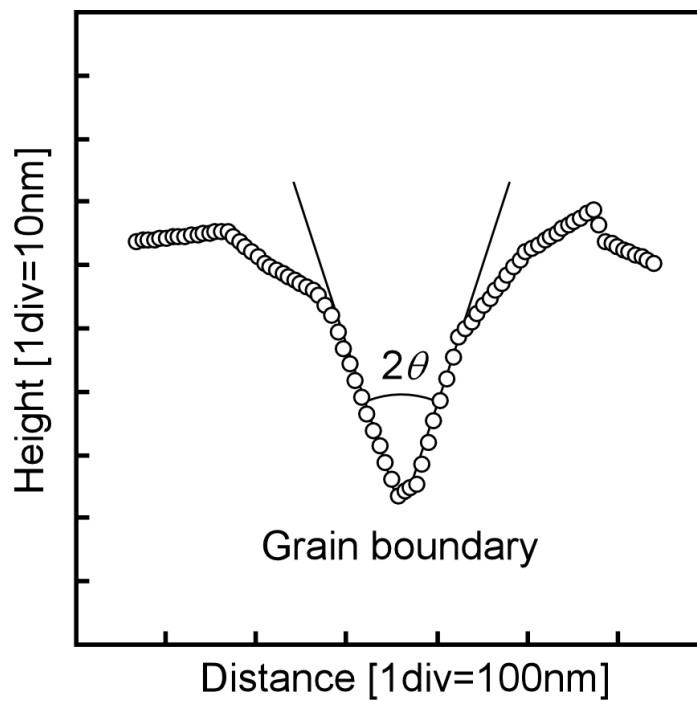


Figure 5-4 Definition of grain boundary dihedral angle.

measure the cross-sectional profiles of grain boundary grooves. The measurements were performed using a SHIMADZU SPM-9500 with scanning rates of 0.1 - 0.7 Hz, number of pixels of 256×256 , Z-range of 1 - 4 and a scanning range of $15 \mu\text{m} \times 15 \mu\text{m}$. Fig. 5-4 shows an example of the cross-sectional profile obtained. From the dihedral angle 2θ obtained, the grain boundary energy was evaluated using the equation:

$$\gamma_{gb} = 2\gamma_s \cos \theta \quad (5-1)$$

where γ_{gb} and γ_s are the energies of the grain boundary and the surface, respectively. The dihedral angles were measured at 12 - 40 different positions along each grain boundary on 19 - 50 different boundaries. Strictly speaking, the surface energy depends on surface orientation. Nevertheless, the surface energy was assumed to be isotropic in the present study because little reliable information is available from experiments about the orientation-dependence of surface energy. The AFM measurements were carried out on well-characterized grain boundaries by EBSD/OIM analysis, and the grain boundary energies were statistically analyzed as shown in Table 5-2.

5.3 Results and discussion

5.3.1 Measurement of the cross-sectional profiles of grain boundary grooves

The cross-sectional profiles of grain boundary grooves were measured by AFM to estimate the grain boundary energy under non-magnetic conditions and a magnetic field. Fig. 5-5 shows the grain boundary character distribution (GBCD) map of the specimen annealed at 1023 K for 97.2 ks without and with a 6 T magnetic field after recrystallization at 1163 K. The arrows in this map indicate the grain boundary analyzed by AFM. The grain boundaries were characterized by the coincidence site lattice (CSL) theory [22] before AFM measurement. The cross-sectional profiles of grooves of grain boundary with different characters were measured by AFM. Fig. 5-6 shows the cross-sectional profiles and two-dimensional images of grain boundary grooves obtained by AFM measurements. The dihedral angles of grain boundary grooves were measured from the cross-sectional profiles, and the grain boundary energies normalized by the surface energy (γ_{gb}/γ_s) were evaluated using the eqn. (5-1).

5.3.2 Temperature dependence of grain boundary energy in iron

Using eqn. (5-1), the relative grain boundary energies were evaluated from the cross-sectional profiles of grain boundary grooves formed at different temperatures between 973 K and 1123 K. Fig. 5-7 shows the grain boundary energies in the 99.9%Fe as a function of temperature. The circles give the average values of energies for any types of grain boundaries, the triangles for CSL boundaries and the squares for random boundaries, and N_s indicates the total number of cross-sections of grain boundaries analyzed. Fig. 5-7 reveals that the grain boundary energy in the 99.9% Fe tends to increase with the increase in temperature without a magnetic field. Generally speaking, grain boundary energy in pure metals shows a “negative” temperature-dependence according to

$$\left(\frac{d\gamma}{dT} \right)_{V,P} = -S_I, \quad (5-2)$$

where S_I is the interfacial entropy [8]. On the other hand, grain boundary energy in metals with alloying elements and / or impurities sometimes shows a “positive” temperature dependence due to solute / impurity segregation to grain boundaries [23]. Let us consider the positive temperature dependence of grain boundary energy from the point of view of

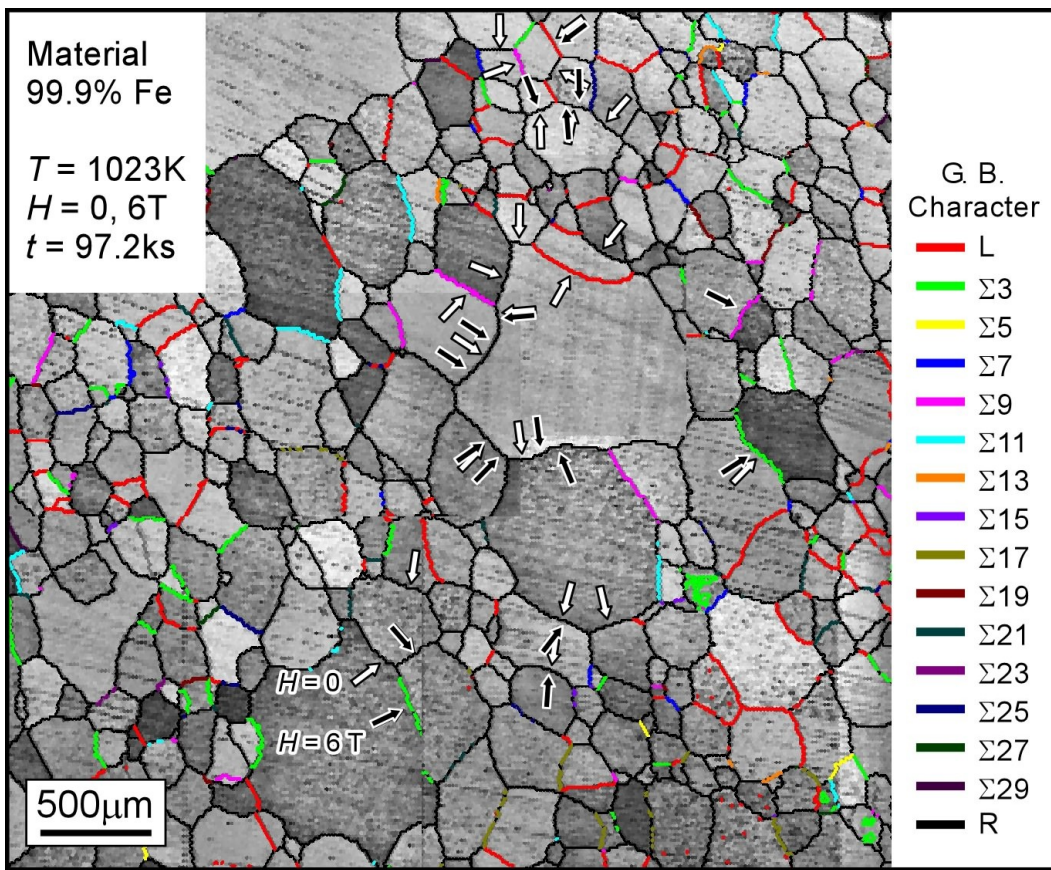


Figure 5-5 Grain boundary character distribution map of pure Fe annealed at 1023K (below Curie temperature) for 97.2ks (a) without and (b) with a 6T magnetic field.

thermodynamics.

From the Gibbs - Duhem equation,

$$SdT - VdP + \sum n_i d\mu_i + Ad\gamma = 0, \quad (5-3)$$

where S is the entropy, V is the volume, T is the absolute temperature, P is the pressure, μ_i are the chemical potentials of individual components, n_i are their corresponding moles in the closed system, A is a grain boundary area and γ is grain boundary energy. Under a constant pressure, the temperature dependence of grain boundary energy is given by,

$$A \frac{d\gamma}{dT} = -S - \sum x_i \left(\frac{d\mu_i^0}{dT} + R \ln x_i \right), \quad (5-4)$$

where μ_i^0 and x_i are the standard potential and the molar fraction of element i , respectively,

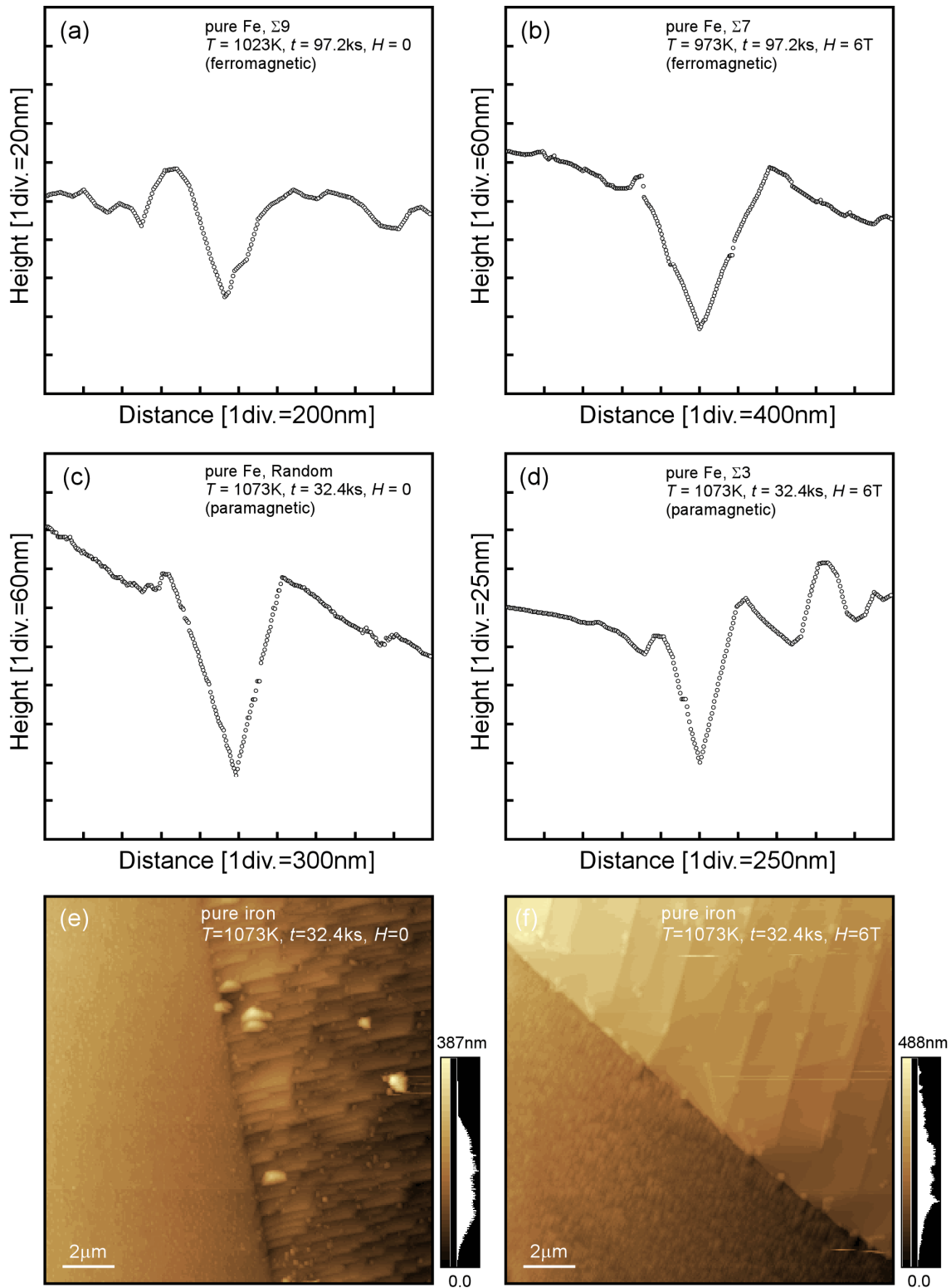


Figure 5-6 Cross-sectional profiles of grain boundary grooves and two dimensional AFM images obtained from 99.9% iron annealed at 973K, 1023K and 1073K without and with a 6T magnetic field.

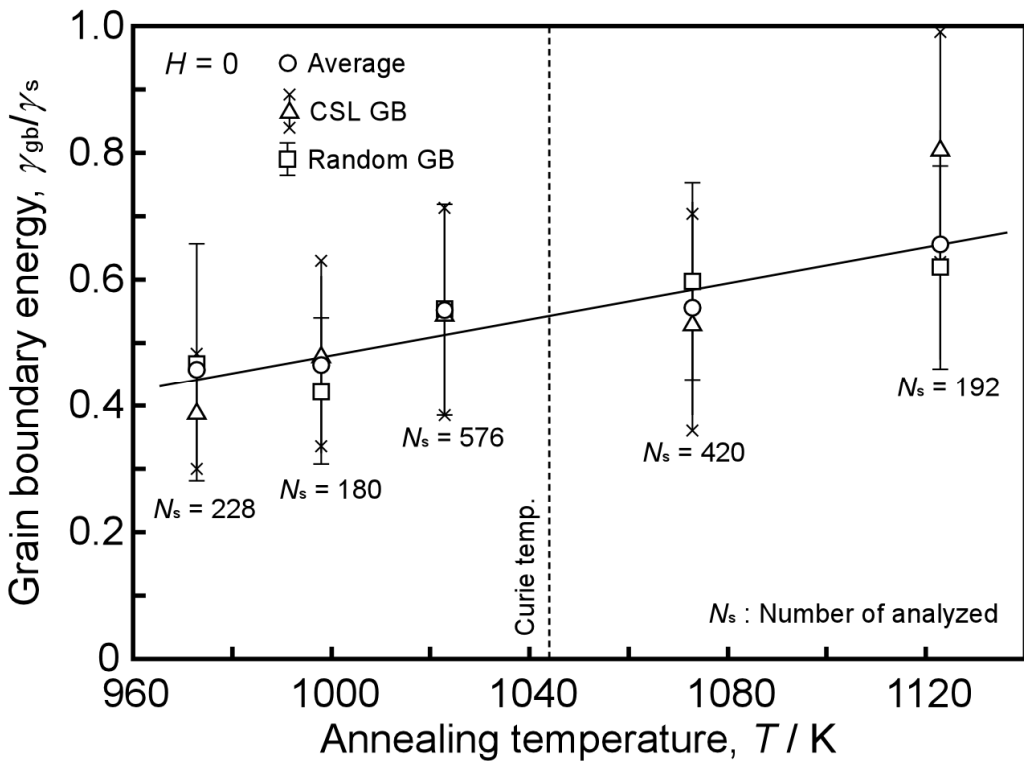


Figure 5-7 Temperature dependence of grain boundary energy in 99.9% Fe.

and R is the gas constant. Assuming that,,

$$\sum x_i \frac{d\mu_i^0}{dT} \ll S, \quad (5-5)$$

eqn. (5-4) can be expressed by,

$$\frac{d\gamma}{dT} = -S_I - \frac{R}{A} \sum x_i \ln x_i, \quad (5-6)$$

where \$S_I = S/A\$. Thus, \$d\gamma/dT\$ would be positive, if

$$S_I < -\frac{R}{A} \sum x_i \ln x_i. \quad (5-7)$$

Unfortunately, there is little reliable information about the interfacial entropy for pure \$\alpha\$-iron. The average interfacial entropy for pure metals was known to be approximately -2.02 J/mol·K [8]. The positive temperature dependence of grain boundary energy observed in 99.9 % Fe may be attributable to impurity segregation even though the amount of impurities (Si, Mn and Cu) was very small. When the right hand side in eqn. (5-7) was calculated with taking into

account of interstitial impurities (C, N and P), the value was approximately -1.79 J/mol·K. Here Mn, S and O atoms which form compounds with Fe were ignored in the calculation. Thus, the eqn. (5-7) was sufficient in 99.9% Fe used in this study, so that the grain boundary energy shows a positive temperature dependence.

5.3.3 Effect of a magnetic field on temperature dependence of grain boundary energy in iron

The effect of a 6 T magnetic field on the grain boundary energy was investigated by the same procedure of the measurement under non-magnetic conditions. Contrary to the results under non-magnetic conditions, the temperature dependence of grain boundary energy became “negative” under a 6 T magnetic field as shown in Fig. 5-8. Tsurekawa *et al.* found that a magnetic field suppressed tin segregation to grain boundaries in Fe-Sn alloys [19]. Accordingly, Fig. 5-8 is likely to reveal intrinsic nature of temperature-dependent grain boundary energy in 99.9%Fe under a magnetic field without any influence of impurities. Because the grain boundary energy measured seems to change more systematically with temperature for random boundaries than that for CSL boundaries, we evaluated the temperature coefficients of the relative energies of random boundaries, γ_{gb}/γ_s to be $1.2 \times 10^{-3} / K$ and $-3 \times 10^{-3} / K$ under non-magnetic conditions and a 6 T magnetic field, respectively. For calculation of the temperature coefficients of grain boundary energy, it is necessary to know the surface energy of α -iron. However, there were no reliable data about surface energy of α -iron, so that the surface energies at different temperatures were estimated by extrapolating temperature-dependent surface energy of δ -iron with bcc structure ($\gamma_s = 1950 - 0.9(T - 1723) \text{ mJ/m}^2$) [8]. If the values extrapolated as surface energy is used, the temperature coefficients for grain boundary energies could be estimated to be $2.7 \text{ mJ/m}^2 \cdot K$ and $-1.2 \text{ mJ/m}^2 \cdot K$ under non-magnetic conditions and a 6 T magnetic field, respectively.

In addition, Fig. 5-8 reveals that the magnetic transformation can affect the temperature dependence of grain boundary energy: the grain boundary energy increased non-linearly with increasing temperature around the Curie temperature under a 6 T magnetic field. This non-linearity of grain boundary energy observed may be explained by the difference between energetic contribution from the applied magnetic field to Gibbs free energy in the ferromagnetic state and that in the paramagnetic state. The magnetic free energy per unit volume for ferromagnetic materials is given by,

$$M^f = -\mu_0 \left(H - \frac{NM_s}{2} \right) M_s, \quad (5-8)$$

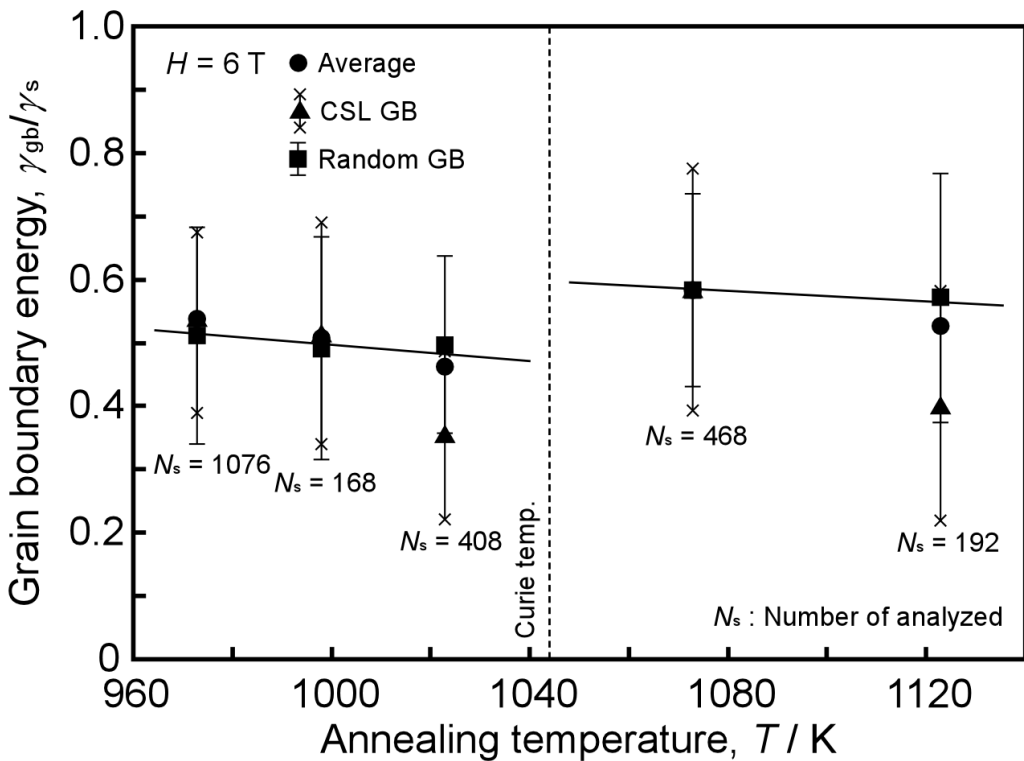


Figure 5-8 Temperature dependence of grain boundary energy in 99.9 % Fe under a 6 T magnetic field.

when $H \gg H_c$, where μ_0 is permeability in vacuum, N is the demagnetizing factor, M_s is the saturation magnetization and H_c is the critical magnetic field strength to achieve the saturation magnetization. On the other hand, that of paramagnetic materials is given by,

$$M^p = -\frac{1}{2} \mu_0 \chi (1 - \chi N) H^2, \quad (5-9)$$

where χ is the magnetic susceptibility. In this experiment, a magnetic field was applied parallel to the long axis of the specimens, so that the demagnetizing factor is assumed to be zero. The saturation magnetization of the pure iron is known to be $\mu_0 M_s = 2.15$ T ($= \text{kg}/\text{s}^2\text{A}$) [24]. From eqn. (5-8), the magnetic free energy under a 6 T ($= 4.77 \times 10^3$ kA/m) magnetic field is estimated to be $M^f = 1.03 \times 10^7$ J/m³. On the other hand, that of paramagnetic α phase, M^p , does not significantly change even under a strong magnetic field because the magnetic susceptibility, χ , of paramagnetic α iron is extremely small (2.1×10^{-4} [25]). Thus, the

non-linearity of grain boundary energy observed would be related to changes in magnetic free energy involved in magnetic transformation. The difference between magnetic free energy in ferromagnetic state and that in paramagnetic state is estimated to be approximately 1×10^7 J/m³. On the other hand, the energy difference at the Curie temperature, obtained by extrapolating temperature dependence of grain boundary energies in the ferromagnetic state and the paramagnetic state to the Curie temperature, is approximately 0.27 J/m². Since the recent theoretical calculations suggested that the local magnetic moment of iron atoms increases in approximately 4 - 5 layers near (310)Σ5 grain boundary [26, 27], if the grain boundary width is assumed to be 1 nm, the difference in grain boundary free energy is estimated to be 2.7×10^8 J/m³. This estimated value is approximately one order larger than that expected from the magnetic free energy change mentioned above. However, the estimated value can significantly change depending on the grain boundary width. Fitzsimmons *et al.*, who evaluated the magnetic moment near grain boundary in nickel using neutron scattering, found an increase in the magnetic moment near the grain boundary within approximately 10nm [28]. This is a controversial problem about the grain boundary width associated with magnetism.

By the way, the saturation magnetization considerably decreases near the Curie temperature and becomes zero at the Curie temperature under a non-magnetic field. However, an external magnetic field can induce magnetization even beyond the Curie temperature. The saturation magnetization was estimated at the Curie temperature under a 6T magnetic field to be 0.6 T (=kg/s²A) by applying the molecular field theory [29]. Under a magnetic field, the Gibbs - Duhem equation can be given by,

$$SdT - V(dP + dM) + \sum n_i d\mu_i + Ad\gamma = 0, \quad (5-10)$$

and then

$$\frac{d\gamma}{dT} = -S_1 + \frac{V}{A} \frac{dM}{dT} - \frac{R}{A} \sum x_i \ln x_i. \quad (5-11)$$

Combining eqn. (5-11) with eqn. (5-8) with $N = 0$, following equation can be obtained:

$$\frac{d\gamma}{dT} = -S_1 - \frac{V}{A} H\mu_0 \frac{dM_s}{dT} - \frac{R}{A} \sum x_i \ln x_i. \quad (5-12)$$

Therefore, if the third term is ignored in right-hand side of eqn. (5-12); *that is*, considering the specimen as pure iron, the grain boundary energy under a magnetic field will change with temperature near the Curie temperature as schematically shown in Fig. 5-9.

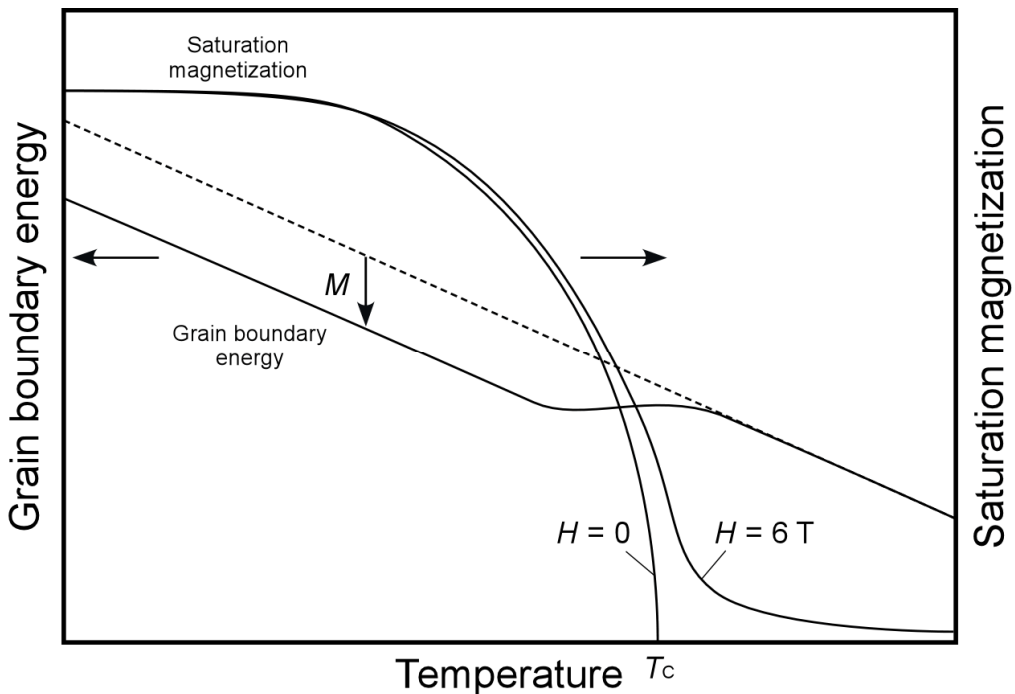


Figure 5-9 Schematic explanation of temperature dependence of grain boundary energy under a magnetic field. For comparison, changes in saturation magnetization with temperature are shown in the figure.

5.3.4 Effect of a magnetic field on misorientation dependence of grain boundary energy

Grain boundary energies generally depend on misorientation angle (grain boundary character). A large variety of the data at each temperature in Fig. 5-7 and 5-8 could result from this dependence of misorientation angle. The effect of a magnetic field on the misorientation dependence of the grain boundary energy was investigated. Fig. 5-10 shows the grain boundary energies at 973 K in the ferromagnetic state and at 1073 K in the paramagnetic state under (a) non magnetic conditions and (b) a 6 T magnetic field, as a function of the misorientation angle determined by OIM software. Although the grain boundary energies seem to show a maximum around 40 degree in misorientation, it is difficult to find any significant relationships between the grain boundary energy and misorientation angle irrespective of whether a magnetic field being applied. This is probably because the rotation axis for each grain boundary was not distinguished in Fig.5-10. The OIM software

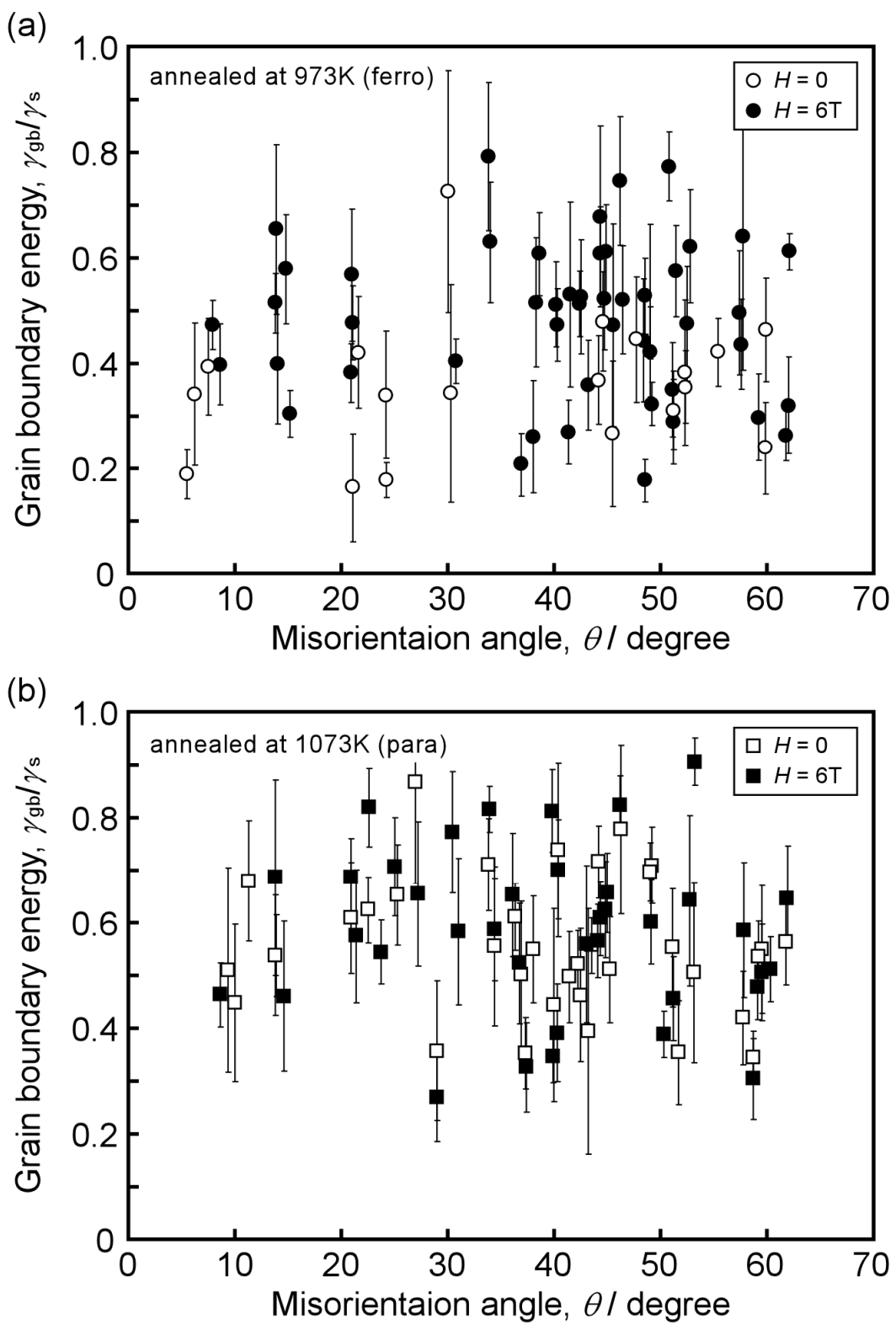


Figure 5-10 Grain boundary energy vs the minimum rotation angle as misorientation for 99.9 % Fe under non-magnetic and 6 T magnetic fields (a) at 973 K and (b) 1073 K.

only dictates the minimum angle as a misorientation from the 24 equivalent variants of angle / rotation axis pairs. Accordingly, the 24 angle/axis pairs of each grain boundary were assessed, and the boundaries with respect to $<100>$, $<110>$ and $<111>$ rotation axis were examined. Here, the tolerance of rotation axes from the exact direction interested was defined as 5 degree. Since the number of boundaries having either $<100>$ or $<110>$ were not enough, the misorientation dependence of grain boundary energy about $<111>$ rotation axis will be shown in Fig. 5-11. Fig. 5-11 (a) and (b) are the results under non-field and a 6 T magnetic field, respectively. It is found that the energy cusps occur at $\Sigma 3$, $\Sigma 7$ and $\Sigma 13$ CSL boundaries, irrespective of whether a magnetic field being applied. Furthermore these energy cusps appear more significantly when a magnetic field was applied. Sautter *et al.* have suggested that impurity segregation at grain boundaries reduces the energy of high energy boundaries more than the energy of low energy boundaries, so that energy of low and high energy boundaries is equalized with the increase in impurity segregation and eventually the energy cusps at special boundaries will disappear [15]. In addition, Tsurekawa *et al.* found that the grain boundary segregation of tin was suppressed by the application of a magnetic field [19]. These previous reports give us an insight to explain the results shown in Fig. 5-11. As the result of suppression of grain boundary segregation of impurities of Si, Mn, Cu in the 99.9% Fe by application of a magnetic field, the energy cusps at CSL boundaries may appear more observably due to the increase in grain boundary energies at random boundaries. This is because the effect of grain boundary segregation on grain boundary energy is more significant for random boundaries than that for CSL boundaries. An increase in the misorientation dependence of grain boundary energy due to a magnetic field was also reported for an Fe-0.8at%Sn alloy [30].

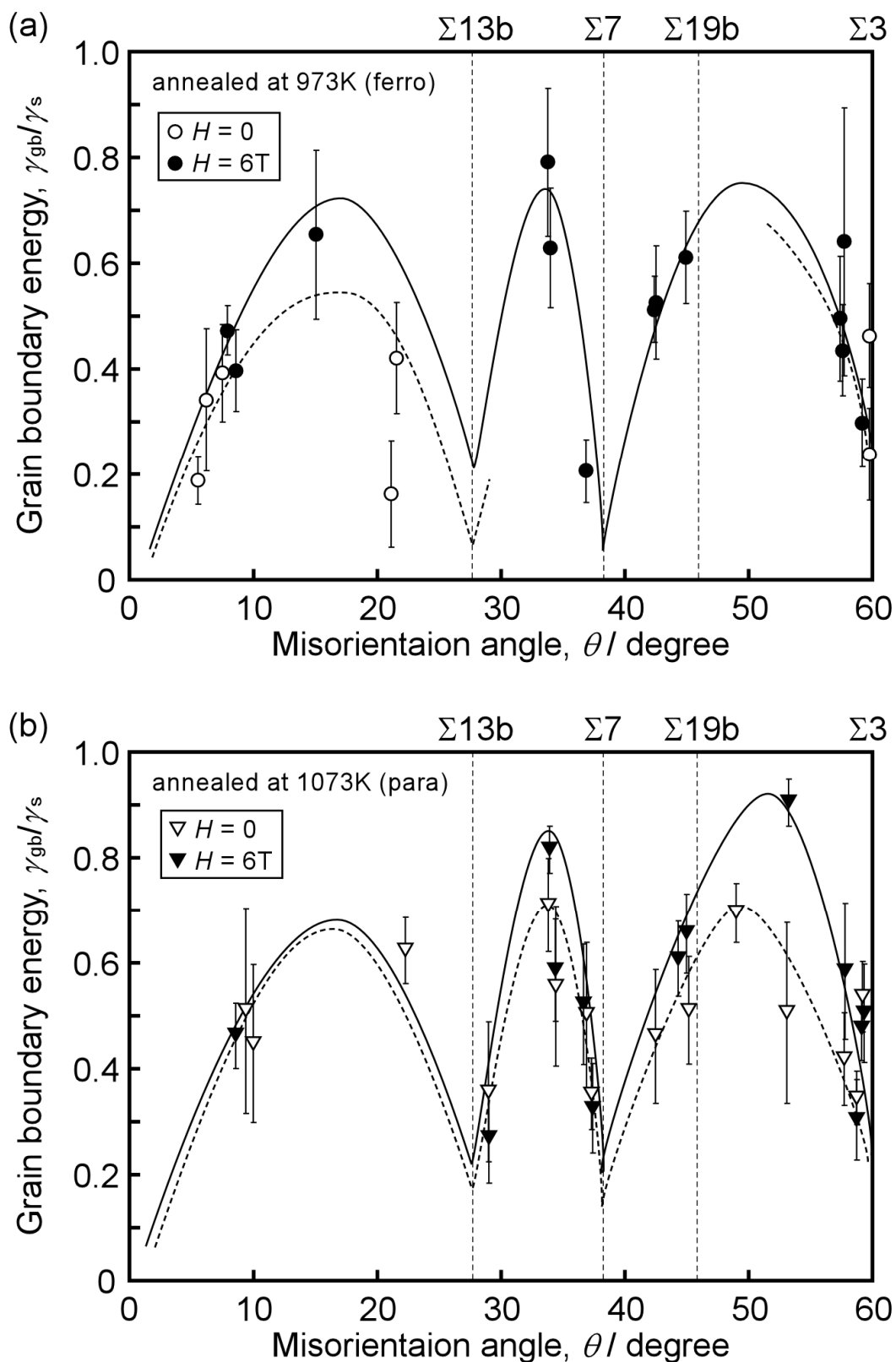


Figure 5-11 Grain boundary energy vs misorientation angle around $<111>$ rotation axis for 99.9 % Fe under non-magnetic and 6 T magnetic fields (a) at 973 K and (b) 1073 K.

5.4 Summary

In this chapter, the effect of a strong magnetic field on the grain boundary energy in 99.9% iron was experimentally studied. The following conclusions were obtained.

- (1) Grain boundary energy in the 99.9 % Fe increased with the increase in temperature under non magnetic field. On the other hand, the energy decreased under a 6 T magnetic field, and the energy changed non-linearity around the Curie temperature due to the difference between energetic contribution of the magnetic field to Gibbs free energy in ferromagnetic state and that in paramagnetic state.
- (2) The non-linearity of grain boundary energy around Curie temperature under a magnetic field might be due to the difference between energetic contribution of the magnetic field to Gibbs free energy in ferromagnetic state and that in paramagnetic state.
- (3) There were not any significant relationships between the grain boundary energy and misorientation angle irrespective of whether a magnetic field being applied. When the misorientation angle for each grain boundary was examined around the <111> rotation axis, the misorientation dependence on grain boundary energy was clearly confirmed.
- (4) Grain boundary energy increased and its misorientation dependence was enhanced under a magnetic field in the 99.9 % Fe. This is due to suppression of solute and impurities segregation to grain boundaries by a magnetic field.

References

- [1] S. Kobayashi, S. Tsurekawa and T. Watanabe: *Acta Mater.*, **53** (2005), 1051.
- [2] G. Gottstein and L. S. Shvindlerman: *Grain Boundary Migration in Metals - Thermodynamics, Kinetics, Applications*, CRC Press (1999).
- [3] T. Watanabe: *Res Mechanica*, **11** (1984), 47.
- [4] C. G. Dunn and F. Lionetti: *Met. Trans.*, (1949), 125.
- [5] W. T. Read and W. Shockley: *Phys. Rev.*, **78** (1950), 275.
- [6] H. Gleiter and B. Chalmaers: *High-Angle Grain Boundaries*, Pergamon Press (1972).
- [7] G. C. Hasson and C. Goux: *Scripta Metall.*, **5** (1971), 889.
- [8] L. E. Murr: *Interfacial Phenomena in Metals and Alloys*, Addison-Wesley Pub.Comp (1975).
- [9] A. Otsuki, H. Isono and M. Mizuno : *J. de Physique, Colloque C5*, **49** (1988), C5-563.
- [10] D. Wolf: *Phil. Mag. A.*, **62** (1990), 447.
- [11] H. Nakashima and M. Takeuchi: *Tetsu-to-Hagane*, **86** (2000), 357. (in Japanese)
- [12] A. Otsuki: *Interface Sci.*, **9** (2001), 293.
- [13] Y. Amouyal, E. Rabkin and Y. Mishin: *Acta Mater.*, **53** (2005), 3795.
- [14] M. P. Seah and C. Lea: *Phil. Mag.*, **31** (1975), 627.
- [15] H. Sautter, H. Gleiter and G. Baro: *Acta Metall.*, **25** (1977), 467.
- [16] E. D. Hondros: *Proc. Roy. Soc., A***286** (1965), 479.
- [17] T. Watanabe, Y. Suzuki, S. Tanii and H. Oikawa: *Phil. Mag. Lett.*, **62** (1990), 9.
- [18] Y. D. Zhang, C. Esling, J. S. Lecomte, C. S. He, X. Zhao and L. Zuo: *Acta Mater.*, **53** (2005), 5213.
- [19] S. Tsurekawa, K. Okamoto, K. Kawahara and T. Watanabe: *J. Mater. Sci.*, **40** (2005), 895.
- [20] Y. Iijima, K. Kimura and K. Hirano: *Acta Metall.*, **36** (1988), 2811.
- [21] T. Watanabe: *J. Physique*, **46** (1985), 555.
- [22] M. L. Kronberg and F. H. Wilson: *Metals Trans.*, **185** (1949), 501.
- [23] D. Gupta: *Interface Sci.*, **11** (2003), 7.
- [24] K. Honda and S. Kaya: *Sci. Rep. Tohoku Imp. Univ.*, **15** (1926), 721.
- [25] W. Sucksmith and R. R. Pearce: *Proc. Roy. Soc. Lond.*, A**167** (1938), 189.
- [26] M. Söb, I. Turek, L. Wang and V. Vitek: *Proc. 10th Int. Metallur. Mater. Conf. METAL2001*, (2001), 1 (CD-ROM).
- [27] K. Hamble, D. D. Vvedensky and S. Crampin: *Phys. Rev. B*, **47** (1993), 4810.
- [28] M. R. Fitzsimmons, A. Roll, E. Burkhardt, K. E. Sickafus, M. A. Nastasi, G. S. Smith and R. Pynn: *NanoStruct. Mater.*, **6** (1995), 539.
- [29] B. D. Cullity, *Introduction of Magnetic Materials*, Addison-Wesley, Reading, MA (1972).
- [30] R. Sumi, N. Toda, H. Fujii and S. Tsurekawa: *Rev. Adv. Mater. Sci.* (accepted).

Chapter 6

Magnetism of grain boundary

6.1 Introduction

It is well-known that properties of polycrystalline materials are greatly affected by the presence of grain boundaries [1]. Experimental studies, particularly using bicrystals, revealed that individual grain boundaries have inherent properties according to their character and structure [2, 3]. The bulk properties of polycrystalline materials are determined by the contribution of many interconnecting grain boundaries with different characters as well as by intrinsic bulk properties. Therefore, it is of great importance to quantitatively analyze the grain boundary microstructure in polycrystalline materials. In particular, when a magnetic field effect is applied to the specimen during microstructural evolution, the magnetic properties of grain boundaries may play an important role in the resultant microstructure. Yamaura *et al.* investigated the effect of grain boundary microstructures on the Barkhausen noise associated with the dynamic interaction between grain boundaries and magnetic domains [4]. They found that the Barkhausen noise near the grain boundary increased with increase in the misorientation angle between two adjacent grains in silicon steel. Kawahara *et al.* investigated the interaction between the grain boundaries and magnetic domain walls [5]. They found that the pinning effect on the domain wall migration depended on the grain boundary character. These phenomena would be closely related with the magnetism of grain boundaries. However, a study of the magnetism of grain boundaries has been very scarcely made and the magnetism of grain boundaries has not been fully understood until recently.

The studies so far have suggested that importance of grain boundary magnetism to understand the magnetic field effect on metallurgical phenomena [6-10]. Therefore, it is essential to understand the magnetism of grain boundaries in materials, particularly ferromagnetic materials. Recently it has been revealed that the electronic states of atoms near the grain boundaries change with the geometrical disordered structure using electron energy loss spectroscopy (EELS) on TEM [11-14]. In addition, a change in electronic states of atoms near grain boundaries was found to significantly affect the magnetic moment of atoms in ferromagnetic materials [15-19]. Hampel *et al.* calculated the magnetic moment of $\Sigma 5(310)$

grain boundary in bcc iron using the layer Korringa-Kohn-Rostoker (LKKR) technique and found to increase the magnetic moment near the grain boundary [15]. Šob and coworkers investigated the magnetic moment of atoms near the $\Sigma 5$ grain boundary in a bcc iron and an fcc nickel using the first principle calculation [16, 18]. They constructed the structural model of the $\Sigma 5(310)$ tilt grain boundary in a bcc iron and concluded that the magnetic moment within several layers from the boundary core increased due to the change in atomic sphere radius. Thus the magnetic moment of atoms has been theoretically anticipated to increase near the grain boundary in ferromagnetic materials. On the other hand, Fitzsimmons *et al.* experimentally estimated the local magnetic moment near the grain boundary in nickel using neutron diffraction method [19]. However the local magnetic moment near the grain boundary has not been experimentally estimated in iron based materials so far.

Although the neutron diffraction method is often used to measure the magnetic moment of atoms, it is difficult for this method to analyze the local magnetic moment near the grain boundary. In 2001, Pease *et al.* proposed a new experimental technique for measurement of the local magnetic moment from 3d L_3/L_2 white line ratio on a TEM-EELS profile [20]. The relationship between the white line ratio in EELS spectrum and magnetic moment was firstly pointed out in 1991 by Kurata *et al.* [21]. Then the magnetic moments of atoms near the grain boundaries can be experimentally estimated by the application of this technique.

In this chapter, the local magnetic moments near the grain boundaries were investigated in pure iron and Fe-Sn alloy using TEM-EELS technique. On the basis of results obtained, the grain boundary character dependence of local magnetic moment and the effect of impurity atoms were discussed.

6.2 Experimental

6.2.1 Preparation of the specimens

The materials used were pure iron (99.9%) and an Fe-0.8at%Sn alloy. The Fe-0.8at%Sn alloy was prepared by vacuum melting electrolytic iron and high purity tin (99.999%). The ingot was hot-forged to a plate 10 mm thick and then hot-rolled into 1.2 mm thick sheet at 873 K. The chemical compositions of these specimens are shown in Table 6-1. The pure iron and Fe-0.8at%Sn specimens of 10 mm \times 5 mm \times 1mm in dimensions were cut out and were annealed at 973 K for 6 h in a vacuum of 6×10^{-4} Pa, respectively. For TEM/EELS analysis,

Table 6-1 Chemical composition (at%) of 99.9% Fe and Fe-0.8at%Sn specimens.

Material	C	S	N	O	P	Sn	Si	Mn	Cu
Fe	0.005	<0.003	0.028	0.456	<0.003	-	0.039	0.063	0.011
Fe-0.8at%Sn	0.12	0.005	0.012	0.049	0.004	0.80	-	0.001	-

the annealed specimens were mechanically polished to thin sheets of approximately 100 μm thick and then rectangular sheets of 1.5 mm \times 1 mm in dimensions were cut out using a diamond cutter. Thereafter, the sheets were thinned by a twin-jet technique in a mixture of acetic acid, perchloric acid and methanol with 9:1:1 by volume at 20 V and 0.1 A. Prior to TEM/EELS analysis, the character of individual grain boundaries in the TEM samples were determined by OIM analysis as shown in Fig.6-1.

The pure titanium specimen for TEM/EELS analysis was also prepared as a standard specimen for EELS spectrum. The specimen was annealed at 1023 K for 6 h in a vacuum of 2×10^{-3} Pa. The annealed specimen was mechanically polished to thin sheets of approximately 100 μm thick and then trepanned into 3 mm ϕ using an electric discharge machine. Thereafter, the sheet was thinned by a twin-jet technique in a mixture of 1-butanol, perchloric acid and methanol with 1:7:12 by volume at 40 V and 0.1 A at 233 K.

6.2.2 Measurement of white lines using TEM-EELS method

TEM/EELS analyses were conducted on a Philips FEG-TEM Tecnai F20 equipped with electron energy loss spectroscope. A part of incident electrons to the specimen loses energy due to the inelastic scattering caused by the interaction between constituent atoms and electrons in the TEM observation. The amount of energy loss is estimated from the deflection angle of energy-loss-electrons deflected by a magnetic field in the TEM/EELS technique. When the energy value and shape of EELS spectra are analyzed using this technique, the scientific knowledge concerning the type of atoms or their electronic structure can be obtained with high spatial and energetic resolution. The schematic illustration of the principle of TEM/EELS technique and the EELS spectrum are shown in Figs 6-2 (a) and (b), respectively. The monochromatic incident electrons lose energy by various elemental excitation processes which occur during transmission through specimen. These transmission electrons are dispersed depending on their energy by the magnetic prism. Then only the electrons with

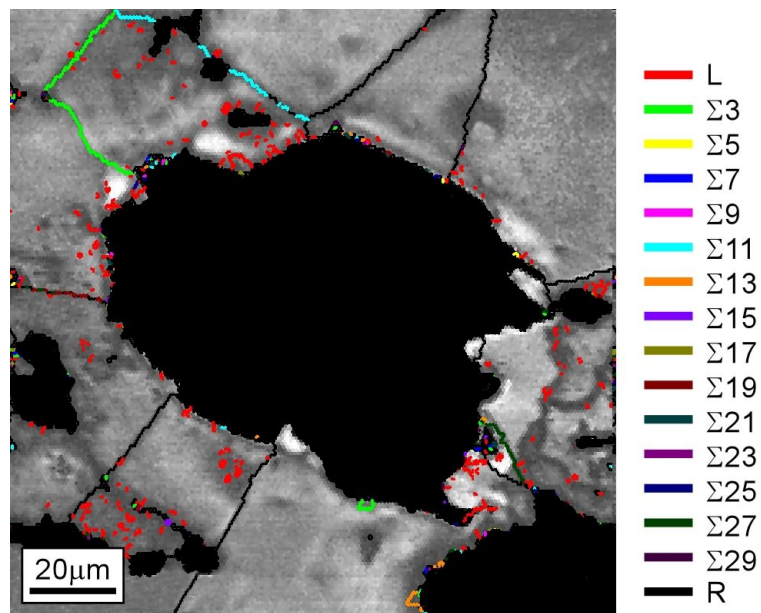


Figure 6-1 The grain boundary character distribution map of pure iron specimen for TEM/EELS analysis.

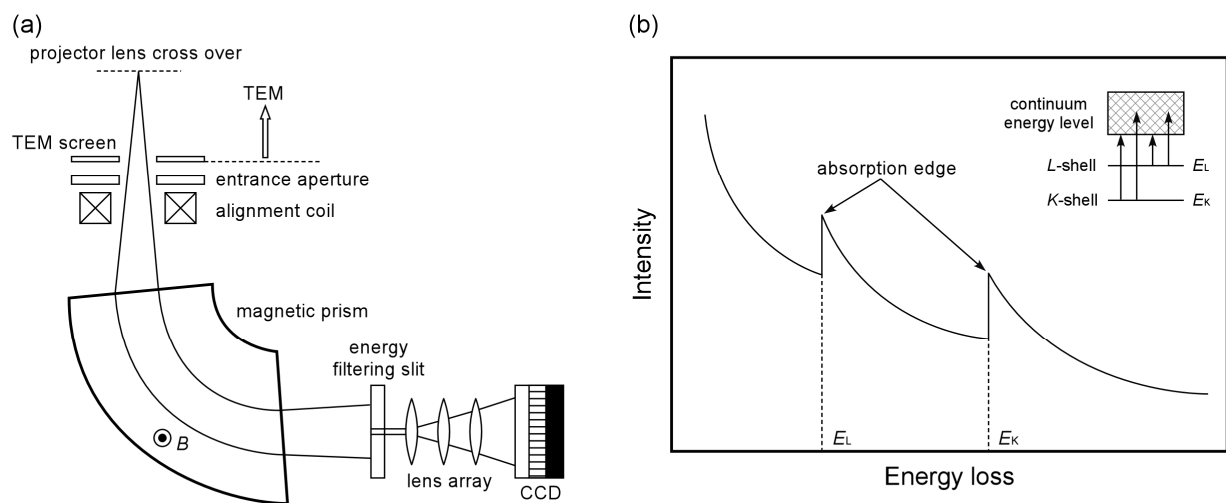


Figure 6-2 The schematic illustrations of principle of TEM/EELS analysis and EELS spectrum with absorption edges occurred by excitation of electrons during electron beam transmission through the specimen.

specific energy are selected by the energy filtering slit. Thereafter EELS spectrum can be obtained from the intensity measurement by multichannel detector as shown in Fig.6-2 (b). The absorption edges depending on the state of energy-loss-electrons are observed in the EELS spectrum. The measurable energy in current spectroscope is usually ranging from 0 to 3000 eV. Accordingly, it is possible to measure the energy from the localized level in bandgap to the valence excitation spectrum and the core electron spectrum in principle. The energy resolution significantly depends on the monochromaticity of incident electrons in the TEM/EELS technique. Generally, assured energy resolution is approximately 0.5 – 0.7 eV in the commercial instrument of FEG-TEM/EELS.

In this study, the EELS spectra were measured in pure iron, Fe-0.8at%Sn alloy and pure titanium. Conventional TEM observations were performed at an accelerating voltage of 200 kV and the electron beam size was approximately 10 nm. The energetic intensities at absorption edges in the EELS spectra (L_2 and L_3 peaks) were evaluated and the intensity ratio L_3/L_2 , which is called “white-line” ratio, was calculated in each spectrum.

6.2.3 Evaluation of magnetic moment

It has been found that the white-line ratio observed in the EELS technique generally does not become statistical ratio in $3d$ transition metals and intermetallic compounds. From the experiments and theoretical analyses, the white-line ratio R was found to change depending on the $3d$ electrons in the ground state (local magnetic moment). In addition, the white-line ratio was confirmed to increase with increasing magnetic moment. Then the local magnetic moment was determined from the white-line ratio using the parameterization method proposed by Pease *et al.* [20]. The method is described as follows.

The white-line ratio as a function of magnetic moment is shown in Fig. 6-3 [20]. The numerical values in the figure indicate the number of $3d$ occupied electrons. The white-line ratio increases linearly with increase in the magnetic moment in the metals with more than five $3d$ occupied electrons as shown in Fig. 6-3. On the other hand, it increases nonlinearly with the increase in magnetic moment in the metals with less than five $3d$ occupied electrons. When the number of electrons in the ground state N is more than five and electrons are arranged to maximize the spin according to the Pauli exclusion principle and the Hund’s rule, all the electrons ejected into unoccupied $3d$ band are minority spin. However, in the case of $3d$ occupied electrons are less than five, as the electrons eject into the unoccupied $3d$ band corresponding to both spin-up and spin-down orientation, the shape of the ratio versus

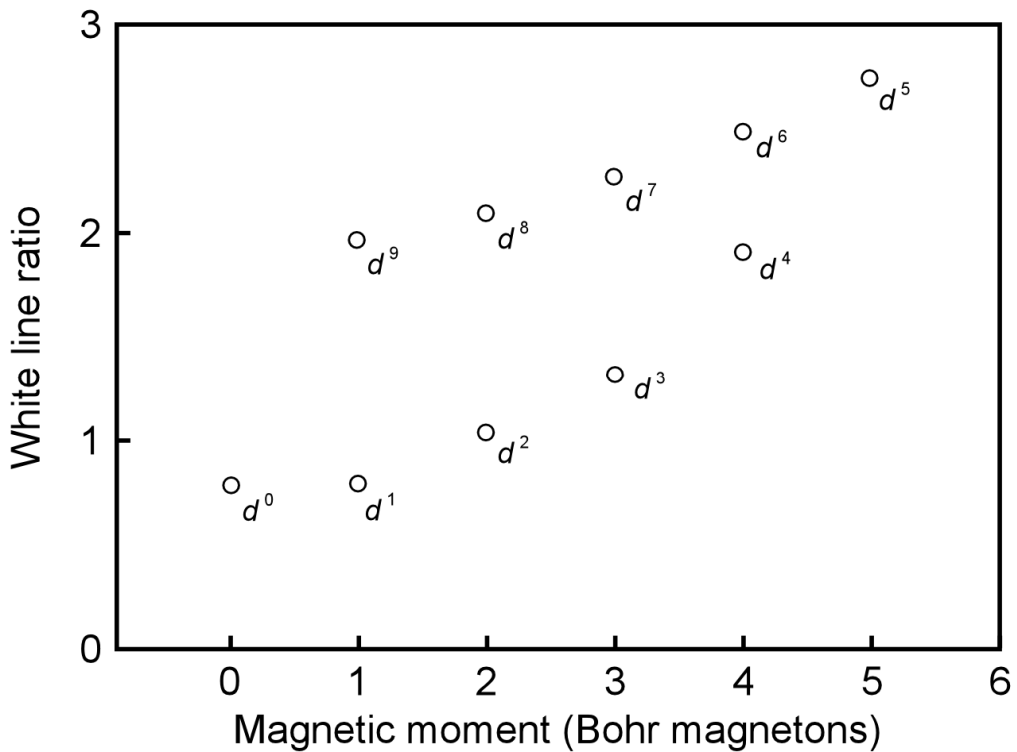


Figure 6-3 Plot of L_3/L_2 white line ratio versus magnetic moment [20].

moment plot is quite different from the case of $3d$ counts exceeding five. Thus, a function of $F(m)$ on the basis of the consideration of the spin direction and existing probability is defined. $F(m)$ is a function of magnetic moment and given by,

$$F(m) = (P_{\downarrow} - P_{\uparrow})m, \quad (6-1)$$

where P_{\downarrow} is the existing probability of ejected electrons with spin-down, P_{\uparrow} is the existing probability of ejected electrons with spin-up and m is the magnetic moment. The occupation of the $3d$ band is taken as N and the number of $3d$ holes is therefore $(10 - N)$. The following relationship is obtained by,

$$N_{\uparrow} + N_{\downarrow} = N, \quad (6-2)$$

$$N_{\uparrow} - N_{\downarrow} = m, \quad (6-3)$$

where N_{\uparrow} is the number of spin-up electrons and N_{\downarrow} is the number of spin-down electrons. Here P_{\downarrow} is assumed to be given by the total number of spin-down holes divided by the total number of holes, leading to eqn. (6-4) below.

$$P_{\downarrow} = \frac{5 - N_{\downarrow}}{10 - N}. \quad (6-4)$$

Similarly, P_{\uparrow} is given by eqn. (6-5).

$$P_{\uparrow} = \frac{5 - N_{\uparrow}}{10 - N}. \quad (6-5)$$

$F(m)$ can be described as follows using the magnetic moment m from above equations.

$$F(m) = \frac{m^2}{10 - N}. \quad (6-6)$$

The next, Pease *et al.* empirically developed the equation for corrected white-line ratio R_{corr} [20]. The corrected white-line ratio R_{corr} can be determined by the subtracting the following R' from L_3/L_2 ratio.

$$R' = 0.8 + 0.015n^2 \quad (6-7)$$

$$R_{corr} = R - R' \quad (6-8)$$

where n is 2 for Ti, 3 for V, 6 for Fe, 8 for Ni and 9 for Cu. On the basis of eqns. (6-6) and (6-7), Fig. 6-4 can be obtained from replotted Fig. 6-3. The good linear relationship between the corrected white-line ratio and the $F(m)$ can be confirmed as shown in Fig. 6-4.

Using these results, the local magnetic moment can be evaluated by EELS analysis in transition metals. On the basis of this method, the local magnetic moments near grain boundaries were measured in pure iron and Fe-0.8at%Sn alloy.

6.3 Results and discussion

6.3.1 Analysis of EELS spectra

To make standard curve for determination of the magnetic moment from EELS data, the measurement of EELS spectra was conducted in iron and titanium, which are well-known magnetic moment. Fig. 6-5 shows the examples of EELS spectra obtained from grains in iron and titanium. To establish the numerical proportionality between white-line intensity ratio and the magnetic moment, the white-lines must be isolated from the background intensity. The background intensity was modeled by step functions because the L_2 and L_3 edges for Ag, which has no white-lines, exhibit step function [14]. As the L_2 and L_3 white-lines were overlapped with each other in titanium as shown in Fig. 6-5 (b), the white-lines were isolated by modeling the background with a double step function. A straight line was fit to the background immediately following the L_2 white line and then extrapolated into the white-line

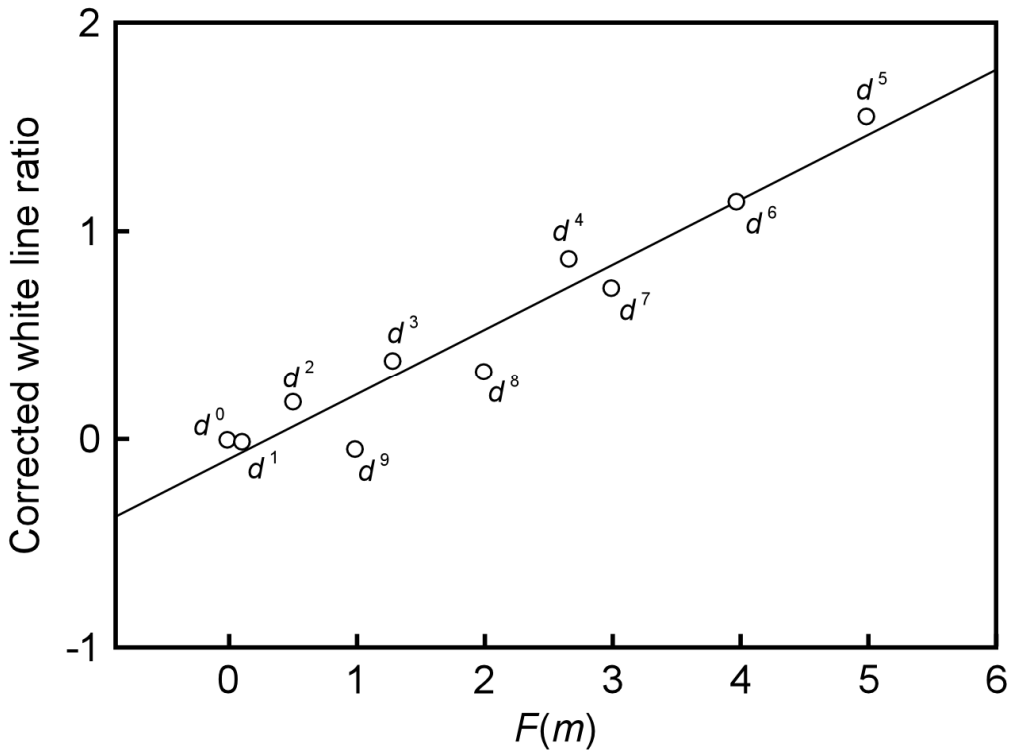


Figure 6-4 The relationship between the corrected white line ratio and the $F(m)$ [20].

regions. The white-line ratios were estimated from the area ratios of L_3 intensity to L_2 intensity as shown in Fig. 6-5. From the EELS spectra of iron and titanium, the relationship between the white-line ratio and the magnetic moment was examined. Here the magnetic moments of titanium and iron were discussed in connection with eqn. (6-6). Titanium is not magnetic [22] and $F(m)$ is zero for any finite value of the $3d$ count. Hund's rule of maximum spin alignment, which is consistent with the Pauli exclusion principle, is not necessarily expected to be valid for $3d$ transition metals. However, band structure calculations often find that the unoccupied $3d$ band is exclusively minority spins. The calculation shows that a small piece of the spin-up band is above the Fermi level for metallic iron [23]. In the case of iron, the fractional spin-up $3d$ hole count is sufficiently small, which can be neglected in determining $F(m)$. For iron, m is taken to be 2.2 Bohr magnetons from saturation magnetization results and the N value is taken to be 7.8. Fig. 6-6 shows (a) a plot of L_3/L_2 white line ratio versus magnetic moment and (b) corrected white-line ratio versus $F(m)$. For

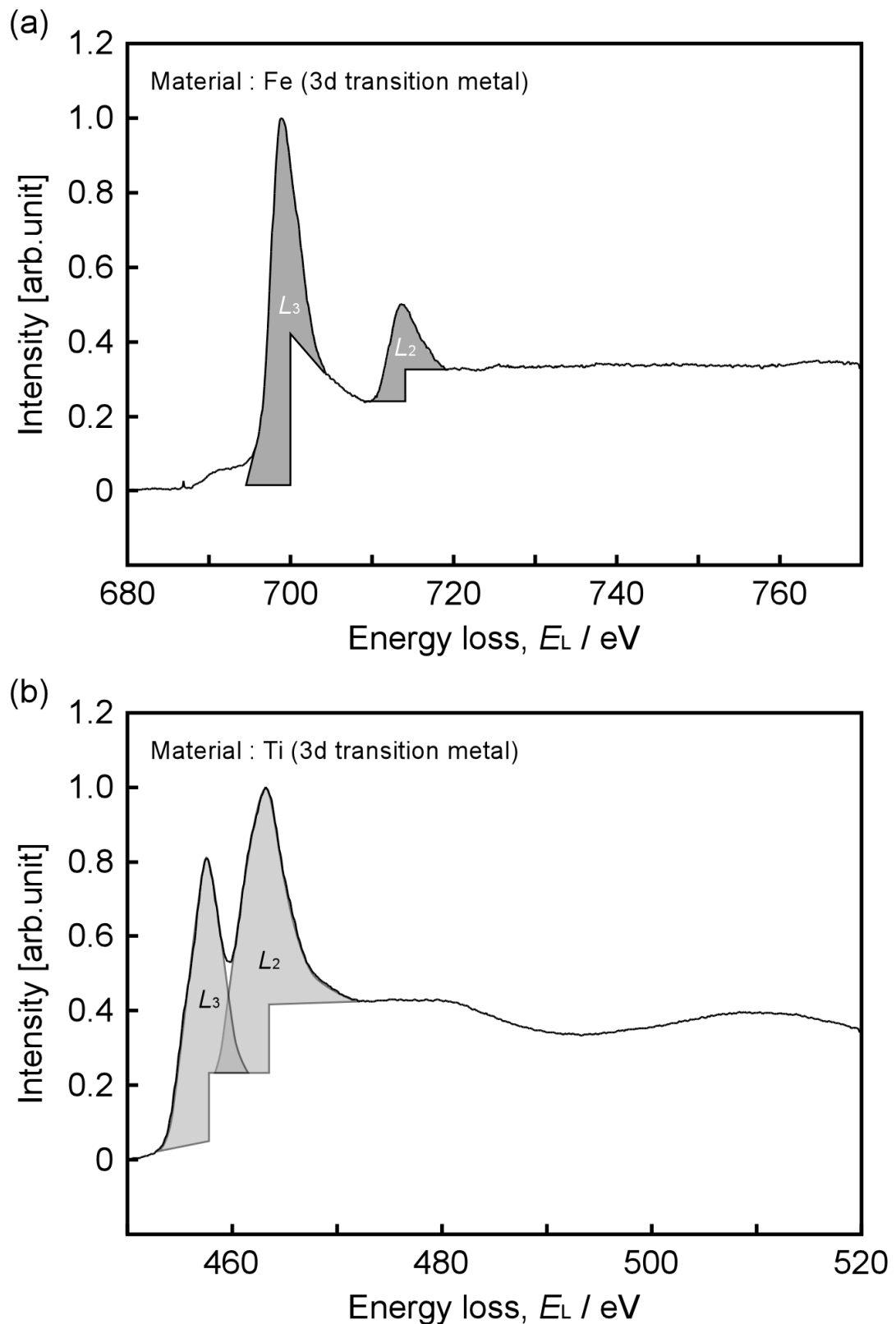


Figure 6-5 L_2 and L_3 edges for (a) Fe and (b) Ti showing isolated white-line intensity from background of step function.

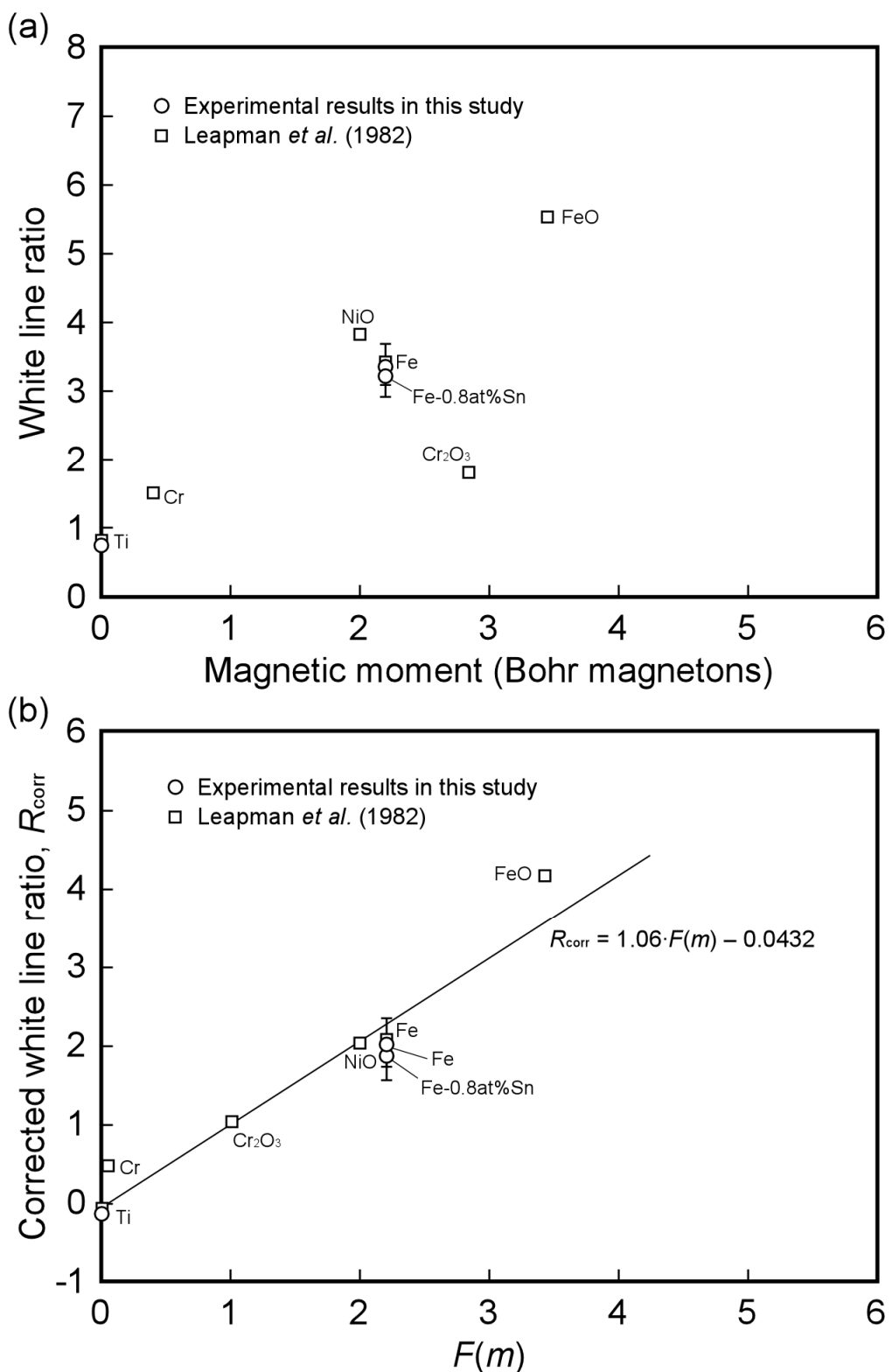


Figure 6-6 (a) Plot of L_3/L_2 white line ratio versus magnetic moment in the various 3d transition metals and alloys and (b) data of (a) as replotted in terms of corrected white line ratio versus $F(m)$.

comparison, the data after Leapman *et al.* [24] are shown in Fig. 6-6. The white-line ratios of iron and titanium obtained in this study were in good agreement with the data after Leapman *et al.* [24]. There is a good linear relationship between the corrected white-line ratio R_{corr} and $F(m)$. This relation can be expressed as,

$$R_{corr} = 1.06 \times F(m) - 0.0432 . \quad (6-9)$$

From eqns. (6-6) – (6-9), the local magnetic moment can be described by,

$$m = \sqrt{2.2 \times (R_{corr} + 0.0432)} . \quad (6-10)$$

The analysis of EELS spectra gives the quantitative value of local magnetic moment using eqn. (6-10). Then the EELS spectra at grain boundaries were measured in pure iron and Fe-0.8at%Sn alloy and the local magnetic moments at grain boundaries were evaluated. The details will be noted in the next section.

6.3.2 Change of magnetic moment of atoms near the grain boundaries

Fig. 6-7 shows the EELS profiles obtained (a), (c) at the grain interior across a $\Sigma 3$ boundary, (b), (d) at the grain interior across a random grain boundary and (e) at the $\Sigma 3$ and (f) at the random boundaries in pure iron. The EELS spectra from the grain interior were measured at the areas sufficiently away from the grain boundaries. The L_3 and L_2 absorption edges were observed at the loss energies of approximately 710 eV and 725 eV, respectively. There are no significant differences between these spectra obtained from the grain interior and grain boundaries. However the white-line L_3/L_2 height ratio is slightly larger for the random grain boundary than for the grain interior. Fig. 6-8 shows the EELS profiles obtained from the grain interior and grain boundaries in the Fe-0.8at%Sn alloy. There are no observable differences between them.

The white-line intensity ratios of these EELS spectra in Figs. 6-7 and 6-8 were evaluated. Thereafter, the local magnetic moments at grain boundaries and grains were quantitatively estimated using eqn. (6-10). Fig. 6-9 shows changes in the magnetic moment across the $\Sigma 3$ and random grain boundaries in (a) pure iron and (b) Fe-0.8at%Sn. It was found that the local magnetic moment at the random grain boundary increased by approximately 5 - 9 % compared with those at the grain interior. On the other hand, the magnetic moment at $\Sigma 3$ grain boundary was as same as that at the grain interior. Kawahara *et al.* have investigated the interaction between a magnetic domain wall and grain boundaries in pure nickel by Lorentz microscopy [5]. They found that the magnetic domain wall was pinned at the random grain

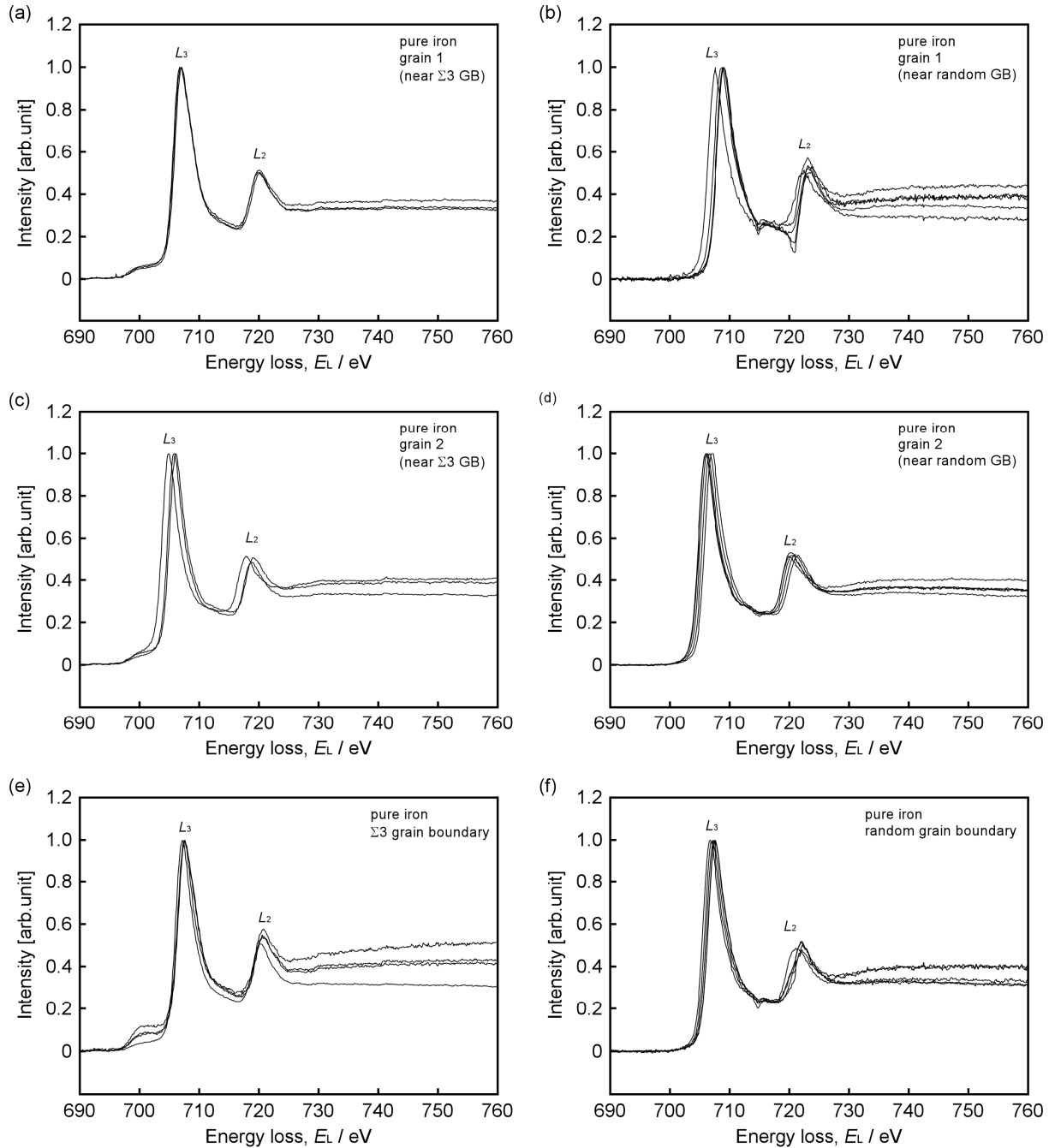


Figure 6-7 (a) – (d) EELS spectra obtained from grains neighboring $\Sigma 3$ and random grain boundaries and (e), (f) obtained at $\Sigma 3$ and random grain boundaries in pure iron.

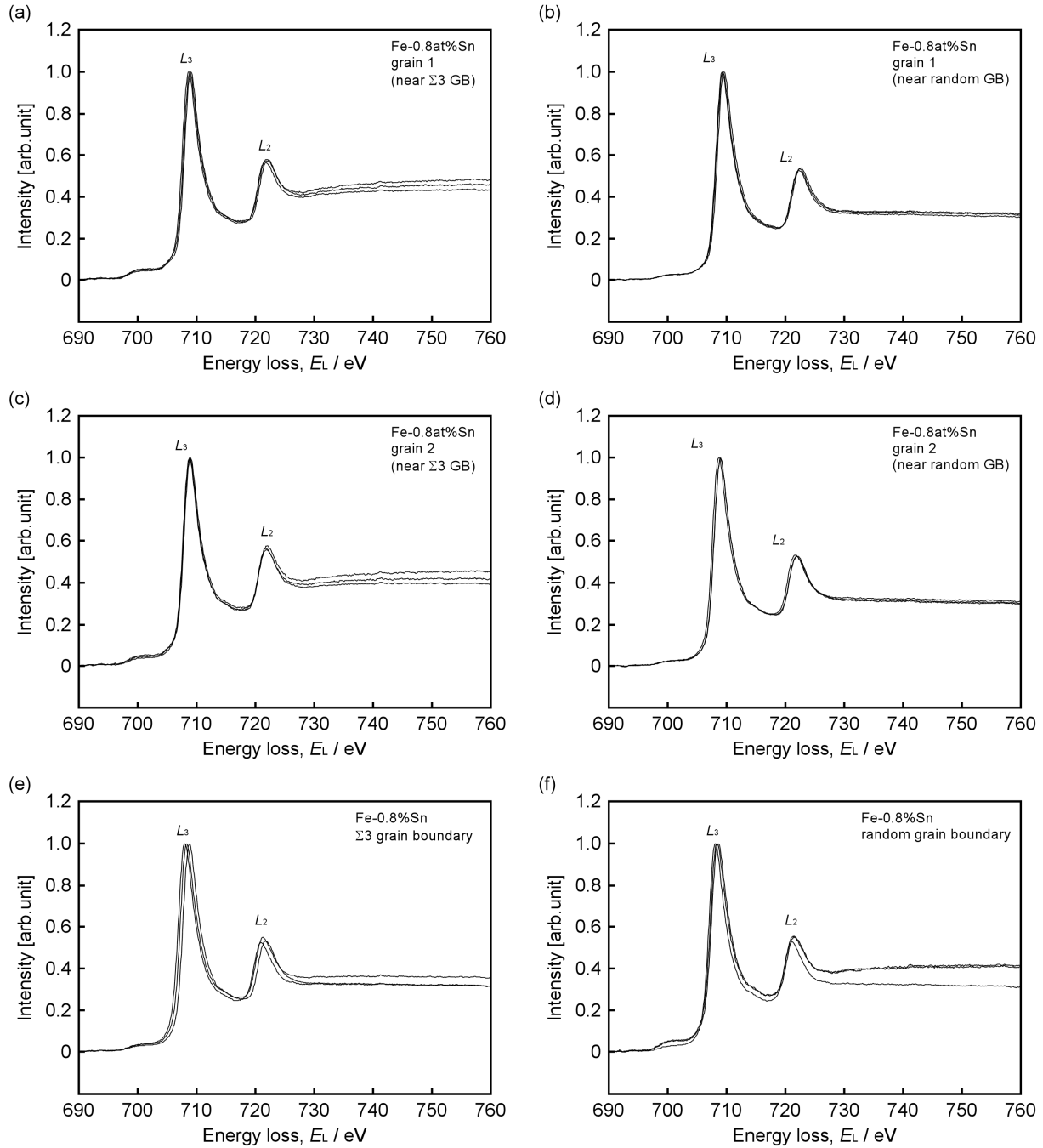


Figure 6-8 (a) – (d) EELS spectra obtained from grains neighboring $\Sigma 3$ and random grain boundaries and (e), (f) obtained at $\Sigma 3$ and random grain boundaries in Fe-0.8at%Sn.

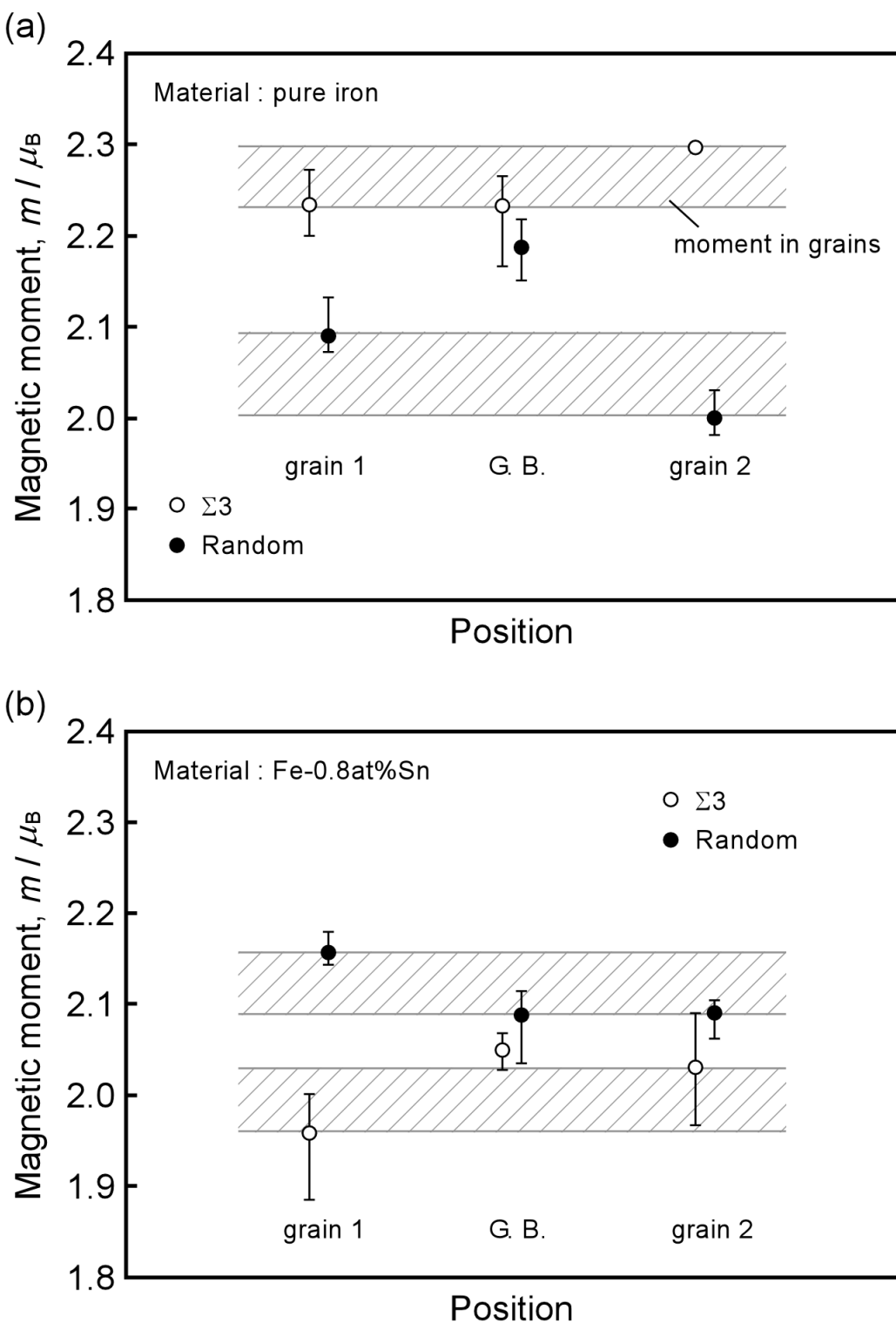


Figure 6-9 The magnetic moments at $\Sigma 3$ and random grain boundaries and at grains neighboring their boundaries in (a) pure iron and (b) Fe-0.8at%Sn.

boundary, whereas that was not pinned at the $\Sigma 3$ grain boundary. When the magnetic domain wall migrates in the bulk polycrystal, the magnetic moments must be inverted at the inner part of domain wall. Therefore the more energy for domain wall migration would be required, if the magnetic moments increase. According to this hypothesis, it is possible to consider that the magnetic domain wall was pinned at the random grain boundary due to the barrier for migration generated by the increase in magnetic moments. Then the observation by Kawahara *et al.* would be corroborative of the experimental results that the magnetic moment increased at the random grain boundary but did not change at the $\Sigma 3$ grain boundary.

The $\Sigma 3$ grain boundary is known to be geometrically coherent boundary, whereas the random boundary is incoherent boundary. The local magnetic moment may increase with decreasing geometrical coherency in atomic arrangement, because Šob *et al.* found using the first principle calculation that an increase in volume causes the increase in the magnetic moment [16]. They showed that the local magnetic moment at (310) $\Sigma 5$ grain boundary in iron increased up to $2.75 \mu_B$ [16], which is by approximately 20 % larger than that of the iron grain of $2.22 \mu_B$. This value is much higher than that of the experimental results in this study. According to the calculation by Šob *et al.*, an increase in local magnetic moment occurred within a few atomic layers from the grain boundary. In this experiment, the beam size in TEM/EELS analysis was approximately 10 nm. Because the width of grain boundary would be at most 1 nm, the EELS spectra at grain boundary includes the information from the grain interior as well as the grain boundary. Thus, a contribution of the grain interior to the EELS spectra measured at the boundary should be subtracted. The shapes of electron beam and grain boundary were simplified as schematically shown in Fig. 6-10. In addition, the grain boundary is assumed to be parallel to the electron beam. When the local magnetic moment at grain boundary is m_{gb} and that at a few atomic layers is $(m_g + m_{gb})/2$, the following equation can be obtained from the linear combination of the magnetic moment of grain boundary, a few atomic layers and grains.

$$\frac{S_0 - (S_{gb} + S_l)}{S_0} m_g + \frac{S_{gb}}{S_0} m_{gb} + \frac{S_l}{S_0} \frac{1}{2} (m_g + m_{gb}) = m, \quad (6-11)$$

where S_0 is the whole area of EELS analysis, S_{gb} is the area of grain boundary, S_l is the area of a few atomic layers with the area of grain boundary removed and m_g is the magnetic moment at grains. Using $m_g = 2.05 \mu_B$, $S_0 = 5 \times 5 \times \pi = 78.5 \text{ nm}^2$, $S_{gb} = 1 \times 10 = 10 \text{ nm}^2$ and $S_l = 2 \times 10 - 1 \times 10 = 10 \text{ nm}^2$ according to the experimental result of random grain boundary in iron, the local magnetic moment was estimated by $2.78 \mu_B$. This value is in good agreement with the result of calculation by Šob *et al.* as mentioned above.

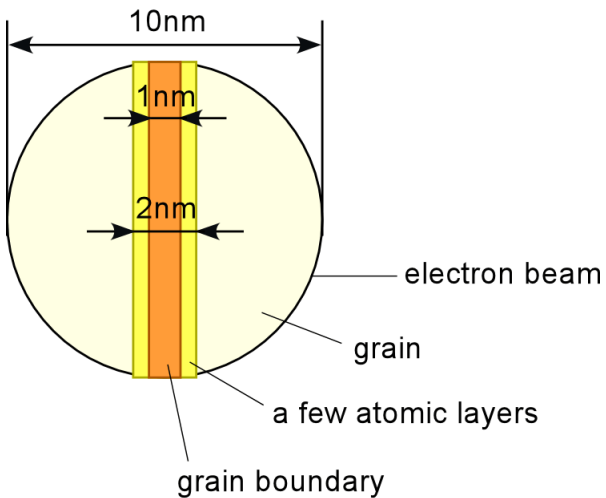


Figure 6-10 The schematic illustration of the shapes of electron beam and grain boundary during EELS analysis for the estimation of the local magnetic moment at grain boundary.

Fig. 6-9 (b) shows the magnetic moment obtained from EELS spectra in the Fe-0.8at%Sn alloy. Any significant changes of magnetic moment were not confirmed at grain boundaries unlike the case of pure iron. As mentioned in the case of pure iron, the increase in the free volume at the grain boundary would play an important role in the increase in local magnetic moment. According to the calculation after Čák *et al.* [18], the local magnetic moment of iron atoms at grain boundary were only very little affected when the substitutional tin atoms were present at the grain boundary. They mentioned that the substitutional tin atoms left the magnetic moment uncharged because of compensation effect of volume. In addition, Ozawa *et al.* investigated the electronic state of tin atoms at grain boundary of bcc iron using Mössbauer analysis [25]. They noted that the ferromagnetic property of iron atoms at grain boundary with tin segregants may be lost, because the tin atoms would provide electrons to iron atoms. In the Fe-0.8at%Sn alloy used in this study, the tin atoms are known to significantly segregate into the grain boundaries. Then the geometrical disordered structure of grain boundaries would be relaxed by the tin atoms and the free volume at grain boundaries would decrease due to the change of chemical bonding. As a result, the local magnetic moment at grain boundary would not significantly change in the Fe-0.8at%Sn alloy.

6.4 Summary

The local magnetic moments near the grain boundaries were investigated in pure iron and Fe-0.8at%Sn alloy using TEM-EELS technique. The grain boundary character dependence of local magnetic moment and the effect of impurity atoms were discussed. The following conclusions were obtained.

- (1) The relationship between white-line ratio of EELS spectrum and the local magnetic moment was revealed using linearization method. The local magnetic moment was found to be described by $m = \sqrt{2.2 \times (R_{corr} + 0.0432)}$.
- (2) The local magnetic moment at random grain boundary increased by 5-9 % in comparison with that at grains, whereas that at $\Sigma 3$ grain boundary did not significantly change. The local magnetic moment would increase with the increase in the free volume between the atoms at the grain boundary.
- (3) The local magnetic moments at grain boundaries does not change in the Fe-0.8at%Sn alloy. This would be due to the relaxation of geometrical disordered structure at grain boundaries by the grain boundary segregation of tin atoms.

References

- [1] T. Watanabe and S. Tsurekawa: *Acta Mater.*, **47** (1999), 4171.
- [2] Y. Ishida (ed.): Grain Boundary Structure and Related Phenomena, *Suppl. Trans., JIM*, **27** (1986).
- [3] A. P. Sutton and R. W. Balluffi: Interfaces in Crystalline Materials, *Oxford Science Publications*, (1995).
- [4] S. Yamaura, Y. Furuya and T. Watanabe: *Acta Mater.*, **49** (2001), 3019.
- [5] K. Kawahara, Y. Ando, K. Nogiwa, Y. Yagyu, S. Tsurekawa and T. Watanabe: *Ann. Chim., Sci. Mater.*, **27** (2002), S269.
- [6] K. Maruta, M. Shimotomai: *J. Crystal Growth*: **237-239** (2002), 1802.
- [7] N. Masahashi, M. Matsuo and K. Watanabe: *J. Mater. Res.*, **13** (1998), 457.
- [8] S. Tsurekawa, K. Kawahara, K. Okamoto, T. Watanabe and R. Faulkner: *Mater. Sci. Eng.*, **A387-389** (2004), 442.
- [9] S. Tsurekawa, K. Okamoto, K. Kawahara and T. Watanabe: *J. Mater. Sci.*, **40** (2005), 895.
- [10] T. Watanabe, S. Tsurekawa, X. Zhao, L. Zuo and C. Esling: *J. Mater. Sci.*, **41** (2006), 7747.
- [11] D. A. Muller, S. Subramanian, P. E. Batson, S. L. Sass and J. Silcox: *Phys. Rev. Lett.*, **75** (1995), 4744.
- [12] N. D. Browning, D. J. Wallis, P. D. Nellist and S. J. Pennycook: *Micron*, **28** (1997), 333.
- [13] T. Sasaki, T. Mizoguchi, K. Matsunaga, S. Tanaka, T. Yamamoto, M. Kohyama and Y. Ikuhara: *Appl. Surf. Sci.*, **241** (2005), 87.
- [14] D. H. Pearson, C. C. Ahn and B. Fultz: *Phys. Rev. B*, **47** (1993), 8471.
- [15] K. Hampel, D. D. Vvedensky and S. Crampin: *Phys. Rev. B*, **47** (1993), 4810.
- [16] M. Söb, I. Turek, L. Wang and V. Vitek: *Proc. 10th Int. Metallur. Mater. Conf. METAL 2001*, (2001), 1.
- [17] E. Wachowicz and A. Kiejna: *Comp. Mater. Sci.*, **43** (2008), 736.
- [18] M. Čák, M. Söb and J. Hafner: *Phys. Rev. B*, **78** (2008), 054418.
- [19] M. R. Fitzsimonns, A. Röll, E. Burkert, K. E. Sickafus, M. A. Nastasi, G. S. Smith and R. Pynn: *Nanostruct. Mater.*, **6** (1995), 539.
- [20] D. M. Pease, A. Fasihuddin, M. Daniel and J. I. Budnick: *Ultramicroscopy*, **88** (2001), 1.
- [21] H. Kurata and N. Tanaka: *Microsc. Microanal. Microstruct.*, **2** (1991), 183.
- [22] J. B. Goodenough: *Magnetism and the Chemical Bond*, Interscience, Wiley New York. London (1963).
- [23] R. Coehorn: *Phys. Rev. B*, **39** (1989), 13072.
- [24] R. D. Leapman, L. A. Grunes and P. L. Fejes: *Phys. Rev. B*, **26** (1982), 614.
- [25] T. Ozawa and Y. Ishida: *J. Japan Inst. Met.*, **43** (1979), 1048. (in Japanese)

Chapter 7

Conclusions

The effects of strong magnetic fields on fundamental metallurgical phenomena (diffusion and grain nucleation and growth) were investigated in iron-based materials to obtain comprehensive knowledge of the mechanism of magnetic field effects on microstructural evolution. In addition, the fundamental physical properties of grain boundaries of iron closely concerning with the grain nucleation and growth were also investigated. The following conclusions were obtained.

The effects of strong magnetic fields on metallurgical phenomena

- Diffusion

(1) The diffusivity of carbon in both α - and γ -iron is suppressed under a 6 T magnetic field.

Furthermore the diffusivity in α -iron is retarded more than that in γ -iron. The activation energy of carbon diffusion did not change when a static magnetic field was applied. The difference between the entropy of carbon atoms in tetrahedral and octahedral sites decreases by the application of a magnetic field due to the magnetostriction of ferromagnetic α -iron and its effect on site occupancy, so that the carbon diffusion would be retarded.

(2) A “negative” magnetic field gradient can enhance the carbon diffusion in α -iron.

Numerically, it was proven that the increase in carbon diffusion by the application of a magnetic field gradient was due to the increase in flux of carbon atoms induced by the magnetic potential gradient. The diffusion coefficient was found to increase monotonically with the increase in strength of magnetic field gradient. In addition, the diffusion coefficient could be described as the linear function of the strength of a magnetic field gradient.

- Solid solubility
- (3) The solid solubility limit of carbon increased by twice when a 6 T magnetic field was applied at the ferromagnetic temperature ranging from 950K to 1000K. The solid solubility limit of carbon will shift to higher concentration under a static magnetic field, as the free energy curve of ferrite phase will be lowered. In addition, The solid solubility limit of carbon increased with the increase in magnetic field strength and shows a maximum at 4 T magnetic field.
- Nucleation and growth
- (4) The crystallization from an $\text{Fe}_{78}\text{Si}_9\text{B}_{13}$ amorphous alloy under a magnetic field at 853 K causes development of a {110} sharp texture when a 6 T magnetic field is applied in a direction parallel to the specimen surface. The <001> orientation, which corresponds to the easy magnetization direction in the {110} textured grain structure, lies randomly in the {110} ribbon surface. The {110} grains preferentially grow, and the fraction of crystallized volume is increased by the application of a magnetic field of 6 T in $\text{Fe}_{78}\text{Si}_9\text{B}_{13}$ alloy.
- (5) The crystallization of $\text{Fe}_{73.5}\text{Si}_{13.5}\text{B}_9\text{Nb}_3\text{Cu}_1$ amorphous alloy under a magnetic field also enhanced a {110} texture formation of α -Fe(Si) grains. The preferential nucleation of {110} oriented grains due to a magnetic field would be predominantly responsible for the texture formation rather than the preferential grain growth. The application of a magnetic field increased the nanocrystallization kinetics, particularly the nucleation rate of the ferromagnetic α -Fe(Si) grains from the paramagnetic $\text{Fe}_{73.5}\text{Si}_{13.5}\text{B}_9\text{Nb}_3\text{Cu}_1$ amorphous phase.

Physical properties of grain boundary under a magnetic field

- Grain boundary energy

(6) Grain boundary energy in the 99.9%Fe increased with the increase in temperature under non magnetic conditions. On the other hand, the energy decreased under a 6 T magnetic field, and the energy discontinuously changed around the Curie temperature probably due to the difference between energetic contribution of the magnetic field to Gibbs free energy in ferromagnetic state and that in paramagnetic state. Grain boundary energy increased and its misorientation dependence was enhanced under a magnetic field in the 99.9%Fe. This is probably due to suppression of solute and impurities segregation to grain boundaries by a magnetic field.

- Magnetism of the grain boundary

(7) The relationship between white-line ratio of EELS spectrum and the local magnetic moment was revealed using linearization method. The local magnetic moment was found to be described by $m = \sqrt{2.2 \times (R_{corr} + 0.0432)}$. The local magnetic moment at random grain boundary increased by 5-9 % in comparison with that at grains, whereas that at $\Sigma 3$ grain boundary did not significantly change. The local magnetic moment would increase with the increase in the free volume between the atoms at the grain boundary. The local magnetic moments at grain boundaries does not change in the Fe-0.8at%Sn alloy. This would be due to the relaxation of geometrical disordered structure at grain boundaries by the grain boundary segregation of tin atoms.

Acknowledgement

My deepest appreciation goes to Professor A. Toshimitsu Yokobori, Jr. whose enormous support and insightful comments were invaluable during the doctoral course of my study.

I am indebted to Professor Masumi Saka and Professor Hiroki Kuwano whose meticulous comments were an enormous help to me.

I am also indebted to Professor Sadahiro Tsurekawa (Kumamoto University) who gave me invaluable comments and warm encouragements.

I wish to express my sincere thanks to Professor Harry K. D. H. Bhadeshia (University of Cambridge) for his useful comments and valuable suggestions in my study of the carbon diffusion under a static magnetic field and his hospitality during my stay in Cambridge.

I would particularly like to thank Mr. Takashi Matsuzaki for his valuable advice and his dedicated efforts on my experiments in this study.

I am very grateful to Professor Hiroshi Kubota, Mr. Masao Yoshioka and Mr. Takayuki Mizogami (Kumamoto University) for their valuable cooperation in SIMS analysis.

Special thanks also go to Professor Yasuhiro Morizono (Kumamoto University) who prepared the explosive welded diffusion couple of iron and steel.

I received generous support from Dr. Seiichiro Ii (National Institute for Materials Science) in analyzing the local magnetic moment at the grain boundary by TEM/EELS technique.

I wish to express my sincere thanks to Dr. Takateru Yamamuro and Dr. Mitsuhiro Matsuda (Kumamoto University) for their supports in my study.

I wish to express special thanks to Dr. Ryuji Sugiura, Mr. Toshihito Ohmi and Ms. Reiko Suto in Yokobori laboratory for their assistance.

I am also indebted to Professor Tadao Watanabe whose warm support and meticulous comments during the course of my study made enormous contribution to my work.

I am obliged to all of the members in Yokobori laboratory and Tsurekawa laboratory at Kumamoto University. I really had a great time with them and could not think of any good words except for "*thank you*" for their contribution to a very pleasant working environment.

Acknowledgement

I thankfully acknowledge the support of the 21st COE Program, “The Exploration of the Frontiers of Mechanical Science Based on Nanotechnology” and COE (Center of excellence) Research (No.11CE2003) from the Ministry of Education, Culture, Sports, Science and Technology. In addition, I would also like to thank a Grant-in-Aid for JSPS Fellows (19·3284) from the Japan Society for the Promotion of Science (JSPS) that made it possible to complete my study.

During the past three years as a doctoral student, I have had the opportunity to tap into the knowledge and experience of a great number of individuals who all contributed to this dissertation and my professional development as an engineering scholar in one way or another. Now is the time to thank each of them.

Last but not least, I cannot conclude these acknowledgements without mentioning my family. I would like to express my gratitude to my family for their moral support and warm encouragements. Their endless love, passion and patience as well as their sharing in both happiness and sadness have motivated my every effort and inspiration in producing this thesis.

Sendai, January 2009

Hironobu Fujii

List of publications

I. Original papers in international journals (refereed)

1. The Control of Texture and Grain Boundary Microstructure by Magnetic Annealing
Materials Science Forum, **495-497** (2005), 1151-1158.
T. Watanabe, S. Tsurekawa, H. Fujii and T. Kanno
2. Evolution of a sharp {110} texture in microcrystalline Fe₇₈Si₉B₁₃ during magnetic crystallization from the amorphous phase
Philosophical Magazine Letters, **86** (2006), 113-122.
H. Fujii, S. Tsurekawa, T. Matsuzaki and T. Watanabe
3. Crystallization Kinetics and Texture Evolution in Iron-based Amorphous Alloys under a Magnetic Field
Materials Science Forum, **558-559** (2007), 1371-1376.
S. Tsurekawa, H. Fujii, V. A. Yardley, T. Matsuzaki and T. Watanabe
4. Thermodynamic Study of Magnetic Field-Enhanced Nanocrystallisation in Amorphous Fe-Si-B(-Nb-Cu)
Materials Transactions, **48** (2007), 2826-2832.
Victoria A. Yardley, Sadahiro Tsurekawa, Hiromichi Fujii and Takashi Matsuzaki
5. Nanocrystallization of Fe_{73.5}Si_{13.5}B₉Nb₃Cu₁ soft-magnetic alloy from amorphous precursor in a magnetic field
Journal of Materials Science, **43** (2008), 3837-3847.
Hiromichi Fujii, Victoria A. Yardley, Takashi Matsuzaki and Sadahiro Tsurekawa
6. Impact of a magnetic field on grain boundary energy in 99.99% iron and iron-tin alloy
Review on Advanced Materials Science, (accepted)
Ryohei Sumi, Naoki Toda, Hiromichi Fujii and Sadahiro Tsurekawa

II. Proceedings of international conference (refreed)

1. Optimization of microstructure in iron-based nanocrystalline soft magnetic materials by magnetic crystallization towards innovation of magnetic properties
Proceedings of the 5th International Symposium on Electromagnetic Processing of Materials (2006), 567-572.
Hiromichi Fujii, Takashi Matsuzaki and Sadahiro Tsurekawa

III. Conference and symposium presentations (International conferences)

1. The Control of Texture and Grain Boundary Microstructure by Magnetic Annealing
14th Intern. Conf. on Texture of Materials (ICOTOM-14), Leuven, Belgium, (2005, 7)
T. Watanabe, S. Tsurekawa, H. Fujii and T. Kanno
2. Magnetic crystallization of iron-based amorphous alloys: kinetics, texture evolution and magnetic properties
A summer school on Electromagnetic Processing of Mateirals, Northeastern University, Shenyang, China, (2006.9)
H. Fujii, T. Matsuzaki and S. Tsurekawa

3. Modelling magnetic field effects on the crystallisation of amorphous Fe-Si-B alloys
Multiscale Modeling of extended defects and phase transformations at material interfaces, Wroclaw, Porland (2006.9)
V. A. Yardley, H. Fujii and S. Tsurekawa
4. Optimization of microstructure in iron-based nanocrystalline soft magnetic materials by magnetic crystallization towards innovation of magnetic properties
The 5th International Symposium on Electromagnetic Processing of Materials (EPM 2006), Sendai, Japan, (2006, 10)
H. Fujii, T. Matsuzaki and S. Tsurekawa
5. Magnetic crystallization of iron-based amorphous alloys: kinetics, texture evolution and magnetic properties
The 1st Tohoku-PNU Joint Workshop on Mechanical Science based on Nanotechnology, Pusan National University, Busan, South Korea, (2007, 1)
H. Fujii, T. Matsuzaki and S. Tsurekawa
6. Magnetic crystallization for enhancement of soft magnetic properties in nanocrystalline $\text{Fe}_{73.5}\text{Si}_{13.5}\text{B}_9\text{Nb}_3\text{Cu}_1$ alloy
The 4th International Symposium on Mechanical Science based on Nanotechnology, Sendai, Japan, (2007, 2)
H. Fujii, T. Matsuzaki and S. Tsurekawa
7. Crystallization Kinetics and Texture Evolution in Iron-based Amorphous Alloys under a Magnetic Field
Recrystallization and Grain Growth III, Jeju Island, Korea, (2007.6)
S. Tsurekawa, H. Fujii, V. A. Yardley, T. Matsuzaki and T. Watanabe
8. Texture evolution and kinetics of nanocrystallization in $\text{Fe}_{73.5}\text{Si}_{13.5}\text{B}_9\text{Nb}_3\text{Cu}_1$ amorphous alloy under a magnetic field (poster presentation)
XII International Conference on Intergranular and Interphase Boundaries, Barcelona, Spain, (2007.7).
Hiromichi Fujii, Takashi Matsuzaki, Victoria Yardley and Sadahiro Tsurekawa
9. Impact of a magnetic field on grain boundary energy in pure iron and Fe-Sn alloy
4th International Conference on Diffusion in Solids and Liquids, DSL-2008, Barcelona, Spain, (2008.7).
Ryohei Sumi, Naoki Toda, Hiromichi Fujii and Sadahiro Tsurekawa
10. Carbon diffusion in pure iron under a magnetic field
MS&T 2008 conference, Pittsburgh, USA, (2008.10).
Hiromichi Fujii and Sadahiro Tsurekawa
11. Grain boundary energy in 99.99% purity iron under a magnetic field
The 3rd Asian Workshop and Summer School on Electromagnetic Processing of Materials, Shanghai, China, (2008.10).
Naoki Toda, Hiromichi Fujii and Sadahiro Tsurekawa
12. Diffusion of carbon in iron under a magnetic field
The 3rd Asian Workshop and Summer School on Electromagnetic Processing of Materials, Shanghai, China, (2008.10).
S. Tsurekawa, H. Fujii, S. Nakamichi and T. Watanabe

IV. Conference and symposium presentations (Domestic conferences)

1. The Control of Grain Orientation in Fe₇₈Si₉B₁₃ Alloy by Magnetic Crystallization from Amorphous Precursor
The 135th JIM Meeting, Akita University, (2004, 9).
Hiromichi Fujii, Takashi Matsuzaki, Sadahiro Tsukada and Tadao Watanabe
2. The control of grain orientation in iron-based nanocrystalline materials by magnetic crystallization from amorphous precursor
The 149th ISIJ Meeting, Yokohama National University, (2005, 3).
Hiromichi Fujii, Takashi Matsuzaki and Sadahiro Tsukada
3. The microstructure and magnetic properties of iron-based nanocrystalline material fabricated by magnetic crystallization from amorphous precursor
The 137th JIM Meeting, Hiroshima University, (2005, 9).
Hiromichi Fujii, Takashi Matsuzaki and Sadahiro Tsukada
4. Control of Grain Microstructure and Enhancement of Saturation Magnetization in Nanocrystalline Fe-Si-B-Nb-Cu Alloy by Magnetic Crystallization
16th MRS-J symposium, "Novel Functions of Nano-Interfaces: Understanding and Design of Their Chemical, Mechanical and Electronic Properties", Nihon University, (2005, 12)
Hiromichi Fujii, Takashi Matsuzaki and Sadahiro Tsukada
5. Magnetic crystallization of Fe_{73.5}Si_{13.5}B₉Nb₃Cu₁ amorphous alloy
The 152nd ISIJ Meeting, Niigata University, (2006, 9).
Hiromichi Fujii, Victoria Yardley, Takashi Matsuzaki and Sadahiro Tsukada
6. Modelling of Magnetic Field-Enhanced Crystallization from an Amorphous Precursor
The 139th JIM Meeting, Niigata University, (2006, 9).
V. A. Yardley, Hiromichi Fujii and Sadahiro Tsukada
7. Kinetics of nanocrystallization under a magnetic field in Fe_{73.5}Si_{13.5}B₉Nb₃Cu₁ alloy
The 153rd ISIJ Meeting, Chiba Institute of Technology, (2007, 3).
Hiromichi Fujii, Victoria Yardley, Takashi Matsuzaki and Sadahiro Tsukada
8. Carbon diffusion in alpha iron under a strong magnetic field
The 142nd JIM Meeting, Musashi Institute of Technology, (2008, 3).
Hiromichi Fujii and Sadahiro Tsukada
9. The effect of a magnetic field on grain boundary energy and diffusion
Workshop on ISIJ, "The effect of a magnetic field on microstructural evolution", (2008, 8).
Hiromichi Fujii, Naoki Toda and Sadahiro Tsukada
10. Carbon diffusion in iron under a static magnetic field and field gradient
The 143rd JIM Meeting, Kumamoto University, (2008, 9).
Hiromichi Fujii and Sadahiro Tsukada
11. The effect of a magnetic field on grain boundary energy and surface diffusion in 99.99% iron
The 143rd JIM Meeting, Kumamoto University, (2008, 9).
Naoki Toda, Hiromichi Fujii and Sadahiro Tsukada
12. Interstitial diffusion and grain boundary energy under a strong magnetic field
Workshop on lattice defect engineering, JIM, (2008, 9).
Hiromichi Fujii, Naoki Toda and Sadahiro Tsukada

V. Research grants

1. Magnetic-field effects on metallurgical phenomena related to microstructural control of polycrystalline materials
Grant-in-Aid for JSPS Fellows (900,000 Yen (2007), 900,000 Yen (2008)).

VI. Prizes

1. Award from Dean of the School of Engineering, Tohoku University (2006.3)
2. Distinguish paper award for young scientists, The Japan Institute of Metals (2008.9)